Slamming And Whipping Analysis Of Ships

PhD Thesis

$$(EIv'')'' = q - \rho A\ddot{v}$$

Sopheak Seng

DCAMM Special Report No. S151
December 2012

DTU Mechanical Engineering
Department of Mechanical Engineering

SLAMMING AND WHIPPING ANALYSIS OF SHIPS

Sopheak Seng

TECHNICAL UNIVERSITY OF DENMARK

DEPARTMENT OF MECHANICAL ENGINEERING

SECTION OF FLUID MECHANICS, COASTAL AND MARITIME ENGINEERING

Preface

This thesis is submitted as partial fulfillment for the degree of Doctor of Philosophy at the Technical University of Denmark (DTU), Lyngby, Denmark. The work has been supervised by Prof. Preben Terndrup Pedersen and Prof., Dr. techn., Jørgen Juncher Jensen.

The major part of this work has been carried out in the Mechanical Engineering (MEK) Department during the time between May 2009 and December 2012. Between January 2010 to April 2010, the time was spent as a visiting student at Centre for Ships and Ocean Structures (CeSOS), Norwegian University of Science and Technology (NTNU), Trondheim, Norway.

SOPHEAK SENG

Lyngby, Denmark
December 20, 2012

The thesis was successfully defended April 18, 2013. A few misprints and minor errors were pointed out by the evaluation committee. Corrections for these misprints and errors as well as minor improvements have been made to the text in this official edition of the thesis.

SOPHEAK SENG

Lyngby, Denmark
April 30, 2013

Acknowledgements

Firstly, I would like to express my gratitude to Prof. Preben Terndrup Pedersen. He was my main supervisor during the first year of the project until he retired on October 15th, 2010 at an age of 70. Still, after his retirement he has been very active and has provided guidance and support until the very last day of the project. Without him, this project would never exist.

Secondly, I would like to thank Prof., Dr. techn., Jørgen Juncher Jensen not only for his excellent supervision, but also for encouraging and challenging me throughout the whole project. He has inspired and helped to shape my thoughts into the direction I see myself heading in the current research effort.

Many people have helped me with technical and practical problems related to the HPC cluster, the administration, and the project in general. I would like to thank them all for spending their time helping this project to proceed as smooth as possible. Special thanks go to Dr. Niels Gjøl Jacobsen for introducing me to the wave relaxation and generation framework.

Part of the present work is supported by EU FP7 project TULCS (Tools for Ultra Large Container Ships, project no. 234146) which provides experimental data for a validation of the numerical tools and implementations. The main financial support, however, has been provided by DTU, American Bureau of Shipping and the Danish Maritime Fund (grant no. 2009-03). Their support and involvement are essential for the project, which I greatly acknowledge and appreciate.

Executive Summary

Slamming on ships is a short duration impact occurring in extreme sea conditions. The most exposed parts of the ship are the bow flare, the forward bottom, and the stern. In comparison with the slowly varying wave loads, the impact loads typically increase sharply and disappear shortly after. Normally, the duration of impact is much less than 1 s. A severe impact can easily induce a transient vibration in the hull girder. This vibration is known as whipping. The concern is that additional stresses caused by the whipping vibration may, eventually, lead to a failure of the hull girder. An analysis of slamming induced responses may require an accurate prediction of not only the slamming loads but also the conditions under which slamming occurs. The challenge of predicting the occurrence of slamming is a key motivating factor in the development of a time-domain free-surface CFD simulation in this project. The presented work focuses on hull-girder responses in terms of VBM (vertical bending moment) amidships induced by bow flare slamming.

A two-phase Navier-Stokes solver provided by OpenFOAM® (an open source CFD software package), where the free surface is captured by a VOF (Volume-of-Fluid) formulation, has been adapted to study bow flare slamming on container vessels during critical wave episodes when moving in head seas. The deformation of the hull girder is evaluated according to the classical non-uniform Timoshenko theory.

Initially, the two-phase flow solver was validated for its capability to predict sufficiently accurate slamming loads in water-entry problems. Numerical predictions are compared against measurements for wedges, circular cylinders, and a two-dimensional bow flare section slamming into a calm free surface. The two-phase flow solver is found to predict slamming loads well. These works have provided insight into the basic numerical grid requirements for resolving slamming loads accurately. Hence, a criterion for defining a characteristic cell size suitable for resolving slamming loads has been proposed. In addition, the vertical slamming loads can be modeled accurately using a decomposition into an acceleration term and a velocity term with variable coefficients, which depend on the penetration depth and the geometry of the body. In principle, when these coefficients have been determined, the model can provide an accurate prediction of vertical forces on the body slamming into a calm free surface in any arbitrary motion. Although the general validity of the model has not been proven, the predictions of the decomposition model have been shown to be nearly as accurate as the predictions of the CFD simulations in three different test cases.

Directly related to this project is the development of a numerical wave tank. Waves are introduced into the computational domain by imposing potential flow wave solutions at the wave-maker boundaries. This wave generation technique is versatile and has been used for the purpose of introducing deterministic conditional waves into the computational domain. The conditional waves, which are the most

probable critical wave episodes, are determined from FORM (First-Order Reliability Method) analyses by conditioning on a given response. In this project, these analyses concern an extreme response of VBM amidships. For each conditional wave, the FORM analysis uses a non-linear time-domain strip theory to evaluate the responses, and provides a probability of exceedance in terms of the reliability index β associated with the given response. A case study using two container vessels has shown that it may be possible to use an MCF (Model Correction Factor) approach to transfer β to responses evaluated by the free-surface CFD method. Hence, useful statistical properties can be derived very efficiently from the CFD results.

In a comparison to non-linear strip theory, the CFD method provides high-resolution results at a far higher accuracy. Furthermore, the responses in the CFD method are evaluated based on implicit loads. Both low-frequency wave loads and high-frequency excitations from slamming events are evaluated implicitly. To account for whipping effects in the vertical bending moment, the flow solver is coupled to a Timoshenko beam solver using a two-way strongly-coupled partition scheme. A validation study for the implementation has been carried out using measurements from flexible segmented model tests of a 9,400 TEU container vessel. A reasonable agreement has been found between the numerical predictions and the experimental observations in the test cases where the contribution from the elastic deformation to the VBM is small. In one case, the measurements show resonance behaviors in the wetted 2-node vertical bending mode. In this case, the resonance effect can also be observed in the numerically predicted VBM except that the magnitude of the response is smaller than the measurements. Comparing the dry natural frequencies of 2-node and 3-node vertical bending modes, the numerical prediction using the non-uniform Timoshenko beam is very similar to the model tests. The mode shape of the 3-node mode, however, does not agree; maybe due to the difficulty in extracting the mode shapes from weak and inaccurate measurements. Unfortunately, there are many indicators showing several inconsistencies between the measurements and the numerical results.

Synopsis (in Danish)

Kortvarige væskeslag ("slamming") på skibsskrog forekommer i ekstrem sø med stejle bølger. De meste udsatte områder er skibets bovkonstruktion, bund og agterskib. Et kraftigt væskeslag kan inducere transiente vibrationer i skrogbjælken, især for lange og fleksible skibe. Udfordringen i at forudsige forekomsten af slamming er en afgørende motiverende faktor for at udvikle og benytte CFD simuleringer med fri overflade i dette projekt. Formålet med projektet har været at udvikle en simpel metode til at bestemme korttidsfordelingen af slamminginducerede whipping belastninger på skrogbjælken. Arbejdet præsenteret i afhandlingen fokuserer udelukkende på skrogbjælkens gensvar i form af det vertikale bøjningsmoment.

Først testes og valideres den benyttede to-fasede CFD model (luft og vand) i to dimensioner. De numeriske resultater sammenlignes med kraftmålinger for en kile, en cirkulær cylinder og en skibslignende sektion, som falder vertikalt på stillestående vandflade. Det er fundet at den to-fase CFD model kan estimere slamming belastninger nøjagtigt. Endvidere er det vist ved tre forskellige test, at slamming belastninger ved fald på stillestående vandflade i to-dimensioner i det lodrette plan kan modelleres ved at kombinere et accelerationsled og et hastighedsled med tilhørende koefficienter, der udelukkende afhænger af neddykningsdybde og sektionens geometri. I princippet kan disse koefficienter estimeres fra to CFD simuleringer, og kan genbruges til at estimere slamming belastninger ved en vilkårlig bevægelse af skibskroget.

I projektet er der udviklet en numerisk bølgetank. Bølger er introduceret i den numeriske tank ved at påskrive bølgeprofiler baseret på potentialstrømningsteori på randen. Denne teknik er blevet brugt til at simulere en deterministisk, betinget bølge. Betingede bølger er her defineret som de meste sandsynlige bølger bestemt ud fra en FORM analyse (First-Order Reliability Method), betinget på et givet gensvar. FORM analysen benytter ikke-lineær tidsdomæne strip teori til at evaluere gensvaret og sandsynligheden for overskridelse i form af pålidelighedsindeks β. Et casestudie for to container skibe har vist, at det er muligt at bruge en MCF (Model Correction Factor) teknik til at overføre β til gensvaret evalueret på baggrund af CFD simuleringer, som derved får samme statistiske sandsynlighed. Sammenlignet med den ikke-lineære strip teori giver CFD metoden resultater med høj opløsning med en langt højere nøjagtighed. Desuden er gensvaret beregnet ved CFD simuleringer baseret på implicitte belastninger, således at såvel de lavfrekvente bølgebelastninger som de højfrekvente slamming belastninger medtages automatisk. Det fleksible skrogs gensvar er beregnet ved at benytte den klassiske Timoshenko bjælke model koblet med den benyttede CFD model i en tovejs FSI (Fluid-Structure-Interaction) model. Implementeringen er valideret ved hjælp af målinger på en fleksibel segmenteret model af et 9400 TEU containerskib. Der er konstateret en god overensstemmelse mellem de numeriske resultater og målinger i tilfælde hvor den elastiske deformation

har et lille bidrag til VBM. I et tilfælde viser målinger resonans i den to-knuders vertikale svingning. Tilsvarende resonans kan ses i de numeriske resultater, der dog er fundet at have mindre amplitude end målingerne.

Contents

Preface iii

Acknowledgements v

Executive Summary vii

Synopsis (in Danish) ix

1 Introduction 1
- 1.1 State-of-the-art . . . 5
  - 1.1.1 Added Mass Model . . . 7
  - 1.1.2 BEM . . . 8
  - 1.1.3 Free Surface CFD . . . 10
- 1.2 Motivation & The Challenges . . . 11
- 1.3 Present Contributions . . . 12
- 1.4 Thesis Outline . . . 13

2 Mathematical Formulation 15
- 2.1 Governing Equations for Two-Phase Flow . . . 16
- 2.2 Arbitrary Lagrangian-Eulerian (ALE) Formulation . . . 19
- 2.3 Automatic Mesh Motion . . . 21
- 2.4 Rigid Body Motion in 6 DOF . . . 24
- 2.5 Modelling a Flexible Hull Girder . . . 29
- 2.6 Boundary Conditions . . . 33
  - 2.6.1 Wall . . . 34
  - 2.6.2 Inlet . . . 35
  - 2.6.3 Outlet . . . 35
  - 2.6.4 Symmetry Plane . . . 36
  - 2.6.5 Open Boundary . . . 36
- 2.7 Wave Generator & Relaxation Zones . . . 37
  - 2.7.1 Numerical Wave Generator . . . 37
  - 2.7.2 Inlet & Outlet Relaxation Zones . . . 38

3 Solution Algorithms & FSI Coupling Schemes 43
- 3.1 The PISO Scheme . . . 45
- 3.2 A Variable Step Size Adams-Bashforth-Moulton Method . . . 49
- 3.3 Strongly Coupled FSI . . . 52

4 Water Entry Problems **55**
4.1 Convergence Study . . . 57
4.1.1 Convergence of the Slamming Load on a Wedge . . . 62
4.1.2 Convergence of the Slamming Load on a Horizontal Circular Cylinder . . . 64
4.2 Wedge Shape . . . 65
4.3 Circular Cylindrical Shape . . . 71
4.4 Ship-like 2D Section . . . 73
4.5 CFD & the Classical Flat Plate Approximation . . . 76
4.5.1 Slamming Forces on a 2D 30° Wedge . . . 78
4.5.2 Slamming Forces on 2D Bow Flare Ship-like Section . . . 79
4.6 Truncated 3D Bow Flare Model . . . 83
4.7 Summary . . . 90

5 Numerical Wave Tank **93**
5.1 The Performance of the Relaxation Zone & Wave Generator . . . 94
5.1.1 Balancing the Volume Flux . . . 95
5.1.2 Reflection Coefficient . . . 100
5.2 Simulations of Conditional Waves . . . 101
5.3 Summary . . . 107

6 Slamming in Conditional Waves **109**
6.1 FORM & Probabilistic Design Considerations . . . 110
6.2 Critical Wave Episodes by FORM . . . 112
6.3 FORM & Slamming on Ships . . . 116
6.3.1 A Panamax Container Ship (KCS) . . . 118
6.3.2 A Post-Panamax Container Ship . . . 122
6.4 Summary . . . 126

7 Hydroelasticity in Slamming **127**
7.1 The Elastic Backbone Model . . . 128
7.2 Selected Regular Wave Conditions . . . 131
7.3 Numerical Setup & Initial Conditions . . . 133
7.4 Whipping & Springing Responses in Regular Waves . . . 135
7.4.1 VBM at 5 Cuts . . . 135
7.4.2 Resonance Effect . . . 137
7.4.3 Heave & Pitch Motion . . . 142
7.5 Summary . . . 145

8 Conclusions & Recommendations **147**
8.1 Conclusions . . . 147
8.2 Suggestions for Further Work . . . 150

References **151**

A Artificial Compressive Term **161**

B The Convective Velocity in ALE Formulation **165**

C Stodola's Method **169**

List of PhD Theses Available from the Department 173

Chapter 1

Introduction

A sea-going vessel moving in waves experiences many types of loads. Those, which act continuously on the hull, are hydrostatic loads and slowly varying loads due to wind, wave, and viscous friction. In addition, there are extreme loads, which occasionally occur, known as Green water and slamming. Green water occurs when a large volume of water flows violently across the deck and can cause severe damage to on-board equipment. Slamming, on the other hand, is a violent short duration impact between the fluid surface and the hull, which typically occurs in rough weather with steep waves.

On a monohull, the most exposed areas for slamming are the stern, the bow flare and the forward bottom. Stern slamming occurs mainly in following seas at slow speed where the rapid vertical motion of the free surface causes an impact on the flat stern. Bottom slamming occurs in connection with a large pitch motion that causes the forward part of the vessel to emerge from the water. A subsequent re-entry may lead to an impact scenario between the bottom and the free surface. The bottom slamming may be followed by a bow flare slamming depending on circumstances; i.e. whether the entry velocity is still high enough or the splash up free surface is critically positioned and hits the bow flare at a relatively small impact angle. Another scenario, which may lead to bow flare slamming, is when the vessel is moving in oblique seas and the incident wave reaches its breaking point, forming a steep front at the moment it hits the flare area. This is also known as wave slapping. Other slamming related events are wet-deck slamming and internal sloshing. The former is observed mostly on high-speed catamarans and the latter can be an issue on LNG carriers.

Slamming may cause damage to local structures. There are many reports of slamming related damages ranging from cracks and buckling of plate panels to loss of a whole bow visor, see e.g. Yamamato et al. (1985) and the report of the Joint Accident Investigation Commission (JAIC (1997)). In September 1994, the Ro-Ro Passenger Vessel MS Estonia sank in the Baltic Sea. The weather was rough and the official investigation JAIC (1997) concludes that bow flare slamming was the most likely cause of the disaster. A heavy wave hit the bow doors causing the visor to separate and to open the ship's bow door. Thereafter, water started to flood into the vehicle deck. The damaged ship listed badly to starboard and sank in less than one hour after the slamming incident.

Even though slamming occurs locally, the impact can cause the hull girder to vibrate. The process is known as whipping, which is a transient hull vibration induced

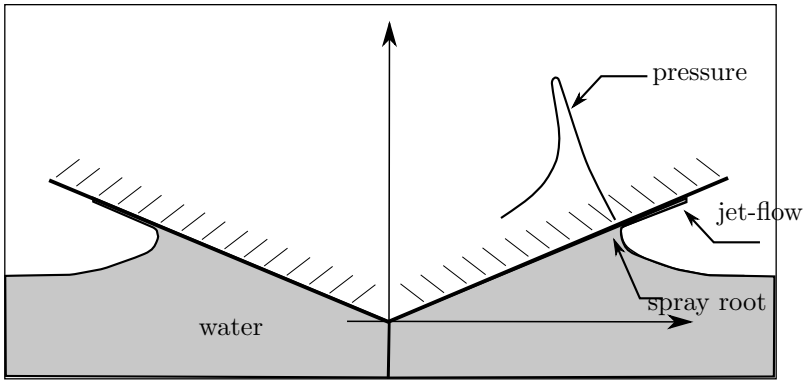

Figure 1.1: A sketch of water pile up on a wedge penetrating a calm free surface. Adopted from Yettou et al. (2006)

by the impulse of the slamming load. A typical slamming impact lasts less than a fraction of a second. The induced whipping vibration, however, may last several seconds and can be detected as fast variations in the acceleration. Large accelerations may have a negative effect on cargos as well as discomfort to passengers. Early in the design phase of large ships, it is desirable to include a whipping response analysis because whipping may also cause a noticeable increase in the extreme value of hull girder bending moment, see e.g. Pedersen & Jensen (2009). In January 2007 the 4419 TEU container ship MSC Napoli experienced a failure of the hull girder when passing the English Channel in rough weather. An investigation done by Marine Accident Investigation Branch (MAIB (2008)) identified whipping as a plausible cause of the collapse of the hull girder. A whipping effect assessment done by BV (2008) concludes that whipping may cause an increase of wave bending moments for the MSC Napoli by as much as 30%. Indeed the whipping response induced by a single severe slamming can be enough to cause a collapse of the midship section. The maximum responses do not occur during the short duration of the impact but later in the subsequent whipping response.

The operation of the vessel is important for the occurrence of slamming events. For shipmasters, it has been a common knowledge for a long time that a speed reduction and changing course may help to reduce the probability of slamming. Ochi & Motter (1974) recommends a speed reduction when the probability of slamming is larger than 3% (i.e. 3 slamming occurrences for every 100 passing waves).

Slamming occurs because the structure, and a considerable amount of fluid collide with each other. It is well known that the relative angle between the structural surface and the fluid surface is very important in slamming. Often, the initial study is done on a rigid wedge with a fixed deadrise angle penetrating a calm free surface at a high velocity. Many experimental studies (see e.g. Yettou et al. (2006)) have confirmed that the free surface deforms as illustrated in Fig. 1.1. The displacement of the wedge causes a water pile-up forming a jet-flow with spray roots located at the intersection between the free surface and the body surface. The spray root moves along with the expanding wetted area. The smaller the deadrise angle is, the faster the wetted area expands. Even if the penetration velocity is not high, the small deadrise angle causes the wetted area to expand rapidly with a large acceleration of the fluid. In fact, the large fluid acceleration is usually the reason why researchers neglect the effect of the gravitational force since the gravitational acceleration will be small compared to the fluid acceleration caused by the slamming impact. The

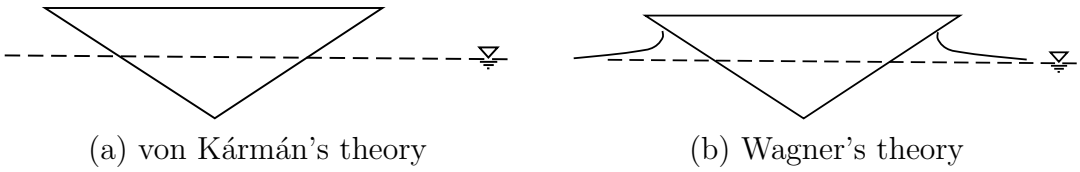

Figure 1.2: (a) The momentum theory of von Karman neglects the water pile-up profile. (b) The Wagner's theory accounts for the pile-up profile.

wetted area is important for the pressure distribution since the peak pressures are located at the spray roots and move with the spray roots as illustrated in Fig. 1.1.

Experimental studies have shown that with deadrise angles smaller than $4^o \sim 5^o$, air may be trapped creating air pockets. The high pressure causes the trapped air to be compressed, limiting the peak pressure. The compressibility of the fluid and the air pocket acts like a spring causing a high frequency oscillation of the compressed air volume. The overall effect of trapped air is to lower peak pressures on the slamming area. This is also known as the air-cushion effect. In a controlled environment, the trapped air can be produced. In reality, however, trapped air may not occur very often since air can escape more easily on an uneven and 3D slamming surface.

Historically, the first paper about slamming was written by von Kármán (1929). The interest was to predict slamming load on seaplane floats during landing. Von Kármán's theory is based on a momentum formulation and is well known for its simplification of the water pile-up profile. Basically, the water pile-up is neglected and the wetted length is evaluated up to the intersection with the undisturbed free surface. The theory was extended to account for the water pile-up profile by Wagner (1932). Figure 1.2 illustrates the major difference between von Kármán's theory and Wagner's theory. The important implication is that the wetted length is different in the two theories. A simplified 2D analysis of a blunt body impact, as shown briefly in Section 4.5, reveals the importance of the wetted length in an estimation of the slamming loads. The fact that the simplified slamming force may be written in terms of rate of change in added mass, has inspired researchers to pursue slamming problems using approximate and empirical momentum formulations, see e.g. Payne (1994; 1995), Fairlie-Clarke & Tveitnes (2008), and Kapsenberg & Thornhill (2010). The formulation is also known as momentum slamming in which the slamming load is calculated continuously mainly using the time derivatives of the added mass.

The empirical approach presented in Kapsenberg & Thornhill (2010) also accounts for the water pile-up as formulated in the Wagner's theory. The method is fast and efficient since the parameters are pre-calculated and tuned specifically to the vessel. For example, the added mass for different draughts and submergence are pre-calculated using a 3D BEM (Boundary Element Method) code. Kapsenberg & Thornhill (2010) has shown that it is possible to provide a reasonably accurate prediction of the slamming force using this method. The challenge, however, is how to fine-tune the parameters so the slamming estimations are applicable for a particular vessel.

Full-scale experiments on slamming are rarely done. Although on-board measurements exist, the extreme weather condition is seldom encountered. Occasionally the responses of the vessel show signs of slamming. The lack of an accurate estimate of the actual sea profile, however, put a strong limit to the usefulness of the full-scale

measurements. Usually, the tuning of the parameters is carried out against scaled model tests where the results are scaled to full scale using the Froude scaling law. This scaling method, however, may not be applicable for scaling the short duration impact forces since, at full scale, the important phenomena such as trapped air and air entrainment may contribute differently to the slamming forces. As of today, there is no well-proven method for scaling impact forces, which accounts for the effect of trapped air and air entrainment. Bredmose & Bullock (2008) investigated the scaling effect of the maximum pressure inside an axisymmetric air-pocket trapped during a wave impact on a vertical wall using an ideal gas with the adiabatic index $\gamma = 1.4$. The idealized piston type compression is written (cf. Bredmose & Bullock (2008))

$$\left(\frac{p_{\max}}{p_0}\right)^{\gamma/(\gamma-1)} + (\gamma-1)\left(\frac{p_{\max}}{p_0}\right)^{-1/\gamma} - \gamma = cS \tag{1.1}$$

where $p_0 = 10^5$ Pa is the reference atmospheric pressure and S is the geometric scaling factor. The function c is a problem dependent constant. Bredmose & Bullock (2008) extend a 1D piston type compression model to axisymmetric compression in 2D and 3D, and the corresponding c functions are

$$\text{1D:} \quad c = \frac{1}{2}\frac{\gamma-1}{p_0}\rho u_0^2(\alpha-1) \tag{1.2a}$$

$$\text{2D:} \quad c = \frac{\gamma-1}{p_0}\rho u_0^2 \ln\alpha \tag{1.2b}$$

$$\text{3D:} \quad c = \frac{3}{2}\frac{\gamma-1}{p_0}\rho u_0^2(1-1/\alpha) \tag{1.2c}$$

Where u_0 is the initial velocity of the piston extended from position x_0 to αx_0. Most importantly, the Froude scaling law dictates a linear dependency, $(p-p_0)/p_0 \sim S$ while the scaling shown in Eq. (1.1) has an asymptotic relation $(p-p_0)/p_0 \sim S^{3.5}$ for large cS. Bredmose & Bullock (2008) discussed that the Froude scaling law is too conservative for scaling the typical laboratory pressures, which are typically well below $p - p_0 < 300$ kPa.

Another issue with measurements is the difficulty in measuring sharp rising pressures and forces. A high sampling rate, typically more than 2 kHz, is required to capture the peak pressures. Mounting a pressure probe on a smooth surface introduces small bumps and cavities causing an unwanted air pocket to form easily above the probe location. The force measurements may also be contaminated by frictional forces in the mounting rig. Moreover, isolating the actual impact force is not easy since the inertia force may not be easy to estimate. Nevertheless, there are many published papers presenting experimental results of slamming using simple geometries such as a wedge or a circular cylinder aiming for validating numerical tools, see e.g. Greenhow & Lin (1983), Aarsnes (1996) and Tveitnes et al. (2008). In Aarsnes (1996), a ship-like bow flare section was used in vertical drop tests on still water. The ship-like section was mounted on a vertical sliding rig to enforce the vertical motion. The setup is far from a realistic slamming in waves, but it is a necessary step since the setup allows a better control of the impact conditions, e.g. fixed penetrating velocities and relative impact angles. Even though the setup is practically the same, the results of the experiments may contain a large scattering.

The large uncertainty in the measurements has been recognized for a long time especially with the measured slamming pressures. However, the total impulse, which is the time integration of the forces, does not vary much. The implication is that the total momentum before and after the slamming impact is approximately the same in each trial, but the duration of impact may vary considerably.

The random nature of the slamming phenomena has motivated many researchers to approach the slamming problems using statistical tools. Perhaps, the most famous statistical work on slamming was done by Ochi (1964b; 1964a). Ochi's statistical analysis, however, is restricted to bottom slamming where the forward part of the vessel has emerged from the free surface and re-enters at a relatively high velocity. Ochi defined a threshold relative impact velocity for bottom slamming. Ochi's recommended threshold value is:

$$v_{cr} = 0.093\sqrt{gL} \tag{1.3}$$

where g is the gravitational acceleration and L is the length of the vessel. The probability of bottom slamming can be estimated as the joint probability between the bow emergence and the exceedance of the threshold velocity during the re-entry. The expression becomes, cf. Jensen (2001)

$$Pr\{slam\} = \exp\Big(-\frac{T^2}{2s_z^2} - \frac{v_{cr}^2}{2s_{\dot{z}}^2}\Big) \tag{1.4}$$

where T is the draught at the slamming location and z is the relative vertical position. The symbols s_z and $s_{\dot{z}}$ are the standard deviation of z and its time derivative $\dot{z}$, respectively. The introduction of the threshold velocity is obviously a simplification of the conditions which lead to bottom slamming. It provides a very abrupt definition for the occurrence of the bottom slamming whereas, in reality, the fluid loads act continuously on the structures. Eventually, the statistical analysis of the slamming phenomena shall be extended to bow flare and stern slamming; but the existing methods for slamming load predictions are not yet well established and efficient enough to carry out a reliable short-term and long-term extreme value statistic accounting for the slamming-induced effects on the local and global structures.

1.1 State-of-the-art

The effect of slamming shall be evaluated with the focus on structural responses of interest. Jensen et al. (2009) presented a simplified method to account for whipping in the estimation of an extreme value of the wave-induced vertical bending moment. The hull girder was modelled using a non-uniform Timoshenko beam and the whipping process was analyzed as a free vibration problem assuming that the duration of the impact is very short compared to the highest natural period of the hull girder. The use of modal superposition, together with these simplifications, allows the equation of motions to be written as (cf. Jensen et al. (2009))

$$\ddot{u}_i + 2\xi\Omega_i\dot{u}_i + \Omega_i^2 u_i = \frac{P_i(t)}{M_i} \tag{1.5}$$

where u_i is the unknown modal coefficient of mode i; ξ is the damping coefficient; and Ω_i is the natural frequency of mode i. The dot represents the time derivative. The slamming load projected into the modal coordinate is represented by P_i; and M_i is the modal normalization. To apply the initial conditions, Eq. (1.5) is integrated once to obtain the modal velocity

$$\dot{u}_i(t) = \int_0^t \frac{P_i(\tau)}{M_i} d\tau - 2\xi\Omega_i u_i(t) - \Omega_i^2 \int_0^t u_i(\tau) d\tau \tag{1.6}$$

Two initial conditions are required. The first one is to assume zero initial deflection, $u_i(0) \approx 0$. The second one is that the free vibration starts out with a non-zero initial velocity i.e. $\dot{u}_i(0) \neq 0$. The latter condition can be justified by the previous assumption of impact with a very short duration. During slamming, some energy is transferred to the hull girder but the duration is so short that the hull girder has no response other than to accelerate very fast and reach the assumed finite initial velocity. Let t_s be the duration of impact, the initial conditions are

$$u_i(0) \approx 0 \quad ; \quad \dot{u}_i(0) \approx \int_0^{t_s} \frac{P_i(\tau)}{M_i} d\tau \tag{1.7}$$

The solution to this free vibration problem is well known, see e.g. Inman (2001),

$$u_i(t) = \frac{\dot{u}_i(0)}{\tilde{\Omega}_i} \sin(\tilde{\Omega}_i t) \exp(-\xi_i \Omega_i t) \tag{1.8}$$

where $\tilde{\Omega}_i = \Omega_i \sqrt{1 - \xi_i^2}$ is the damped frequency. Only a few main parameters are required in the solution, see Jensen et al. (2009). These are the length of the vessel, the moulded breadth, the draught, the block coefficient and the bow flare coefficient. The parameters required for the slamming load calculations are the deadrise angle (α), the breadth B_l, and the draught d_l at the longitudinal position of the slamming location. If the bow flare sections are to be approximated by a wedge model, t_s can be estimated from (cf. Zhao & Faltinsen (1993)) $t_s \approx B_l \tan\alpha/(3\dot{z})$, where $\dot{z}$ is the relative vertical impact velocity between the body surface and the free surface. The main issue with this model, however, is the estimation of the slamming load $P_i(t)$ which may require further simplification of the slamming event. Pedersen & Jensen (2009) introduces the so-called slamming impulse $I_i = \int_0^{t_s} P_i(t)dt$ and argued that the detailed time variation of the slamming load is less important in the estimation of the maximum whipping bending moment. Thus, it is sufficient to know the total impulse I_i which is the time integral of the slamming force.

Analytical methods based on potential flow theory exist but are limited to impact on calm water for simple geometries such as a wedge, a cylinder, a cone, a sphere or an ellipsoid. For validation purposes, the analytical methods are very useful. The similarity solution by Dobrovol'skaya (1969) was the first complete solution for a symmetric impact of a 2D wedge on still water. In the solution, the gravity effect is ignored and the impact velocity is assumed constant. Dobrovol'skaya (1969) transformed the problem into a non-linear singular integral equation of function $f(t)$, $t \in [0, 1]$ (Eq. (4.25) in Dobrovol'skaya (1969)) which can be evaluated numerically.

The velocity and pressure distribution on the 2D wedge can be evaluated when the function $f(t)$ is known.

Recently, efforts on solving the water-entry problem analytically are presented in Mei et al. (1998) and Korobkin (2004). By means of double-body conformal-mapping solutions and approximated boundary conditions (known as the generalized Wagner's method, Zhao et al. (1996)), Mei et al. (1998) were able to provide a semi-analytic solution scheme for a wide range of 2D body sections including a wedge, a circular cylinder and general section geometries representable by Lewis forms (Landweber & Macagno (1967) and Kerczek & Tuck (1964)). Mei et al. (1998) presented the solution assuming a constant impact velocity; and later, the solution for the wedge impact was extended to account for variable impact velocities by Yettou et al. (2007).

The analytical work by Korobkin (2004) was based on the so-called Logvinovich model where the pressure distribution over the wetted area is evaluated from the Bernoulli equation with the nonlinear terms included. The original work of Logvinovich (1969) accounts for the splash-up effect of the free surface and applies the flat-disc approximation (see also Section 4.5) which can be justified for a blunt body impact. The real shape of the body is not accounted for when solving for the velocity potential. Korobkin (2004) called his model a Modified Logvinovich Model (MLM) and recognized that it can be generalized to the three-dimensional impact problem. In his later work, Scolan & Korobkin (2001) and Korobkin & Scolan (2006), the model was successfully extended to calculate impact forces on 3D blunt bodies assuming elliptical water lines. Applying analytical models mentioned above in a realistic engineering case is not straight forward since the approximate conditions during the symmetric water-entry on calm water are still very far from typical slamming events in rough sea.

Several empirical and numerical methods have the potential to be applied in a real sea state. These are:

- the added mass model
- the nonlinear boundary element methods (BEM) solving the generalized Wagner problem
- the free surface CFD methods

A discussion of the advantages and disadvantages of these methods is given in the following sections.

1.1.1 Added Mass Model

The work published by Payne (1994; 1995) was concentrated on the force acting on a planing hull where the wetted surface exposed to slamming can be approximated by a prismatic surface with deadrise. Empirical formulas for water pile-up and vertical forces on a prismatic hull were formulated.

Later, an empirical approach utilizing the momentum theory for estimating slamming loads on bow flare segment was presented in Kapsenberg & Thornhill (2010). Following the classical momentum theory, the impact force is written as the rate of change of the momentum where the added mass of the accelerated fluid is taken into account. With some simplifications, the equation for the impact force is written as (cf. Kapsenberg & Thornhill (2010)):

$$\boldsymbol{F} = \Big(\frac{\partial a_{11}}{\partial x}u + \frac{\partial a_{33}}{\partial z}w\Big)\boldsymbol{u} + a_{11}\dot{\boldsymbol{u}} \tag{1.9}$$

where $\boldsymbol{u} = \{u, w\}^T$ and $\dot{\boldsymbol{u}}$ are the local relative velocity and acceleration between the fluid and the slamming area. The added masses a_{11} and a_{33} are the infinite frequency added mass evaluated using a 3D BEM method. In their primary investigation, the work was concentrated on bow flare slamming. Therefore, the bulb was removed.

Experimental measurements as well as CFD calculations (ANSYS CFX 11.0) were presented comparing the slamming forces and pressures on a preselected bow segment. The model is empirical and the local wetted surface must be prescribed. Several tuning parameters are introduced to account for local pile-up of water and bow wave. The tuning parameters are to be evaluated from CFD calculations or experiments. While the results presented in Kapsenberg & Thornhill (2010) seem reasonable, the process of finding an appropriate set of tuning parameters can be very cumbersome. Furthermore, there is no justification that the approach can be generalized to all sea states and slamming conditions; and there may be no easy way to account for the presence of the bulb.

1.1.2 BEM

The boundary element method is commonly applied for solving hydrodynamic problems. For slamming related problems the work based on BEM can be found e.g. in Greenhow & Lin (1985), Zhao & Faltinsen (1993) and Zhao et al. (1996).

The BEM can provide a solution for potential flow problems with linear or nonlinear free surface and body boundary conditions. There is no accounting for viscous effects. Often, also the gravitational effect is neglected in a slamming problem. However, it may be important especially in a mild impact where the acceleration of the fluid cannot be assumed much larger than the gravitational acceleration. When needed the graviational force can be included in the BEM method.

An early work applying BEM to slamming problems was published by Greenhow & Lin (1985) where the solution accounts for a fully nonlinear free surface and body boundary conditions in two-dimensional water-entry problems. A wedge was used in the demonstration. The jet-flow, see Fig. 1.1, produces a very problematic free surface, which is difficult to discretize. Indeed, BEM has problems following the complex free surface deformation induced by the jet-flow.

Later work, using the BEM, was done by Zhao & Faltinsen (1993) also using two-dimensional wedges for the validation purposes. The wedge shape is very useful for the numerical validation due to its simple shape and the existence of an asymptotic solution for small deadrise angles as well as the fact that the similarity solution, in principle, is valid for any deadrise angle. The numerical technique applied in Zhao & Faltinsen (1993) is not restricted to a wedge shape but can be applied to a wide range of two-dimensional cross sections. The nonlinear free surface condition without the gravitational field is satisfied, as well as the exact body boundary condition. Zhao & Faltinsen (1993) simplified the jet-flow by removing the flow region where the pressure is otherwise approximately equal to the atmospheric pressure. Thus, the fluid domain does not contain the whole jet-flow, and the problem becomes simpler to handle. A criterion on the angle between the free surface and the body surface is

empirically defined to cut off the jet-flow. For example, when the angle is smaller than 6° (i.e. the free surface is almost parallel to the body surface) the jet-flow is removed. Using this technique, the results for deadrise angles from 4° to 40° were presented.

Zhao et al. (1996) extended the BEM method to handle flow separation at a knuckle on a pre-defined location on a curved surface. In the same paper, they proposed a new approximation of the water-entry problem, which became known as the generalized Wagner theory. The results were compared with measurements from drop tests performed at Marintek. The simplification was that the complicated pile-up free surface was reduced to a flat free surface extended from the spray root. In other words, the free surface boundary conditions were satisfied not on the exact free surface but on the approximate flat free surface at the pile-up level. This simplification provided a good approximation to the slamming force on the wedge when compared to the similarity solution and the experiments. Later, the theory was adopted by several researchers for slamming calculations. One of the most noticeable works which took the slamming calculation one step further toward a direct calculation in a realistic sea state was published by Tuitman & Malenica (2009).

The slamming loads presented in Tuitman & Malenica (2009) are evaluated explicitly. The triggering mechanism for the slamming calculation is a pre-defined threshold velocity similar to the one proposed by Ochi (1964b; 1964a) for bottom slamming. The pressure distribution in three-dimensions is evaluated using 2D-strips defined based on the instantaneous local impact angle which can be perpendicular or oblique to the longitudinal direction of the hull girder. There is no theoretical justification for the 2D-strip approach but the approach provides a practical approximation of the distribution of the slamming pressure in 3D. Thus, the slamming load is accounted for approximately and explicitly.

The use of BEM to solve for the slamming loads includes several difficulties, such as:

- Singularity at the initial contact point on a curved surface: The initial transition from dry to wet body surface introduces a singularity in the velocity potential causing the pressure to be infinite. This is not a significant limitation since the evaluation of the slamming loads can be set to initiate from a small submergence of the body. However, this may prove problematic when the relative angle between the free surface and the surface of the body is small.

- Free-surface separation: The free surface may separate. Around a sharp corner (knuckle), the location of the separation point is well defined and can be imposed directly. However, the separation may occur on a smooth curved surface and the location of the separation point must be explicitly derived using empirical criteria, see e.g. Zhao et al. (1996).

- Body curvature: Around the bulbous bow, the strong curvature of the hull surface can be very challenging to handle by BEM. Often, the implementation applies the generalized Wagner method to simplify the free surface boundary conditions. Consequently, the cross section of the body is modified such that any concave surface is removed before the slamming calculation.

While these issues are manageable, the need for introducing several empirical criteria

may prove very tedious and not attractive. Furthermore, it is still a big challenge to show how slamming loads can be evaluated in a realistic sea state using BEM.

1.1.3 Free Surface CFD

The term CFD has been widely used to refer to numerical methods solving RANS (Reynolds-averaged Navier-Stokes) or Navier-Stokes equations using the FVM (Finite Volume Method) or the FDM (Finite Difference Method) to discretize the whole fluid domain. For slamming problems, the CFD method must be extended to account for the free surface and the floating body.

Several free surface capturing methods have been adopted for an investigation of slamming impacts during a water-entry in calm water. The most commonly used are the VOF method (volume of fluid, Hirt & Nichols (1975)) and the LS (level set, Osher & Sethian (1988)). Muzaferija et al. (1999) performed drop test simulations using a wedge and a 2D bow flare section and compared the vertical slamming forces with the available experiments proving that the VOF-based free surface CFD method is capable of predicting the short duration impact loads to a reasonable accuracy. A similar finding was published by Kleefsman et al. (2005) using the VOF approach but with a reconstruction of the free surface based on a local height function. One of the attractions of VOF is the conservation of mass and volume which may prove very difficult to obtain if the free surface is captured using Level Set (LS).

One of the recent papers with level set applied to slamming problems was published by Zhang et al. (2010). Most interestingly, Zhang et al. (2010) adopted the so-called immersed boundary method (see Mittal & Iaccarino (2005) for an excellent review) for handling the body motion. Using the immersed boundary method a very complex body motion can be simulated. Another example of the application of level set in slamming related problems was published in Kim et al. (2008) and in Yu & Chen (2007). The highlight of their work is the use of FANS (Finite-Analytic Navier-Stokes, Chen et al. (1990)), and overset grid. FANS applies local (on cell level) analytic solutions of the linearized convective transport equations in the numerical solution scheme. The local analytic solutions are very difficult to obtain on cells other than simple rectangular or triangular cells emphasizing a need for analytical or numerical coordinate transformations from the physical coordinate to the computational coordinates. The physical coordinate applied in Chen et al. (1990) is a body-fitted curvilinear coordinate; and to ease the grid generation the overset grid approach has been adopted. Besides the flexibility in handling a complex geometry, the overset grid configuration allows a complex rigid body motion. The main advantage of using the finite analytic method is its superior numerical accuracy, stability and its rapid convergence behavior. The combination of level set, overset grid and FANS produces a versatile and stable two-phase flow solver with many applications ranging from slamming and wave run-up on rigid ships and offshore structures to vortex-induced vibrations (VIV) problems on risers, see Chen et al. (2008). However, using the FANS approach may prove difficult in handling the flexural deformation of the body required to resolve a fully coupled hydroelastic response such as the whipping of the hull girder.

The whipping responses may introduce an important coupling between the flow and the structural deformation for very large vessels where the structure of the hull is relatively soft. This coupling is generally referred to as an FSI problem

(Fluid-Structure-Interaction). An implicit coupling for the rigid-body motion in waves has been done successfully by many researchers, but the step toward a coupling with a flexible body has been very demanding. Often, a full 3D finite element code is coupled explicitly to the flow solver for efficiency. Concerning the vertical flexibility of the hull girder of a monohull, the structural model can be simplified to a beam model. Such a simplification has already been implemented in Oberhagemann et al. (2008). A more advanced structural modeling was presented in Cabos et al. (2011).

The use of a free surface CFD method in slamming problems provides several advantages. These are:

- High-resolution results: The load distributions as well as the local and global responses are of high-resolution. At the research stage, where there is a need for a better insight in the slamming loads, the high-resolution is desirable.
- Jet-flow and free surface separation can be captured: The jet-flow may not be significant for the slamming load since the pressure distribution inside the jet-flow is very close to the atmospheric pressure. However, a re-entry of the jet-flow may cause a disturbance on the free surface and the surrounding pressure field. One particular example is wave impacts on a vertical wall, see e.g. Bullock et al. (2007). The initial impact creates a jet-flow parallel to the vertical wall. The volume of water pile-up, eventually, loses its momentum due to the gravitational field, which falls back and merges with the remaining fluid causing an increase in the pressure field. The re-entry of the pile-up water may create a secondary impulse in the slamming force.
- Complicated body-shapes can be simulated
- Air pocket and the compressibility effect can be modelled: There are very few publications on slamming load evaluations, which account for air pocket and the compressibility effect of the fluid. Nevertheless, the work published in Bredmose & Bullock (2008) shows that the compressibility effect can be accounted for using a free surface CFD method.
- Direct calculation: The free surface CFD method provides a flow solution with fewer assumptions compared to the potential flow solution provided by e.g. BEM. There is a possibility to include the viscous effects as well as modelling the turbulence.

It shall be emphasized that some of the features mentioned above have not yet been proven reliable. However, the versatility of the free surface CFD methods makes it very attractive. The major barrier preventing the free surface CFD method to be used more widely in practical design cases is the huge demand on the computational resources. Other typical problems, one may encounter, are unwanted numerical diffusion, slow convergence and poor numerical stability. A proper evaluation requires not only a knowledge of the applied numerical schemes, but also a good understanding of the physics of the flow.

1.2 Motivation & The Challenges

In a realistic sea state, the slamming event is a highly random process. During the design phase, attention shall be paid not only on the deterministic load cases but

also on the short-term and long-term statistical properties of the events. Most of the long-term statistical properties can be derived from the short-term statistics. Therefore, the work shall be concentrated on the short-term responses.

Based on the previous review, it can be concluded that there is still a need for a rational method to evaluate slamming and whipping responses. Among the methods discussed previously, the CFD approach can provide the largest flexibility and direction calculation of the slamming loads. However, a direct application of CFD in a statistical analysis will be very impractical because of the huge CPU requirement. Hence, an interesting and very important challenge is how to derive short-term statistical properties of slamming events from the CFD results without having a need to perform a very large number of simulations. Therefore, directly related to this work is the development and implementation of the numerical methods required to perform a slamming simulation in a realistic sea state.

The objectives of the current project are: firstly to develop a CFD tool for direct calculations of slamming loads and whipping responses in a realistic sea state; and secondly to investigate possible applications of CFD in a short-term response analysis of a large flexible vessel taking into account the influence of the slamming induced effects.

As mentioned previously, there are several categorizations of the slamming events. These are bottom, bow flare, stern and wet-deck slamming. The focus of the current work is the bow flare slamming on a monohull moving at a constant forward speed in head sea. The primary structural response of interest is the extreme value of the global vertical bending moment in the hull girder, which may increase significantly due to the slamming-induced whipping vibration in the hull girder.

The open source CFD package known as OpenFOAM will be used in the project. The package provides an free surface incompressible Navier-Stokes solver where the free surface is captured by a VOF (Volume-of-fluid) technique. The tasks directly related to the project are

- Numerical wave tank: The VOF-based NS solver exists as a standard solver in OpenFOAM. The challenge is to further develop and setup a numerical wave tank. The task includes an implementation of a wave-maker, wave absorption, and a stable mesh motion to account for a floating body. In addition, a structural model for the hull girder is required as well as a stable coupling between the structural deformation and the free surface NS solver.

- Validation: The free surface NS solver needs to be validated, especially for its capability for predicting slamming loads.

- Evaluation: Any proposed method for incorporating the CFD approach in a short-term statistical analysis will need to be evaluated.

1.3 Present Contributions

The main contributions of the present research effort, which relate to slamming on ships, are:

- The open source CFD package has been extended with several features aiming for a direct simulation of a slamming event in waves. A wave-maker for

generating regular waves and conditional waves has been implemented along with a relaxation technique to prevent wave reflection from the outlet boundary. In the process, a new adaptive scheme for evaluating local coefficient for wave relaxation has been proposed. The classical modal superposition approach to solve for the deflection of a non-uniform Timoshenko beam has been coupled to the flow solver in a two-way strongly coupled partitioning scheme. Compared to the finite element solution implemented in Oberhagemann et al. (2008), the classical modal superposition approach provides solutions through direct numerical integrations of the beam equations. All numerical implementations have been done for use on massively parallel processing platforms.

- A validation study using 2D water entry problems has been carried out for the flow solver, see Chapter 4. From the validation study, a criterion for defining a characteristic cell size suitable for resolving slamming loads has been proposed, see Section 4.1.2. The application of the flow solver has been further extended to investigate the feasibility of approximating slamming loads and the associated total impulse using a 2D strip approach.

- Using the validated CFD code, it has been shown that the vertical force in a two-dimensional water-entry problem can be modelled using a decomposition model similar to the classical flat plate model (see Section 4.5), except that the parameters related to the wetted length are estimated from the two-dimensional CFD results. In three different test cases, it is shown that the decomposition model can provide predictions of the vertical slamming forces which are of comparable accuracy to the two-dimensional CFD results. Although the general validity of the model has not been proven, the results of these three test cases show that only one single CFD simulation is required to determine the parameters, and these parameters can be used in the decomposition model to predict vertical slamming loads in a wide range of impact velocities.

- A review of the state-of-the-art statistical methods for evaluating the probability integral for a rare event such as slamming on ship is provided. A further investigation has been performed focusing on the use of a model-correction factor to transfer short-term statistical properties derived by FORM (First-Order Reliability Method) to the CFD results. The possible application of the CFD method in a short-term extreme response statistical analysis is discussed.

- A hydroelastic coupling using the non-uniform Timoshenko beam model has been validated against measurements of a post-Panamax container ship moving at a constant forward speed in regular head sea. A discussion on the use of FORM in slamming problems is provided.

1.4 Thesis Outline

The remaining chapters of this thesis are organized as follows:

- Chapter 2 is devoted to describe the underlying mathematical model for the VOF-based incompressible NS solver and the numerical techniques applied to solve the flow equations, the structural deformation and the strong hydroelastic coupling.

- Chapter 3 describes the numerical solutions and algorithms for solving the coupled flow equations.
- Chapter 4 describes the details of the validation study performed to assure that the adopted flow solver is capable of predicting the short duration slamming loads.
- Chapter 5 provides a discussion on the capability of the wave-maker as well as a limitation related to the adopted wave generation and relaxation technique. Furthermore, a discussion related to simulations of conditional waves derived by FORM is provided.
- Chapter 6 discusses the possible use of the model correction factor in combination with the CFD method to derive statistical properties for slamming events in a realistic sea state.
- Chapter 7 provides a validation of the implemented hydroelastic coupling between the Timoshenko beam solver and the flow solver. The hydroelastic effects seen in whipping and springing responses are discussed.
- Several conclusions can be made from the present research effort. These are summarized in Chapter 8 along with suggestions for further investigations.

Chapter 2

Mathematical Formulation

A numerical study of the wave-induced slamming on ships sailing in rough seas requires a so-called numerical wave tank, which is a numerical model of a physical wave tank. There are two important components in a wave tank i.e. a wave maker and a wave absorption system. A numerical wave tank must support a time domain simulation in a bounded domain with floating body motions, and the simulated waves must be as physical as possible. Using an open source CFD tool box known as OpenFOAM® (see Weller et al. (1998), Jasak et al. (2004)) a numerical wave tank has been developed. This chapter presents the mathematical formulation and the modelling techniques applied in the numerical wave tank. These include:

- An incompressible multi-phase flow solver with the free surface captured by a volume-of-fluid (VOF) technique. The arbitrary Lagrangian Eulerian (ALE) formulation has been applied for handling of body motions in a dynamic mesh morphing environment.
- A rigid body motion solver in 6 degree-of-freedom (6 DOF).
- A Timoshenko beam model to account for the flexibility of the hull girder.
- An artificial method for wave generation where the wave properties and the corresponding wave kinematics are prescribed at the wave-maker boundary.
- A wave absorption system based on a relaxation zone technique, which can be applied at the outlet as well as at the inlet to minimize wave reflection in the numerical wave flume.

The first report on VOF can be found in Nichols & Hirt (1975). Several years later, Hirt & Nichols (1981) published a more complete description of the VOF technique. Since then, several works have been reported with major modifications related to the algorithm to locate the free surface and keep the interface sharp as it moves through a computational grid, see e.g. Youngs (1982), Muzaferija et al. (1999) and Ubbink & Issa (1999).

The VOF-based flow equations applied in the current study follow the original VOF method (Hirt & Nichols (1981)) using a single fluid formulation where the flow in both phases (water and air) is described by a single set of equations with a spatial weighted average of mass density and viscosity. A numerical implementation of the flow solver exists in OpenFOAM® using the finite volume method on a collocated unstructured mesh. A face-based discretization procedure is applied

allowing computation on any arbitrary convex polyhedral cell shape. More details can be found in Jasak (1996).

2.1 Governing Equations for Two-Phase Flow

Many complex phenomena exist in a wave related impact problem. These are for example trapped/entrained air, steep breaking wave impact, and hydroelastic effects. It is seldom that all the physical effects can be included in the flow solver. Therefore, it is important to emphasize the assumptions and limitations of the flow solver. In general the assumptions applied in the mathematical formulation are

- **Incompressible flow :** Consequently this assumption means trapped air and air entrainment will not be accounted for. The trapped air can be compressed and acts like a cushion and may lower impact pressure considerably. Applying the incompressible assumption will cause the predicted pressure to be conservative. Similar effects can be observed when air entrainment occurs. The entrainment of air causes the sea water to be slightly compressible with the same effect of lower impact pressure. While it is reasonable to assume an incompressible flow in many impact-related cases, the assumption is not valid when air trapping or air entrainment are dominating.

- **The effects of surface tension are negligible :** In large scale free surface flow such as slamming on ships, the surface tension is considered not important.

- **Immiscible fluid :** It is assumed that there is no homogeneous mixing between sea water and air.

- **Turbulence has a secondary effect in slamming :** Without accounting for turbulence the viscous shear stress on the body and in the flow will not be correctly estimated. The turbulence is neglected since the typical duration of slamming impact is less than a fraction of a second, which is too short for turbulence to develop.

The principle of VOF is the introduction of the so-called phase fraction function α to describe the amount of fluid in a control volume. In a two-phase fluid flow i.e. water and air, the value of the phase fraction function is $\alpha = 1$ if the control volume is completely filled with water, and $\alpha = 0$ if there is only air. At the interface between the two fluids, the value of α is between [0, 1]. Using the single fluid formulation, the mass density ρ and viscosity μ are evaluated as

$$\rho = \alpha\rho_{\text{water}} + (1-\alpha)\rho_{\text{air}} \tag{2.1}$$

$$\mu = \alpha\mu_{\text{water}} + (1-\alpha)\mu_{\text{air}} \tag{2.2}$$

where ρ_{water} and ρ_{air} are, respectively, the density of water and air which are constant according to the assumption of an incompressible flow.

The fluid velocity vector in a Cartesian coordinate system $O(x, y, z)$ is $\boldsymbol{u} = \{u, v, w\}^T$. The principle of mass conservation states that the total mass of an arbitrary volume $m = \int_\Omega \rho\, dV$ is conserved i.e.

$$\frac{d}{dt}\int_{\Omega} \rho \, dV = 0 \tag{2.3}$$

According to the Reynolds transport theorem (see e.g. Belytschko et al. (2000)) the following relation is valid for any smooth scalar function ϕ

$$\frac{d}{dt}\int_{\Omega} \phi \, dV = \int_{\Omega} \left(\frac{\partial \phi}{\partial t} + \nabla \cdot (\phi \boldsymbol{u}) \right) dV \tag{2.4}$$

where Ω represents a control volume. The Reynolds transport theorem combined with Eq. (2.3) leads directly to mass conservation equation expressed in a conservative form as

$$\frac{\partial \rho}{\partial t} + \nabla \cdot (\rho \boldsymbol{u}) = 0 \tag{2.5}$$

It is important to notice that ρ may have a spatial variation since the two fluids $(\rho_{\text{water}}, \rho_{\text{air}})$ are considered as a single fluid with the density ρ given in Eq. (2.1). In other words, ρ_{water} and ρ_{air} are assumed constant due to the assumption of an incompressible flow while ρ is not necessary constant but has a time-and-space dependency. Thus, applying the chain rule, Eq. (2.5) becomes

$$\frac{\partial \rho}{\partial t} + \boldsymbol{u} \cdot \nabla \rho + \rho \nabla \cdot \boldsymbol{u} = 0 \tag{2.6}$$

The first two terms in Eq. (2.6) represent the rate of change of ρ subjected to a space and time dependent velocity field. Assuming an incompressible flow the volume $\Omega = \int_{\Omega} dV$ is constant i.e. the time derivative of the volume is zero and applying the Reynolds Transport Theorem, Eq. (2.4), yields the so-called divergence free condition for the velocity field

$$\frac{d}{dt}\int_{\Omega} dV = \int_{\Omega} \nabla \cdot \boldsymbol{u} \, dV = 0 \quad \Rightarrow \quad \nabla \cdot \boldsymbol{u} = 0 \tag{2.7}$$

and the mass conservation Eq. (2.6) yields a transport equation for ρ

$$\frac{\partial \rho}{\partial t} + \boldsymbol{u} \cdot \nabla \rho = 0 \tag{2.8}$$

Thus, there is no mass diffusion in the flow but ρ is allowed to be freely convected with the flow. Substituting Eq. (2.1) in (2.8) yields the well known transport equation for the phase fraction function seen in a VOF formulation

$$\frac{\partial \alpha}{\partial t} + \boldsymbol{u} \cdot \nabla \alpha = 0 \tag{2.9}$$

By definition, α must be bounded between [0, 1]. A careful attention on discretizing and solving Eq. (2.9) is required in order to fulfill the boundedness criteria and to

preserve the sharpness of the interface between the two fluids. Different techniques have been developed for a proper treatment of the convective term (the second term in Eq. (2.9)), e.g. CICSAM (Ubbink & Issa (1999)), HRIC (Muzaferija et al. (1999)), and PLIC (Youngs (1982)). The former utilizes a high resolution compressive numeric scheme and the latter uses a method of geometrical interface reconstruction. In OpenFOAM, the transport equation is handled using an interface compression technique where an artificial compressive term is added to Eq. (2.9). The modified equation is written in a conservative form as

$$\frac{\partial \alpha}{\partial t} + \nabla \cdot (\alpha \boldsymbol{u}) + \nabla \cdot [\alpha(1-\alpha)\boldsymbol{u}_r] = 0 \tag{2.10}$$

where $\boldsymbol{u}_r = \boldsymbol{u}_{\text{water}} - \boldsymbol{u}_{\text{air}}$ is the relative velocity between water and air. A description and a derivation of the compressive term (the third term in Eq. (2.10)) can be found in Berberovic et al. (2009), see also Appendix A. In a single fluid formulation, the fluid property is averaged by the phase fraction and the relative velocity $\boldsymbol{u}_r$ is zero by definition. However, it is reintroduced here to allow a better control of the numerical diffusion near the interface. The third term is only effective within the interface region where the value of α is between 0 and 1. Away from the interface the value of α will be either exactly or very close to 0 or 1 and the coefficient $\alpha(1-\alpha)$ will cause the third term to vanish. The relative velocity $\boldsymbol{u}_r$ is unknown and can be chosen based on experience. Using a large value of $\boldsymbol{u}_r$ will yield a sharp interface. However, there can be potential numerical problems related to a discontinuity at the interface.

As discussed in Appendix A, $\boldsymbol{u}_r$ shall be divergence free and has a direction pointed toward the normal direction of the nearest point on the interface. Still, the compressive term is artificial and has no physical justification related to the convection of the interface. Applying Eq. (2.10) is equivalent to artificially increasing the convective velocity by $\boldsymbol{u}_r(2\alpha - 1)$. By modelling $\boldsymbol{u}_r$ to satisfy the divergence free condition and the direction criteria (see Appendix A), it is optimistically assumed that the only effect of the artificial term is to compress the phase fraction field toward a sharper interface.

Neglecting surface tension, the principle of momentum conservation leads to the incompressible Navier-Stokes equations. In tensorial form, the equation is written

$$\frac{\partial(\rho \boldsymbol{u})}{\partial t} + \nabla \cdot (\rho \boldsymbol{u}\boldsymbol{u}^T) - \nabla \cdot \boldsymbol{\sigma} = -\nabla p + \rho \boldsymbol{g} \tag{2.11}$$

where the viscous stress tensor $\boldsymbol{\sigma}$ for an isothermal Newtonian Stokes fluid after applying the divergence free condition is $\boldsymbol{\sigma} = \mu(\nabla \boldsymbol{u} + \nabla \boldsymbol{u}^T)$, meaning that

$$\nabla \cdot \boldsymbol{\sigma} = \nabla \cdot \mu \nabla \boldsymbol{u} + \nabla \mu \cdot \nabla \boldsymbol{u}^T \tag{2.12}$$

Due to the averaging in Eq. (2.2), the term $\nabla \mu$ is not necessary vanishing at the interface. In the derivation of Eq. (2.12), following identities have been applied:

$$\nabla \cdot \mu \nabla \boldsymbol{u} = \mu \nabla^2 \boldsymbol{u} + \nabla \mu \cdot \nabla \boldsymbol{u}$$
$$\nabla \cdot \mu \nabla \boldsymbol{u}^T = \mu \nabla (\nabla \cdot \boldsymbol{u}) + \nabla \mu \cdot \nabla \boldsymbol{u}^T$$

The symbol $\boldsymbol{g} = \{g_x, g_y, g_z\}^T$ in Eq. (2.11) is the gravitational acceleration vector and p is the total pressure. It is beneficial to introduce the so-called excess pressure p_d, cf. Rusche (2002), defined as

$$p = p_d + \rho \boldsymbol{g} \cdot \boldsymbol{x} \tag{2.13}$$

where $\boldsymbol{x} = \{x, y, z\}^T$ is the position vector. The second term on the right-hand side is equivalent to the hydrostatic and aerostatic pressure evaluated as if the fluid is at rest. One of the benefits of introducing p_d is that the boundary condition for p_d is simpler than if the total pressure was applied directly. It shall be emphasized that the term $\rho \boldsymbol{g} \cdot \boldsymbol{x}$ is time dependent due to the time dependency of ρ. Using the excess pressure, the momentum equation, Eq. (2.11), yields

$$\frac{\partial(\rho \boldsymbol{u})}{\partial t} + \nabla \cdot (\rho \boldsymbol{u}\boldsymbol{u}^T) - \nabla \cdot \boldsymbol{\sigma} = -\nabla p_d - (\boldsymbol{g} \cdot \boldsymbol{x})\nabla \rho \tag{2.14}$$

In summary, the set of equations for the VOF-based incompressible flow are

Incompressibility:	$\nabla \cdot \boldsymbol{u} = 0$	(2.15a)
Mass:	$\frac{\partial \alpha}{\partial t} + \nabla \cdot (\alpha \boldsymbol{u}) + \nabla \cdot [\alpha(1-\alpha)\boldsymbol{u}_r] = 0$	(2.15b)
Momentum:	$\frac{\partial(\rho \boldsymbol{u})}{\partial t} + \nabla \cdot (\rho \boldsymbol{u}\boldsymbol{u}^T) - \nabla \cdot \boldsymbol{\sigma} = -\nabla p_d - (\boldsymbol{g} \cdot \boldsymbol{x})\nabla \rho$	(2.15c)
Definitions:	$\alpha = [0,\ 1]$	(2.15d)
	$\rho = \alpha \rho_{\text{water}} + (1-\alpha)\rho_{\text{air}}$	(2.15e)
	$\mu = \alpha \mu_{\text{water}} + (1-\alpha)\mu_{\text{air}}$	(2.15f)
	$p = p_d + \rho \boldsymbol{g} \cdot \boldsymbol{x}$	(2.15g)
	$\boldsymbol{\sigma} = \mu(\nabla \boldsymbol{u} + \nabla \boldsymbol{u}^T)$	(2.15h)

These equations are expressed in a conservative form. The following identities can be applied to manipulate and rearrange the equations

$$\nabla \cdot (\alpha \boldsymbol{u}) = \boldsymbol{u} \cdot \nabla \alpha + \alpha \nabla \cdot \boldsymbol{u} \tag{2.16}$$

$$\nabla \cdot (\rho \boldsymbol{u}\boldsymbol{u}^T) = \boldsymbol{u} \cdot \nabla(\rho \boldsymbol{u}) + \rho \boldsymbol{u}(\nabla \cdot \boldsymbol{u}) \tag{2.17}$$

$$\boldsymbol{u} \cdot \nabla(\rho \boldsymbol{u}) = \rho \boldsymbol{u} \cdot \nabla \boldsymbol{u} + \boldsymbol{u}(\boldsymbol{u} \cdot \nabla \rho) \tag{2.18}$$

2.2 Arbitrary Lagrangian-Eulerian (ALE) Formulation

The fundamental objective of the description of the fluid flow is to express the primitive variables and any physical quantity of the flow in a reference domain. In this section, three different reference domains are introduced: the Eulerian $(\boldsymbol{x}, t)$, the Lagrangian $(\boldsymbol{X}, t)$, and the ALE $(\boldsymbol{\chi}, t)$:

- **Eulerian :** The flow is described on a fixed spatial coordinate $(\boldsymbol{x}, t)$.
- **Lagrangian :** The physical quantities are a function of material coordinates $(\boldsymbol{X}, t)$ which move with the fluid particle.
- **ALE :** The flow is described on a spatial coordinate $(\boldsymbol{\chi}, t)$ which may move in an arbitrary manner.

The formulation in Eqs. (2.15) is based on the classical Eulerian formulation commonly applied in fluid dynamics. As time evolves, the primitive variables, i.e. fluid velocity $\boldsymbol{u}$ and pressure p, are examined at fixed grid points. Any flow formation can be described at the expense of many grid points to capture the resolution of flow details.

Another classical approach is known as the Lagrangian formulation where the primitive variables are associated directly with individual fluid particles and follow them as they move. While the Eulerian formulation describes any physical quantity in a spatial domain $(\boldsymbol{x}, t)$, the Lagrangian formulation describes the same quantity in a material domain $(\boldsymbol{X}, t)$. The differences in the functional form of the same physical quantity are due to the use of different reference domains.

The main attraction of the ALE formulation is that the reference domain $(\boldsymbol{\chi}, t)$ can be chosen arbitrary. Thus, the ALE formulation allows the computational mesh i.e. the control volume to be changed in an arbitrary manner as long as the mesh velocity can be evaluated. The mesh velocity emerges from the material derivative term written as (see Appendix B)

$$\frac{\partial f_{\mathrm{L}}}{\partial t}\Big|_{\boldsymbol{X}} = \frac{\partial f_{\mathrm{ALE}}}{\partial t}\Big|_{\boldsymbol{\chi}} + \boldsymbol{u}_c \cdot \nabla f_{\mathrm{ALE}} \tag{2.19}$$

where f is a functional form of any physical quantity with sub indices "L" to indicate the use of a Lagrangian formulation and "ALE" the Arbitrary Lagrangian-Eulerian formulation. The convective velocity is $\boldsymbol{u}_c \equiv \boldsymbol{u} - \boldsymbol{u}_m$ where $\boldsymbol{u}_m$ is the mesh velocity and $\boldsymbol{u}$ is the fluid particle velocity. In a particular case, when the reference domain is a fixed grid, the convective velocity will be exactly equal to the material velocity. Thus, the description of the flow can become the same as the Eulerian formulation. On the other hand, the ALE formulation can easily become the same as the Lagrangian formulation if reference domain is chosen to be the material domain.

In the estimation of the mesh velocity $\boldsymbol{u}_m$ the so-called Space Conservation Law (SCL) must be satisfied. A detailed derivation of SCL is given in Warsi (1981). The derivation in Warsi (1981) expressed the SCL in the differential form as (cf. Warsi (1981)),

$$\frac{1}{\sqrt{g}} \frac{\partial \sqrt{g}}{\partial t}\Big|_{\boldsymbol{\chi}} - \nabla \cdot \boldsymbol{u}_m = 0 \tag{2.20}$$

where g is the determinant of the metric tensor g_{ij} introduced in a tensor calculus to generalize the calculation of the distance element in a curvilinear coordinate system. The integral form of SCL follows directly from the Reynolds transport theorem, Eq. (2.4), applied with $\phi = 1$, i.e.

$$\frac{d}{dt}\Big|_{\boldsymbol{\chi}} \int_{\Omega} dV - \oint_{\partial\Omega} \boldsymbol{u}_m \cdot \boldsymbol{n}\, dS = 0 \tag{2.21}$$

where $\boldsymbol{n}$ is the unit normal vector of the surface (positive pointing outward). The importance of SCL has been recognized for a long time, see e.g. Thomas & Lombard (1979), Warsi (1981), and Demirdžić (1982). A violation of the space conservation law will introduce mass conservation errors in the form of artificial mass sources allowing the solution to converge to an unrealistic flow field with the errors largest in areas where large changes in the mesh occurred. A mesh refinement will not help to reduce the errors but reducing the time step may help, see e.g. Demirdžić & Perić (1988).

When applying the ALE formulation to the flow equations, any material derivative will need to be replaced by the relation shown in Eq. (2.19). This change and the additional constraint of SCL are the only major changes reflected by the use of the ALE formulation. The governing flow equations in the ALE formulation are

Incompressibility: $$\nabla \cdot \boldsymbol{u} = 0 \tag{2.22a}$$

Space: $$\frac{d}{dt}\Big|_{\boldsymbol{\chi}} \int_{\Omega} dV - \oint_{\partial\Omega} \boldsymbol{u}_m \cdot \boldsymbol{n}\, dS = 0 \tag{2.22b}$$

Mass: $$\frac{\partial \alpha}{\partial t}\Big|_{\boldsymbol{\chi}} + \boldsymbol{u}_c \cdot \nabla\alpha + \nabla \cdot [\alpha(1-\alpha)\boldsymbol{u}_r] = 0 \tag{2.22c}$$

Momentum: $$\frac{\partial(\rho\boldsymbol{u})}{\partial t}\Big|_{\boldsymbol{\chi}} + \nabla \cdot (\rho\boldsymbol{u}\boldsymbol{u}_c^T) - \nabla \cdot \boldsymbol{\sigma} = -\nabla p_d - (\boldsymbol{g} \cdot \boldsymbol{x})\nabla\rho \tag{2.22d}$$

Definitions: $$\alpha = [0,\, 1] \tag{2.22e}$$

$$\rho = \alpha\rho_{\text{water}} + (1-\alpha)\rho_{\text{air}} \tag{2.22f}$$

$$\mu = \alpha\mu_{\text{water}} + (1-\alpha)\mu_{\text{air}} \tag{2.22g}$$

$$p = p_d + \rho\boldsymbol{g} \cdot \boldsymbol{x} \tag{2.22h}$$

$$\boldsymbol{\sigma} = \mu(\nabla\boldsymbol{u} + \nabla\boldsymbol{u}^T) \tag{2.22i}$$

$$\boldsymbol{u}_c = \boldsymbol{u} - \boldsymbol{u}_m \tag{2.22j}$$

Notice the strong similarity between Eqs. (2.22) and (2.15). The only difference here is that the convective velocity is now the relative velocity between the fluid and the mesh. In addition, it shall be emphasized that the mesh velocity $\boldsymbol{u}_m$ does not need to satisfy the divergence free condition but is constrained to obey the space conservation law (SCL).

2.3 Automatic Mesh Motion

The flow equations presented in Section 2.2 are discretized based on the finite volume method (FVM). All basic variables, primitive as well as conservative, are defined on a collocated arrangement. The ALE formulation allows body motion to be defined in terms of dynamic motion of the body boundaries. The grid points on the moving body are constrained to move according to the required motion of the body. The

internal grid points, however, can be moved more freely. The only requirement applied to the internal grid points is that the finite volume mesh remains valid and the quality of each cell remains sufficiently good. The implementation of the ALE code requires a mesh update procedure. The contents of this section are designated to describe the automatic mesh-updating procedure applied in the present work.

It is important to emphasize that there are two basic mesh-updating strategies: mesh morphing without topology changes and mesh adaptation with topology changes. When the topology and the connectivity of the mesh is changing the flow field must be mapped and transferred on to the new mesh, followed by a recalculation of the flow field to assure that the flow field satisfies the flow equation on the new mesh. A complex motion can be simulated using a mesh adaptation technique, but it may prove very computationally intensive mainly due to the mesh refinement and adaptation, the remapping and the re-computation. The mapping procedure is not necessary if the mesh is only deformed and the topology of the mesh remains unchanged. Using an automatic mesh morphing strategy requires no additional work other than a mesh morphing technique.

Several mesh morphing techniques can be applied within the finite volume framework, see e.g. Jasak & Tuković (2007). The most commons are:

- **Spring analogy :** The mesh points are considered to be connected by artificial springs which can be introduced as linear springs (see e.g. Batina (1990)), or in combination with torsional springs.

- **Pseudo-solid :** The mesh is treated as if it was a linear elastic solid (see e.g. Johnson & Tezduya (1994) and Jasak & Weller (2000)). The displacement of the mesh points are computed using the solid body rotation stress equations assuming an equilibrium state and small deformations.

- **Laplacian smoothing :** The governing equation for the mesh motion is taken as the Laplace equation with a variable diffusivity coefficient. Along the boundary of the domain, the displacements are provided as boundary conditions to the Laplace equation. The movement of the internal mesh points can to be controlled using the diffusivity coefficient.

- **Algebraic interpolation :** Interpolation techniques or any other explicit definition of the mesh points can be used. The only requirement is that the quality of the mesh remains good enough for the computation. One of the interesting interpolation techniques which can handle large deformation and rotation is presented in Bos (2009) using the so-called Radial Basis Function (RBF) for the interpolation. The computational requirement, however, can be very large depending on whether the construction of the RBF uses global or compact support.

- **Solid body motion :** The whole mesh is moved as it was a solid body. This technique can be applied when the moving boundaries move as a rigid body. There is no need to deform the internal mesh since the whole mesh can simplify follow the rigid body motion in 6 degree-of-freedom. The major difficulty, however, is related to the specification of the boundary conditions in an open domain e.g. with an inlet wave boundary where the boundary condition depends strongly on the spatial location of the boundary points.

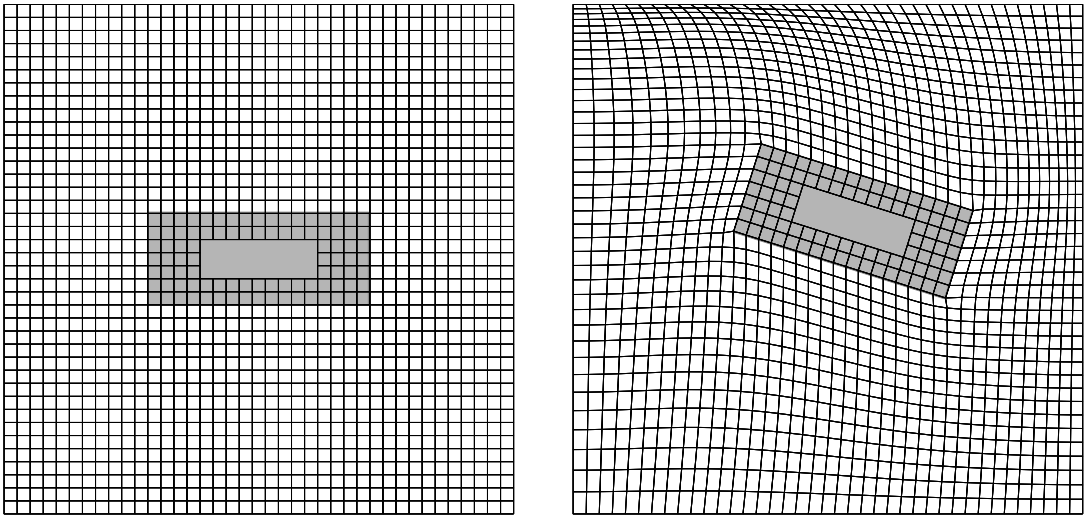

(a) initial mesh (b) deformed mesh

Figure 2.1: The deformation of the internal points can be restricted to an outer region of the domain. The inner region (shaded area) follows the translational and rotational motion of the moving boundary without any deformation.

The Spring Analogy approach without the torsional spring is not robust enough to be applied in an unstructured polygonal mesh, see Farthal et al. (1998). Introducing the torsional spring may help at the cost of more computational power to solve the non-linear coupled system. In comparison, the governing equation for the Pseudo-solid and the Laplacian smoothing strategies are linear yielding a sparse matrix equation to be solved using a standard solver.

In the present work, the mesh update strategy is based on the Laplacian mesh smoothing technique. An implementation of the Laplacian mesh smoothing technique exists in the OpenFOAM software package. However, there is a need to keep the mesh deformation adjacent to the surface of the moving boundaries non-deformed. Therefore, the Laplacian smoothing is applied only outside a predefined inner region of the mesh.

Let $\boldsymbol{x}$ be the point displacement field and γ be the diffusivity coefficient, the Laplacian of $\boldsymbol{x}$ is

$$\nabla \cdot \gamma(r) \nabla \boldsymbol{x} = 0 \quad ; \quad \gamma(r) \equiv \frac{1}{r^2} \tag{2.23}$$

where r is the distance to the moving boundary. The distribution of the diffusivity coefficient γ is set according to the inverse quadratic distance to the moving boundaries. Close to the moving boundaries, the diffusivity coefficient is large and thereby, the gradient of the displacement $\boldsymbol{x}$ is small yielding a small relative displacement for points close to the moving body which helps to preserve the quality of the cells near the moving boundaries. Several other choices for γ are presented in Löhner & Yang (1996), and Jasak & Tuković (2007). One of the possible choices is an exponential function. In the present work, the inverse quadratic distance relation has been chosen.

It is a common practice to distribute mesh points in a way that the interesting flow region has a high grid resolution to capture the flow features in interest. The quality

of the finite volume cells within these regions shall remain as good as possible in order to keep the accuracy of the results at an acceptable level. A way to preserve the cell quality is to keep the large mesh deformation outside regions of interest. The control of the deformation across the domain can be done through the diffusivity coefficient γ, but the cell quality is best preserved if they are moved according to the motion of the moving boundaries. An example is given in Fig. 2.1. The grey area follows the translational and rotational motion of the moving boundary. This technique may prove difficult to apply with multiple independently moving boundaries, or if the moving boundaries are deformed in an irregular manner. Therefore, the choice may depend strongly on the particular case. For demonstration purposes, a rectangular region has been selected in Fig. 2.1 to follow the moving boundary. In principle, the selection can be irregular in shape. Furthermore, Fig. 2.1 shows that there is a limitation on how much the initial mesh can be deformed. If the displacement of the moving boundary is extreme with respect to the current domain configuration, one will have to resort to a different mesh update strategy.

The boundary conditions for solving the Laplacian of the displacement are assumed to be known. On open boundaries, e.g. the inlet, the outlet, or the top boundary, which represent an open-air boundary, any suitable boundary condition may apply including a slip boundary condition. More details about different types of boundary condition can be found in Section 2.6.

2.4 Rigid Body Motion in 6 DOF

The equations of motion for a ship in 6 degree-of-freedom (6DOF) have been derived and described in many standard textbooks but the definition of the reference coordinate system may vary, see e.g. SNAME (1950), Marsden & Ratiu (1999), and Jensen (2001). Therefore, it is important to define the frame of reference in which the governing equations are valid. The frame of reference used to describe the fluid flow is the ALE reference domain described in Section 2.2. In addition, a body-fixed frame of reference is introduced to simplify the description of the 6DOF equations of motion. Both reference frames are Cartesian systems and defined according to the right-hand rule. More precisely, the two frames of reference are defined as follows:

- **Inertial reference frame, $O(x_0, y_0, z_0)$:** This is sometimes called the Newtonian frame of reference in which the Newton's law may applied directly without a need to apply any fictive forces such as centrifugal or Coriolis forces. The initial frame of reference is fixed in a sense that it does not rotate or accelerate. The z_0-axis is positive pointing upward while the (x_0, y_0)-plan lay horizontally and follows the right-hand rule.

- **Body-fixed reference frame $B(x, y, z)$:** This reference frame is fixed on the floating body. It may rotate or accelerate according to the motion of the body. Its origin is chosen to coincide with the center of gravity (COG) assuming that the COG is located on the symmetry plane of the body such that the coordinate axes coincide with the principle axes of inertia.

Figure 2.2 illustrates the two frame of references. The 6DOF system consists of three translations and three rotations. The translational motions along (x_0, y_0, z_0)-axes are surge, sway and heave and the rotational motions about the three axes are roll, pitch,

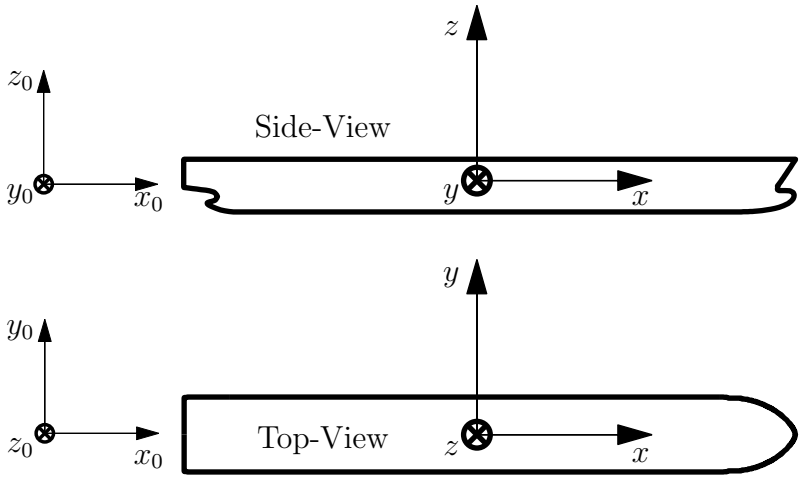

Figure 2.2: The body-fixed reference frame $B(x, y, z)$ and the Newtonian reference frame $O(x_0, y_0, z_0)$

and yaw. It is important to emphasize that these 6DOF motions can be thought of as the motions of the body-fixed reference frame. Thus, surge, sway, heave, roll, pitch and yaw are defined relative to the inertial reference frame. Furthermore, the rotational angles need to be defined more precisely since the transformation between the inertial reference frame and body-fixed frame is not unique. Several conventions exist for representing three-dimensional rotations. These are e.g. the classic Euler angles, the Tait-Bryan angles, or a quaternion representation. The convention applied in the present work follows the convention applied in SNAME (1950) also known as Tait-Bryan angles with zyx-convention. The transformation from the inertial reference frame $O(x_0, y_0, z_0)$ to the body-fixed reference frame $B(x, y, z)$ is done sequentially as follows:

1. **Yaw:** Rotate about z_0-axis by the yaw angle (ψ). The x_0 and y_0 axes will move to new positions called x_1 and y_1. The z_0 axis remains unchanged, see Fig. 2.3a.

2. **Pitch:** Rotate about y_1-axis by the pitch angle (θ). The x_1-axis will move to its final position x and the z_0 axis will move to a new position called z_1. The y_1 axis remains unchanged, see also Fig. 2.3b.

3. **Roll:** Rotate about x-axis by the roll angle (ϕ). The y_1 and z_1 axes will move to their final positions y and z, see Fig. 2.3c.

Right-hand rule is applied to determine the positive direction. Figure 2.3 illustrates the three steps described above. The corresponding matrix presentation for the transformation is

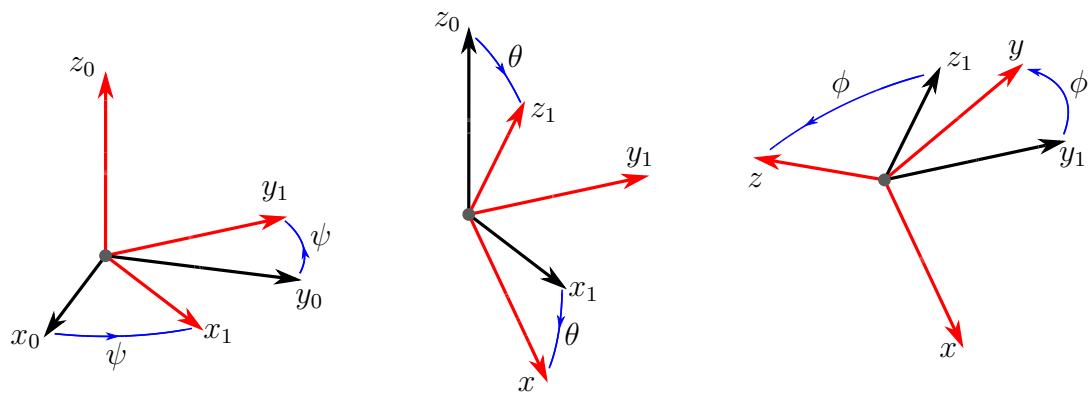

(a) Yaw (b) Pitch (c) Roll

Figure 2.3: The transformation from the inertial reference frame to the body-fixed reference frame. In this example the three angles are $(\phi,\, \theta,\, \psi) = (45^o,\, 35^o,\, 60^o)$

$$\mathbf{R} = \begin{bmatrix} c_z & -s_z & 0 \\ s_z & c_z & 0 \\ 0 & 0 & 1 \end{bmatrix} \begin{bmatrix} c_y & 0 & s_y \\ 0 & 1 & 0 \\ -s_y & 0 & c_y \end{bmatrix} \begin{bmatrix} 1 & 0 & 0 \\ 0 & c_x & -s_x \\ 0 & s_x & c_x \end{bmatrix}$$

$$\Rightarrow \quad \mathbf{R} = \begin{bmatrix} c_z\, c_y & -s_z\, c_x + c_z\, s_y\, s_x & s_z\, s_x + c_z\, s_y\, c_x \\ s_z\, c_y & c_z\, c_x + s_z\, s_y\, s_x & -c_z\, s_x + s_z\, s_y\, c_x \\ -s_y & c_y\, s_x & c_y\, c_x \end{bmatrix} \tag{2.24}$$

such that

$$\boldsymbol{\tau}_O = \mathbf{R}\, \boldsymbol{\tau}_B \tag{2.25}$$

where $\mathbf{R}$ is the transformation matrix and $\boldsymbol{\tau}$ is a vector with the subscript O denotes the inertial reference frame and B the body-fixed frame. The notations (s_x,s_y,s_z) and (c_x,c_y,c_z) denotes the cosine and sine of roll (ϕ), pitch (θ) and yaw (ψ).

In the Newtonian frame of reference the force balance is given by the Newton's second law

$$\boldsymbol{f}_O = m_t \dot{\boldsymbol{v}}_O \tag{2.26}$$

where m_t is the total mass of the body; $\boldsymbol{f}_O$ is the vector representation of the net force acting on the body and $\dot{\boldsymbol{v}}_O$ is the translational velocity with the dot indicating the time derivative. The forces acting on the body are mainly the gravitational force, the propulsion force and the fluid force. The gravitational force is simply $m_t\boldsymbol{g}$ where $\boldsymbol{g}$ is the gravitational acceleration in vector form. The propulsion force, which is commonly modelled in the body-fixed frame, must be transformed into the Newtonian frame of reference before insertion in Eq. (2.26). The fluid force is commonly evaluated as a surface integral of the pressure and viscous shear stress as

$$\boldsymbol{f}_{O,\text{fluid}} = \int_S \Big(p\boldsymbol{n} + \boldsymbol{\sigma} \cdot \boldsymbol{n} \Big)\, dS \tag{2.27}$$

where $\boldsymbol{n}$ is the surface unit normal vector and S indicates the surface of the body. Both hydrostatic and hydrodynamic forces are accounted for in the integral since p is the total fluid pressure and $\boldsymbol{\sigma}$ is the viscous stress tensor evaluated at the body surface. It is convenient to solve for the translational velocity and acceleration using the Newtonian frame of reference as shown in Eq. (2.26) since the fluid force is readily obtained in the Newtonian frame of reference.

On the other hand, the momentum balance is more convenient to solve in the body-fixed coordinate system $B(x, y, z)$ defined to align with the principle axes of inertia and with origin at the center of mass. The vectorial form of the equation reads

$$\mathbf{R}^T \boldsymbol{\tau}_O = \mathbf{I}_B \dot{\boldsymbol{\omega}} + \boldsymbol{\omega} \times (\mathbf{I}_B \boldsymbol{\omega}) \tag{2.28}$$

where $\boldsymbol{\omega}$ denotes the angular velocity with respect to the body-fixed reference frame and $\boldsymbol{\tau}_O$ denotes total torque about the center of gravity expressed in the Newtonian frame of reference. The mass moment of inertia about the principle axes is given in the form of a diagonal matrix $\mathbf{I}_B$. The transformation matrix $\mathbf{R}$ is defined in Eq. (2.24). Since the roll (ϕ), pitch (θ), and yaw (ψ) are defined in the earth-fixed reference frame, their relation with $\boldsymbol{\omega}$ is (cf. SNAME (1950))

$$\begin{pmatrix} \dot{\phi} \\ \dot{\theta} \\ \dot{\psi} \end{pmatrix} = \begin{bmatrix} 1 & \frac{s_z s_y}{c_y} & \frac{c_z s_y}{c_y} \\ 0 & c_z & -s_z \\ 0 & \frac{s_z}{c_y} & \frac{c_z}{c_y} \end{bmatrix} \boldsymbol{\omega} \tag{2.29}$$

with the dot notation applied for the time derivative. The chosen location of the body-fixed frame makes the inertia tensor $\mathbf{I}_B$ a diagonal tensor. Hence, one needs to specify only three mass moments of inertia about the three principle axes. Moreover, the gravitational force will not contribute to the total torque $\boldsymbol{\tau}_O$ since the origin coincides with the center of gravity of the body. The torque induced by the fluid force is

$$\boldsymbol{\tau}_{O,\text{fluid}} = \int_S (\boldsymbol{x} - \boldsymbol{x}_{\text{CG}}) \times \Big(p\boldsymbol{n} + \boldsymbol{\sigma} \cdot \boldsymbol{n} \Big) \, dS \tag{2.30}$$

where $\boldsymbol{x}_{\text{CG}}$ is the location of the center of gravity. It shall be emphasized that Eqs. (2.26) and (2.28) are decoupled such that surge, sway and heave can be solved for independently of Eq. (2.28). Furthermore, the momentum balance defining the equations for roll, pitch and yaw, Eq. (2.28), are nonlinear and require an appropriate solution procedure. A numerical solution for the 6DOF equation of motions coupled with the flow solver is provided in Chapter 3.

Modelling the hull girder as a rigid beam, the vertical shear force $Q_{\text{rigid}}(x)$ and the vertical bending moment $M_{\text{rigid}}(x)$ can be computed in the one dimensional body-fixed coordinate as

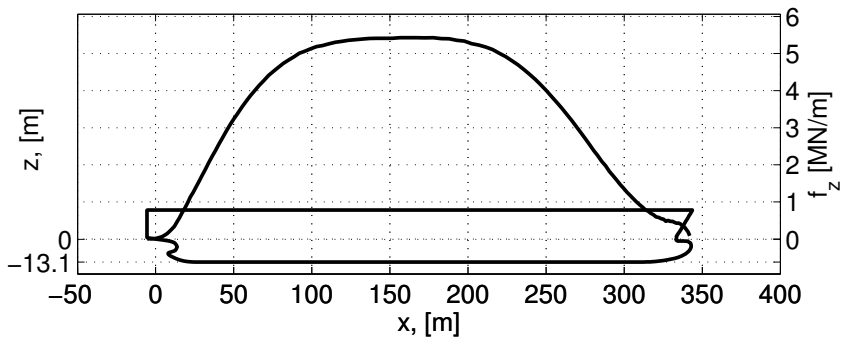

Figure 2.4: An example of the 1-D fluid load distribution in still water

$$Q_{\text{rigid}}(x) = -\int_{x_{\min}}^{x} q(\tilde{x})\, d\tilde{x} \tag{2.31a}$$

$$M_{\text{rigid}}(x) = -\int_{x_{\min}}^{x} (x-\tilde{x}) q(\tilde{x})\, d\tilde{x} \tag{2.31b}$$

where $q(x)$ is the vertical load distribution on the ship. Given a mass distribution $m(x)$, the total vertical force per unit length is written as

$$q(x) = f_z(x) - m(x)\Big[g + \ddot{z} - (x - x_{\text{LCG}})\ddot{\theta}\Big] \tag{2.32}$$

where L denotes the length of the vessel and $(\ddot{z}, \ddot{\theta})$ are the acceleration in heave and pitch, respectively. The gravitational acceleration is $g \equiv 9.81\,\text{ms}^{-2}$. The location of the longitudinal center of mass is x_{LCG} and the vertical component of the fluid force is represented by $f_z(x)$ i.e. the force per unit length with the hydrostatic and hydrodynamic forces written in the body-fixed frame of reference. Notice, that Eq. (2.32) assumes small angular deformations such that the projection of the gravitational force, the centrifugal forces and the Coriolist forces are neglected. Including these effects, however, does not cause a significant increase in the computational time.

The fluid load on the hull is provided by the fluid solver mainly as a pressure distribution on a three-dimensional hull surface. To determine $f_z(x)$, the three-dimensional load needs to be transferred and reduced to one dimension. At a given x location, the transverse two-dimensional hull profile is determined by intersecting a transverse plane with the hull. The fluid loads on the three-dimensional hull are interpolated onto the intersection curve and the force per unit length can be determined from a curve integral written as

$$f_z(x) = \int_C \Big(p\boldsymbol{n}\cdot\boldsymbol{i}_z + (\boldsymbol{\sigma}\cdot\boldsymbol{n})\cdot\boldsymbol{i}_z\Big) ds \tag{2.33}$$

where $\boldsymbol{i}_z = (0,0,1)^T$ is the vertical component of the body-fixed coordinate. An example of $f_z(x)$ in calm water is shown in Fig. 2.4. At both ends of the vessel

the free-free boundary condition must hold, which implies that the shear force and bending moment must be zero at both ends. These conditions will be satisfied as long as $f_z(x)$ is consistent with heave and pitch accelerations computed from Eqs. (2.28) and (2.29). However, small errors associated with the interpolation converting from the loads on the three-dimensional hull surface to the one dimensional line load can be seen in the vertical bending moment. Because $M_{\text{rigid}}(x)$ is the integral of $q(x)$, a small error in the $f_z(x)$ will cause $M_{\text{rigid}}(x)$ to violate the free-free boundary condition. Two correction coefficients (c_1, c_2) can be introduced to $f_z(x)$ and $xf_z(x)$ to assure consistency. The equations are

$$(\mathbf{R}^T \boldsymbol{f}_o) \cdot \boldsymbol{i}_z = \int_L \tilde{f}_z(x)dx - m_t g \tag{2.34a}$$

$$(\mathbf{R}^T \boldsymbol{\tau}_o) \cdot \boldsymbol{i}_y = c_2 \int_L x\tilde{f}_z(x)dx - x_{LCG} \int_L \tilde{f}_z(x)dx \tag{2.34b}$$

where $\tilde{f}_z(x) = c_1 f_z(x)$ is the corrected one dimensional vertical force. The first correction, Eq. (2.34a), compensates for the errors made in the interpolation and the curve integral. The second correction, Eq. (2.34b) compensates for the differences of the total moments calculated based on one dimensional and three dimensional loads. Because the errors in $f_z(x)$ are small, the correction made through (c_1, c_2) will be small as well.

2.5 Modelling a Flexible Hull Girder

With the increasing size of container vessels, concern has been expressed about the importance of the flexibility of the hull girder on structural responses in waves. Specifically, a number of full scale and model tests have shown that a significant increase in the wave induced bending moment can occur in realistic seaways and operational conditions, see Aalberts & Nieuwenhuijs (2006), Zhu et al. (2011), and Miyake et al. (2009). One of the important issues, which affects large vessels, is that the encounter frequency is more likely to be within the range of the natural frequencies of the hull girder causing whipping and springing responses to occur more frequently. Due to the higher flexibility of the larger ship and the risk of resonant excitation of the structural modes, a calculation method based on the rigid body assumption is no longer necessarily accurate enough. Hence, there is a need to include the flexibility of the hull girder in both experimental and numerical studies.

To approach the hydroelastic problem numerically, the fluid solver needs to be coupled to a structural solver. The most advanced, but also structurally most complicated model, is the 3D FEM model. Alternatively, a Timoshenko beam model can be applied; see Bishop & Price (1979), Xia et al. (1998), Hirdaris et al. (2009) and Senjanović et al. (2009). Commonly, only vertical bending is included in the beam model since the horizontal bending may have a strong coupling with torsion and it is questionable if a beam model can account for torsion accurately; especially for an open hull. The consequence of only accounting for the vertical bending is that the simulation is limited to head seas or following seas.

In the present work, the OpenFOAM CFD toolbox has been extended with a classical non-uniform Timoshenko beam model coupled with the flow solver to

account for the flexibility of the hull girder. In the rest of this section, it is assumed that the one-dimensional axis of the Timoshenko beam is a body-fixed coordinate system with its origin located on the symmetry plane of the vessel. The center of gravity is assumed to be on the same symmetry plane and x_{CG} denotes its location with respect to the one-dimensional beam axis. The total length of the non-uniform Timoshenko beam is L extending from x_{min} and x_{max}. The equations of motions are written (cf. Jensen (2001)):

$$\frac{\partial}{\partial x}\Big[EI\Big(1+\mu\frac{\partial}{\partial t}\Big)\frac{\partial\phi}{\partial x}\Big]+kGA\Big(1+\epsilon\frac{\partial}{\partial t}\Big)\Big(\frac{\partial\nu}{\partial x}-\phi\Big)-mr^2\frac{\partial^2\phi}{\partial t^2}=0 \tag{2.35a}$$

$$\frac{\partial}{\partial x}\Big[kGA\Big(1+\epsilon\frac{\partial}{\partial t}\Big)\Big(\frac{\partial\nu}{\partial x}-\phi\Big)\Big]-m\frac{\partial^2\nu}{\partial t^2}=-f(x,t) \tag{2.35b}$$

where m, r, EI, kGA are the mass distribution, radius of gyration, and structural stiffness properties of the hull defined as non-uniform beam. The total mass, the center of gravity, the mass moment of inertia, the total force and moment are evaluated as follows:

Total mass: $$m_t=\int_{x_{\text{min}}}^{x_{\text{max}}} m\,dx \tag{2.36a}$$

Center of gravity: $$x_{\text{CG}}=\frac{1}{m_t}\int_{x_{\text{min}}}^{x_{\text{max}}} m\,x\,dx \tag{2.36b}$$

Mass moment of inertia: $$I_{\text{yy}}=\int_{x_{\text{min}}}^{x_{\text{max}}} m(x-x_{\text{CG}})^2\,dx \tag{2.36c}$$

Total force: $$f_{\text{z}}(t)=\int_{x_{\text{min}}}^{x_{\text{max}}} f(x,t)\,dx \tag{2.36d}$$

Total moment: $$\tau_{\text{y}}(x_{\text{CG}},t)=\int_{x_{\text{min}}}^{x_{\text{max}}} (x-x_{\text{CG}})f(x,t)\,dx \tag{2.36e}$$

The symbol ν denotes the vertical deflection and ϕ denotes the angular deformation. It is assumed in the following that the damping coefficients μ and ϵ are equal and independent of the longitudinal position x. The forcing term $f(x,t)$ is the force distribution acting on the hull which is mainly the fluid force, the gravitational force and the body forces related to whether the equations are solved on the body-fixed or the inertial frame of reference.

Denote $M=M(x,t)$ as the vertical bending moment and $Q=Q(x,t)$ as the shear force, the constitutive equations are

$$M(x,t)=EI\Big(1+\mu\frac{\partial}{\partial t}\Big)\frac{\partial\phi}{\partial x}\quad;\quad Q(x,t)=kGA\Big(1+\epsilon\frac{\partial}{\partial t}\Big)\Big(\frac{\partial\nu}{\partial x}-\phi\Big) \tag{2.37}$$

implying that the vertical bending moment and the shear force can be evaluated either from the constitutive equations or from the equilibrium condition, Eqs. (2.35), which are

$$M(x,t) = \int_{x_{\min}}^{x} \left[mr^2 \frac{\partial^2 \phi}{\partial t^2} - Q(\tilde{x},t) \right] d\tilde{x} \tag{2.38a}$$

$$Q(x,t) = \int_{x_{\min}}^{x} \left[m \frac{\partial^2 \nu}{\partial t^2} - f(\tilde{x},t) \right] d\tilde{x} \tag{2.38b}$$

Mathematically, there is no difference between Eqs. (2.37) and (2.38) provided that $\nu(x,t)$ and $\phi(x,t)$ are the exact solutions of Eqs. (2.35). Numerically, Eqs. (2.37) and (2.38) may produce different results. Using the constitutive equations (Eq. (2.37)), it is necessary to evaluate spatial derivatives of ν and ϕ while the equilibrium equation (Eq. (2.38)) requires an evaluation of the integrals. From a numerical point of view, the integral operation is more stable and less susceptible to local errors. Nevertheless, Eqs. (2.37) and (2.38) should produce the same results. An evaluation of the agreement between the two equations can be used to estimate the accuracy and consistency of the numerical results.

The Timoshenko beam equations can be discretized and solved using the finite element method which requires at least a 3rd-order shape function since a lower order function may exhibit a very slow convergence rate. Conveniently, a modal superposition method can be applied to simplify the solution of the beam equation. Using the formulation in Jensen (2001), the solutions by the modal superposition method are written as

$$\nu(x,t) = \sum_{j}^{\infty} u_j(x) w_j(t) \quad ; \quad \phi(x,t) = \sum_{j}^{\infty} \varphi_j(x) w_j(t) \tag{2.39}$$

where $u_j = u_j(x)$, $\varphi_j = \varphi_j(x)$ are the modal shape functions and $w_j = w_j(t)$ are the corresponding modal coefficients. The sub index j denotes the degree-of-freedom which can be rigid body modes or flexible modes (also known as generalized modes). The rigid body motions are heave and pitch in the present context. The flexible modes are the planar vertical vibrational modes, e.g. 2-node or 3-node vertical bending modes. Figure 2.5 shows the convention for the generalize modes where the ∞ has been replaced by a discrete number n for practical reasons. By definition, mode shapes must be orthogonal and fulfill the boundary conditions of concern. For a floating vessel the boundary condition applied to both ends of the beam is the free-free boundary condition i.e. $M(x_{\min}) = M(x_{\max}) = 0$ and $Q(x_{\min}) = Q(x_{\max}) = 0$.

Mode shapes can be determined from an eigenvalue problem formulated on a free vibration with no external forces applied to the beam. Following the d'Alembert principle, the free vibration problem is a harmonically oscillating system with the free-free boundary condition. Inserting Eq. (2.39) into Eqs. (2.35) yields

$$-\frac{d}{dx}\left(EI \frac{d\varphi(x)}{dx} \right) - kGA \left[\frac{d\,u(x)}{dx} - \varphi(x) \right] = \omega^2 m r^2 \varphi(x) \tag{2.40a}$$

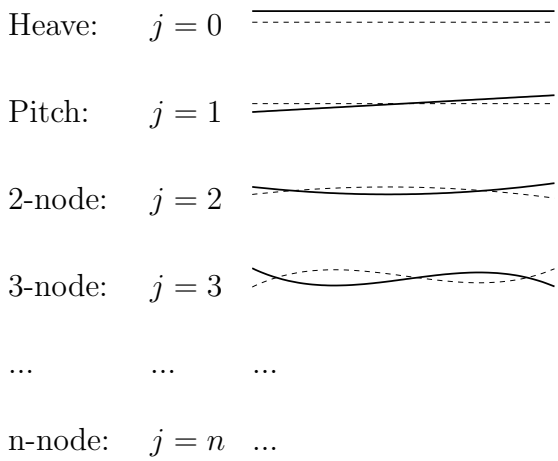

Figure 2.5: Numering of the generalized mode shapes

$$-\frac{d}{dx}\Big\{kGA\Big[\frac{d\,u(x)}{dx} - \varphi(x)\Big]\Big\} = \omega^2 m\, u(x) \tag{2.40b}$$

which are the equations defining the solutions for the mode shapes. The equations are written in conservative form implying that the material properties EI, kGA, m and r^2 may have a spatial variation and must be differentiable at least once. The frequency associated with each mode shape is ω. The frequency for the rigid body motion i.e. heave and pitch are $\omega_0 = \omega_1 = 0$ Hz.

It can be shown that the orthogonality conditions for the generalized mode shapes are

$$\int_L \Big(mr^2\varphi_i\varphi_j + mu_iu_j\Big)\,dx = \begin{cases} 0 & \text{for} \quad \omega_i \neq \omega_j \\ A_j & \text{for} \quad \omega_i = \omega_j \end{cases} \tag{2.41}$$

where A_j, the value of the integral with $i = j$, is called the generalized mass. The orthogonality conditions must be satisfied for all combinations of generalized mode shapes including the rigid body modes. For heave and pitch modes, the shape functions which satisfies the free-free boundary conditions are

$$\text{heave, j=0}: \quad u_0 = 1 \qquad \varphi_0 = 0 \qquad \omega_0 = 0 \tag{2.42}$$

$$\text{pitch, j=1}: \quad u_1 = x - x_{\text{CG}} \qquad \varphi_1 = 1 \qquad \omega_1 = 0 \tag{2.43}$$

An illustration of the rigid modes is shown in Fig. 2.5. There are several numerical techniques to solve Eq. (2.40) for the flexible mode shapes. Without using a complicated finite element approach, a good alternative iterative solution was presented by Collatz (1963), the so-called Stodola's method, see also Jensen (2001) and Appendix C. Initially, an arbitrary deflection consistent with the applied boundary conditions is assumed. The corresponding bending moment and shear force are calculated and a new and improve deflection is evaluated by a direct integration of the governing differential equation. The new deflection is subsequently adjusted to satisfy the

boundary conditions and the corresponding frequency is evaluated. The iteration repeats until the frequency has converged. The iterative scheme will always converge to the first fundamental mode. To determine higher modes, the orthogonality condition is applied and lower modes are removed from the intermediate solutions. Appendix C provides a step-by-step description of the iterative scheme with a consideration of the accuracy and convergence of numerical integration methods.

Assuming that the normal and tangential damping coefficient are equal i.e. $\mu = \epsilon$, and applying the orthogonality condition i.e. Eq. (2.41), the governing Timoshenko beam equation, Eq. (2.35), reduces to

$$\ddot{w}_j + \mu\omega_j^2\,\dot{w}_j + \omega_j^2\,w_j = \frac{1}{A_j}\int\limits_L u_j(x)f(x,t)\,dx \quad \text{for} \quad j = 0, 1, ..., n \tag{2.44}$$

which is the governing equation for the model coefficient w_j. The right-hand side of the equation is the external force projected onto the modal coordinate j. Since the frequency of the rigid body modes is zero, the modal equation for heave and pitch reduces to

$$\text{Heave:} \quad \left.\begin{array}{l} u_0 = 1 \\ A_0 = m_t \end{array}\right\} \Rightarrow m_t\ddot{w}_0 = f_z(t) \tag{2.45a}$$

$$\text{Pitch:} \quad \left.\begin{array}{l} u_1 = x - x_{\text{CG}} \\ A_1 = I_{\text{yy}} + \int\limits_L mr^2dx \end{array}\right\} \Rightarrow \Big(I_{\text{yy}} + \int_L mr^2dx\Big)\ddot{w}_1 = \tau_{\text{y}}(x_{\text{CG}}, t) \tag{2.45b}$$

which are the governing equation for the rigid body motion and clearly show that the generalized modes formulation can also be applied to the pure rigid body motion.

Since the modal equation (Eq. (2.44)) is a system of ordinary differential equations traditional numerical integration technique such as the 4th-order explicit Runge-Kutta scheme can be applied. Nonetheless, it is important to emphasize that the mass distribution m is the structural mass implying that the dry mode shapes are applied in the formulation. Consequently, the consistency of the formulation depends strongly on an accurate and implicit prediction of the applied force distribution $f(x,t)$, cf. Eq. (2.35b), which must include the hydrodynamic related added-mass and damping.

Furthermore, $f(x,t)$ may have a strong dependency on the local deflection and the associated dynamics of the flexible beam creating a tightly coupled system of equations. In such case, Eq. (2.44) must be solved implicitly using an appropriate numerical method. In the best case scenarios, $f(x,t)$ is known and the dependency on the deflection is weak such that each individual mode in Eq. (2.44) can be solved individually as a decoupled system.

2.6 Boundary Conditions

The ALE governing equations for flow is solved in a finite domain. To obtain a unique solution, the boundary conditions must be specified. The transport equation for the phase fraction requires a boundary condition for the phase fraction α. The velocity and pressure are strongly coupled dictated by the momentum equation with

the velocity constrained to obey the divergence free condition. In principle, only the boundary condition for the velocity $\boldsymbol{u}$ is required. The momentum equation, however, is split such that the velocity and pressure are computed separately. The splitting requires the boundary condition for the pressure p to be specified as well.

There are three types of boundary conditions: the Dirichlet type, the Neumann type and a mixing between the two. For the Dirichlet condition the boundary values are specified directly e.g. $\boldsymbol{u} = \textit{constant}$ at the inlet. For the Neumann type, the boundary value is defined in terms of its spatial gradient e.g. $\partial\alpha/\partial\boldsymbol{n} = 0$ on the solid body. A mixing between the two types is possible such that the boundary condition is a combination of a function value and its derivatives.

In the present work, several types of boundary conditions are used in simulations. These are named after their physical representation: solid wall, inlet, outlet, symmetry plane, and open boundary. The wall type boundaries are e.g. surface of the hull, sea bed or solid walls of a wave tank. While the sea bed can be considered fixed, the surface of the hull may be moved in the fluid domain. The inlet and outlet boundaries are designed to permit the flow to enter or exit the computational domain. The inlet condition is usually known, but the outlet is not. More details are presented in the following subsections.

2.6.1 Wall

The surface of the solid body is considered impermeable. Using the no-slip condition, the fluid velocity is set equal to the velocity of the surface of the body. Thus, on the surface of a fixed solid wall, the fluid velocity is $\boldsymbol{u} = 0$. On the surface of the hull moving with a velocity $\boldsymbol{u}_{\mathrm{B}}$, the fluid velocity shall be

$$\boldsymbol{u} = \boldsymbol{u}_{\mathrm{B}} \tag{2.46}$$

While the no-slip condition $\boldsymbol{u} = \boldsymbol{u}_{\mathrm{B}}$ is no doubt the most physically correct boundary condition on a physical impermeable surface, there are certain situations where the solid surface should be treated as a slip boundary condition. For example, when simulating a vessel sailing on infinitely deep water, the computational boundary, which represents the sea bed, may be more appropriately defined using a slip condition to minimize the effect of a numerical truncation of an infinite domain. The slip boundary condition only enforces the impermeable condition of the surface, which is

$$\boldsymbol{u} \cdot \boldsymbol{n} = \boldsymbol{u}_{\mathrm{B}} \cdot \boldsymbol{n} \tag{2.47}$$

stating that the fluid velocity normal to the solid surface complies with the normal velocity of the surface itself. There is no mass or volume flux through the surface. The fluid velocity parallel to the surface, however, is unrestricted.

For the pressure, the wall boundary condition is less intuitive, but can be derived from the momentum equation. Applying a dot product of $\boldsymbol{n}$ (surface unit normal vector) to the momentum equation and enforcing the condition for an impermeable wall on the velocity field yields the boundary condition for the excess pressure,

$$\boldsymbol{n} \cdot \nabla p_d = \boldsymbol{n} \cdot (\nabla \cdot \boldsymbol{\sigma}) - (\boldsymbol{g} \cdot \boldsymbol{x}) \nabla \rho \cdot \boldsymbol{n} \quad \text{for} \quad \boldsymbol{x} \in \partial\Omega \tag{2.48}$$

where $\boldsymbol{\sigma}$ is the viscous shear stress tensor as shown in Eq. (2.12). The first term on the right-hand side is the surface normal gradient of the shear stress, which can be taken as zero. In the second term, $\nabla\rho \cdot \boldsymbol{n}$ is the surface normal gradient of ρ. Applying the incompressible fluid assumption, the surface normal gradient of ρ shall be zero if the surface of the solid body is either fully wet or fully dry. Numerically, ρ may vary across the interface. However, its gradient normal to the surface of the solid body is approximated by zero since there is no account for the surface tension in the fluid. Hence, the boundary condition for the excess pressure becomes:

$$\frac{\partial p_d}{\partial \boldsymbol{n}} \approx 0 \quad \text{for} \quad \boldsymbol{x} \in \partial\Omega \tag{2.49}$$

The implication of this approximation is that the surface normal gradient of ρ is zero everywhere. Thus, for the phase fraction, the wall boundary condition (without accounting for the surface tension) is

$$\frac{\partial \alpha}{\partial \boldsymbol{n}} \approx 0 \quad \text{for} \quad \boldsymbol{x} \in \partial\Omega \tag{2.50}$$

2.6.2 Inlet

For a simple laminar constant inflow condition, the boundary condition for $\boldsymbol{u}$ is the Dirichlet boundary condition specifying directly the value of $\boldsymbol{u}$ at the inlet boundary. The constant inflow velocity may represent a physical current in the flow, but also an artificial current due to a moving frame of reference. Imposing the artificial current is a way to simulate a vessel moving forward at a constant speed. A non-accelerating frame of reference is defined to follow the constant forward speed of the vessel. If the spatial coordinate of the moving frame is $\boldsymbol{x}'$, and the vessel is moving at a constant velocity $\boldsymbol{u}_0$, the relation between the initial reference frame and the moving reference frame is

$$\boldsymbol{x} = \boldsymbol{u}_0\, t + \boldsymbol{x}' \tag{2.51}$$

such that $\dot{\boldsymbol{x}} = \boldsymbol{u}_0 + \dot{\boldsymbol{x}}'$ and the zero current velocity in the initial frame is equivalent to an artificial backward flow $\dot{\boldsymbol{x}}' = -\boldsymbol{u}_0$ in the non-accelerated forward moving frame of reference. Applying the coordinate transformation, Eq. (2.51) to the governing equation yields no changes provided that the flow variables such as phase fraction, velocity and pressure fields are defined in space and time relative to the moving, but non-accelerating frame of reference.

For the pressure, if the exact pressure at the inlet boundary is not known the boundary value must be extrapolated from the internal field. When the velocity boundary condition is defined as the Dirichlet type, the boundary condition for the pressure can be approximated as the Neumann type presented in Eq. (2.49).

2.6.3 Outlet

The flow field at the outlet is usually not known. When the outlet boundary is located far behind the vessel, the flow field is weakly influence by the presence of

the vessel. In such a case, it is assumed that the outlet flow field is confined to an undisturbed flow condition. On the other hand, it is not always practical to extend the outlet boundary too far away since the computational domain then will be too large for the available processing power. The approximation applied to the velocity field in the present work is that the Neumann type zero gradient is applied locally where the flow is flowing out of the domain and the Dirichlet type $\boldsymbol{u} = 0$ is applied elsewhere. This is known as a mixed *inlet-outlet* boundary condition where the local inflow at the outlet is restricted and the local outflow is approximated based on the extrapolation of the internal flow field.

In the presence of an incident wave field, this boundary condition will produce artificial wave reflection such that numerically generated waves are reflected from the outlet boundary into the domain yielding an erroneous flow field inside the area of interest. Several specialized outlet boundary conditions exist in the literature developed to absorb wave energy at the outlet boundary and minimize the reflection, see Clément (1996) and Luppes et al. (2010). While the approximation presented in Luppes et al. (2010) seems to work well, similar performance can be achieved using the classical sponge layer or a relaxation technique. In Clément (1996), a relaxation zone and an absorbing boundary condition are applied in tandem to make use of advantages from both techniques and maximize the performance of the wave absorption. In the present work, relaxation zones are introduced to avoid problems with reflecting waves at the outlet boundary. The technique has been applied in Engsig-Karup (2006) with a high-order Boussinesq-type wave simulation and later was adopted in the work of Jacobsen (2011) to relax waves simulated using a VOF-based URANS flow solver. The approach is to modify the flow solution, such that within each time step, after solving for the flow field, the solution inside the relaxation zone is post-processed and smoothly relaxed toward a predefined condition. The key to obtain a smooth relaxation is an appropriate modelling of the relaxation coefficient. For the purpose, a new model of the relaxation coefficient is proposed. More details are presented in Sec. 2.7.

2.6.4 Symmetry Plane

When the flow field and the vessel are symmetric about a plane, the computational effort can be reduced by introducing a smaller domain accounting only one side of the symmetry plane. The boundary conditions are

- The velocity normal to the symmetry plane is zero
- The gradient of the pressure normal to the symmetry plane is zero.

The symmetry plane boundary condition is very similar to the slip-wall condition except that it is applied not only to velocity but to all variables. The symmetry plane boundary condition is applied in the present work when simulating a vessel moving in head sea.

2.6.5 Open Boundary

The top boundary of the computational domain shall represent an open air space. The approximation, introduced at this boundary, is that the total pressure p_0 is

constant and equal to the atmospheric pressure i.e. the operating pressure p is written as

$$p = p_0 - \frac{1}{2}\rho|\boldsymbol{u}|^2 \left[1 - \text{pos}(\phi)\right] \tag{2.52}$$

In terms of the excess pressure p_d, see definition in Eq. (2.13), p_0 is set to zero yielding

$$p_d = -\frac{1}{2}\rho|\boldsymbol{u}|^2 \left[1 - \text{pos}(\phi)\right] \quad \text{on} \quad \partial\Omega \tag{2.53}$$

The flux ϕ through the boundary varies depends on the internal field of the flow and determines the flow direction through the boundary. The function pos() is defined as $\text{pos}(\phi) = 1$ for $\phi > 0$ and $\text{pos}(\phi) = 0$ for $\phi <= 0$. That is, the flux is positive for a flow out of the domain and negative for a flow into the domain. As seen in the above expression, the outlet flow is varied locally on the boundary to allow keeping the total pressure constant.

2.7 Wave Generator & Relaxation Zones

Waves in a physical wave tank are generated using either a flap type or a piston type wave-maker. The relation between the paddle displacement and the output wave amplitude, commonly presented as a transfer function, are derived using the potential flow theory solving the Laplace equation for the velocity potential with or without a linearization of the free surface conditions. In principle, waves in any direction can be generated using a multi-paddle system. The quality of the generated wave field depends strongly not only on the paddle configuration, but also on the accuracy of the transfer function to predict the generated wave given a paddle motion. Errors may be observed as spurious waves travelling on top of the main wave causing a local amplification or a reduction in the wave height. A sophisticated controlling algorithm with a feedback loop can be constructed to obtain a good matching between the target wave and the wave realized in the physical wave tank. An excellent review on the wave-maker theory can be found in Sand (1979).

2.7.1 Numerical Wave Generator

In the numerical wave tank, the same approach can be adopted to introduce waves into the flume i.e. the flap or piston motion is simulated to mimic the behavior of the physical wave-maker. On the other hand, the wave kinematics provided by potential flow theory can be prescribed directly at the wave-maker boundary. The technique has been applied in Nielsen (2003) and later in Jacobsen (2011) which proved to be versatile since, in principle, any types of wave can be introduced into the flume. In the work of Jacobsen (2011), the types of wave introduced into the wave flume are: 1st and 2nd-order Stokes waves (Dean & Dalrymple (1991)), 1st-order cnoidal waves (Svendsen (2006)), and monochromatic wave solutions by the stream function theory (Fenton (1988)).

In the present work, the stream function wave theory has been applied to introduce regular long-crested monochromatic waves into the numerical wave flume simulating

a vessel moving at constant forward speed in head seas. In addition, the same wave generator technique is applied to introduce deterministic conditional waves (Jensen (2001)) for a study of slamming in an extreme sea state.

The stream function wave is a fully nonlinear solution to the steady regular wave solving an irrotational flow using a stream function formulation and a solution based on a Fourier expansion. The first publication is provided by Rienecker & Fenton (1981) where they present the fully non-linear stream function solution as,

$$H(x,t) = \sum_{j=1}^{N} A_j \cos\Big[jk(x - c\,t)\Big] \tag{2.54a}$$

$$\Psi(x,z,t) = B_0(z+h) + \sum_{j=1}^{N} \frac{B_j}{jk} \frac{\sinh\Big[jk(z+h)\Big]}{\cosh(jkh)} \cos\Big[jk(x - c\,t)\Big] \tag{2.54b}$$

with the velocity field defined as

$$\boldsymbol{u}(\boldsymbol{x},t) = \left\{ \frac{\partial \Psi(x,z,t)}{\partial z},\, 0,\, -\frac{\partial \Psi(x,z,t)}{\partial x} \right\}^T \tag{2.54c}$$

The mean water level is $z = 0$ and the water depth is h with the sea bed assumed to be flat. The propagation direction is from "left" to "right" (positive-x direction). The coefficients B_j are constants corresponding to the particular wave characteristic with wave number k and phase velocity c (celerity). An iterative solution algorithms including a Fortran code to determine B_j is provided by Fenton (1988). An arbitrary high-order solution can be obtained.

On the other hand, the stochastic wave applied in the present work is based on the linear wave theory where the stochastic wave elevation $H(x,t)$ is written as

$$H(x,t) = \sum_{i=1}^{n} a_i \cos(k_i x - \omega_i t + \theta_i) \tag{2.55}$$

where the phase θ_i are considered to be stochastic variables and the amplitudes a_i are deterministic variables. Given a wave spectrum $S(\omega_i)$, e.g. the Pierson Moskowitz (PM) spectrum, the amplitudes can be written as (cf. Jensen (2001)),

$$a_i = \sqrt{2S(\omega_i)\Delta\omega_i} \tag{2.56}$$

with n discrete frequencies ω_i predetermined to cover the wave spectrum. Using a second order stochastic wave is possible at the expense of more computational time since the summation terms of the second order wave elevation is growing by $O(n^2)$.

2.7.2 Inlet & Outlet Relaxation Zones

To minimize reflections of outgoing waves at the outlet boundary, a relaxation technique is applied. At each time step, the fluid solution is post-processed such that inside a predefined relaxation zone, the computational results are altered by

a blending function that accounts for the intermediate computed flow field and a target flow field. The computational result shall be smoothly relaxed. Given a target velocity field $\boldsymbol{u}_e$ and the unaltered computed velocity field $\boldsymbol{u}_p$, the modified velocity field is written as

$$\boldsymbol{u} = \gamma \boldsymbol{u}_e + (1-\gamma)\boldsymbol{u}_p \tag{2.57}$$

As already mentioned in Sec. 2.6.3, this relaxation technique has been applied previously in Mayer et al. (1998), Fuhrman (2004), Engsig-Karup (2006), and recently in Jacobsen (2011). Because the relaxation is applied explicitly in a post-processing step, it is possible to introduce the relaxation zone at the inlet such that waves caused by wave interaction with an oscillating body can be damped out. Without a proper relaxation, the radiating waves may propagate upstream toward the inlet boundary and reflect back into the domain polluting the flow field. When a relaxation is applied at the inlet, the flow field is relaxed toward the imposed incident wave field.

To obtain a smoothly modified internal flow field, it is required that the relaxation coefficient γ and its spatial derivatives are equal zero along the interface connecting the relaxation zone and the internal field of the computational domain. There are many possibilities to choose a functional shape of the relaxation coefficient. Mayer et al. (1998) used a profile written as

$$\gamma(\beta) = b\beta^3 + (1-b)\beta^6 \tag{2.58}$$

where β is the dimensionless distance which, in the present formulation, is defined as $\beta = 1 - (x - x_{\text{start}})/(x_{\text{end}} - x_{\text{start}})$, and b is a free parameter in between [0, 2]. In Fuhrman (2004) and Jacobsen (2011), their choice is

$$\gamma(\beta) = \frac{\exp(\beta^{7/2}) - 1}{\exp(1) - 1} \tag{2.59}$$

which produces a profile similar to Eq. (2.58) (with $b \approx 0.35$). Engsig-Karup (2006) used a function when rewritten using β yields,

$$\gamma(\beta) = \beta^p \tag{2.60}$$

with a parameter p chosen, e.g. $p = 6$. This expression can become exactly as Eq. (2.58) if b in Eq. (2.58) is set to $b = 0$. A few examples are shown in Fig. 2.6. The choice of a given profile may depend strongly of the problem and the specified length of the relaxation zone. Most importantly, the choice is not unique.

Noticeably, in all these previous works the profile is made constant in time. The spatial variation of γ is fixed and the same profile is applied to relax the flow field in every time step. In the present work, it is found that, doing so, the relaxation can become too severe depending on the time step size. To illustrate the problem, we can consider Eq. (2.57) with the target velocity $\boldsymbol{u}_e = 0$. The flow field inside the relaxation zone will be,

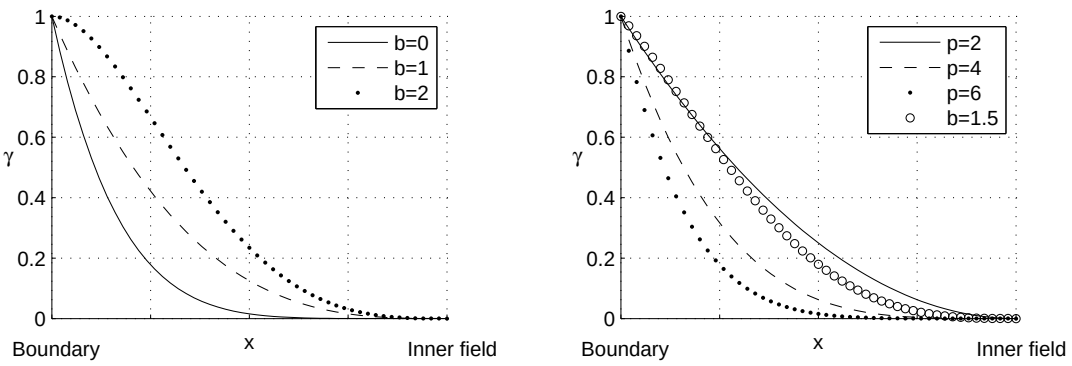

(a) Eq. (2.58) (b) Eq. (2.60)

Figure 2.6: Examples of relaxation profiles applied in: (a) Mayer et al. (1998), and (b) Engsig-Karup (2006)

$$\boldsymbol{u} = (1-\gamma)\boldsymbol{u}_p \tag{2.61}$$

that is, in every time step, the computed flow field is reduced by a constant factor. Between a time interval t_1 and t_2, the computation is proceeded using n steps in total, and the velocity at t_2 applying the relaxation will be approximately,

$$(\boldsymbol{u})_{t_2} \approx (1-\gamma)^n (\boldsymbol{u}_p)_{t_1} \tag{2.62}$$

The velocity may have a stronger variation dictated by the governing equation of the flow and the applied boundary condition. If the size of the time step is fixed, the coefficient γ can be defined manually for the particular wave profile. Nevertheless, the constant relaxation $(1-\gamma)^n$ is problematic since it depends strongly on n. Thus, when the size of the time step is changing one may need to adjust the relaxation profile once again to assure the proper behavior of the relaxation zone. The re-adjustment of the relaxation coefficient may appear manageable in those cases where the time step size is kept constant during the simulation. In other cases, an adaptive time step scheme is applied and it is more convenient if the profile of the relaxation coefficient automatically adapts to follow the variation of the time step size.

Consider a fluid particle entering a local control volume where the target relaxation is set to γ_{tar}. Using the approximation shown in Eq. (2.62), and demand that $(1-\gamma)^n = 1-\gamma_{\text{tar}}$ when the particle leaves the control volume, yields

$$\gamma = 1 - (1-\gamma_{\text{tar}})^{|\boldsymbol{u}|\Delta t/\Delta s} \tag{2.63}$$

This equation is proposed and applied in the current study. It provides a way to adjust the relaxation coefficient dynamically using the local flow condition. The target profile γ_{tar} can be defined using any of the previously known functions, e.g. Eq. (2.58). The magnitude of the local flow velocity is $|\boldsymbol{u}|$ and the time step size is Δt and the local characteristic cell size is Δs. The exponent $|\boldsymbol{u}|\Delta t/\Delta s$ looks very similar to the local Courant Number except that Δs can be more freely specified. In the present work, it is found reasonable to set $\Delta s = 0.5\Delta x$ where Δx is the local cell size in the flow direction.

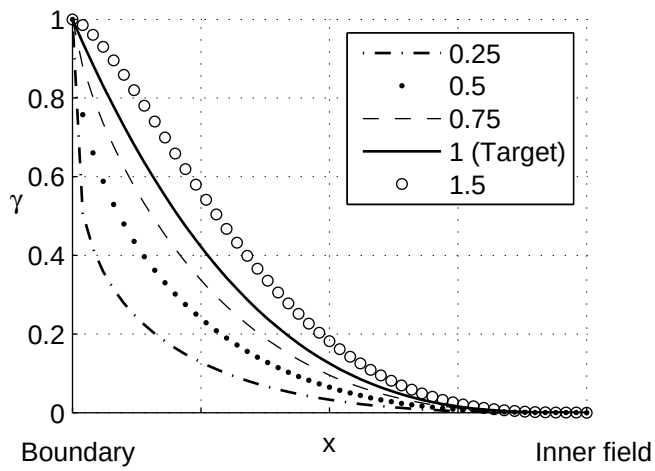

Figure 2.7: An example of profiles produced by Eq. (2.63). The target profile corresponds to $|\boldsymbol{u}|\Delta t/\Delta s = 1$ and γ may change dynamically depending on the local flow variation.

Thus, when applying Eq. (2.63), the local relaxation coefficient is adjusted dynamically similar to applying a different relaxation profile except that the profile is not fixed, but is changed in space and time. Between two locations inside the relaxation zone, the local value for the relaxation coefficient may be very different depending on the local flow field. The adjustment is made toward a smaller relaxation if the local fluid momentum is already very small. Figure 2.7 shows an example of the profiles produced by Eq. (2.63). Numerical tests and the performance of the relaxation technique applied with the proposed relaxation profile will be discussed in Chapter 5.

Chapter 3

Solution Algorithms & FSI Coupling Schemes

The governing VOF-based Navier-Stokes equations in the ALE formulation are discretized and solved using the well known finite volume method (FVM). All the variables are arranged in a collocated manner. A very comprehensive description of a FVM implementation can be found in many standard textbooks, see e.g. Ferziger & Perić (2001). A more specific implementation using an object-oriented programming language with a tensorial approach to describe the governing equation is presented in Weller et al. (1998), Jasak (1996), Rusche (2002) and the OpenFOAM programmer's guide (2012).

In the implementation, one important feature is worth mentioning. That is, the face-based data structure which enables the use of an unstructured polyhedral mesh. The computational mesh is described, first by a list of points, second by a list of polygonal faces where each face is described as a list of 3 or more points, and finally a list of polyhedral cells is described by assigning faces to cells. For example, each face is labelled as "belonging to" a unique cell number. To identify neighboring cells, each face assumes to be attached to two neighboring cells: one is its "owner" and the other one is its "neighbor". Most importantly, there is no information about the cell structure. There is no difference between regular or irregular cells other than a list of points and faces. Consequently, the discretization procedures are done on each face without any assumption of the cell shape. Almost all implemented discretization schemes treat structured and unstructured cells equally.

The standard procedure in the finite volume discretization is to integrate the governing equation in space and time over each cell. The volume integration is converted to a surface integration using Gauss's theorem, which states that

$$\text{For a vector field:} \quad \int_{\Omega} \nabla \cdot \boldsymbol{u} \, dV = \oint_{\partial\Omega} \boldsymbol{u} \cdot \boldsymbol{n} \, dS \tag{3.1}$$

$$\text{For a scalar field:} \quad \int_{\Omega} \nabla p \, dV = \oint_{\partial\Omega} p\boldsymbol{n} \, dS \tag{3.2}$$

These expressions are valid for a vector field (e.g. $\boldsymbol{u}$) or a scalar field (e.g. p). Assuming that the computational cell is a polyhedral control volume composed of flat faces, the closed surface integral can be converted to a summation of the integral over each individual face, such that

$$\oint_{\partial\Omega} \boldsymbol{u} \cdot \boldsymbol{n}\, dS = \sum_f \int_f \boldsymbol{u} \cdot \boldsymbol{n}\, dS = \sum_f \phi_f \tag{3.3}$$

where f indicates that the integral is to be performed over the surface of the presumed flat cell faces. The face integral in the summation term on the right-hand side is the total volume flux through the face. Introducing the spatial average face velocity $\boldsymbol{u}_f$, the total volume flux through each face can be evaluated as

$$\phi_f \equiv \int_f \boldsymbol{u} \cdot \boldsymbol{n}\, dS = \boldsymbol{u}_f \cdot \boldsymbol{S}_f \tag{3.4}$$

where $\boldsymbol{S}_f$ is the standard notation in OpenFOAM for face area vector[1]. The corresponding mass flux defined in terms of the spatial average face velocity is $(\rho \boldsymbol{u}_f) \cdot \boldsymbol{S}_f$ where ρ is the density. The average face values are commonly obtained through interpolation, e.g. by the means of a Central Difference scheme (CD), an Upwinding scheme (UD) or some other interpolation schemes. An additional correction is required when the mesh is non-orthogonal. That is, no correction is necessary when $\boldsymbol{n}$ is parallel to the vector connecting the centroids of the neighbor cells on either side of the face. A description of many commonly used interpolation schemes and techniques to treat a non-orthogonal mesh can be found in Muzaferija (1994), Jasak (1996), and in a standard text book such as Ferziger & Perić (2001).

Gauss's theorem is to be applied to all gradient and divergence terms. The time derivative terms, however, yield a volume average such that

$$\frac{\partial}{\partial t} \int_\Omega \rho \boldsymbol{u}\, dV = \frac{\partial}{\partial t}(\rho_{\mathrm{P}} \boldsymbol{u}_{\mathrm{P}} V) \tag{3.5}$$

where V is the total volume of the cell and the subscript $_{\mathrm{P}}$ denotes the volume averaging defined as

$$\boldsymbol{u}_{\mathrm{P}} \equiv \frac{1}{V} \int_\Omega \boldsymbol{u}\, dV \tag{3.6}$$

In the standard finite volume notation, $_{\mathrm{P}}$ is also called the cell averaged value. A complete list of the finite volume discretization of the difference terms in the governing equation can be found in OpenFOAM programmer's manual (2012). For convenience, a list containing only terms applied in this work is presented in Table 3.1.

[1] $\boldsymbol{S}_f \equiv \boldsymbol{n}\, A_f$, i.e. the face area is $|\boldsymbol{S}_f| = A_f$ and $\boldsymbol{n} = \boldsymbol{S}_f / A_f$

Table 3.1: Finite volume discretization of different terms. Using Gauss's theorem, the volume integration is converted to a surface integration, which is then discretized to a discrete summation assuming flat faces polygonal cells. Vector fields $(\boldsymbol{u}, \boldsymbol{u}_c)$, Scalar fields (ρ, p), Face area vector $(\boldsymbol{S}_f)$

-	Term	FVM Discretization
Time derivative	$\frac{\partial(\rho \boldsymbol{u})}{\partial t}$	$\frac{\partial}{\partial t}(\rho_{\mathrm{P}} \boldsymbol{u}_{\mathrm{P}} V)$
Divergence term	$\nabla \cdot \boldsymbol{u}$	$\sum_f \boldsymbol{u}_f \cdot \boldsymbol{S}_f$
Gradient term	$\nabla \rho$	$\sum_f \rho_f \boldsymbol{S}_f$
Convection term	$\nabla \cdot (\rho \boldsymbol{u} \boldsymbol{u}_c^T)$	$\sum_f (\rho_f \boldsymbol{u}_{c,f} \cdot \boldsymbol{S}_f) \boldsymbol{u}_f$
Laplacian term	$\nabla \cdot \rho \nabla p$	$\sum_f \rho_f (\nabla p)_f \cdot \boldsymbol{S}_f$

3.1 The PISO Scheme

In this section, the focus is on the solution algorithms for solving the ALE governing equation of the two-phase flow. The governing equation, see Eq. (2.15), defines a strong coupling between the velocity field and the pressure. A solution algorithm known as the PISO-scheme (Pressure Implicit Splitting of Operators, Issa (1985)) is provided by the OpenFOAM software package. The PISO-scheme is a variant of the SIMPLE-scheme (Semi-Implicit Method for Pressure Linked Equations, Patankar (1980)) which is more suitable for a transient flow problem. The application of the PISO scheme in the present work is outlined below.

The PISO scheme contains two major steps: a predictor and a corrector step. The momentum equation needs to be re-arranged into a velocity-pressure coupling equation system. At first, the terms involving velocity fields are collected on the left-hand side of the momentum equation and discretized using the finite volume method. The semi-discretized momentum equation reads

$$[\mathcal{A}][U] = [\mathcal{H}] - [\nabla p_d] - [(\boldsymbol{g} \cdot \boldsymbol{x}) \nabla \rho] \tag{3.7}$$

where $\mathcal{A}$ and $\mathcal{H}$ are the discretization operators providing weighting coefficients corresponding to the applied scheme. The unknown velocities are arranged in the matrix $[U]$. It shall be noted that $\mathcal{A}$ and $\mathcal{H}$ are dependent on the unknown convective velocity field. That is, the convective velocity must be provided to evaluate and construct $[\mathcal{A}]$ and $[\mathcal{H}]$. Furthermore, the pressure p_d is unknown and its solution is tightly coupled with the unknown divergence free velocity field. Given a convective velocity field, the flow solution is written

$$[U] = [\mathcal{A}]^{-1} \Big\{ [\mathcal{H}] - [\nabla p_d] - [(\boldsymbol{g} \cdot \boldsymbol{x}) \nabla \rho] \Big\} \tag{3.8}$$

in which a Poisson equation for the pressure can be derived by using the divergence free condition of the velocity field. That is, evaluating the divergence of Eq. (3.8)

$$\nabla \cdot \Big([\mathcal{A}]^{-1} [\nabla p_d] \Big) = \nabla \cdot [\mathcal{A}]^{-1} \Big\{ [\mathcal{H}] - [(\boldsymbol{g} \cdot \boldsymbol{x}) \nabla \rho] \Big\} \tag{3.9}$$

the use of the PISO-scheme for solving the velocity-pressure coupling can be summarized as follows:

1. **Momentum predictor:** Solve Eq. (3.8) for $[U]^{(0)}$ using the previously known pressure field. The approximate velocity field found at this stage is $[U]^{(0)}$ and does not obey the divergence free condition because the applied pressure field is only a rough estimate.

2. **Momentum corrector:** There are several sub-operations in the corrector step. These are

   (a) Evaluate $[\mathcal{A}]^{(k)}$ and $[\mathcal{H}]^{(k)}$ corresponded to $[U]^{(k)}$, where k denotes the number of sub-iteration (initially $k = 0$)

   (b) Using $[\mathcal{A}]^{(k)}$ and $[\mathcal{H}]^{(k)}$, solve Eq. (3.9) for the pressure field $p_d^{(k)}$

   (c) Evaluate the next estimate $[U]^{(k+1)}$ by using Eq. (3.8) with $[\mathcal{A}]^{(k)}$, $[\mathcal{H}]^{(k)}$ and $p_d^{(k)}$

   (d) Repeat (a) until convergence

Notice that in Step 2c the velocity in the $[\mathcal{H}]^{(k)}$ operator is evaluated at a different iteration level than $[U]^{k+1}$ which is why the term "operator splitting" has been used to name the scheme. In the momentum predictor step the implicit solution of Eq. (3.8) is required implying a need for a linear equation solver. In Step 2c, however, the solution of Eq. (3.8) is readily obtained due to the use of the operator splitting technique. The similarity with the SIMPLE scheme, Patankar (1980), exists in a sense that the SIMPLE scheme follows:

Step 1 → Step 2a → Step 2b → Apply under-relaxation → repeat Step 1

The major difference between the SIMPLE-scheme and the PISO-scheme is that there is no under-relaxation in the PISO-scheme. Furthermore, the corrector step in the PISO-scheme is performed several times yielding a much more efficient scheme for a time dependent problem where the size of the time step is already small due to the stability constraint. In the original paper by Issa (1985), it was found that $k = 2$ is sufficient for a transient problem.

Rhie & Chow (1983) demonstrates that an appropriate interpolation is required when using a collocated arrangement of the variables. Problems arise due to the occurrence of decoupled weighting coefficients when applying an interpolating operator on the gradient to evaluate a second order spatial derivative. While Rhie & Chow (1983) provides a well known solution for the interpolation scheme, the implementation in OpenFOAM uses a slightly different approach to avoid the problem. Instead of interpolating on the gradient, Gauss's theorem is applied to the second order derivative terms. The technique is described comprehensively in Jasak (1996) and is generally applied in OpenFOAM. At first, Eq. (3.7) is considered at the cell level such that each row in the matrix reads

$$a_{\mathrm{P}}\boldsymbol{u}_{\mathrm{P}} + \sum_{\mathrm{N}}^{\mathrm{nei}} a_{\mathrm{N}}\boldsymbol{u}_{\mathrm{N}} = \boldsymbol{b}_{\mathrm{P}} - \nabla p_{\mathrm{d}} - (\boldsymbol{g}\cdot\boldsymbol{x})\nabla\rho \tag{3.10}$$

where the subscript $_{\mathrm{N}}$ denotes the neighbor cells, while the total number of neighboring cells is $_{\mathrm{nei}}$. In principle, a polyhedral cell may have an arbitrary number of neighbors. The central weighting coefficient is a_{P} while a_{N} are the weighting coefficients for its neighbors. The Poisson equation for the pressure corresponds to Eq. (3.9) considered at the cell level is

$$\nabla\cdot\frac{1}{a_{\mathrm{P}}}\nabla p_{\mathrm{d}} = \nabla\cdot\boldsymbol{u}_{\mathrm{P}} + \nabla\cdot\frac{1}{a_{\mathrm{P}}}\Big\{\boldsymbol{b}_{\mathrm{P}} - \sum_{\mathrm{N}}^{\mathrm{nei}} a_{\mathrm{N}}\boldsymbol{u}_{\mathrm{N}} - (\boldsymbol{g}\cdot\boldsymbol{x})\nabla\rho\Big\} \tag{3.11}$$

Applying the divergence free condition and Gauss's theorem (see Table 3.1) yields

$$\sum_{f}^{\mathrm{faces}} \frac{1}{(a_{\mathrm{P}})_f}(\nabla p_d)_f\cdot\boldsymbol{S}_f = \sum_{f}^{\mathrm{faces}} \frac{1}{(a_{\mathrm{P}})_f}\Big\{\boldsymbol{b}_{\mathrm{P}} - \sum_{\mathrm{N}}^{\mathrm{nei}} a_{\mathrm{N}}\boldsymbol{u}_{\mathrm{N}} - (\boldsymbol{g}\cdot\boldsymbol{x})\nabla\rho\Big\}_f\cdot\boldsymbol{S}_f \tag{3.12}$$

where $_{\mathrm{faces}}$ denotes the total number of cell faces. This expression is the foundation for the equation system for the cell average pressure $(p_d)_{\mathrm{P}}$ provided that the face average pressure gradient $(\nabla p_d)_f$ is given in terms of $(p_d)_{\mathrm{P}}$ and its neighbors $(p_d)_{\mathrm{N}}$. For example, using the CD-scheme yields, cf. Jasak (1996)

$$(\nabla p_d)_f\cdot\boldsymbol{S}_f = \frac{|\boldsymbol{S}_f|}{|\boldsymbol{d}|}\Big[(p_d)_{\mathrm{N}} - (p_d)_{\mathrm{P}}\Big] \tag{3.13}$$

where $\boldsymbol{d}$ is the cell-center distance vector to the neighbor cell. As shown in Eq. (3.12) only the face average first derivative of p_d is required to solve the pressure equation. Hence, there is no need to apply a Rhie & Chow interpolation (1983).

In summary, the solution algorithms of the flow solver, solving the ALE based governing equation (Eqs. (2.22)) using the PISO scheme can be shown schematically as in Fig. 3.1. The flowchart seen in Fig. 3.1 does not consider how to couple the flow solver with the rigid body or flexible motion solver. A discussion on the subject will be presented in Sec. 3.3.

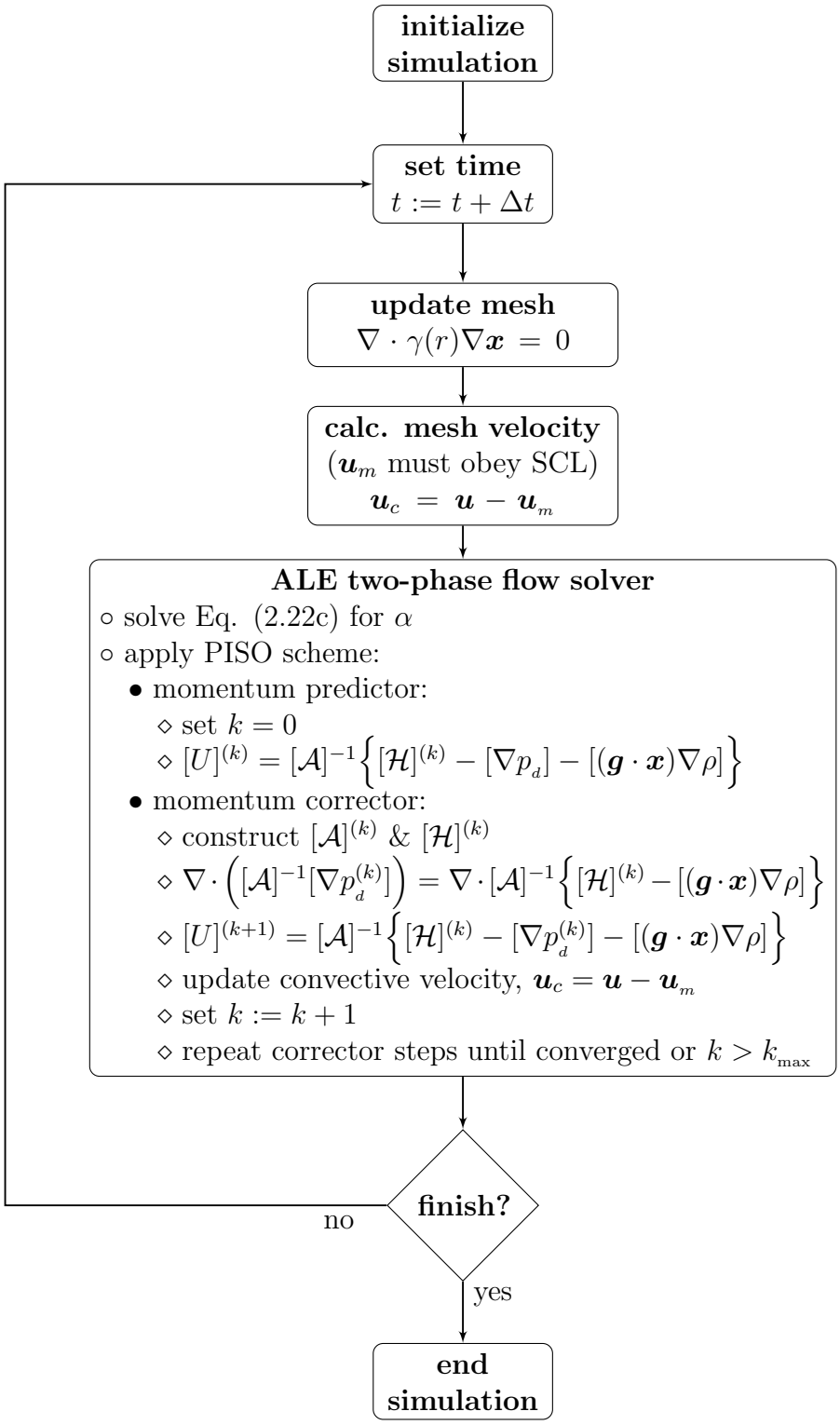

Figure 3.1: A flowchart representation of the PISO solution algorithms applied in the ALE flow solver

3.2 A Variable Step Size Adams-Bashforth-Moulton Method

The governing equations for the rigid body motion and the flexible Timoshenko beam model are a system of ordinary differential equations (ODE). There are several competing numerical solvers for a system of ODEs. Most numerical ODE solvers fall into two categories: *multistep* and *multistage* methods. The classical Runge-Kutta scheme is an example of the multistage method where the solution for the next time step is a weighting of several solutions at some intermediate steps. The solution of the previous time steps are discarded and the scheme acquires new intermediate solutions and uses them exclusively to evaluate the solution for one full-size time step. In contrast to this, the multistep approach reuses the previous solutions without having to evaluate several new intermediate solutions.

Using a free surface CFD solver, the evaluation of a new solution is expensive. Therefore, the multistep approach can be very attractive. A multistep method known as Adams-Bashforth-Moulton Method has been adopted in the present work to solve the governing equations for the body motion with the flexible Timoshenko beam model superimposed on top of the rigid body motion. In general, we seek a numerical solution for an ordinary differential equation written as

$$\dot{y} = f(t, y) \tag{3.14}$$

with the initial value $y(t_0) = y_0$. Taking a discrete time step Δt, the analytical solution at the next time step is

$$y(t_0 + \Delta t) = y_0 + \int_{t_0}^{t_0+\Delta t} f(t, y)\, dt \tag{3.15}$$

The function $f(t, y)$ is to be approximated by a Lagrange polynomial. The difference between many numerical schemes can be found in the approximation of f. The explicit 2nd-order Adams-Bashforth method uses previous known values, two steps back at times (t_{00}, f_{00}) and (t_0, f_0), to extrapolate for the function value at $(t_0 + \Delta t)$. Taking into account that the time step may vary, the previous step size can be defined as $\Delta t_0 = t_0 - t_{00}$ with a time step ratio written as

$$w = \frac{\Delta t}{\Delta t_0} \tag{3.16}$$

In an implicit Adams-Bashforth-Moulton method, the Lagrange polynomial also contains function values of the unknown time $(t_0 + \Delta t)$. Following Ascher et al. (1997), the family of a variable step size implicit-explicit schemes can be generally written as

$$\text{Explicit:} \quad \frac{w^2(2\gamma - 1)}{\Delta t(1 + w)} y_{00} + \frac{w - 2\gamma w - 1}{\Delta t} y_0 + \frac{1 + 2\gamma w}{\Delta t(1 + w)} y_1 =$$

$$-\gamma w f_{00} + (1+\gamma w) f_0 \quad (3.17a)$$

$$\text{Implicit:} \quad \frac{w^2(2\gamma-1)}{\Delta t(1+w)} y_{00} + \frac{w-2\gamma w-1}{\Delta t} y_0 + \frac{1+2\gamma w}{\Delta t(1+w)} y_1 =$$

$$\frac{\beta}{2} f_{00} + (1-\gamma-\frac{\beta(1+\frac{1}{w})}{2}) f_0 + (\gamma+\frac{\beta}{2w}) f_1 \quad (3.17b)$$

where (y_1, f_1) denotes the solution at time $(t_0 + \Delta t)$. Two weighting coefficients (γ, β) have been introduced with a value chosen between 0 and 1. A different choice of (γ, β) produces a different approximation of f, thus a different scheme. For example, the explicit Leap-Frog scheme with a constant time step corresponds to choosing $w = 1, \gamma = 0$ i.e.

$$\frac{1}{2\Delta t}(y_1 - y_{00}) = f_0 \quad (3.18)$$

A particular choice of $(\gamma, \beta) = (\frac{1}{2}, \frac{1}{8})$ has been chosen in the present study corresponding to the Modified Crank-Nicholson Adams-Bashforth scheme (MCNAB) named in Ascher et al. (1997). The name implies that the scheme is similar to applying the Crank-Nicholson scheme for the implicit part and a second order Adams-Bashforth for the explicit part. It has been shown in Ascher et al. (1997) that the scheme has a small truncation error and exhibits a superior numerical damping of high-frequency errors.

Krenk (2006) presented a time integration algorithm where the high-frequency errors can be controlled through an explicit introduction of damping terms added to coefficient matrices in a state-space formulation. An algorithm with optimal damping was derived. Properties such as being unconditionally stable, third-order accuracy, fourth-order damping of high-frequency components, and exact energy conservation are very attractive. However, the work presented in Krenk (2006) was limited to linear dynamic systems. In the current project, the equation of motions with rigid or flexible body assumptions, are strongly coupled with the free surface flow solver creating a nonlinear coupled dynamic system. The algorithm presented in Krenk (2006) cannot be used directly in the current study. Therefore, the explicit-implicit scheme, Eq. (3.17), (also known as a predictor-corrector scheme) has been chosen. With $(\gamma, \beta) = (\frac{1}{2}, \frac{1}{8})$ the explicit and implicit scheme reads

$$\text{Explicit:} \quad y_1 = y_0 + \frac{\Delta t}{2}\Big[(2+w)\dot{y}_0 - w\dot{y}_{00}\Big] \quad (3.19a)$$

$$\text{Implicit:} \quad y_1 = y_0 + \frac{\Delta t}{16w}\Big[(8w+1)\dot{y}_1 + (7w-1)\dot{y}_0 + w\dot{y}_{00}\Big] \quad (3.19b)$$

The implicit scheme is to be solved iteratively. Initially, when $\dot{y}_{00}$ is not available, the explicit Euler-scheme can be applied. The scheme is written as:

$$\text{Explicit Euler:} \quad y_1 = y_0 + \Delta t\, \dot{y}_0 \quad (3.20)$$

The iterative procedure is that the explicit scheme is applied to estimate the initial guess for y_1 whereas the iteration within the corrector step uses the implicit scheme

until convergence. Under-relaxation may be applied within the corrector step to improve the numerical stability.

The implementation of the integration scheme shown in Eq. (3.19) for solving the translational rigid body motion in Eq. (2.26) has been done as follows:

1. **Set time:** Define Δt and evaluate w
2. **Predictor:** Set initial corrector iteration $k = 0$. Apply Eq. (3.19a) for the velocity and Eq. (3.19b) for the position.
   - $(\boldsymbol{v}_o)_1^k = (\boldsymbol{v}_o)_0 + \frac{\Delta t}{2}\left[(2+w)\left(\frac{\boldsymbol{f}_o}{m_t}\right)_0 - w\left(\frac{\boldsymbol{f}_o}{m_t}\right)_{00}\right]$
   - $(\boldsymbol{x}_o)_1^k = (\boldsymbol{x}_o)_0 + \frac{\Delta t}{16w}\left[(8w+1)(\boldsymbol{v}_o)_1^k + (7w-1)(\boldsymbol{v}_o)_0 + w(\boldsymbol{v}_o)_{00}\right]$
3. **Corrector:** Apply Eq. (3.19b) to both the velocity and the position
   - Evaluate $\left(\frac{\boldsymbol{f}_o}{m_t}\right)_1^k$ which corresponds to $(\boldsymbol{v}_o)_1^k$ and $(\boldsymbol{x}_o)_1^k$
   - $(\boldsymbol{v}_o)_1^{k+1} = (\boldsymbol{v}_o)_0 + \frac{\Delta t}{16w}\left[(8w+1)\left(\frac{\boldsymbol{f}_o}{m_t}\right)_1^k + (7w-1)\left(\frac{\boldsymbol{f}_o}{m_t}\right)_0 + w\left(\frac{\boldsymbol{f}_o}{m_t}\right)_{00}\right]$
   - $(\boldsymbol{x}_o)_1^{k+1} = (\boldsymbol{x}_o)_0 + \frac{\Delta t}{16w}\left[(8w+1)(\boldsymbol{v}_o)_1^{k+1} + (7w-1)(\boldsymbol{v}_o)_0 + w(\boldsymbol{v}_o)_{00}\right]$
   - Relax $(\boldsymbol{v}_o)_1^{k+1}$ and $(\boldsymbol{x}_o)_1^{k+1}$ if diverged.
   - Increase $k := k+1$ and repeat the corrector until convergence

The algorithm always applies the implicit scheme to evaluate the position vector $\boldsymbol{x}_o$. The evaluation of the force vector $\boldsymbol{f}_o$ is not specified in the algorithm since it can be provided or evaluated by any means. When coupled to the ALE flow solver, $(\boldsymbol{x})_1^k$ and $(\boldsymbol{v})_1^k$ are to be transferred to the flow solver such that $(\boldsymbol{f})_1^k$ can be evaluated. A similar algorithm is applied to solve Eq. (2.28) for the rotational motion as well as Eq. (2.44) for the modal coefficients of the Timoshenko beam solution. Within the corrector loop, the divergence is checked such that an appropriate under-relaxation can be applied. Denote $\delta = [0,\, 1]$ as the relaxation coefficients, the changes in the solution between each iteration is relaxed as

$$(\boldsymbol{v}_o)_1^{k+1} := \delta(\boldsymbol{v}_o)_1^{k+1} + (1-\delta)(\boldsymbol{x}_o)_1^k \tag{3.21}$$

Here, the symbol ":=" means the variable on the left-hand side is evaluated explicitly using the expression on the right-hand side. The runtime selection of δ is done using

$$\delta := \min\left[1,\, \max\left(0.2,\, (2 - \frac{\epsilon^{k+1}}{\epsilon^k})\delta\right)\right] \tag{3.22}$$

where ϵ^k is the relative error defined as

$$\epsilon^k = \frac{\left|(\boldsymbol{v}_o)_1^k - (\boldsymbol{v}_o)_1^{k-1}\right|}{|(\boldsymbol{v}_o)_1^k|} \tag{3.23}$$

As seen in Eq. (3.22), the smallest relaxation coefficient is limited to 0.2. When defining δ, the objective is to keep the solution stable. Another adaptive control algorithms known as the Aitken's algorithm (1926) can be applied to accelerate the convergence assuming the convergence rate is of first order such that for each iteration the error is

$$\left.\begin{array}{l} e^k \approx Ce^{k-1} \\ e^{k+1} \approx Ce^k \end{array}\right\} \Rightarrow e^{k+1} \approx \frac{(e^k)^2}{e^{k-1}} \tag{3.24}$$

where the error embedded in the solution within each iteration is evaluated from $y_1^k = y_1 + e^k$ with y_1 being the exact solution. Equation (3.24) implies that the exact solution can be written as

$$y_1 \approx y_1^{k-1} - \frac{\left[y_1^k - (y_1^{k-1}\right]^2}{y_1^{k-1} + y_1^{k+1} - 2y_1^k} \tag{3.25}$$

The Aitken's algorithm improves the convergence by using Eq. (3.25) to modify the solution at every second iteration such that

$$y_1^{k+1} := y_1^{k-1} - \frac{\left(y_1^k - y_1^{k-1}\right)^2}{y_1^{k-1} + y_1^{k+1} - 2y_1^k} \tag{3.26}$$

In the current work, the use of Aitken's algorithm has not been found stable enough which is why the relaxation shown in Eq. (3.22) has been used exclusively.

3.3 Strongly Coupled FSI

The term FSI (Fluid Structure Interaction) implies the coupling between the fluid solver and the structural solver. When the problem is stiff, the coupling is critical and a strong implicit coupling is important to maximize the stability of the numerical solution. The coupling algorithm can be constructed in many ways. These can be put into two categories: *monolithic* or *partitioned* approach.

The monolithic approach solves the flow equations and the structural equation simultaneously. The governing equation for fluid flow is discretized and rearranged to yield a matrix equation. A simultaneous solution of both fluid flow and structural deformation will require that the structural problem can be setup and embedded directly into the matrix equation for the fluid flow. The obvious advantage of using the monolithic approach is that the solution of the FSI problem is fully implicit, but it is not always straightforward how the coupled matrix equation can be setup. The difficulty associated with formulating and solving the coupled matrix equation can easily outweigh the benefit of using the monolithic approach. For the partitioned approach, on the other hand, the fluid solver and the structural solver are working alternately. The information produced by the flow solver is transferred to the structural solver such that a new structural solution can be obtained. Depending on the construction of the partitioned scheme, the information may be transferred once

in every time step or several times in an iterative manner to achieve a tighter coupling of FSI. Between the two solvers, information is transferred through the so-called FSI interface commonly being the surface of the structure. Using a partitioned scheme, a new source of error is introduced into the solution. Besides the spatial and temporal discretization errors, the so-called partitioning error exists if the partitioned scheme is constructed such that the FSI coupling is weak or the iteration has not yet converged to a fully implicit solution. The main advantage of using the partitioned scheme is its simplicity. The risk, however, is that the partitioning error can be significant. Using an iteration technique to improve the coupling will help to reduce the error, but the iteration does not always converge.

The FSI coupling scheme formulated in the present work can be categorized as a strongly coupled partitioned scheme. The fluid solver provides the force and moment to the motion solver where the rigid body motion and planar vertical deflection are solved for. The fluid mesh as well as the corresponding fluid solution is updated and the iteration continues until convergence. Given the force vector $\boldsymbol{f}_o$ and torque $\boldsymbol{\tau}_o$ the information required from the motion solver is mainly the current location of the center of mass $\boldsymbol{x}_{\mathrm{CG}}$ and the orientation matrix $\mathbf{R}$ as well as the structural deformations evaluated according to the Timoshenko beam theory. In a Newtonian frame of reference, each point on the rigidly moving boundary is updated as

$$\boldsymbol{x} = \boldsymbol{x}_{\mathrm{CG}} + \mathbf{R}\mathbf{R}_0^T(\boldsymbol{x}_0 - \boldsymbol{x}_{0,\mathrm{CG}}) \tag{3.27}$$

where the subscript 0 denotes the initial value. Assuming small deflections, the local structural deformation is superimposed on top of the rigid body motion. The boundary points are distributed similarly as

$$\boldsymbol{x} = \boldsymbol{x}_{\mathrm{CG}} + \mathbf{R}\mathbf{R}_0^T(\boldsymbol{x}_{flex} - \boldsymbol{x}_{0,\mathrm{CG}}) \tag{3.28}$$

where $\boldsymbol{x}_{flex}$ is equivalent to $\boldsymbol{x}_0$ which is simply the initial points of the undeformed body. The flexibility of the hull girder is accounting for through $\boldsymbol{x}_{flex}$. According to the solution of the Timoshenko beam, $\boldsymbol{x}_{flex}$ are calculated in the body-fixed coordinate system. Thus, at any time instant, the vector $\boldsymbol{x}_{flex}$ is computed using the initial position $\boldsymbol{x}_0 = (x, y, z)$ as

$$\boldsymbol{x}_{flex} = \boldsymbol{\nu}(x) + \mathbf{Q}^T(x)(\boldsymbol{x}_0 - \boldsymbol{x}_{0,flex(x)}) \tag{3.29}$$

where $\boldsymbol{\nu}(x)$ is the vertical deformation and $\boldsymbol{x}_{0,flex}(x)$ is the initial deflection given as function of the longitudinal position x. The rotation matrix $\mathbf{Q}$ is a function of x and is computed according to the total local angular deformation i.e. the rotation of the cross-section due to bending and shear consistent with the Timoshenko beam theory.

Between the structural solver and the flow solver, information is transferred back and forth creating a two-way strong hydroelastic coupling scheme. As illustrated in Fig. 3.2, the explicit predictor step of the motion solver is applied once, immediately after a time increment. The information extracted from the flow solver is $\boldsymbol{f}_o$ and $\boldsymbol{\tau}_o$, whereas the motion solver provides the updated location of the moving boundaries.

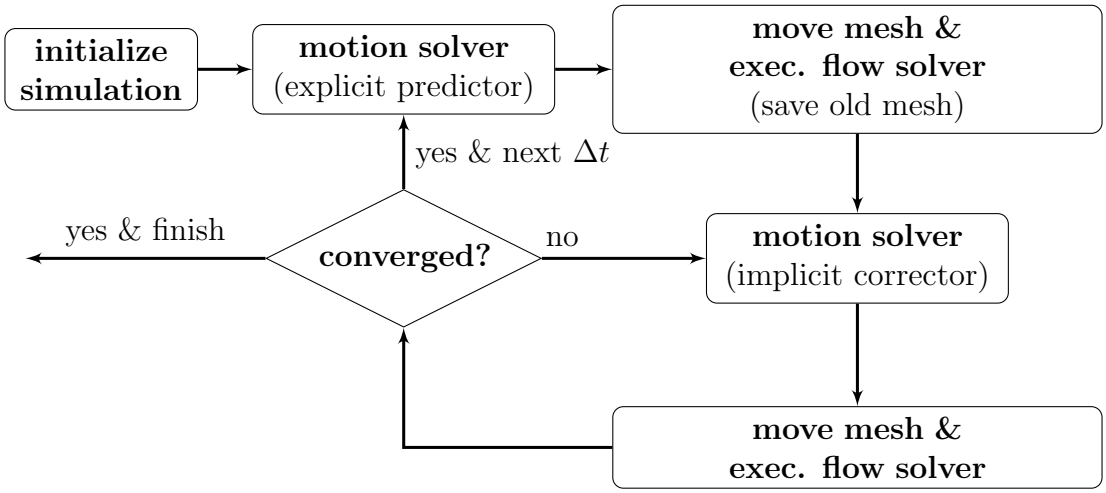

Figure 3.2: Flowchart of the FSI strong coupling scheme

Chapter 4

Water Entry Problems

It is a very challenging task to determine the slamming loads on ship hulls in a consistent manner. One of the reasons is that slamming loads are highly random due to the stochastic nature of the sea conditions. They are dependent on the complex deformations of the free surface and the surface of the body. The free surface may separate and there are high impact loads, which act on the wetted surface for a short time period. Furthermore, physical phenomena such as trapped air and structural flexibility can play a role.

Thus, for predictive purposes, it is necessary to introduce some simplifications to the problem. A practical approach to simplify the calculations of hull girder responses is to use a strip theory where the evaluation of the forces acting on the hull is carried out using 2D analyses on each individual strip. The strip theory has shown its usefulness regarding estimations of low frequency wave forces. However, its performance in a slamming problem as well as the 3D effects of slamming are not yet fully understood. Another uncertainty in applying a 2D approximation is related to the determination of the longitudinal extension of the slamming area. Consequently, the results obtained by using a strip theory need supplements in terms of experimental data or empirical knowledge, which may not be available in the conceptual design phase.

Many research works have been carried out to reveal the effects of a slamming impact. Often, the study is restricted to two-dimensional (2D) bodies. The step toward solving the slamming problems in three-dimensions is not so obvious. There are many challenges no matter whether the approach is numerically based, analytically or experimentally based. In order to validate and identify the limitations of the numerical tools, experimental results, usually in 2D, are compared against the numerical predictions.

The work presented this chapter aims for validating the current VOF-based flow solver. Several 2D and 3D simulations of rigid body impact into calm water are compared to available experiments. A sketch of the numerical tank is shown in Fig. 4.1. The air phase is initialized with $\alpha = 0$ and water $\alpha = 1$. The initial flow velocity field is set to zero while the test object is released from a position slightly above the initial calm water line. The kinematics of the test object are imposed according to the measurements. The boundary conditions are also presented in Fig. 4.1. Mainly, there are two types of boundary conditions applied in the setup: the wall type and the open boundary. The no-slip wall boundary conditions are imposed on the side walls, the bottom and the surface of the test object. The open boundary

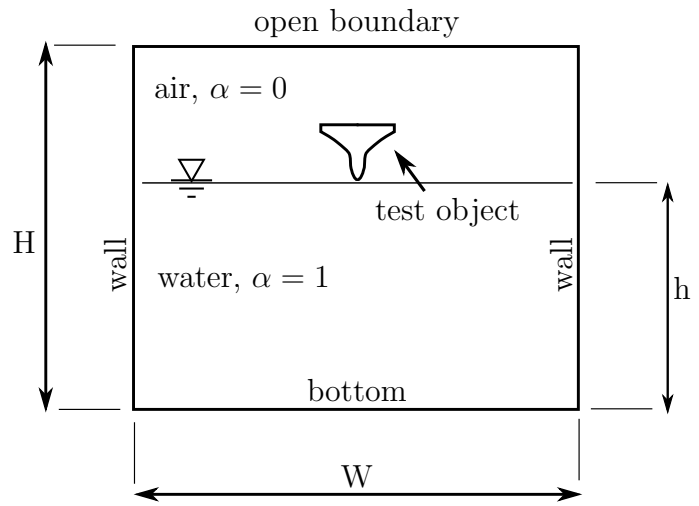

Figure 4.1: A sketch of the numerical setup of a water-entry simulation. Tank width (W), Height (H), water depth (h).

shall simulate the open space on the top side of the domain. The mathematical formulation of these boundary conditions can be found in Sec. 2.6.

The validation study is done initially on wedge-shape bodies where experimental data and similarity solutions for the vertical slamming force are available from Zhao et al. (1996) and Zhao & Faltinsen (1993). Next, the circular cylindrical shape is used in the study. Finally, a realistic bow flare section is tested against experiments available from Aarsnes (1996). The same experimental data has been used by Brizzolaraa et al. (2008) to make a comparison between a range of commercial CFD codes using different numerical approaches, e.g. BEM (Boundary Element Method), SPH (Smoothed Particle Hydrodynamic), and VOF provided by the commercial CFD software packages: FLUENT and FLOW-3D. One of the conclusions was that the predicted pressures, forces and their variation in time are very sensitive to the velocity profile of the falling motion. In order to obtain a good agreement with the experiment, the velocity profile needs to be accurately predicted.

The work done by Muzaferija et al. (1999) and Kleefsman et al. (2005) has already proved that the VOF-based NS solver is capable of estimating slamming loads during a water entry. Nevertheless, the implementation in OpenFOAM has not yet been well tested and the flow solver uses the artificial interface compression scheme to evaluate the transport equation for the phase fraction. The findings, which will be presented in detail in this chapter, are:

- A mesh convergence study on the classical dam break problem shows that a grid convergence of the free surface during splashing and breaking is difficult to achieve. On the other hand, the experimental investigation may have difficulty achieving a reproducible measurement as well. Without the complicated breaking of the free surface, the slamming load has 1st-order convergence behavior. The convergence rate of the peak pressure is demonstrated in a water-entry of a 30° wedge.

- The current VOF-based flow solver is capable of predicting slamming force on wedges accurately in water-entry problems. The trapped air effect cannot be accounted for in the present flow solver due to the incompressible flow

assumption. Nevertheless, deadrise angles as small as 2.5^o and 4° have been tested. A similarity solution for a 4° wedge exists which agrees well with the simulated results. For the ship-like bow flare section, the numerically predicted slamming forces agree well with the measurement. Even though there are signs of numerical instability due to the quality of the digitized velocity profile, it is found that the correct prediction of the kinematics of the falling motion is critical for the evaluation of the slamming force. In addition to the simulation where the kinematics of the body are directly imposed, a free fall simulation has been performed. The results show that the current flow solver is capable of predicting the slamming load and the falling motion accurately.

- Simulating a water-entry of a circular cylinder is challenging, especially at the initial impact, due to the small contact angle with the free surface. The slamming force at this initial impact, however, is comparable with the experiment and beyond the initial contact, the force is in an excellent agreement with the experiment.

- A decomposition model for the vertical forces in water-entry problems will be presented. Given a kinematic profile of the body, the model provides vertical slamming forces which are as accurate as the CFD results.

- A study of a truncated 3D bow flare in a constant-speed water-entry problem shows that it is possible, at least for the current case, to apply a 2D strip integration to obtain the total impulse of the bottom and bow flare slamming. Compared to the full 3D simulation, the slamming forces on each strip are overestimated due to the 2D assumption and yet the total impulse which is a time integration of the slamming force is not affected much by the deviation in the peak forces.

- The study of the 3D bow flare model reveals complicated free surface deformations and separation. During the bottom impact, the free surface may separate due to the curvature of the bottom profile. In some circumstances, the free surface accelerates rapidly toward the upper part of the bow and hit the flare area at a relatively small angle. The impact can be classified as a bow flare slamming which, in general, can be significant depending on the relative impact angle. In the full 3D simulation, a similar pile up of the separated free surface can be observed. The impact forces in the 3D simulation, however, are less intense partly because the fluid can escape more freely in the three-dimensional space.

- The separation of the free surface during the bottom slamming is also responsible for some trapped air at the upper region of the bulb, which may exist long after the bow flare slamming. Due to the assumption of the incompressible flow, the current VOF-based flow solver is considered insufficient to predict the fluid pressure here correctly.

4.1 Convergence Study

In this section, the requirement on mesh resolution in a slamming simulation is studied. The peak pressure may be concentrated around the spray root. This region

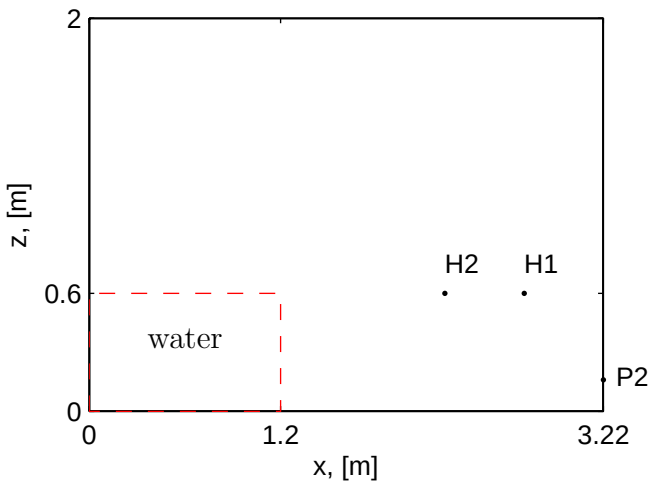

Figure 4.2: A sketch of computational domain for the dam break simulations. The pressure probe P2 is located at (3.22, 0.16) m, and water level gauges H1 ($x = 2.725$ m), H2 ($x = 2.228$ m)

with high pressure is important for slamming loads. The mesh density within this region must be sufficient to resolve the varying pressure distribution.

There are possible convergence problems related to the way the free surface is captured by a volume of fluid method (VOF) especially when the free surface starts to break locally, see e.g. Hänninen et al. (2012). While Hänninen et al. (2012) tested the grid convergence for the simulation of a passenger ship sailing in head seas in steep waves, similar problems may arise during slamming simulations. The classical dam break problem is well suited to illustrate the convergence problem during splashing and break-up of the free surface. Initially, some volume of water is kept inside a tank. The flow is investigated for the case where the side wall of the tank is removed instantaneously and water begins to flow violently toward an obstacle. The problem is relevant to green water loadings as well as impact loads on superstructures.

Zhou et al. (1999) did an experimental study of the dam break problem and published the impact pressure as well as the water level measured at two locations in the flow. Zhou et al. (1999) reported that there were problems with the repeatability of the experiments. The experimental setup was otherwise the same in the repeated tests. Still, the results show some variations. One of the problems with the experimental study of slamming pressures in general is the averaging of the pressure over the measuring area. Thus, the size of the pressure transducer may matter. In Zhou et al. (1999), it is reported that the pressure transducer is 90 mm in diameter, which is relatively large when compared to the total volume of water in the tank (approximately 224 mm depth at rest).

A sketch of the tank is shown in Fig. 4.2 and the numerical results for three different grid resolutions are shown in Fig. 4.3. With the cell aspect ratio equal 1 uniformly distributed insize the computational domain, the spatial increment Δx or Δz can be used to characterize the cell size. For these three meshes, the characteristic cell sizes are 12.5, 6.25, and 3.125 mm which are referred to as the coarse, medium and fine mesh, respectively. The column of water begins to flow out at time $t = 0$ s. The flow is moving toward the right wall of the tank, Fig. 4.3b. An impact occurs when the front toe hits the wall causing a splash of water rushing upward along the

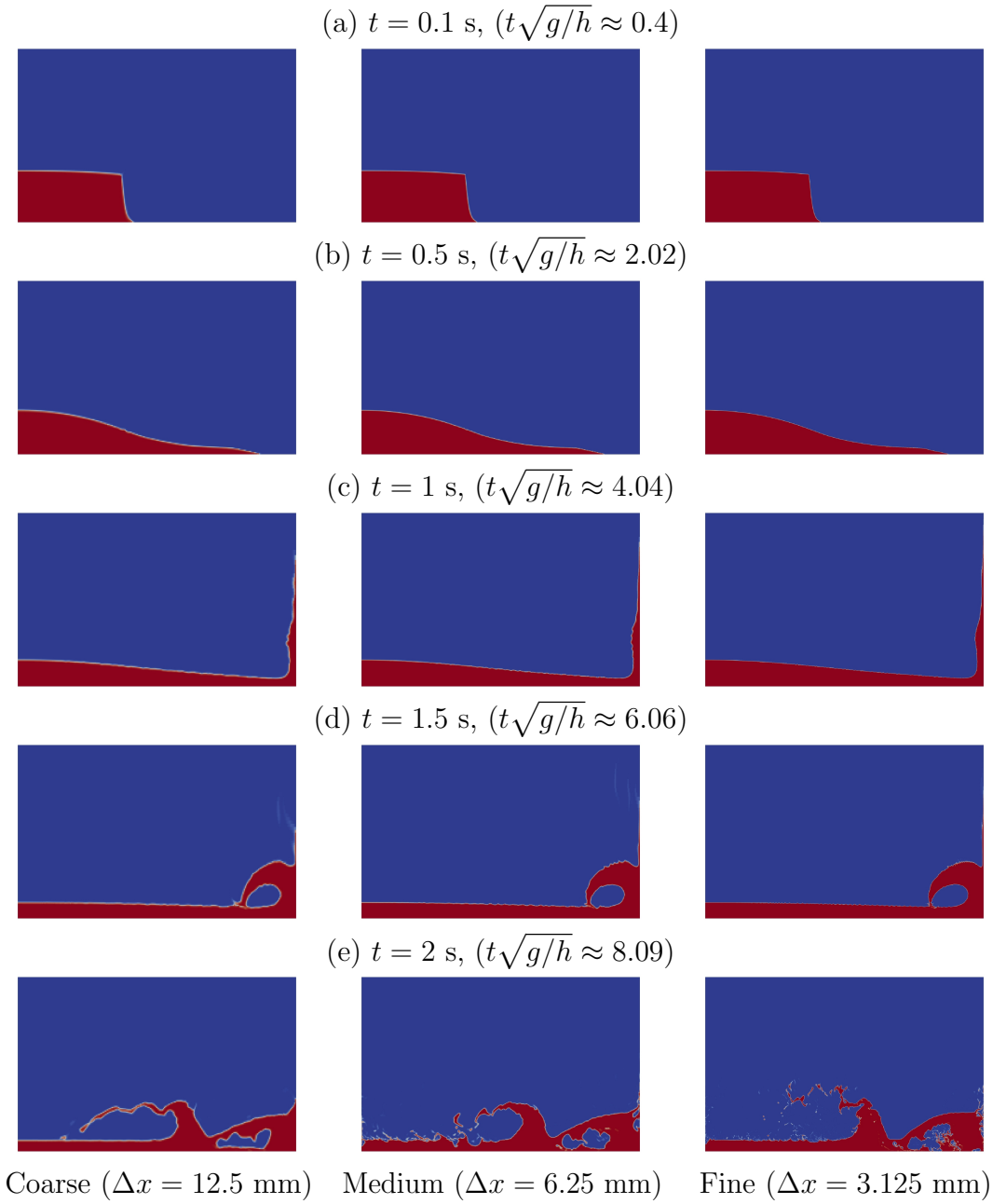

Figure 4.3: Snapshots of the free surface in a dam break problem (Red is water, Blue is air). The complicated break up of the free surface does not converge easily. Coarse grid 21.000 Cells (left column), Medium grid 73.000 Cells (middle column), Fine grid 258.000 Cells (right column)

vertical wall, Fig. 4.3c. Eventually the pile up water loses its momentum and starts to fall down creating a backflow in the process, Fig. 4.3d. The strong jet of the backflow is aimed directly toward the flume causing a hydraulic jump as seen in Fig. 4.3e. It is clear to see that the free surface from the three different grid resolutions agree well before occurrence of the subsequence complicated splash and break-up of the free surface in, Fig. 4.3e. The most important feature to notice about Fig. 4.3 is that the breaking of the free surface shows no sign of convergence. The snapshots of the free surface predicted by the coarse mesh (left column in Fig. 4.3) show less breaking behavior in the jet of the backflow compared to the prediction of the finer grid. In the medium and fine grids, the small drops hit the flume creating a very different free surface with many more small cavities. In addition, the trapped air due to the backflow has different shapes when the grid is refined.

Because the local deformation of the free surface is important for the magnitude of the slamming load, it must be emphasized that the current VOF-based flow solver may have difficulties in predicting a breaking free surface. The origin of the problem is possibly the handling of the free surface. As explained in Chapter 2 the current VOF-based flow solver introduces an artificial compressive velocity to keep the interface sharp; and this is possibly the limitation of such treatment of the free surface. It is possible that other competitive schemes such as HRIC (Muzaferija et al. (1999)), PLIC (Youngs (1982)), or CICSAM (Ubbink & Issa (1999)) perform better. The results presented in Nielsen (2003), Colicchio et al. (2002), however, suggest that these competitive schemes still have problems producing a correct breaking mechanism of the free surface. An important point shown by Fig. 4.3 is that there is always a limit on how many computational cells one can afford to run, and within the affordable number of cells the complicated break-up of the free surface may not yet converge introducing a large numerical uncertainties in predicted slamming loads.

The water level measured at $H1$ and $H2$ (see Fig. 4.2) show a clear sign of the influence of the backflow and breaking of the free surface. As seen in Figs. 4.4a and 4.4b, the water level compares well with the experiment before the backflow and the complicated splashing occurs at $t\sqrt{g/h} \approx 6$. From the numerical results, the water level η is estimated by integrating the volume fraction function α with respect to the vertical coordinate, i.e.

$$\eta = \int_{z_{min}}^{z_{max}} \alpha \, dz + z_{min} \tag{4.1}$$

where z_{min} and z_{max} are predefined to cover the expected range of the free surface level. Alternatively, the isosurface for $\alpha = 0.5$ can be used. Between the two methods, the estimated free surface levels usually agree well. However, the free surface elevation is not well defined when complicated free-surface mixing and breaking occur. As seen in Fig. 4.4(a & b), the estimated free surface elevation increases apruptly at $t\sqrt{g/h} \approx 6$ due to the backflow.

The predicted pressure compared with the measurements shows similar diverging behavior after $t\sqrt{g/h} \approx 6$. Figure 4.4c shows the maximum pressure sampled over the coverage area of the pressure transducer (90 mm in diameter). It is not clear if the pressure measured during the experiment is the area-average or the maximum

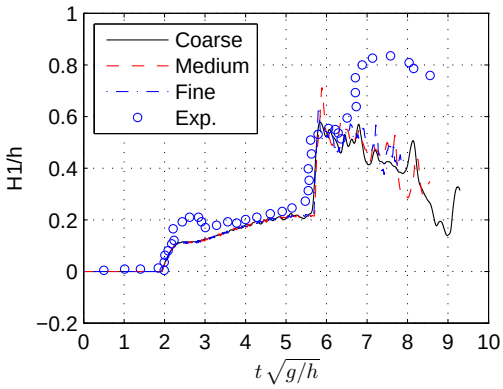

(a) Water level at $H1$

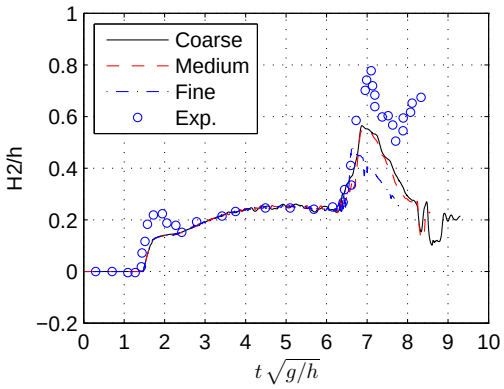

(b) Water level at $H2$

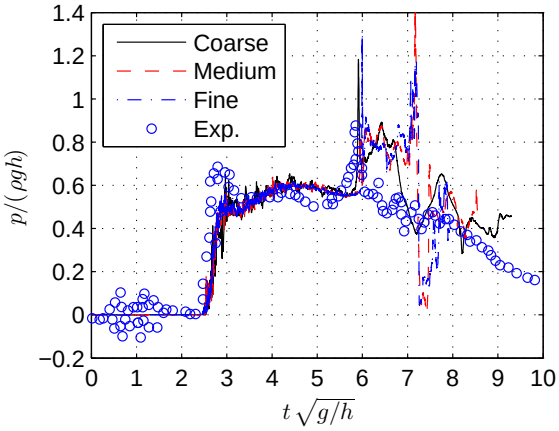

(c) Pressure at P2

Figure 4.4: Water level sampled at H1 and H2 (a) & (b), The maximum pressure within a diameter of 90 mm with the center located at P2 (c)

pressure. The predicted pressure peak is lower than the measurement. In this regards, there is practically no difference between the three grid resolutions. The discrepancy seen in the pressure peak can be caused by the sensitivity to the initial condition as reported in Zhou et al. (1999). The peak in water level at $H1$ and $H2$ (Figs. 4.4a and 4.4b around $t\sqrt{g/h} \approx 2$) also suggest that the front toe of the flow is too small in the numerical prediction. Indeed, it is possible that the front toe may be affected by the way the flap is removed. In the simulations, the removal of the flap is not modeled whereas in the experiment it may take several milliseconds to remove the flap. Thus, at the initial state of the water column may not be the same as in the numerical simulation.

The first peak in the pressure is due to the front toe hitting the wall, Fig. 4.4c at $t\sqrt{g/h} \approx 2.5$. The second peak, $t\sqrt{g/h} \approx 6$, corresponds to the instant the jet of the backflow merges with the flume. These two features are captured by the current flow solver. Beyond $t\sqrt{g/h} \approx 6$, the pressures measured in the experiments show no sign of impulsive pressure. The simulations, however, show a third pressure peak at $t\sqrt{g/h} \approx 7$ corresponded to some remaining water jet which rises almost vertically along the wall during the first impact, now is falling back and collapses close to the location of the pressure transducer. The measurements show a weaker oscillation in the pressure indicating that the water jet stream, which was propelled upward during the first impact, is not exactly the same as in the numerical prediction. Nevertheless, the smaller pressures seen in the measurements are consistent with the expected results from the use of an incompressible flow in a 2D simulation with trapped air existing in the flow.

Even though some of the discrepancies between the measurement and the numerical prediction can be explained, the dam break simulations show that the convergence of the free surface under a dynamic break-up is difficult to achieve. Further study on the grid convergence of the impact loads is concentrated on the case where there is no complicated breaking of the free surface. Sections 4.1.1 and 4.1.2 present results of water-entry simulation of a wedge and a horizontal cylinder, respectively.

4.1.1 Convergence of the Slamming Load on a Wedge

Water entry problems of a wedge shape body have been well investigated both experimentally and theoretically. For validation purpose, slamming loads with a wide range of deadrise angles are compared in Section 4.2. In this section, the result of a grid convergence study is presented.

It is known that the pressure distribution on a wedge slamming into a calm water surface is as shown in, Fig. 4.5a. There is a relatively large pressure gradient at the spray root. Noticeably, the spray root is not stationary but moves along with the wetted surface. Those areas with a high pressure concentration (i.e. the spray root) require a fine grid resolution to resolve. Because the spray root moves, the grid resolution must be fine, not only at a few locations but also on the entire surface that is exposed to slamming loads. For convenience and an easy control of the characteristic cell size ($\Delta\delta$) the unstructured tetrahedral mesh configured as shown in Fig. 4.5b has been adopted in the present grid convergence study.

The convergence of the vertical slamming force and peak pressure are shown in Fig. 4.6 for three different characteristic cell sizes, $\Delta\delta = \{2.5, 1.5, 0.75\} \cdot 10^{-3}\,\mathrm{m}$. In the following, the three different grids will be referred to as the coarse, medium

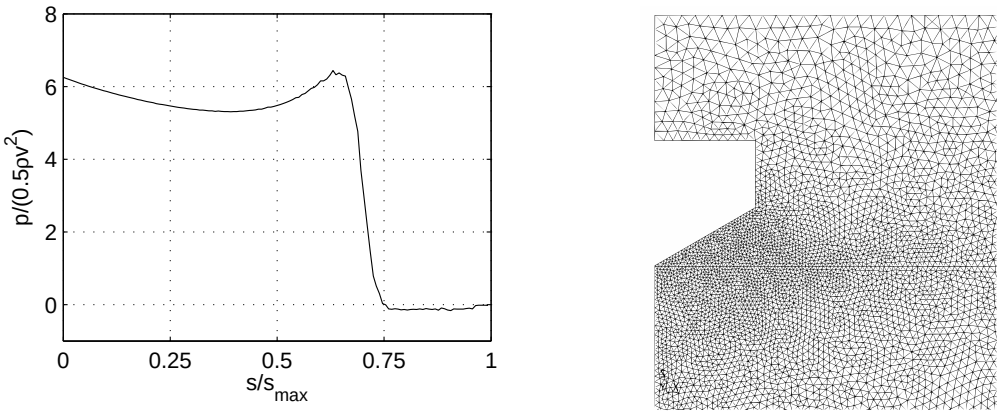

(a) (b)

Figure 4.5: (a) Examples of an instant pressure distribution on the wetted surface of a wedge (30°) slamming on calm water. s is the distance along the surface of the wedge measured from the keel. (b) An example of the tetrahedral mesh adopted in the convergence study

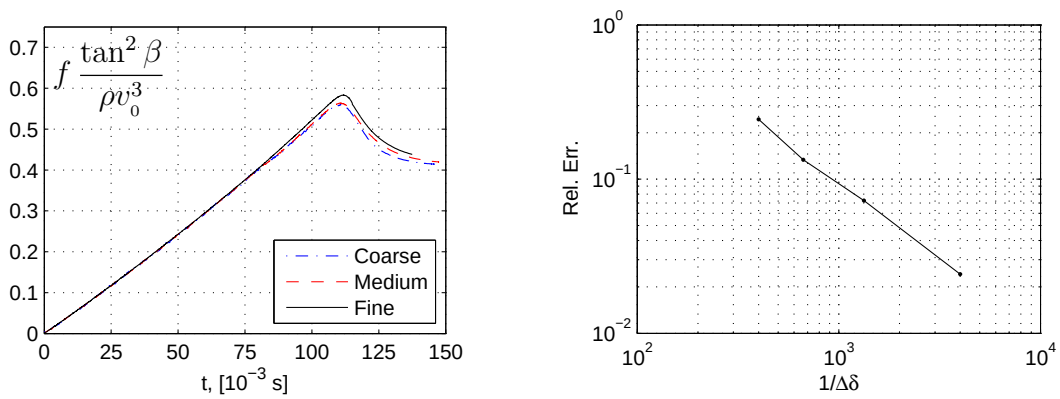

(a) (b)

Figure 4.6: Convergence of the slamming force and the peak pressure on a 30° wedge (a) Normalized vertical force (b) The relative errors of peak pressure at $t = 12.5\,\text{ms}$

and fine grid, respectively (corresponded to ratios $\Delta\delta/s_{max} \approx \{7.22, 4.33, 2.17\} \cdot 10^{-3}$ where s_{max} is the maximum distance on the wetted surface measured from keel to the knuckle). The coarse grid provides approximately 138 cells along the wetted surface of the wedge and the fine grid 1388 cells. The vertical forces shown in Fig. 4.6a have been normalized with respect to $\tan^2\beta/(\rho v_o^3)$, where β is the deadrise angle and v_0 is the initial penetration velocity. The time series of these normalized vertical force shows that the coarse grid provides a result that is almost the same as the medium and the fine grid except around the peak force at 100 ms, Fig. 4.6a (i.e. when the spray root is very close to the knuckle).

The higher resolution in the grid provides a higher resolution of the pressure distribution, which shows that the reduction of the vertical force, due to a reduction in the pressure when the spray root has moved beyond the knuckle, occurs slightly later than for the coarse grid. Furthermore, the coarse grid predicts a smaller pressure peak, which is expected since the pressure peak is highly concentrated locally at the spray root. The convergence of the pressure peak evaluated at $t = 12.5$ ms is shown

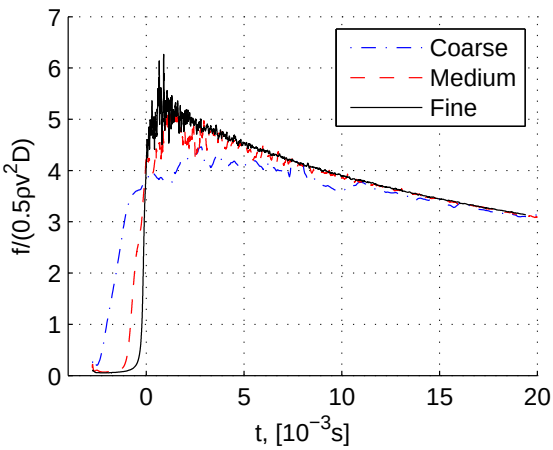

Figure 4.7: Convergence of the slamming force on a horizontal circular cylinder

in Fig. 4.6b. The peak pressure extrapolated for $\Delta\delta \to 0$ is used as the reference for calculating the relative errors shown in Fig. 4.6b. The rate of the convergence is 1st-order consistent with the fact that the applied spatial discretization is the 1st-order Upwinding scheme and the temporal discretization is the 1st-order implicit Euler chosen for a maximum numerical stability.

4.1.2 Convergence of the Slamming Load on a Horizontal Circular Cylinder

A similar mesh configuration, as applied previously on a wedge, has been adopted for a cylindrical shape. The horizontal circular cylinder is forced to hit a calm free surface at a constant penetration velocity of $0.9\,\mathrm{ms}^{-1}$. The coarse, medium and fine grid presented in Fig. 4.7 has the characteristic cell sizes of $\Delta\delta = \{2.5, 0.75, 0.25\} \cdot 10^{-3}\,\mathrm{m}$.

The slamming load on a horizontal circular cylinder rises more abruptly than on a wedge. The peak load occurs almost immediately after the initial contact with the free surface. The very short rise time is very demanding on the grid resolution. As shown in Fig. 4.7, the coarse grid tends to relax the rise time of the force considerably. The difference in the rise time measured up to the peak force are roughly 5, 2.5, and $1\,\mathrm{ms}^{-1}$ for the coarse, medium, and fine grid, respectively. Noticeably, the results using the three grids agree except for the rise time and the peak force. As indicated in Fig. 4.7, the theoretical time for the initial contact is at $t = 0$ s. The vertical forces rise before this theoretical time, but the error becomes smaller when the grid is refined.

The difficulties in predicting the correct rise time and peak force is not so surprising since at the diffusive interface of the VOF approach may have a significant effect on the pressure distribution. The flow equations are solved using the FVM framework with a collocated grid. The primitive variables such as pressure are stored as the cell-average value in each control volume. To evaluate the force on the body, the pressure acting normal on the surface of the body will need to be derived from the cell-averaged pressure. Depending on the applied boundary condition, a problem may arise during the initial contact where the fluid in contact with the surface of the body changes from air to water. The VOF model introduces a blurred and diffused

interface relaxing the discontinuity of the interface. As a result, the sharp-rising pressure cannot be captured but seen rather as a smooth and continuously rising pressure following the diffused interface. The error is reduced by introducing a fine grid within the vicinity of the impact area such that the interface becomes sharper immediately before and during the impact.

This initial contact problem cannot be avoided completely on a collocated grid. However, the problems can be reduced by refining the grid and it occurs only during the initial impact where the relative impact angle is small. Consider, that a VOF model introduces a diffused free surface covering 2 or 3 cells, it can be recommended to put a constraint on the cell thickness to assure a reasonably sharp interface during the initial impact. The constraint can be formulated as

$$\frac{v_r \Delta\tau}{\Delta\delta} > 3 \tag{4.2}$$

where $v_r \Delta\tau$ is the displacement of the contact line during the initial impact. The impact velocity is v_r and the total rise time is $\Delta\tau$ measured up to the peak force. The characteristic cell thickness next to the slamming area denotes $\Delta\delta$. The constraint states that the cell thickness ($\Delta\delta$) next to the slamming area shall be much smaller than $v_r \Delta\tau$. This constraint provides a way to evaluate if the grid applied in the simulation is sufficient to resolve the impact force in a slamming simulation.

The characteristic cell sizes next to the slamming area in the simulations shown in Fig. 4.7 correspond to $v_r \Delta\tau / \Delta\delta \approx \{1.8, 2.4, 3.6\}$ for the coarse, the medium, and the fine grid, respectively. The vertical force rises too early with the coarse grid whereas the fine grid the timing is closer to the theoretical initial contact at $t = 0$ s.

4.2 Wedge Shape

The geometry of a wedge is simple and well defined and has been commonly used in the study of the impact loads. For validation purposes, the experimental work published in Zhao et al. (1996) is applicable. According to Zhao et al. (1996), a wedge model with a deadrise angle of 30° was mounted on a rig designed for free-fall drop tests on calm water. The wedge used in the experiment has a beam width of 0.5 m and a total length of 1 m. The length of the measuring section is 0.2 m located at the middle between two dummy sections. The sketch of the wedge model is shown in Fig. 4.8.

Zhao et al. (1996) provided the velocity profile of the falling motion, see Fig. 4.8. Initially, we aim to reproduce the result of the free-fall drop test using the current VOF-based fluid solver. The rig may introduce some friction reducing the acceleration of the falling motion. To minimize the possible deviation in the predicted kinematic of the falling motion, the measured velocity is imposed directly on to the wedge during the whole simulation.

As seen in Fig. 4.8, the measuring section is located in the middle of the body, which helps to enforce the flow to resemble a 2D flow. Therefore, the numerical simulation is initially done on a 2D setup in a numerical tank with dimensions $(W, H, h) = (4, 2, 1.5)$ m (cf. the sketch in Fig. 4.1). An example of the 2D grid applied in the simulation is shown in Fig. 4.9. The cells next to the body have a characteristic length of $0.75 \cdot 10^{-3}$ m producing approximately 263.000 cells in total.

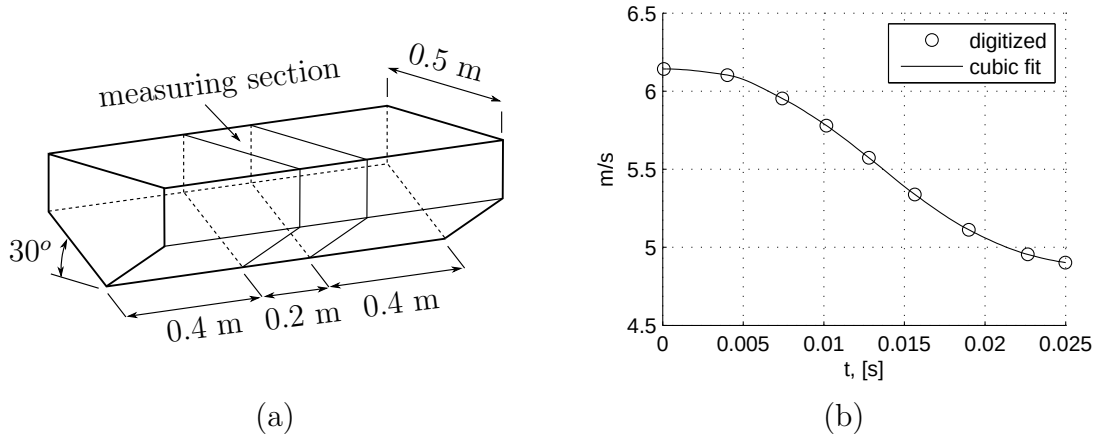

Figure 4.8: Free-fall drop test of a wedge shape body published in Zhao et al. (1996). (a) A sketch of the wedge shape body. (b) Velocity profile measured during the experiment (digitized from Zhao et al. (1996))

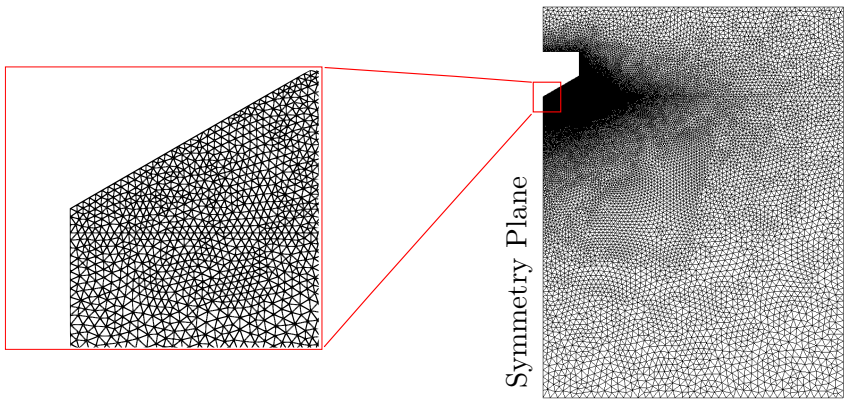

Figure 4.9: A 2D tetrahedral mesh with a symmetry plane (263.000 cells) applied in the simulation

The time series of the vertical force compared to the experiment are shown in Fig. 4.10a. The initial impact is at $t = 0$ s and it takes only 15 ms for the spray root to reach the knuckle. The pressure and the impact force fall rapidly after the bottom part of the wedge is fully wetted. A comparison of the impact force shows clearly that the results of the 2D simulation over-predict the impact pressure despite the fact that the experiment has been designed particularly to encourage a 2D flow. Since the measured velocity is already imposed directly to the wedge motion, it is very unlikely that the deviation is caused by an unaccurate prediction of the falling motion.

Further investigation clearly shows that the smaller slamming force is caused by the three dimensional effect. The same case is simulated using a 3D setup with the wedge modelled to resemble the actual experimental setup in 3D. To save the computational time the numerical model utilizes two symmetry planes of the wedge such that the numerical tank in 3D includes only one quarter of the physical domain. A sketch of the 3D numerical setup is shown in Fig. 4.10b. Using a structured mesh configuration the 3D mesh contains approximately 1.3 million cells in total. As seen in Fig. 4.10a the slamming force evaluated using the 3D setup agrees well with the measurement. The three dimensional effect is causing a lower pressure distribution since the fluid is allowed to escape more freely in the longitudinal direction. This

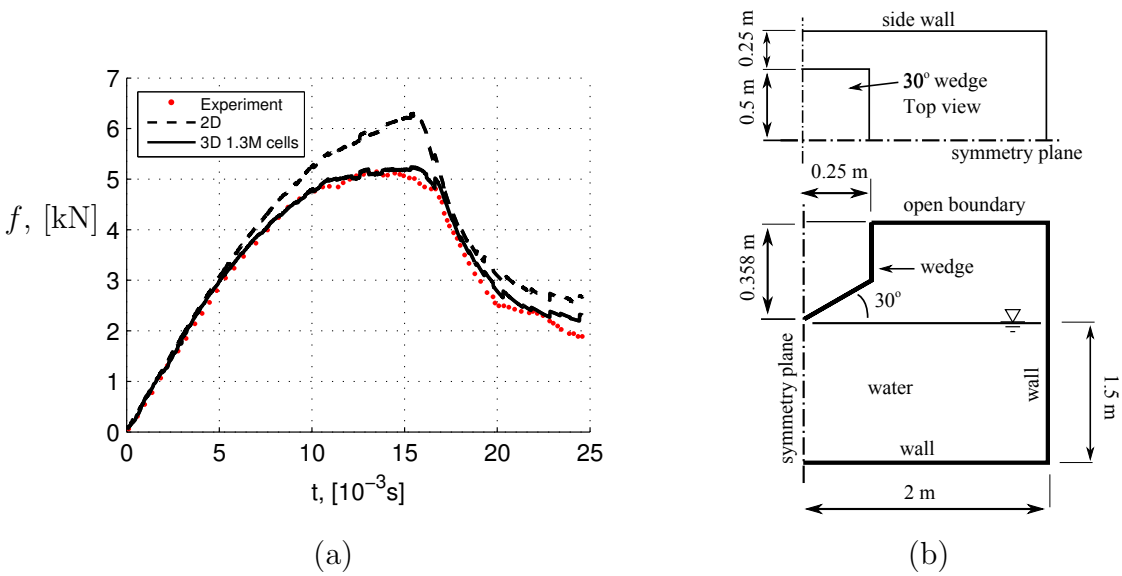

Figure 4.10: Numerical results of the 30° wedge compared with the experiment published in Zhao et al. (1996). (a) Vertical forces 2D vs. 3D, (b) A sketch of the 3D numerical setup

three dimensional effect is well known, but there is no well established theory to predict its magnitude other than to apply a direct simulation.

Two dimensional theories exist for simplified cases assuming a constant penetration velocity. Using the classical flat plate approximation as shown in Section 4.5 and assuming a constant penetration velocity v_0 with a small deadrise angle β, the wetted length c and the slamming force f according to the von Kármán theory can be written as:

$$c_{\text{vkm}}(t) = \frac{v_0\, t}{\tan\beta} \quad \Rightarrow \quad f_{\text{vkm}}(t) = \frac{\pi \rho v_0^3\, t}{\tan^2\beta} \tag{4.3}$$

where the subscript "vkm" denotes the use of the von Kármán theory. The Wagner theory differs only by the wetted length, i.e.

$$c_{\text{wgn}}(t) = \frac{\pi v_0\, t}{2\tan\beta} \quad \Rightarrow \quad f_{\text{wgn}}(t) = \frac{\pi^3 \rho v_0^3\, t}{4\tan^2\beta} \tag{4.4}$$

These approximate solutions can be considered as asymptotic values for f since a very small deadrise angle is assumed. The difference between Eq. (4.3) and (4.4) is the constant coefficient π in (4.3) versus $\pi^3/4$ in (4.4).

Other examples of 2D theories applied to a wedge are the similarity solution by Dobrovol'skaya (1969) and the conformal mapping solution by Mei et al. (1998). Both methods can be applied to a wedge with a wide range of deadrises angle and assuming a non-viscous fluid. The effect of the gravitational acceleration is neglected. Most importantly, the conformal mapping solution uses the approximate free surface condition known as the generalized Wagner theory (Zhao et al. (1996)), i.e. the free surface condition is satisfied on an artificial horizontal free surface extended from the spray root. The similarity solution, on the other hand, contains no further assumption other than a constant penetration velocity. However, the slamming forces

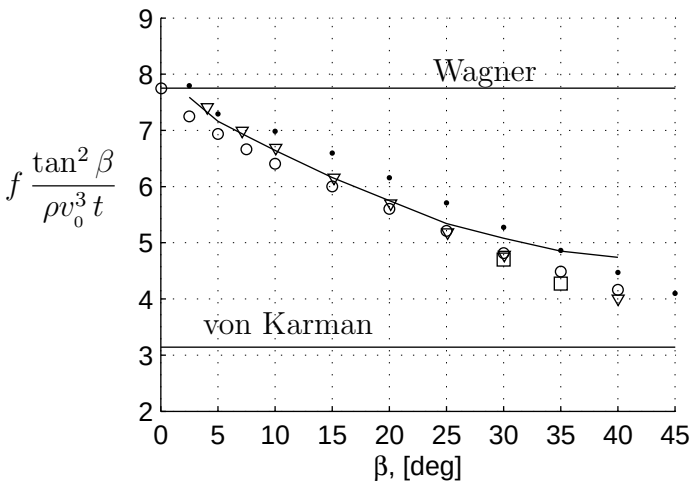

Figure 4.11: Normalized slamming forces at a constant penetration velocity. The present VOF-based flow solver (–), Similarity solution (▽) Dobrovol'skaya (1969), Conformal mapping (o) Mei et al. (1998), Matched asymptotic solution (•) Eq. (4.7), The present VOF-based flow solver neglecting the gravity (□)

are given as an implicit integral equation, which must be evaluated using a numerical method. The numerical challenge in evaluating the integral equation was one of the reasons that no results for a deadrise angle smaller than 30° were provided in the original paper. Several decades later, Zhao & Faltinsen (1993) evaluated the similarity solution down to 4° deadrise angle using a new numerical solution technique and more powerful modern computers to solve the integral equation. The normalized slamming forces using these 2D theories are presented in Fig. 4.11. For the validation purpose, the vertical forces predicted by the current VOF-based flow solver are shown and compared with the similarity solutions for several deadrise angles simulated under a constant penetration velocity. From Fig. 4.11, it is reasonable to conclude that the agreement with the similarity solution is rather good for a deadrise angle smaller than 20°. Figure 4.11 shows also the asymptotic solutions for small deadrise angles, see Cointe (1991), Howison et al. (1991) and Zhao & Faltinsen (1993). The asymptotic formula is written in terms of wetted length $c(t)$ as

$$f_{\text{asy}}(t) = 2\rho v_0 c\frac{dc}{dt}\Big[\int_0^c \frac{dx}{\sqrt{c^2-x^2}} - \int_0^c \frac{dx}{\sqrt{2c(c-x)}}\Big] + 4\rho\Big(\frac{dc}{dt}\Big)^2 \int_0^c \frac{\sqrt{|\tau|}}{(1+\sqrt{|\tau|})^2}\,dx \tag{4.5}$$

where $|\tau|$ is defined through the equation

$$x - c = \frac{\delta}{\pi}(-\ln|\tau| - 4\sqrt{\tau} - |\tau| + 5) \tag{4.6}$$

with $\delta = (\pi/8)v_0^2 c(dc/dt)^{-2}$ being the jet thickness. Using the Wagner's theory with $c_{\text{wgn}}(t) = \frac{\pi v_0\, t}{2\tan\beta}$, the matched asymptotic solution for small deadrise angle can be simplified to

$$f_{\text{asy}}(t) = \frac{\rho v_0^3 t}{\tan^2\beta}\frac{\pi^2}{2}\Big[\frac{\pi}{2} - \sqrt{2} + \frac{1}{\pi}(\sqrt{\tau_0} - 1)\tan\beta\Big] \tag{4.7}$$

where $\tau_0 > 1$ is the root of the following equation

$$\tau_0 = \text{root of}\Big[-\ln|\tau| - 4\sqrt{|\tau|} - |\tau| + 5 + \frac{2\pi^2}{\tan^2\beta} = 0\Big] \tag{4.8}$$

$$\approx \exp\Big[\frac{-833}{7271}(\ln\beta)^3 + \frac{524}{847}(\ln\beta)^2 - \frac{169}{53}\ln\beta + \frac{659}{56}\Big] \tag{4.9}$$

It shall be stressed that the matched asymptotic formula is only asymptotically correct for small deadrise angles. Nevertheless, the trend of the normalized slamming forces is captured well to a deadrise angle as large as 35°, see Fig. 4.11.

It is problematic to evaluate the slamming force on a small deadrise angle since experimental studies have shown that air pockets are very likely to form for a deadrise angle smaller than $4^o \sim 5^o$. In the 2D theories presented above, the trapped air effect is not accounted for due to the assumption of an incompressible, irrotational, non-viscous and weightless fluid.

In the current VOF-based flow solver, however, the gravitational acceleration is accounted for and the fluid is allowed to be viscous and rotational dictated by the nonlinear VOF-based Navier-Stokes equation. Although the fluid is assumed incompressible and the compressibility effect of the trapped air is not accounted for, the current VOF-based fluid solver has been applied with a 4° deadrise angle, see Fig. 4.11. Within the assumption of the incompressible fluid, the results agree well with the matched asymptotic formula as well as the similarity solution by Dobrovol'skaya (1969). The slamming forces evaluated using the conformal mapping are generally too small which probably is due to the approximate free surface boundary condition of the generalized Wagner's theory. However, the conformal mapping solutions converge to the similarity solution for a deadrise angle larger than 25°.

All 2D theories presented in this section predict a slamming force proportional to t given that the penetration velocity is constant. This is equivalent to having a constant rate of change in the wetted length $c(t)$. Therefore, the results of the current CFD simulations as shown in Fig. 4.11 have been forced to obey the proportionality of t through a uniformly weighted least-squares fitting method. The least-squares fitting is necessary since the CFD results are not as smooth as the analytical solution and always contain small numerical errors due to temporal and spatial discretization of the flow domain. Two examples of the fitting are shown in Fig. 4.12. The vertical force rises upon the initial impact at $t \approx 0$ and keeps rising until the spray root reaches the knuckle and the bottom surface of the wedge is fully wetted. The least-squares fitting is applied to the forces and the trend is clear: the smaller deadrise angle, the better the fit is. For a large deadrise angle, which is 35° in this example, the assumption that the vertical force is proportional to t may not be appropriate. As suggested in Fig. 4.12b, a 2nd-order time dependency provides a better approximation. In fact, the 2nd-order time dependency is a better approximation in all deadrise angles presented in Fig. 4.11. The differences, however, are insignificant for small deadrise angles.

One of the missing physical effects in the similarity solution is the neglected gravitational effect. The results shown in Fig. 4.11 suggest that these neglected

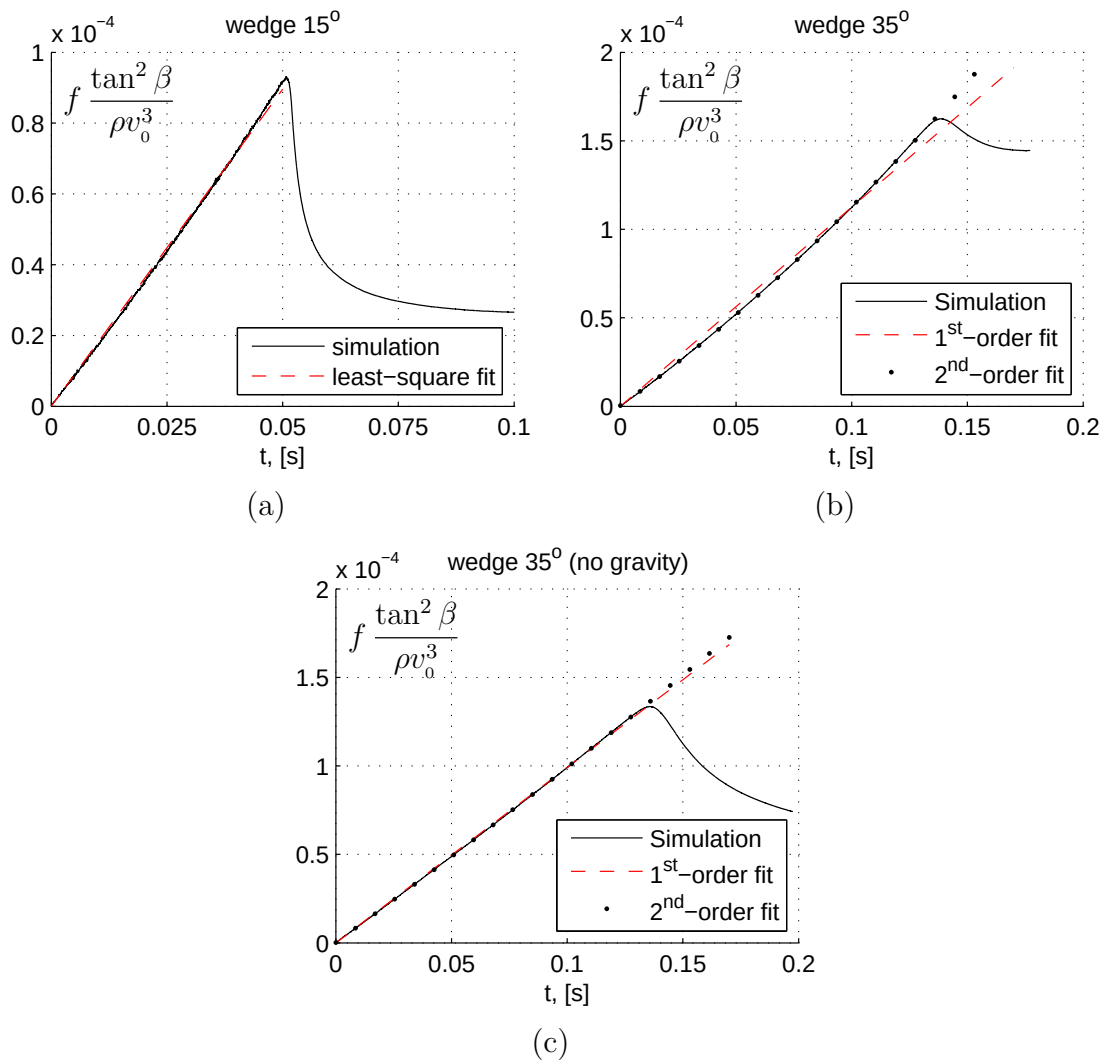

Figure 4.12: Examples of the least-square fit. (a) A least-square fit to the 1st-order time dependency is reasonable for small deadrise angles. (b) A 2nd-order time dependency is more appropriated. (c) The 2nd-order effect cannot be captured without the gravitational field

effects become rather important for a deadrise angle larger than 20°. The effect of the gravity can be easily confirmed by carrying out CFD simulations with the gravitational acceleration set to zero. The results are shown in Fig. 4.12c where the 1st-order time dependency is more obvious when the gravity is not accounted for.

Indeed, in almost all potential flow based formulations the effect of gravity is neglected. However, it is mentioned in Zhao & Faltinsen (1993) that there is no difficulty in accounting for the gravity in their BEM formulation. Based on the results presented in Fig. 4.12, it can be recommended to account for the gravity whenever possible.

The predicted pressure distribution under the wetted surface of a 2D 30° wedge is shown in Fig. 4.13 where s is the extent of the wetted surface measured from the keel, The maximum is $s_{max} = 0.5B/\cos(\beta)$, i.e. the distance between the keel and the lower knuckle where B is the total beam width. As expected, the pressure around the knuckle falls considerably (Fig. 4.13b) after the jet-flow originating from the spray root has moved past the knuckle. Noticeably, the peak pressure at the

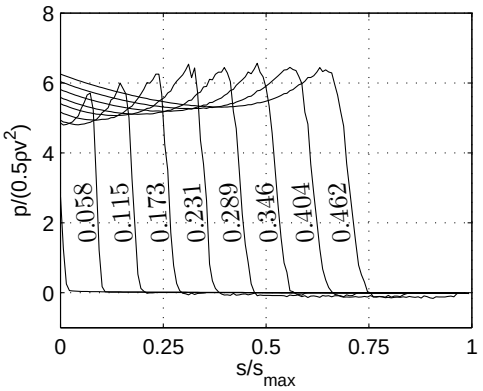

(a) Pressures on the wetted surface at $vt/h_{\max} = 0.058, 0.115, 0.173, 0.231, 0.289, 0.346, 0.404, 0.462$

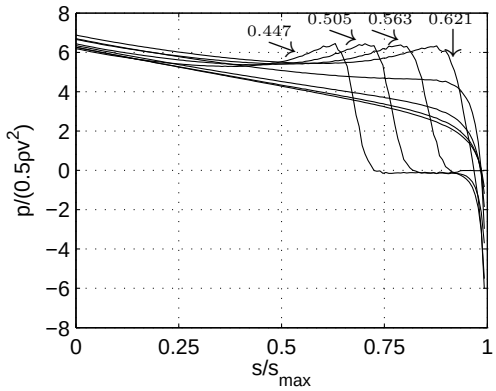

(b) Pressures on the wetted surface at $vt/h_{\max} = 0.447, 0.505, 0.563, 0.621, 0.678, 0.736, 0.794, 0.852$

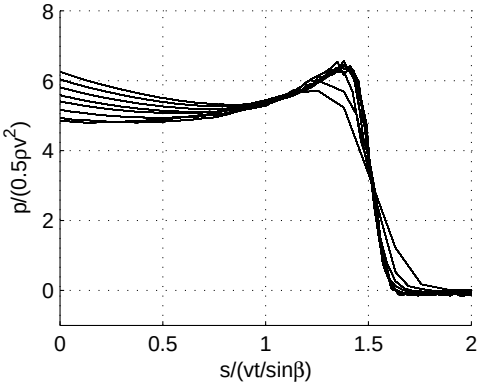

(c) Pressures vs. normalized wettet length

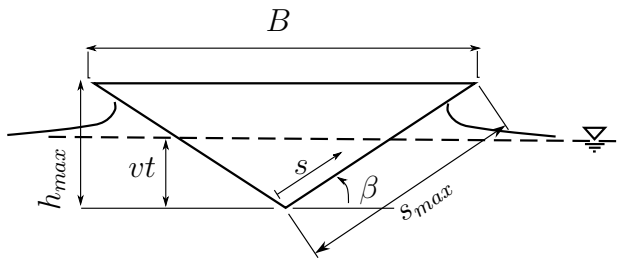

(d) Definition sketch

Figure 4.13: Numerical prediction of the pressure distribution on the bottom surface of a 2D 30° wedge at difference submergences. (a) The jet flow near the spray root has not yet reach the lower knuckle. (b) The pressure around the knuckle falls considerably after the jet flow has moved passed the knuckle. (c) The peak pressure at $s/(vt/\sin\beta) \approx 1.4$ is almost constant in time as long as the jet flow remain attached to the wetted surface

spray root remains almost constant during the impact, Figs. 4.13a & 4.13c. The pressure is generally small at the intersection point between the initial mean water line and the wedge ($s/(vt/\sin\beta) \approx 1$ in Fig. 4.13c), which confirms that the von Karman model will unerpredict the slamming load. Indeed, Fig 4.13c shows that the location of the spray root and the pressure peak is approximately 1.4 time the normalized submergence depth, i.e. 40% more than predicted by the von Karman model.

4.3 Circular Cylindrical Shape

Simulating water entry of a horizontal circular cylinder is challenging due to a nearly flat tangential plane at the initial contact with the free surface causing a very small contact angle. Using BEM, an initial penetration depth must be set due to

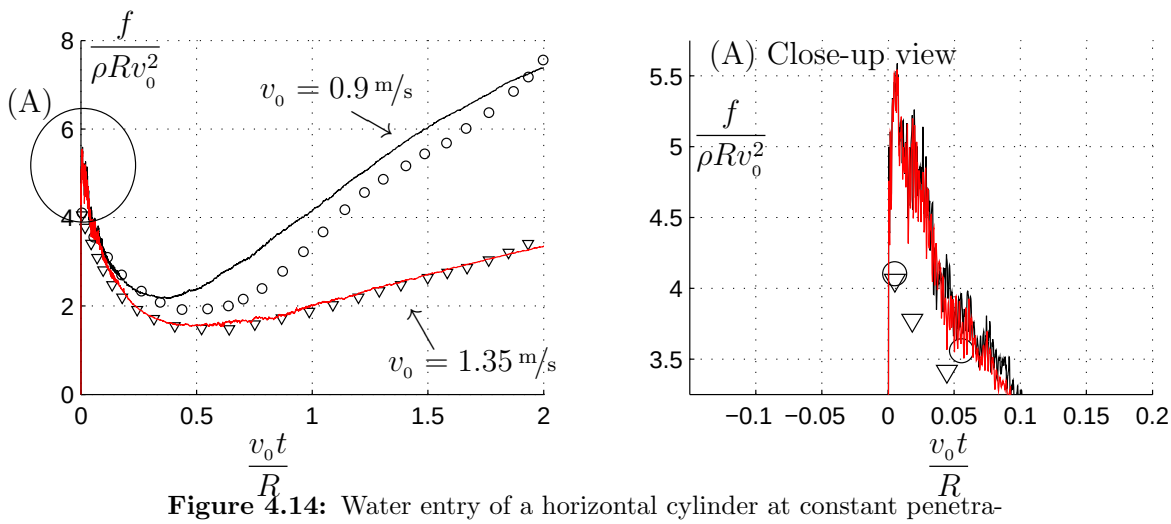

Figure 4.14: Water entry of a horizontal cylinder at constant penetration velocities. Experiment ($\circ, \nabla$) Faltinsen et al. (1977)
, the present VOF-based flow solver (— $v_0 = 0.9\,\mathrm{m/s}$, — $v_0 = 1.35\,\mathrm{m/s}$)

a singularity at the initial theoretical contact point. In addition, the curvature of the circular section may cause the free surface to separate from the body. Thus, the BEM approach requires the free surface separation to be enforced empirically. Using similar 2D theories as mentioned previously in Section 4.2, there is no easy way to account for the separation of the free surface.

Following the classical flat plate approximation (see Section 4.5), a solution for the wetted length is described in Faltinsen (1993) in which a slamming coefficient C_s can be defined as

$$C_s = \frac{f}{\frac{1}{2}\rho v_0^2 2R} \tag{4.10}$$

where R is the radius of the cylinder and the penetration velocity v_0 is assumed to be constant. Using the von Kármán theory, the wetted length is readily obtained from the geometrical relation of the circular body, which yields $C_s = \pi$. Applying Wagner's theory, however, the wetted length is an implicit solution and can be approximated (Faltinsen (1993)) up to second order yielding a larger wetted length than the predicted by the von Kármán theory. Consequently the slamming coefficient is larger when using the Wagner's theory, i.e. $C_s \approx 2\pi$ at the initial of impact.

In the experiment, the challenge remains equally difficult. Early experiments were done in 1977 by Faltinsen et al. (1977) enforcing a 2D flow and a constant penetration velocity. In the experiment, C_s was found to vary between 4.1 and 6.4 indicating that the Wagner's theory is far better than the von Kármán theory. Another experiment was published in 1980 by Campbell & Weynberg (1980) where C_s at the initial impact was found to be 5.1 confirming that the prediction of von Kármán theory ($C_s = \pi$) is too low.

The results of the current VOF-based flow solver compared with the constant speed experiment by Faltinsen et al. (1977) are shown in Fig. 4.14. At the initial impact, the rapid change of the wetted length causes a large numerical noise in the result. Keeping the numerical solution stable at this early stage is difficult since the rapid change of the wetted surface induces a relatively large ventilation of air trying to escape the small gap between the body and free surface. The large velocity

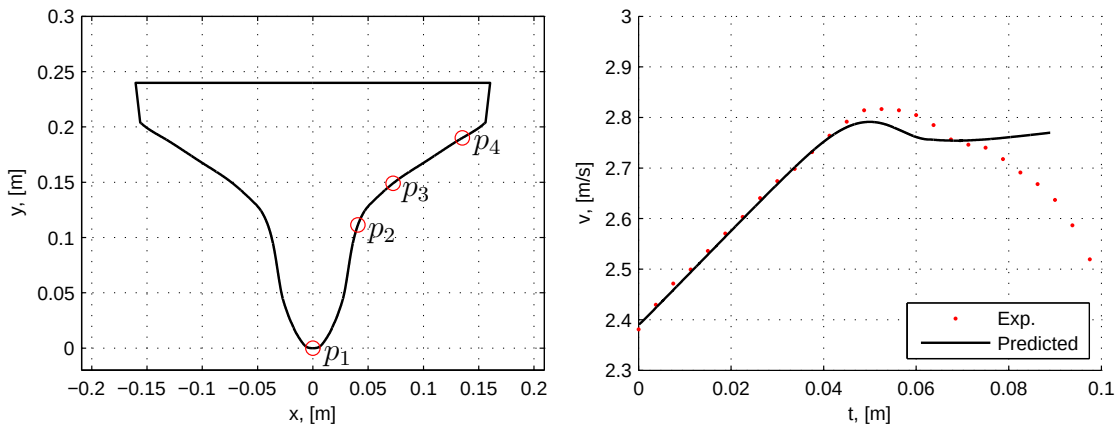

(a) Geometry (b) Velocity

Figure 4.15: (a) A sketch of the bow flare section used in the experiment by Aarsnes (1996) and the location of four pressure probes; (b) The measured velocity digitized from Aarsnes (1996) and the numerical prediction of the present VOF-based flow solver under a free fall simulation. The initial contact with the free surface occurs at $t = 0$ s

combined with the small finite volume cells, which has been necessary to resolve the concentrated pressure near the spray root, is limiting the size of the time step to be as small as $1.25 \cdot 10^{-6}$s. As seen in the close-up view around the peak force, Fig. 4.14, there is still a considerable amount of numerical noise in the solution. The slamming coefficient at the initial impact is estimated from these numerical results to be $C_s \approx 5.25 \pm 0.25$ which is very close to the experimental value of 5.1 by Campbell & Weynberg (1980) and well within the experimental uncertainty (4.1 - 6.4) reported in Faltinsen et al. (1977). Beyond the initial impact, the agreement is almost perfect for case $v_0 = 1.35\,\mathrm{m/s}$. For case $v_0 = 0.9\,\mathrm{m/s}$, the agreement is less convincing. The actual reason, why the results agree for the high penetration velocity and not for the low velocity, is unknown and may not be so easy to investigate without further information about the actual experiments. Nevertheless, it can be observed that the time history of the normalized force for case $v_0 = 0.9\,\mathrm{m/s}$ shows an indication of a low frequency disturbance which may be initiated around $v_0 t/R \approx 0.4$; and later induce a small bump around $v_0 t/R \approx 1.25$. The same can be observed in the numerical prediction except that the magnitude is slightly smaller compared to the measurements.

4.4 Ship-like 2D Section

The previous validation study uses wedge-shape bodies (Sec. 4.2) and horizontal circular cylindrical bodies (Sec. 4.3). The study shows a good agreement between the numerical results and the experiments. Some useful features and limitations have already been revealed such as: the numerical instability of the impact at a small angle, the secondary effect of the gravity, and the pressure reduction caused by a three dimensional effect.

In the following, the study is done using a ship-like bow flare section. Drop test experiments of the bow flare section were published in Aarsnes (1996), see Fig. 4.15. The work done by Brizzolaraa et al. (2008) shows that the kinematics of the falling

motion is very important for the slamming force.

Two configurations are used in the simulations. In the first configuration, the falling velocity of the bow flare section is prescribed using the measured velocity. This is done to eliminate the error in the predicted penetration velocity. The measured velocity is shown in Fig. 4.15b where the initial contact is defined at time $t = 0$ s. In the second configuration, the free fall motion is calculated using the current two-way coupled FSI algorithm. The total mass of the bow flare section is set to 261 kg according to Aarsnes (1996). A comparison between the measured and the predicted velocity profiles are shown in Fig. 4.15b.

As seen in Fig. 4.15b, the bow flare section does not penetrate the free-surface with a constant velocity. Instead, it accelerates downward at a nearly constant acceleration. From the measurement, the acceleration has been estimated to $9.07\,\mathrm{ms}^{-2}$. After about 0.06 s, the wetted surface reaches the upper flare and the velocity of the bow section starts to decrease rapidly due to the significant, additional load on the bow flare. The total physical time to be simulated is approximately 0.1 s. The numerically predicted velocity profile agrees well with the experiment within a time interval from the initial contact at time $t = 0$ s until the spray root is about to move beyond the lower knuckle at time $t = 0.06$ s. The predicted velocity remains nearly constant beyond $t = 0.06$ s whereas the measure velocity is reduced rapidly toward zero. The reduced velocity seen in the experiment was caused by elastic rope used in the brake system of the free fall rig.

The vertical forces and the water pile up profiles are shown in Fig. 4.16. The measurement contains a certain amount of high frequency oscillations, which originates from the drop rig, cf. Aarsnes (1996). The computed vertical force increases smoothly until it reaches a peak value at approximately $t = 0.06$ s. At this time instant, the spray root is about to move beyond the lower knuckle. Beyond this time instant, the vertical force shows sign of abrupt behavior and spikes. These discontinuities are purely numerical caused partly by the digitized velocity profile, and partly by the quality of the grid, which has been deformed too much from the movement of the bow flare. The spikes in the forces are inherited from the pressure field as shown in Fig. 4.17. For a comparison, norminal hydrostatic pressures defined as $\rho \boldsymbol{g} \cdot \boldsymbol{x}$ are also presented in Fig. 4.17. When the motion is calculated as part of the solution using the two-way coupled scheme, the predicted force is smooth but the peak force at $t = 0.06$ s is smaller than the measurement. On of the reasons, which may cause this discrepancy, is the fact that the geometry of the 2D bow flare section has been digitized from Aarsnes (1996). Nevertheless, the interesting features about the vertical forces such as rise time and peak duration are well captured by the simulations.

In the experiments, local pressures at four locations were measured, Fig. 4.15 and 4.17. A very good agreement is observed especially at the keel (p_1). The rise time of the predicted pressures corresponds well to the measurements. However, the peak values are off by a few percent, which is not surprising because the total vertical force as shown in Fig. 4.16 reveals a similar overshooting behavior during the impact on the flare area. The non-physical spiky behavior after the chine submergence can also be seen in the pressure samplings.

Approximately 0.06 s after the initial impact, the computed pressures contain numerically induced high frequency oscillations seen as pressure "spikes" on Fig. 4.17. The general trend of the pressures, however, agrees reasonably well with the

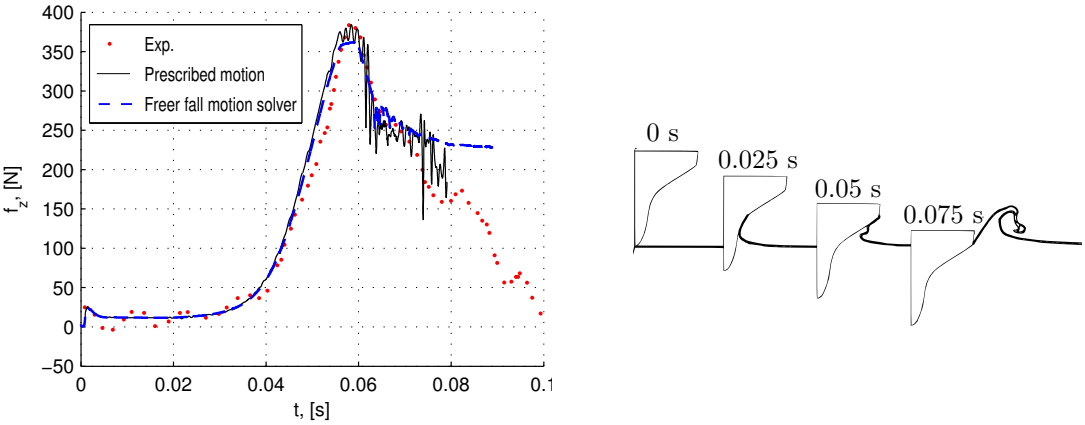

(a) (b)

Figure 4.16: (a) The total vertical forces compared with the experiment by Aarsnes (1996). (b) Snapshots of the simulated free surface at four time instants

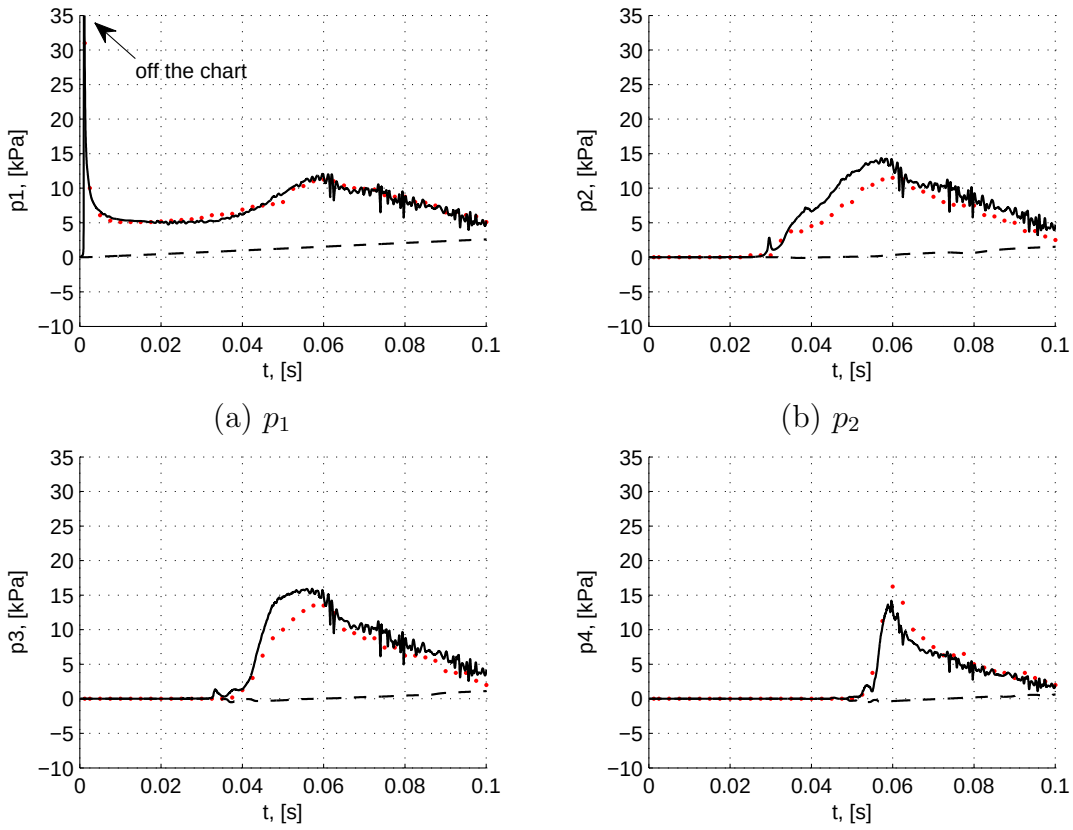

(a) p_1 (b) p_2

(c) p_3 (d) p_4

Figure 4.17: A comparison of pressure probes at four locations (see Fig. 4.15). (–) The present VOF-based flow solver, (•) Experiment by Aarsnes (1996), (- - -) norminal hydrostatic pressure, $\rho \boldsymbol{g} \cdot \boldsymbol{x}$

experiments. The simulation starts at $t = 0$ s where the initial contact between water and the bow flare section takes place. During the whole simulation location p_1 is in contact with water all the time and the computed pressure agrees almost perfectly with the measurement. At locations p_2, p_3, p_4, the computed pressures depend on the accuracy of the predicted pile-up of the free surface. The time instants, where the computed pressures begin to increase at p_2, p_3 and p_4, agrees well with the experiment but the peak values are either overestimated (at p_2 and p_3) or underestimated (at p_4) by 15% to 20%.

From previous experience, it has been found that it is a difficult task to predict an accurate local slamming pressure. In the numerical method, the variation of the local pressure depends strongly on the spatial and temporal discretization as well as the numerical stability of the solver. The sign of instability can be observed as the pressure "spikes" seen in Fig. 4.17. The computational mesh may have been stretched badly due to the large displacement.

Based on the results shown in Figs. 4.16 and 4.17, it is reasonable to conclude that, at least in two-dimensional cases, the current VOF-based flow solver is capable of producing a favorable estimate of the impact force provided that the kinematics of the body motion during the impact are modeled accurately.

4.5 CFD & the Classical Flat Plate Approximation

Consider a 2D water entry problem where a body undergoes a straight vertical motion and is piercing the free surface at velocity $v(t)$. The penetration depth is $h = \int v\,dt$. The potential flow theory is assumed and the trapped air or the compressible effects are not accounted for. The acceleration of the fluid is assumed to be several orders of magnitude larger than the gravitational acceleration, meaning that the infinite high frequency free surface condition for the potential field $\phi|_{z=0} = 0$ can be applied. At the initial impact with a large slamming area, it is considered that the penetration depth h is much smaller than the wetted length c. Therefore, the instantaneous contact area is replaced by an equivalent flat plate at $z = 0$ with the body boundary condition approximately $\partial\phi/\partial z|_{z=0} = -v$ (The direction of the surface normal vector is positive when pointing into the fluid). To some extent this simplification can be justified at the initial stage of the impact of a blunt body. A sketch of the problem to solve is shown in Fig. 4.18. At this point, the impact problem is simplified and the mathematical formulation of the simplified problem is equivalent to a boundary value problem of a flat plate moving in an infinite fluid which has a well-known

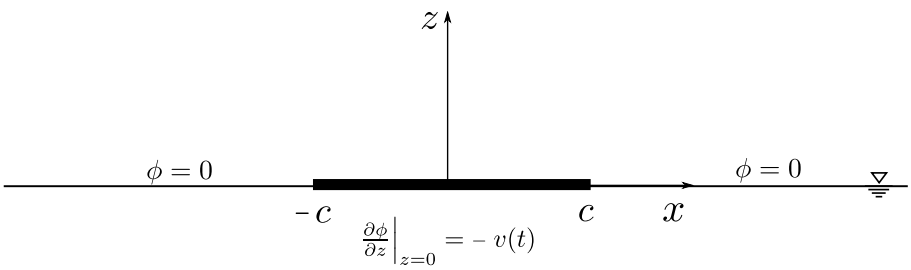

Figure 4.18: Sketch of a simplified water entry problem

classical solution for the potential ϕ, e.g. Newman (1977).

This simplified slamming problem is a classical textbook example of slamming load models, see e.g. Bertram (2000) and Faltinsen (1993). In the following the penetration velocity is considered time dependent. Along the flat plate, the potential is

$$\phi = -v\sqrt{c^2 - x^2} \quad , \quad |x| < c(t) \tag{4.11}$$

Using the Bernoulli equation, the first order pressure along the plate is

$$p = \frac{\rho\, v\, c}{\sqrt{c^2 - x^2}} \frac{dc}{dt} + \rho\sqrt{c^2 - x^2}\frac{dv}{dt} \tag{4.12}$$

and the corresponding vertical force on the plate is

$$f = \frac{\rho}{2}\Big[v\frac{d}{dt}\Big(\pi\, c^2\Big) + \pi\, c^2\frac{dv}{dt}\Big] \tag{4.13}$$

The wetted length $c(t)$ changes depending on the local geometry of the body. At any time instant the boundary value problem is solved using the instantaneous value of the prescribed velocity $v(t)$. Thus, Eq. (4.13) describes the vertical force acting on the body provided that the wetted length is known. The slamming force depends strongly on the wetted length. The formulation does not distinguish between two different situations where (a) the body accelerates instantaneously while already piercing the free surface and (b) the body was out of water and gradually penetrating the free surface.

The key issue here is the estimation of the wetted length $c(t)$ which can be found using a geometric relation. Therefore, the analysis is restricted to be applied to simple geometries such as a wedge with a constant deadrise angle or a circular cylinder. Applying the von Kármán theory, the wetted length is taken as the intersection between the body surface and the initial calm water line i.e. the water pile-up is not accounted for. Thus, the wetted length can be evaluated from the pure geometrical relation of the body at a given penetration depth. For example, a wedge with deadrise angle β has a wetted length according to the von Kármán's theory of $c(t) = h(t)/\tan\beta$. Following the Wagner theory, the water pile-up needs to be accounted for and the wetted length becomes an implicit part of the solution since it depends on the solution of the free surface elevation at the spray root.

Noticeably, the vertical force Eq. (4.13) can be written as

$$f = \frac{\pi\,\rho}{2}\Big[v^2\frac{dc^2}{dh} + c^2\frac{dv}{dt}\Big] \quad ; \quad c = c(h) \tag{4.14}$$

where $c = c(h)$ is re-written as a function of the penetration depth. The simplicity of the formula inspired Korobkin (2012) to suggest to model slamming forces using a decomposition written as

$$f = \rho v^2 F_v + \rho\dot{v} F_w \tag{4.15}$$

where $F_v = F_v(h)$ and $F_w = F_w(h)$ are two functions depending solely on the penetration depth h and can be pre-calculated. The main advantage is that f can be estimated for any given profile of $(h, v, \dot{v})$.

In this section, we will test 4.15 on a 30° wedge and a 2D bow flare section, see Sections 4.5.1 and 4.5.2. The functions F_v and F_w are estimated using the VOF-based incompressible NS flow solver (OpenFOAM). To estimate F_v, we do CFD simulations with constant penetration velocity v_0, i.e.

$$\dot{v} = 0 \quad \Rightarrow \quad F_v = \frac{f}{\rho v_0^2} \tag{4.16}$$

and F_w can be estimated from simulations with $\dot{v}$ set to some constant value, i.e.

$$\dot{v} = const. \quad \Rightarrow \quad F_w = \frac{f}{\rho \dot{v}} - \frac{v^2 F_v}{\dot{v}} \tag{4.17}$$

with F_v known from Eq. (4.16).

4.5.1 Slamming Forces on a 2D 30° Wedge

Considering a water entry problem of a 30° wedge. The beam width is $B = 0.5$ m. The distance to from the keel to the knuckle is $H = 0.5B \tan 30^o \approx 0.144$ m. The objective is to evaluate the decomposition model, Eq. (4.15). Given an arbitrary profile of the falling motion, the results of Eq. (4.15) will be compared against CFD simulations with the given motion imposed on the wedge. Three major steps are performed:

- **Step 1**: Equation (4.16) are evaluated at three constant velocities, $v_0 = 4, 5, 6\,\mathrm{ms}^{-1}$, see the results on Fig. 4.19(a,b).
- **Step 2**: Equation (4.17) are evaluated at three constant accelerations, see the results on Fig. 4.19(c,d). With a constant acceleration, the penetration depth is written as

$$h(t) = \frac{1}{2}\dot{v}t^2 + v_0 t + h_0 \tag{4.18}$$

  The notations in Fig. 4.19 are ($g = 9.81\,\mathrm{ms}^{-2}$)

$$\begin{aligned} \text{v4-3g}: &\quad v_0 = 4\,\mathrm{ms}^{-1}; \dot{v} = -3g \\ \text{v5-5g}: &\quad v_0 = 5\,\mathrm{ms}^{-1}; \dot{v} = -5g \\ \text{v6-6g}: &\quad v_0 = 6\,\mathrm{ms}^{-1}; \dot{v} = -6g \end{aligned}$$

  i.e. $h, v, \dot{v}$ are positive downward and $h_0 = 0$ at mean water level ($z = 0$). Negative accelerations are imposed on the body.
- **Step 3**: Equation (4.15) is tested for a velocity profile as shown in Fig. 4.20. The CFD results agree almost perfectly with Eq. (4.15).

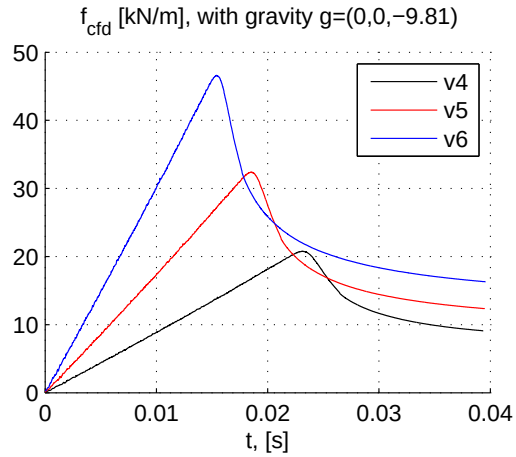

(a) Predicted vertical forces at constant velocities

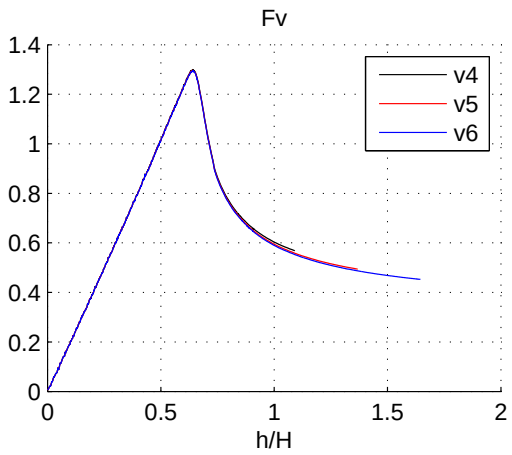

(b) The estimates of $F_v(h)$, Eq. (4.16) at three constant velocities

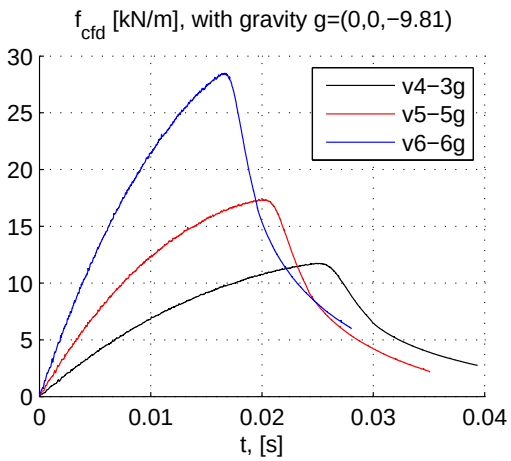

(c) Predicted vertical forces at constant decelerations

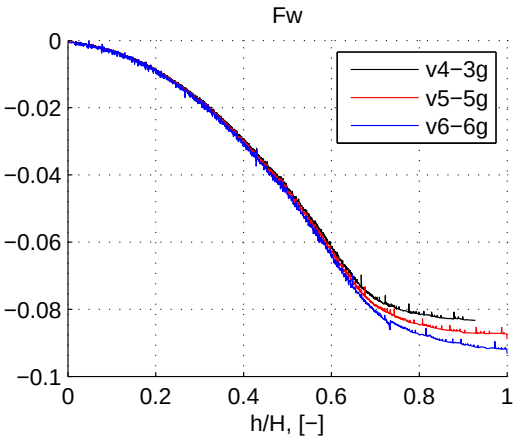

(d) The estimates of $F_w(h)$, Eq. (4.17) at three constant decelerations

Figure 4.19: Drop tests of a 30° wedge. F_v and F_w are estimated from the results of CFD simulations

The results show that the decomposition model, Eq. (4.15), can be applied to the CFD results. Only a few CFD simulations are required in order to estimate $F_v(h)$ and $F_w(h)$ valid for a given shape of the body penetrating a calm free surface. Theoretically, there is no indication shown that the decomposition model can be applied after a free surface separation at the upper knuckle. However, the present test case using a 30° wedge shows that the decomposition model is usable even after the separation of the free surface. In the next sections, the application of the decomposition model is investigated further using a more complicated body shape.

4.5.2 Slamming Forces on 2D Bow Flare Ship-like Section

In the previous section, it has been shown that the decomposition model, Eq. (4.15), can be used to describe the vertical force on a 2D wedge slamming onto a calm water surface. In the following, the decomposition model is applied to the 2D bow flare published in Aarsnes (1996), see also Section 4.4. The vertical distance from keel to the lower knuckle is approximately $H \approx 0.203$ m and the beam width (from edge to

edge) is 0.32 m. Similarly to the 30° wedge case, three steps are performed:

- **Step 1**: Equation (4.16) is evaluated at three constant velocities, $v_0 = 1, 3, 4\,\mathrm{ms}^{-1}$, see the results on Fig. 4.21(a,b). Notice that $v_0 = 1\,\mathrm{ms}^{-1}$ is perhaps too small to be classified as slamming. The profile of F_v corresponding to $v_0 = 1\,\mathrm{ms}^{-1}$ deviates strongly from the other two. It is still in question how to determine the lower and upper limits of the penetration velocity, which can be applied to determine $F_v(h)$. In this particular case, there is no theoretical justification for the choice of the three velocities other than it covers the range of the velocity profile, which will be applied in Step 3 below.

- **Step 2**: Equation (4.17) is evaluated at three constant accelerations, see the results on Fig. 4.21(c,d). The notations in Fig. 4.21(c,d) are as follows:

$$\begin{aligned} \text{v1+2g}: &\quad v_0 = 1\,\mathrm{ms}^{-1}; \dot{v} = +2g \\ \text{v3-1.5g}: &\quad v_0 = 3\,\mathrm{ms}^{-1}; \dot{v} = -1.5g \\ \text{v4-3g}: &\quad v_0 = 4\,\mathrm{ms}^{-1}; \dot{v} = -3g \end{aligned}$$

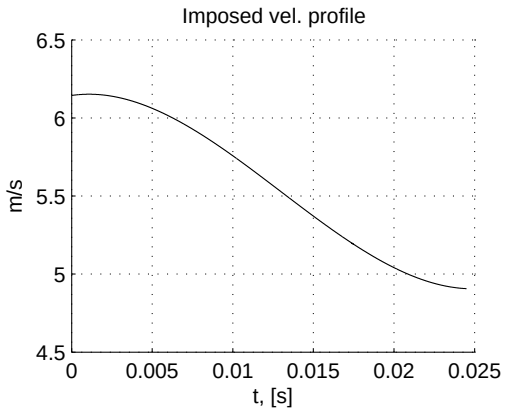

(a) Imposed velocity profile

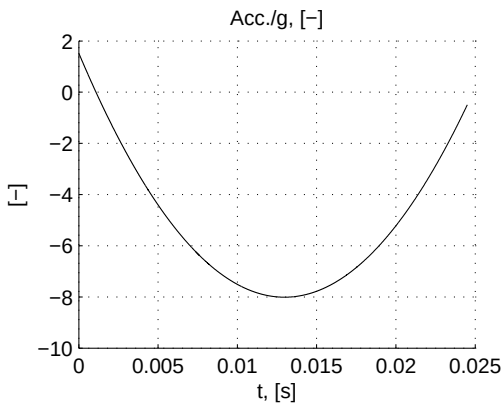

(b) The corresponding acceleration

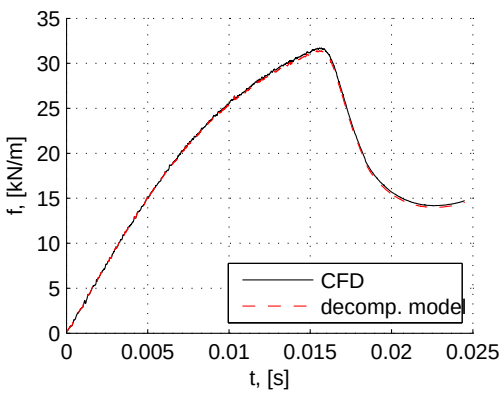

(c) The predicted vertical forces: CFD vs. Eq. (4.15)

Figure 4.20: Drop-test simulations of a 30° wedge. An arbitrary velocity profile is imposed on the wedge. The vertical force predicted by the decomposition model is evaluated against the CFD results.

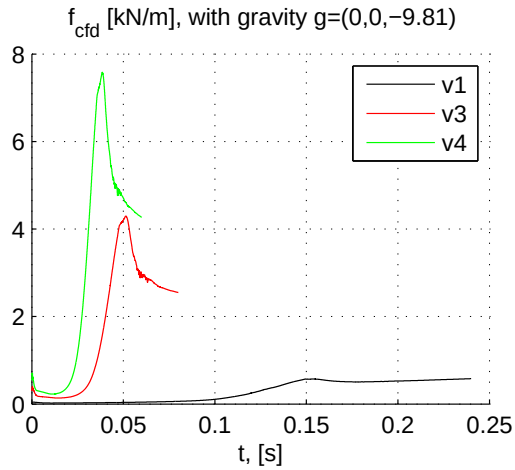

(a) CFD simulated vertical forces at three constant velocities

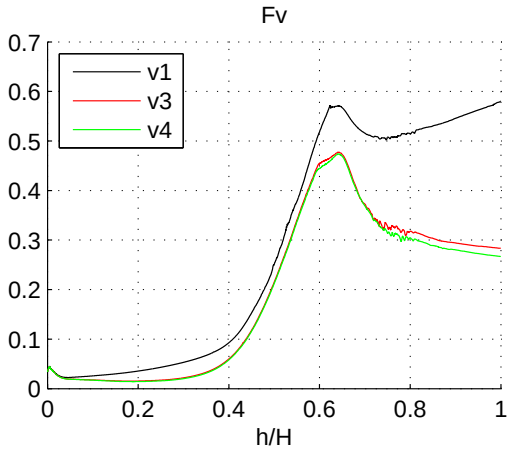

(b) $F_v(h)$ are estimated from the CFD results

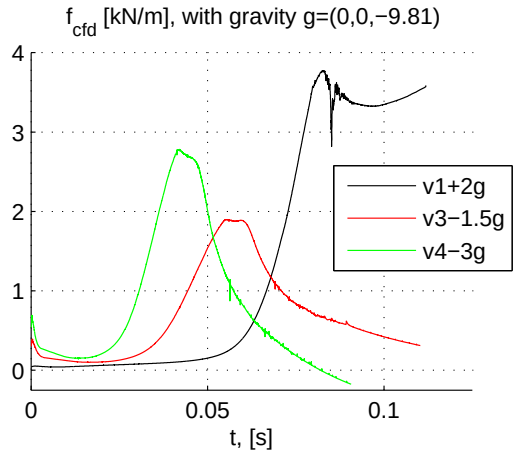

(c) Vertical forces at constant accelerations

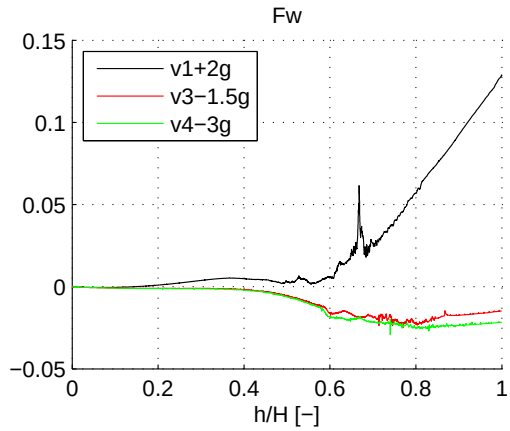

(d) $F_w(h)$ are estimated from the CFD results

Figure 4.21: Drop test simulations of a 2D Ship-like section. F_v and F_w are estimated from the CFD results

where the kinematics of the falling motion is given by Eq. (4.18). With $v_0 = 1\,\mathrm{ms}^{-1}$ the initial penetration velocity is too small, thus the acceleration is set to positive (accelerate instead of decelerate).

- **Step 3**: Equation (4.15) is tested for a velocity profile as shown in Fig. 4.22. The CFD results agree well with Eq. (4.15) except for the "v1+2g" profile where the initial velocity $v_0 = 1\,\mathrm{ms}^{-1}$ is too low to be classified as slamming. The applied velocity and acceleration profiles correspond to the falling motion in a simulated free fall drop test. Clearly, this profile has a nearly constant acceleration, which may not be appropriate for checking the validity of Eq. (4.15). The profile is too similar to the calibration cases, Fig. 4.21(c,d). Therefore we try a new artificial (arbitrary) velocity profile as shown in Fig. 4.23. The comparison using the new profile shows that the calibration velocity $v_0 = 1\,\mathrm{ms}^{-1}$ with $\dot{v} = +2g$ is not applicable whereas the other two are still good even though the imposed velocity profile contains a wide range of deceleration and acceleration, i.e. from $-25g$ up to $250g$.

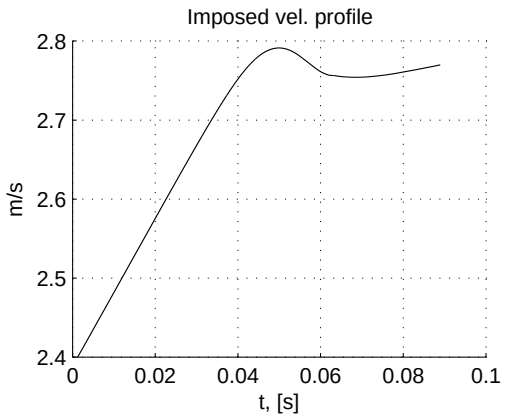

(a) Imposed velocity profile

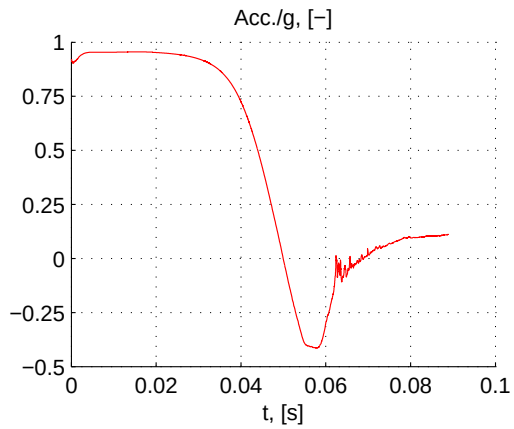

(b) The corresponding acceleration

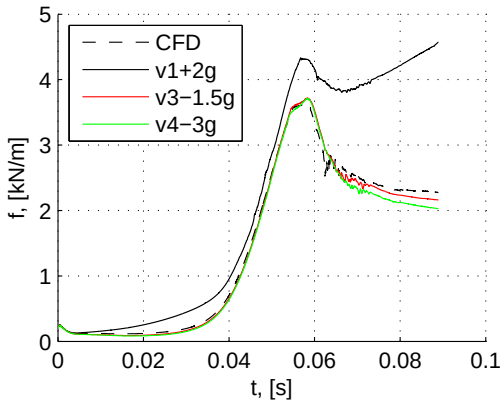

(c) The predicted vertical forces: CFD vs. Eq. (4.15)

Figure 4.22: Free-fall of a 2D ship-like section. In (c), the results of Eq. (4.15) depends strongly on $F_v(h)$ and $F_w(h)$

The force decomposition model produces very promising results showing a wide range of validity. As shown in the results above, the model can be applied not only for a simple geometry with small deadrise angle but also for a complex geometry such as a realistic bow flare section. The decomposition model provides a slamming force during the water entry on calm water, which can be as accurate as CFD, even after the separation of the free surface flow due to a knuckle. Once the functions $F_v(h)$ and $F_w(h)$ have been estimated, the model can be applied given any kinematic motion of the water-entry problem.

However, it is still in question how to choose an appropriate set of velocities, accelerations and decelerations for the calibration of F_v and F_w. Future investigations shall include the three dimensional effects in the slamming forces and forces during water-exit.

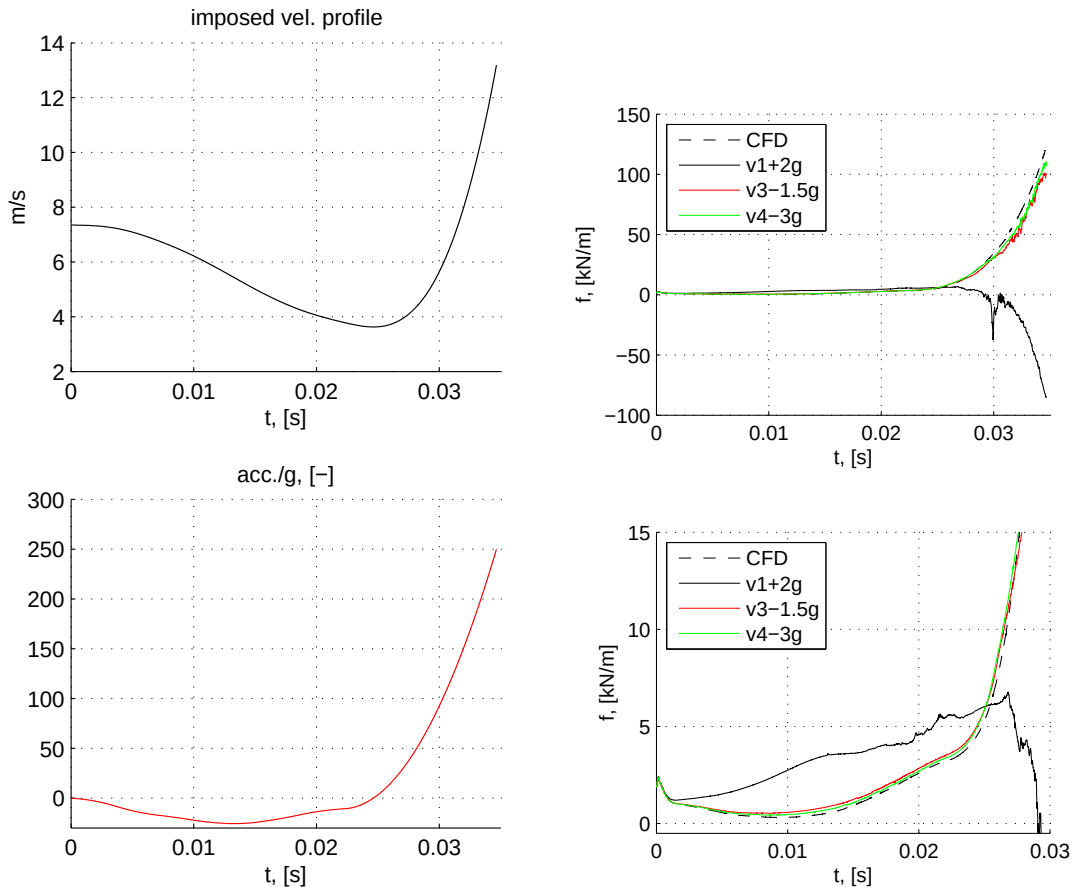

(a) (b)

Figure 4.23: A new more arbitrary profile for the 2D ship-like section. (a) velocity and acceleration. (b) Vertical forces by CFD and Eq. (4.15) with a close-up view in the lower plot

4.6 Truncated 3D Bow Flare Model

Several researchers have adopted a two-dimensional formulation to estimate bottom and bow flare slamming loads. The pressure distribution as well as the total force is determined by an integration over a pseudo three-dimensional representation of the hull, see e.g. Tuitman & Malenica (2009). To get an insight in the three-dimensional flow effects on a realistic bow flare, we shall evaluate and compare the accuracy and performance of the two-dimensional formulation. In the following, a comparison has been carried out between a fully 3D simulation and a 2D strip integration.

The slamming analysis is performed for a fine form Panamax container ship hitting a calm water surface under a constant trim angle. The three-dimensional model used in the numerical experiments is the hull form from the KRISO Container Ship (Kim et al. (2001)). Table 4.1 shows the main dimensions of the vessel. This hull form represents a commercial fine form container ship with a bulbous bow and a bow flare, which is relatively modest, compared to modern ships. The full scale ship does not exist, but the geometry of the hull has been published with the intention of providing data for CFD validation as well as studying flow physics. The current study uses only the forward part with a total length of 100 m. A sketch is shown in Fig. 4.24a including a subdivision in 2D strips (5 m spacing) prepared for the

two-dimensional calculations.

The simulations are done using the incompressible flow solver, which means that the effects caused by trapped air cannot be accounted for. The trapped air acts like a cushion and usually occurs when the relative impact angle between the water surface and the ship hull is relatively small. Since the current VOF-based flow solver cannot capture the physic of trapped air, the initial trim of the KCS model is set to 10° and the impact is assumed symmetric corresponding to a head sea condition with zero heel angle. Furthermore, the non-zero initial trim gives a better representation of the wave slapping and pounding at the front part of the ship. In addition, it shall be stressed that the 2D strips as sketched in Fig. 4.24a are defined to be perpendicular to the still water plane such that the cuts are always parallel to the vertical fall motion.

A constant penetration speed of 10 m/s is imposed on the truncated hull. Using a more realistic velocity profile is considered unnecessary for the purpose for comparing the three-dimensional approach to slamming with the 2D strip integration approach. The setup for the numerical simulation is very similar to the setup of the test cases presented earlier. The significant difference is that the current three-dimensional simulation has a much larger geometric scale. The size of the domain and the water depth are chosen to be sufficiently large such that the blockage effect is as small as we can afford. In 3D, the number of cells increases rapidly with the increasing size of the domain. A compromise has been made such that the total computational domain is $200 \times 232 \times 148$ m with the initial water depth of 100 m. A sketch of the numerical setup is shown in Fig. 4.24b where the truncated hull model is positioned at the center of the computational domain.

Body-fitted meshes of hexagonal and polygon cells have been applied to discretize the domain. The fluid domain is dominated by the hexagonal cells except in those areas where it is necessary to introduce polygon cells in order for the grid to conform to the body and to obtain a reasonable transition from low and high grid-resolution. The mesh density is defined such that there are five density levels as sketched in Fig. 4.24b. Close to the body the mesh density is highest. The coarsest area is defined with level 0 in which the higher levels are defined relative to the characteristic size of this level. The relation is $L_n = L_0/2^n$, where L_0 and L_n are the characteristic size of level 0 and level n, respectively. For an example, if the characteristic length of level 0 is 1 m then the characteristic length of level 2 is $L_2 = 1/2^2 = 0.25$ m. Next to the ship hull, level 4 is defined. This produces near-body cells with a characteristic size of $L_4 = 0.0625L_0$ m. Three meshes are generated for the mesh convergence study with a total number of cells 1.0, 4.2 and 19.8 million. The corresponding near-body cell sizes are approximately 0.75, 0.37 and 0.18 m for the coarse, medium and fine

Table 4.1: Geometry and conditions of the KRISO Container Ship (KCS), Kim et al. (2001)

Scale	1	Lwl (m)	232.5
Bwl (m)	32.2	Lpp (m)	230.0
D (m)	19.0	T (m)	10.8
CB	0.651	Displ. (m^3)	52030
CM	0.985	LCB (%), fwd+	−1.48

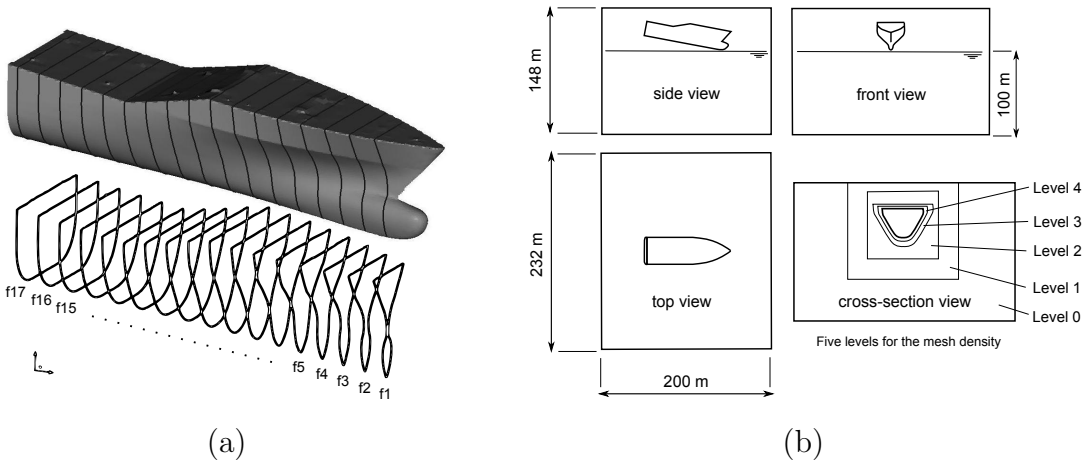

Figure 4.24: A sketch of the forward part of the KCS model with vertical 2D strips used in the 2D evaluations of the slamming loads (a); Numerical setup in 3D (b)

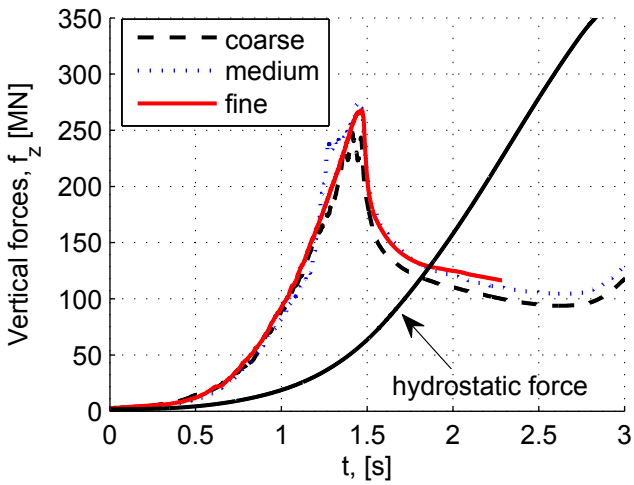

Figure 4.25: Numerically estimated slamming forces. Coarse (1.0 M cells), Medium (4.2 M Cells), and Fine (19.8 M Cells)

mesh, respectively. The computational effort needed to run the fine mesh in 3 s of physical time is approximately 180 hours on 40 CPUs. For the coarse mesh, however, the execution time is only 5.5 hours on 20 CPUs.

As seen in Fig. 4.25, the results of the coarse and fine mesh agree but there are slight differences between the medium mesh and the fine mesh around the time of the peak forces indicating that there are still non-converged small variations in the forces that act locally on the ship hull. The overall trend, however, remains unchanged. The total vertical force is increasing almost monotonically until the spray root of the pileup water reaches the deck. The peak forces occur when the spray root beneath the ship hull exits at the truncated aft part. Beyond this point, the total vertical force keeps rising due to the imposed constant fall velocity. Eventually, the norminal hydrostatic component of the forces (evaluated from norminal hydrostatic pressure defined as $\rho \boldsymbol{g} \cdot \boldsymbol{x}$) becomes dominant as seen in Fig. 4.25.

Because the trim is fixed at 10°, the impact occurs initially on the bulb and the forward bottom part of the bow flare. The numerical results show that the free

surface separates along the side of the bulb and accelerates toward the flare area causing a cavity to form. Eventually, the cavity collapses causing a minor slap to the bow flare from the side and from the front. In such conditions, the slapping will depend strongly on the formation of separation of the free surface. Further away from the bulb, some splash-up water accelerates upward and hits the flare area inducing a bow flare slamming.

To highlight the progress, four snapshots are shown in Fig. 4.26. The bottom area is wider and more flat toward the midship section. The built-up pressure at the bottom of the hull has a high pressure at the spray root similar to water entry of a wedge shape body. The impact on the bulb initiates a separation of the free surface, Fig. 4.26b, causing some trapped air above the bulb. The trapped air exists long after the bow flare impact, Fig. 4.26d. Considering that the current flow solver is solving a VOF-based incompressible NS equations, it is reasonable to assume that the compressibility of trapped air cannot be simulated properly. Even though the simulation can capture the trapped air, there is a possibility that the pressure inside the air pocket and in the surrounding fluid is over estimated.

The separation of the free surface during the bottom slamming causes a complicated splash, which may be very important for the subsequent bow flare slamming. The intensity of the bow flare impact depends on the position of the splash surface relative to the flare angle. For instance, if the splash is moving rapidly toward the flare area, the impact force can be very significant.

The computational power required in a full 3D simulation is huge. At this point, the interest is to investigate if it is feasible to approximate the full 3D results using a strip formulation. The forward part of the ship is divided into several stations each with a length of 5 m. The first station is at the front perpendicular (FP) as sketched in Fig. 4.24. With this configuration, 16 stations can cover more than 25% of the overall length of the current ship.

Two dimensional calculations have been performed on the 2D geometrical profile of each station taken at the vertical plane perpendicular to the calm water line and parallel to the prescribed vertical motion. The motion in the 2D calculations is prescribed in the exact same way as in the full 3D case (i.e. the drop speed is kept constant at $10\,\mathrm{ms}^{-1}$). The number of the required finite volume cells in the 2D simulations is approximately 200.000 cells and the execution time for each station is approximately 3 hours running on a single node (8 cores) of the HPC cluster. The 2D simulation of each station can be done independently. Thus, the total execution time for all stations is in the order of 3 hours provided that the HPC cluster has at least as many nodes as the number of the 2D stations. This is a significant improvement compared to the execution time of the full 3D simulation.

The vertical forces of each station in 2D and 3D are evaluated and compared in Fig. 4.27. The full 3D results are split according to the 2D strips and the pressure forces are evaluated on each strip. The results are shown in Fig. 4.27a. These results are compared with the results of the 2D simulations where each strip is simulated separately. As shown in Fig. 4.27b, the total force evaluated from the 2D strips is clearly over-predicting the peak forces locally on each station as they penetrate the free surface one after another. Because each station is simulated separately as a pure 2D simulation, the initial impact force is too large especially for those stations with the flat bottom located closer to the amidships section, see also Fig. 4.24a. Thus, those spikes seen in the 2D force integration are purely due to the numerical

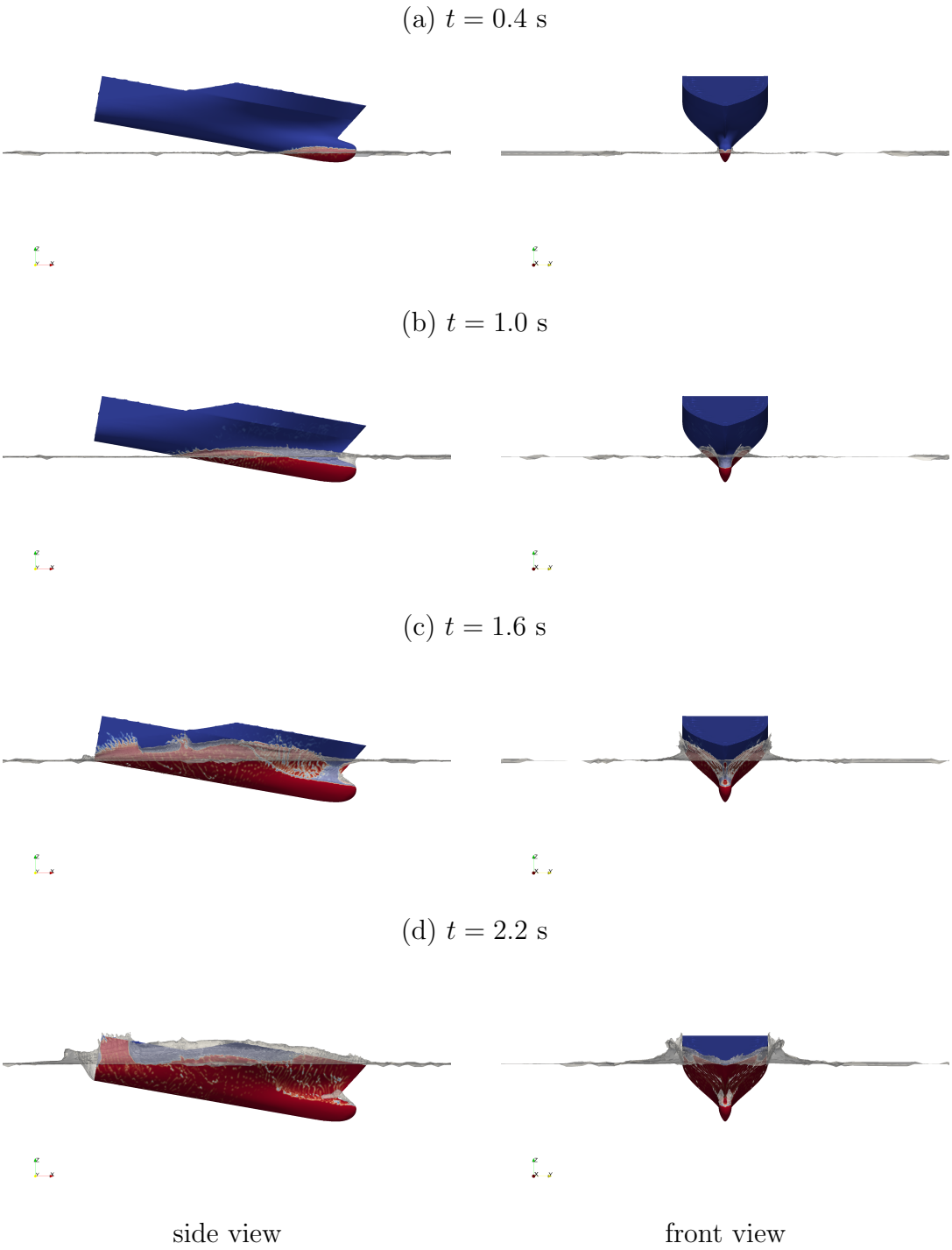

Figure 4.26: Snapshots of the free surface (red color indicates wetted surface) showing initial bottom slamming (a), separation of the free surface (b), the subsequent bow flare slamming (c), and the trapped air in the upper region of the bulb (d)

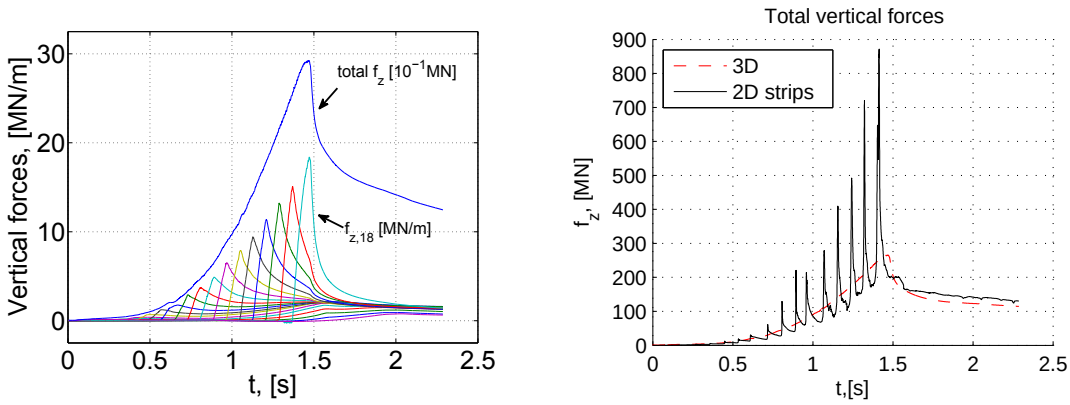

(a) (b)

Figure 4.27: Vertical force on the truncated hull. (a) Full 3D simulations, (b) The total vertical force compared between the 2D strips integration and the full 3D simulation

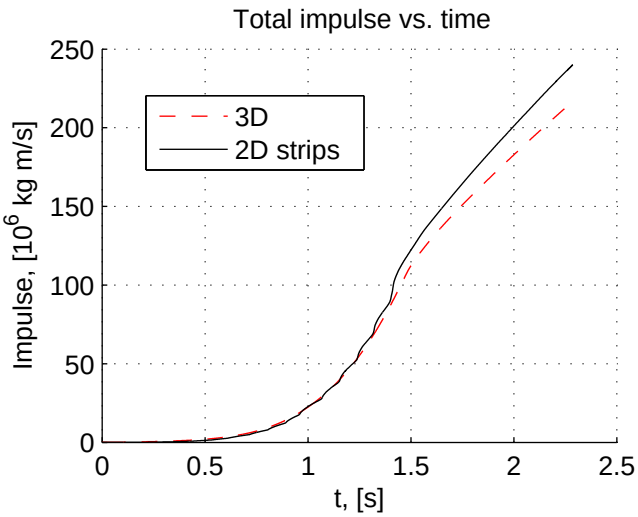

Figure 4.28: The total impulse for the 2D strips integration and the full 3D simulation

procedure in which each 2D section hits the water surface without any trim. With a flat bottom, a 2D simulation cannot account for the trim angle and the result is similar to a flat plate impact on still water. Therefore, the number of spikes becomes proportional to the number of segments (5 m in length here).

The forces presented in Fig. 4.27 are without the norminal hydrostatic component. Each station experiences a peak load at a different time, which is expected since the high pressure area is concentrated at the spray root, which moves past each station at a different time. The imposed constant velocity effectively causes the spray root to move along the flat bottom with a nearly constant velocity. This is seen in the rise time of each station as shown in Fig. 4.27a where the rise time is approximately the same between all stations. This rise time has been estimated to be 85 ms which is much shorter than the overall 3 s impact time on the entire hull. The slopes of the rising forces, however, are gradually steeper because the bottom is flatter toward the midship sections.

The total impulse is shown in Fig. 4.28. The comparison of the total impulse is

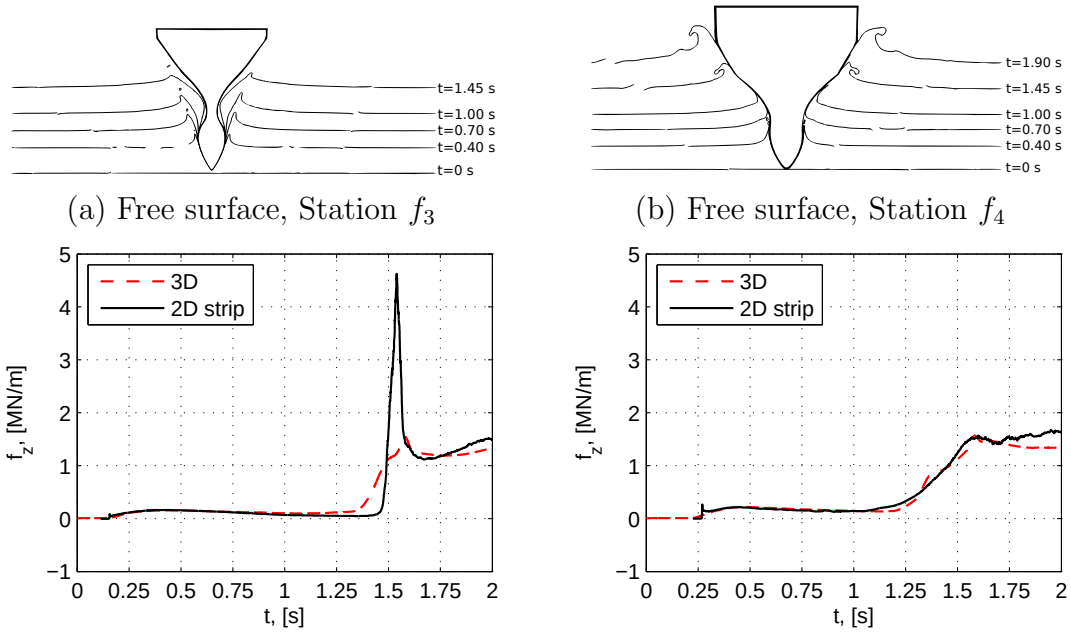

(a) Free surface, Station f_3 (b) Free surface, Station f_4

(c) Vertical force, Station f_3 (d) Vertical force, Station f_4

Figure 4.29: Free surface predicted by 2D simulations (a) & (b), The corresponding vertical forces (c) & (d), The free surface separation at the bulbous bow may cause a severe bow flare slamming

done for the time duration where the spray root has not yet reached the truncated section at the aft part i.e. $t < 1.4$ s. Beyond this point, the total vertical force is significantly reduced due to the fact that the truncated bow flare model is fully submerged (see also Fig. 4.26). Thus, for $t > 1.4$ s the results are not relevant for the comparison. The impulse shown in Fig. 4.28 reveals that the spike forces seen in the 2D strip approach are rather insignificant for the total impulse.

Figure 4.27a shows that there is a relatively small contribution from those stations close to the bulb i.e. station f_1, f_2, f_3, and up to f_6 where the most significant flare area are located. The impacts on station f_7 up to f_{18} are mainly bottom slamming since these stations have a flat bottom with very little or no flare.

The visualization of the 2D results shows similar features as in the 3D case. The bottom impact causes the pile-up water to accelerate rapidly toward the flare area. One important flow feature is clearly seen in the 2D simulations. That is, the free-surface separation during the bottom impact leads to a complex free-surface deformation.

Figure 4.29 shows an example of two different free-surface deformations predicted by the 2D simulations. The shape of the bottom part combined with the high momentum of the pile-up water causes the free surface to separate. Even though the geometrical differences between the bottom parts are small, the formations of the pile-up water are very different.

On station f_3, approximately 3% aft of the forward perpendicular, Fig. 4.29a, the pile-up water is almost parallel to the bow flare creating a small relative impact angle between the free surface and the bow flare. The subsequent bow flare impact becomes very similar to the case of a flat plate impact on still water. A sharp peak in the force, corresponding to this impact, can be observed, see Fig. 4.29c. In the full 3D simulation, this nearly perfect match between the water surface and the bow

geometry usually does not occur and the bow flare impact is less intense due to the 3D effect and the 3D geometry of the bow flare. Even though a similar formation of the pile-up water can be seen in the full 3D simulation, the 3D shape of the bow flare makes it easier for water to escape from the impact zone causing a lower impact force on the slamming area.

It shall be emphasized that these severe bow flare slamming events are observed only in the 2D simulations. The overestimation of the pressure force in 2D simulations is well known in the literature. On station f_4, i.e. 5 m further aft, there is no separation of the free surface during the bottom impact. The free surface deformation, as seen in Fig. 4.29b, shows clearly that the pile-up water follows smoothly the geometrical profile of the section. The agreement between the 2D and the 3D is good up to about 1.75 s whereas the 3D procedure predicts a lower force due to the exit of the spray root at the aft part of the truncated hull. The pressure reduction affects not only the local wetted surface but the surrounding pressure field in the 3D domain.

4.7 Summary

A validation study of the current VOF-based flow solver has been performed by comparing numerical results with experimentally obtained slamming forces for small scale water-entry problems. The conclusion is that slamming loads can be assessed numerically using the current flow solver. However, it is also found that in order to obtain a reliable and converged result, especially in three-dimensional problems, the grid requirement is very fine demanding huge computer resources. This poses some limitations on possible applications of this numerical procedure for practical estimation of slamming loads. Thus, the direct calculation approach using CFD is better suited for calibrations of an approximate, but faster procedure. One possible procedure is to model slamming forces using the decomposition model as presented in Eq. (4.15). This model has been compared against the CFD results in three different cases: one case for a 30° wedge and two cases for a 2D bow flare section. In all three cases, the kinematics of the body was chosen arbitrarily and it has been shown that the vertical forces modelled by Eq. (4.15) can be almost as accurate as the CFD results.

To get an insight into the three-dimensional flow effects, the current flow solver has been applied to evaluate and compare the accuracy of the traditionally used 2D strip calculation procedure. Detailed numerical results show plausible free surface separations during the bottom slamming which also exist in the full 3D simulation. It is seen in the 2D calculation that a large impact force appears when the separated free surface hits the upper part of the bow flare under a small impact angle. The impact force is less severe in the full 3D simulation because the fluid can escape more freely causing the overall pressure to be smaller than in the 2D simulation. However, it is clearly observed that the total impulse obtained from the 2D strip procedure does not deviate much from the more expensive 3D simulation. This provides a hope of being able to evaluate the total impulse using the 2D strip approach in a realistic sea state. On the other hand, the vessel used in the investigation has a hull form with relatively small bow flare. Thus, more evidence is needed in order to draw a firm conclusion.

The potential gain of using the 2D strip approach is reduced computational effort.

For the 2D calculations, it can be reported that each station uses approximately 0.2 million cells, and that the execution time for each station is approximately 3 hours occupying 1 node (8 cores). Thus, 18 stations on 18 nodes can be done within 3 hours. This has to be compared to the much larger computational effort for the 3D simulation which costs approximately 180 hours on 40 cores. Even though there are 18 stations to be simulated the parallel efficiency is very high since each 2D station can be simulated independently on separate computational nodes.

Nevertheless, it is still an open question how to choose the critical slamming area in the slamming calculation. In the present study, 25% of the forward part of the hull has been chosen. The choice is purely empirical and clearly illustrates a need for a more detailed slamming evaluation in realistic sea states.

Chapter 5

Numerical Wave Tank

The intended application of the numerical wave tank in the present study is an accurate evaluation of slamming on a container ship sailing in a realistic sea state. The mathematical formulation of the numerical wave tank can be found in Chapter 2. This chapter is dedicated to assessing the performance of the numerical wave generator and the relaxation technique adopted to prevent the outgoing waves from reflecting back into the domain. Furthermore, the new proposed scheme for an adaptive adjustment of the relaxation profile, Eq. (2.63), needs to be evaluated.

The performance of the relaxation zone is evaluated based on a comparison between two simulations. The first simulation is done on a wave flume made reasonably large such that the simulated waves may propagate over a long distance without being affected by the outlet boundary. The second simulation is done on a smaller domain with the relaxation zone located at the outlet to absorb the outgoing waves. A comparison between the two simulations provides a reasonable estimate of the performance of the applied relaxation zone. The results are presented in Sec. 5.1.

The waves applied in the present work are regular long-crested monochromatic waves and conditional waves formulated as first order stochastic waves. The regular wave case is simulated in a fixed frame of reference whereas the conditional wave simulation is done in a moving frame of reference accounting for a vessel moving at a constant forward speed.

It is commonly known that numerical diffusion may cause an additional damping on the numerically generated wave. The effect can be observed directly as the wave height will decrease further downstream. The dissipation rate of the wave height can be measured in percentage decrement per wavelength.

The current numerical wave generator is first tested for its ability to generate a regular long-crested monochromatic wave, Sec. 5.1; and the effect of the numerical diffusion on the propagated wave is evaluated. Next, the wave generator is set to generate a conditional wave, which includes a wide range of wave frequencies given as a summation of first order potential waves. The nonlinear effects in the free surface and in the wave-wave interaction are evaluated using the current VOF-based flow solver. However, the first order potential wave formulation which is used as an input for the numerical wave maker, is lacking these nonlinear effects. Thus, waves generated in the numerical tank using the present VOF-based flow solver are considered more realistic. A discussion based on a particular example of the simulated conditional wave is given in Section 5.2. The important finding, which will be presented in detail, can be summarized as follows

- While the current wave generation framework is capable of introducing waves into the domain at a reasonable accuracy, there is an issue related to the initial imbalance of the volume flux between the inlet and the outlet causing an uneven mean water level across the numerical wave tank. For an infinite water-depth wave, the error introduced by the imbalance of the volume flux at the initial stage is negligible. However, the error is clearly visible if the Stokes drift is strong and the water depth is relatively shallow. More details are provided in Section 5.1.1.

- Using the dynamic relaxation profile as presented in Section 2.7, the reflection coefficients are significantly reduced while, at the same time, there is no significant effect of changes in the average size of the time step.

- Using the first-order representation for the conditional wave poses several issues related to the mismatch between the imposed first-order potential solution at the boundary and the nonlinear Navier-Stokes solution inside the computational domain. The VOF-based incompressible Navier-Stoke solution is considered more realistic since the solution contains fewer assumptions and accounts for nonlinear wave-wave interactions. Details are presented in Section 5.2.

5.1 The Performance of the Relaxation Zone & Wave Generator

At every time step, the flow solutions inside the predefined relaxation zone are explicitly modified to relax the outgoing waves toward a predefined wave field. The technique has been previously applied in Jacobsen (2011) to simulate regular long-crested monochromatic waves in a fixed frame of reference. The major difference presented here is that the current simulation applies an adaptive relaxation profile making it more convenient to carry out simulations using a variable size for the time step. The work presented in the following provides a basis for a discussion of the transient effect during the startup period, which will be of concern when simulating conditional waves.

The primary test case is the wave condition case C presented in Chapalain et al. (1992). The same test case is presented in Jacobsen (2011) where an implementation of an equivalent wave generation and relaxation framework has been validated. In Jacobsen (2011), it has been shown that the current wave generation framework is capable of capturing a constant propagation form of the monochromatic stream-function wave with a reasonable accuracy. The results of the current simulation confirms this, cf. Fig. 5.1. The harmonic amplitudes taken at several locations along the propagation direction shows that the 1st wave harmonic has the strongest reflection estimated to be approximately 1.5% (see Eq. (5.2) for the definition of the reflection coefficient).

In Jacobsen et al. (2012), the wave generator was tested against the experimental results of triad nonlinear wave-wave interaction in shallow water (published in Chapalain et al. (1992)). The agreement between the numerical prediction and the experiment was good. Jacobsen et al. (2012) also showed that the current wave generation and relaxation framework is versatile.

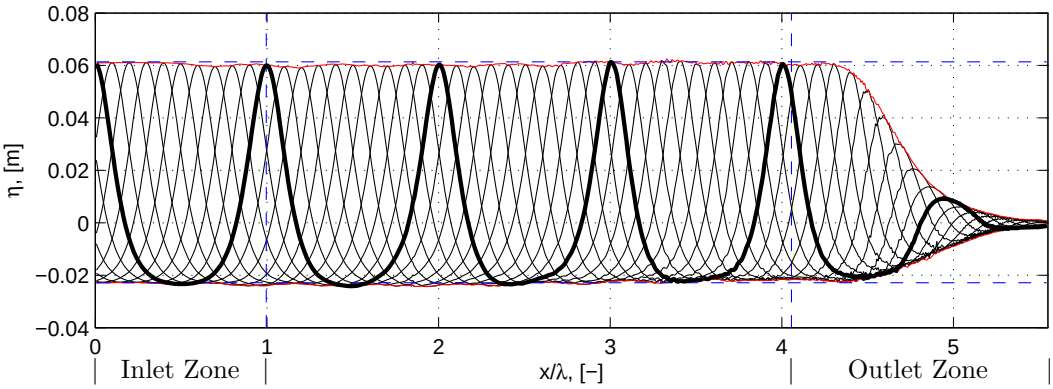

(a) Envelope of the free surface elevations at time $t = 20T \sim 21T$

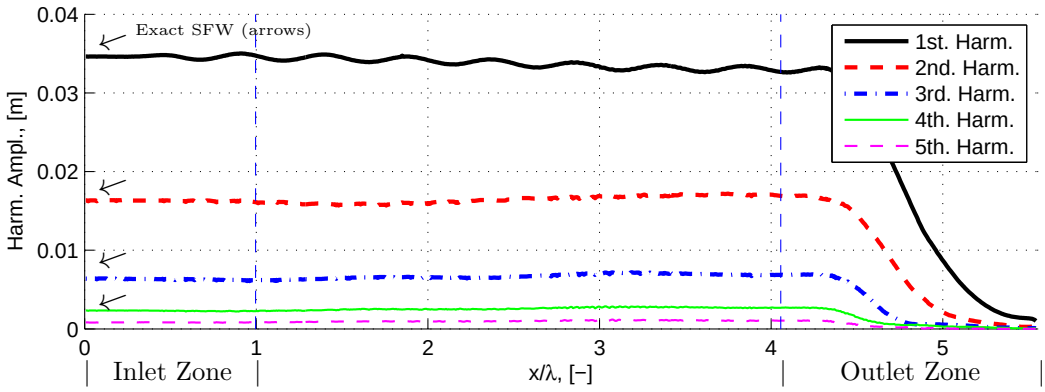

(b) Harmonic amplitudes of the simulated waves

Figure 5.1: A simulation of a regular wave with the stream-function wave (SFW) solution imposed at the inlet: Period $T = 3.5$ s, Depth $h = 0.4$ m, Length $\lambda \approx 7.03m$ (case C in Chapalain et al. (1992)). Reflection coeff. $R \approx 1.5\%$

The work presented in the following will not reproduce and confirm the results shown in Jacobsen et al. (2012), but rather show an important limitation of the adopted wave generation and relaxation framework related to the balance of the volume flux in and out of the numerical wave tank. This limitation is strongly related to the artificial wave generation method where the potential wave solution is imposed directly at the boundary.

5.1.1 Balancing the Volume Flux

While the Chapalain's test case shows a reasonable performance of the current wave generation framework (as also shown in Jacobsen (2011)), it is important to emphasize one limitation related to the balance of the net volume flux inside the inlet and outlet zones. This limitation can be best shown through a simulation of a long-crested regular wave with a strong Stokes drift. The wave height and period are $H = 8$ m, $T = 14$ s and water depth $h = 20$ m. There is no ambient current in the flume. The wavelength according to a high-order stream-function wave theory (Eq. (2.54)), is $\lambda \approx 194.05$ m. The 20 m water depth is relatively shallow and has been used for two purposes: (a) to provoke the nonlinearity in the wave showing whether or not the current VOF-based flow solver can predict the nonlinear wave

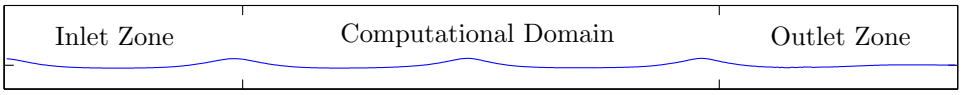

Figure 5.2: A sketch of the numerical wave tank. The inlet and outlet zones are defined to be one wavelength long.

accurately; and (b) to show the possible issues related to the accumulated water due to a nonzero volume flux introduced at the inlet and at the outlet. The problem is not clear in an infinite water depth since the wave characteristics do not change so much when the additional accumulated water is relatively small compared to the total volume inside the numerical tank. Table 5.1 shows the properties of the target wave.

Two relaxation zones are introduced in the numerical wave tank: one at the inlet and one at the outlet, see also Fig. 5.2. The inlet relaxation zone acts as a buffer zone connecting the imposed nonlinear potential wave solution to the two-phase flow Navier-Stokes solver. At the outlet, the relaxation is introduced to damp out the outgoing wave.

Figure 5.3 shows spatial variations of the free surface at a time interval between $99T \sim 100T$. The 10 snapshots was taken over each wave period with the free surface sampled over a distance of 4λ from the inlet boundary. Waves are generated with the high-order stream-function wave solution imposed at the inlet boundary and inside the inlet relaxation zone. As expected the wave profile inside the generation zone (inlet zone) is the same as the imposed stream-function wave solution.

The free surface envelope when using the long domain (14λ) is shown in Fig. 5.3a. The results of the long domain are compared with for the results of the shorter domain, Fig. 5.3b, c, and d.

Noticeably, the simulated wave profiles inside the computational zone do not match exactly to the stream-function wave solution, see Fig. 5.3a. The differences relate to both physical and numerical aspects of wave propagation. There is a fundamental difference in the flow equations where the stream-function solution is imposed at the inlet boundary and the inlet zone generates a wave field that does not necessarily satisfy the Navier-Stokes equation. The flow solution of the VOF-based flow solver provides the necessary correction. In a physical wave tank, the mismatch between the linear input wave-maker and the kinematic of the fully nonlinear waves are seen as spurious waves traveling freely in the tank. As already investigated, see e.g. in Madsen & Sørensen (1993) and Chapalain et al. (1992), any non-linear interaction with the free wave is consequently causing an energy transfer between the harmonics. In the current numerical simulations, the water depth is relatively shallow and the target wave is highly nonlinear. The discrepancy can be clearly detected. Indeed, Fig. 5.3 shows that the simulated wave profile, which is the solution of the incompressible Navier-Stokes equation, is steeper and offsets

Table 5.1: Wave properties of the test case with a strong Stokes drift

Height, H [m]	8	Period, T [s]	14
Length, λ [m]	194.05	Celerity c, [m/s]	13.86
Grid, $(\Delta x, \Delta z)$ [m]	(0.25, 0.5)	Avg. time step Δt, [s]	0.015

(a) Waves simulated in a long wave tank (14λ)

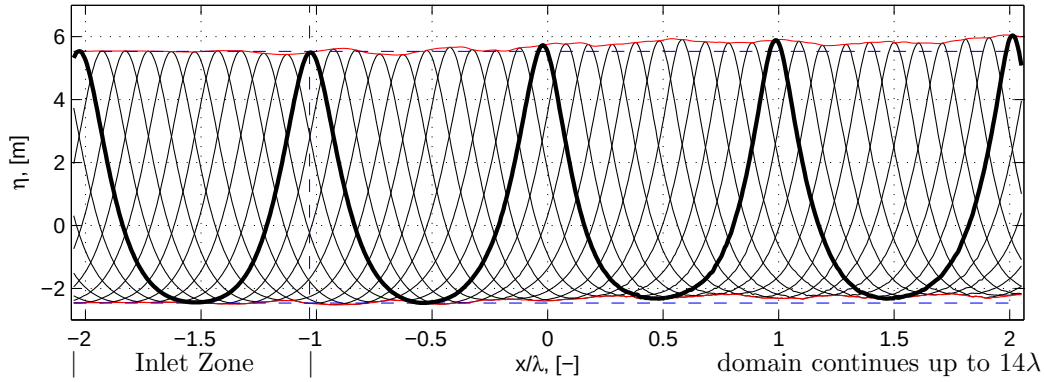

(b) Using a shorter tank (4λ) with the dynamic relaxation profile activated

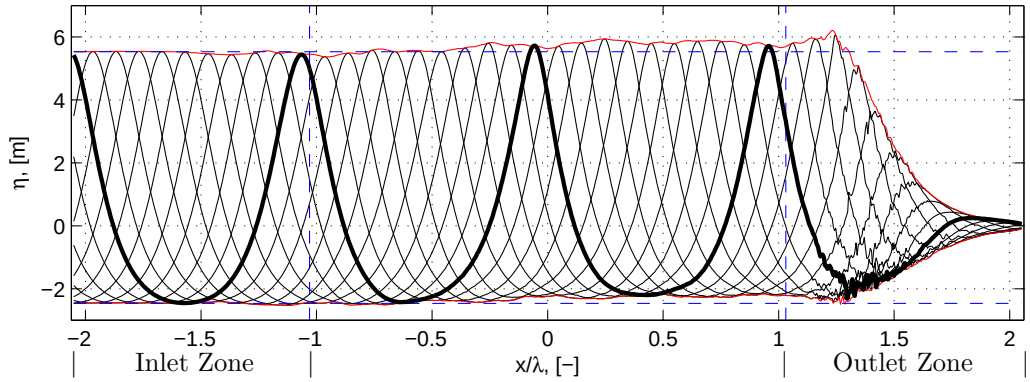

(c) Without the dynamic relaxation (average time step size, $\Delta t \approx 0.1377$ s)

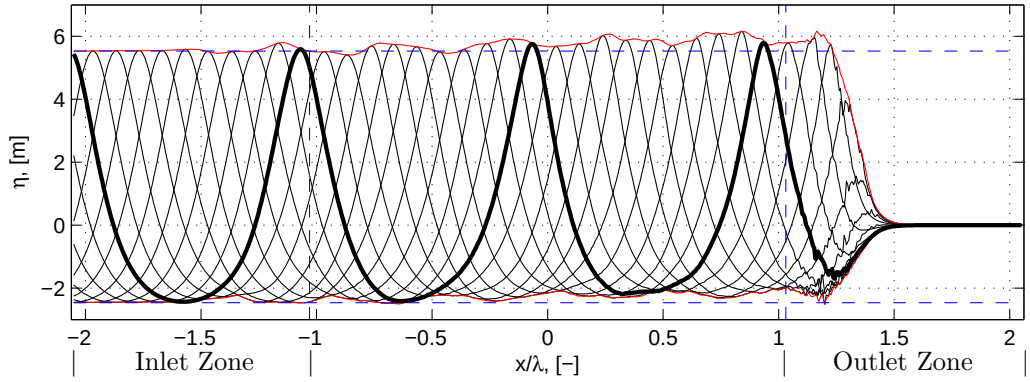

(d) Without the dynamic relaxation (average time step size, $\Delta t \approx 0.0775$ s)

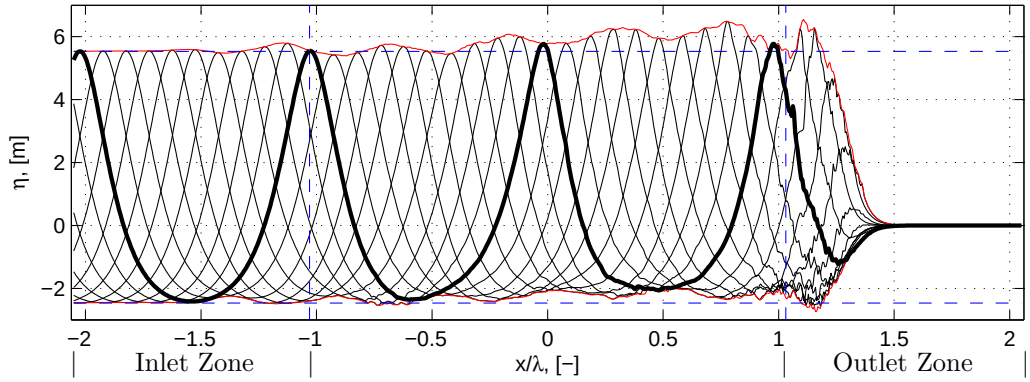

Figure 5.3: Snapshots of the simulated free surface elevation. (Horizontal dashed lines) Wave crest and trough according to SFW solution. (Red solid lines) Amplitudes of the simulated waves

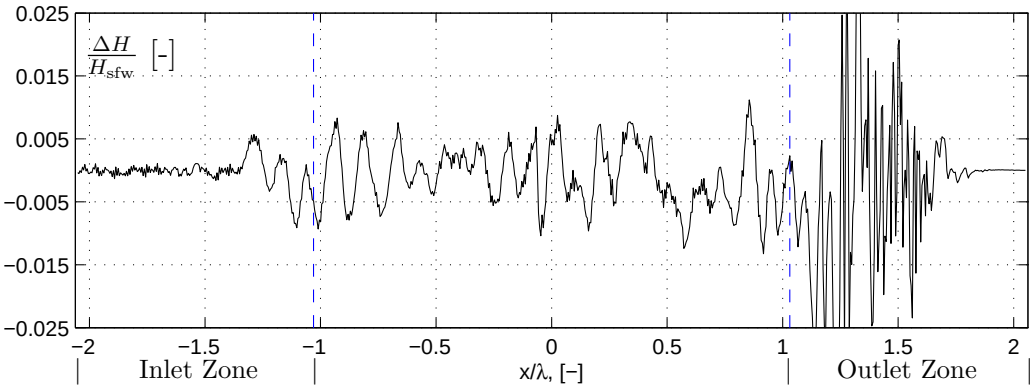

Figure 5.4: Differences in wave height compared between simulations with and without an initialized wave field. In the outlet zone waves are relaxed toward a calm free surface

more toward a larger difference between the crest and trough than predicted by the potential flow theory. As waves propagate further away from the inlet zone, the free surface envelope changes gradually toward the simulated profile, which becomes practically stable at a distance of approximately one wavelength away from the inlet zone. On the other hand, the major missing physical effects, which have not been accounted for in the stream-function wave solution, are the viscous effects of the real fluid flow. In large scale wave propagation problems, these viscous effects should be negligible. Hence, even though the flow solutions inside the numerical tank take into account the viscous effects, the differences in the free surface envelope should not be as much as seen in Fig. 5.3. Therefore, these discrepancies must be numerically related.

It shall be emphasized that the simulated wave profile remains mostly the same with or without the initialization of the wave field at $t = 0$ s, see Fig. 5.4. When the simulation starts from an initialized wave field imposed to be exactly the same as the stream-function wave solution, there is less accumulation of water due to the nonzero volume flux. Still, the simulated wave field develops gradually toward similar results as shown in Fig. 5.3b. Beyond the initial stage, the net flux at the inlet zone is the same as the net flux at the outlet zone. This can be clearly observed as the total volume of water remains stable, see Fig. 5.5.

Nevertheless, there is an offset in the mean free surface elevation. The volume ratio presented in Fig. 5.5d is taken from a simulation where the flume is initialized with the target wave field. Waves propagating though the outlet zone are relaxed toward the target stream-function wave solution. When the inlet and outlet zones are of the same size, it is expected that the volume ratio is oscillating at a constant magnitude from the very beginning of the simulation since the configuration of the numerical tank is equivalent to a cyclic wave condition with the boundary condition at the inlet being the same as at the outlet. The fact that Fig. 5.5d shows an increasing magnitude of the volume ratio in the early stage provides an important evidence showing that the offset is caused by an artificial accumulation of water inside the tank. The accumulated water cannot be easily controlled using the present wave relaxation framework. The magnitude of the total volume ratio is increasing slightly until there is a balance between the volume fluxes in and out of the domain. In the present wave configuration, where the Stokes drift is strong, the accumulated

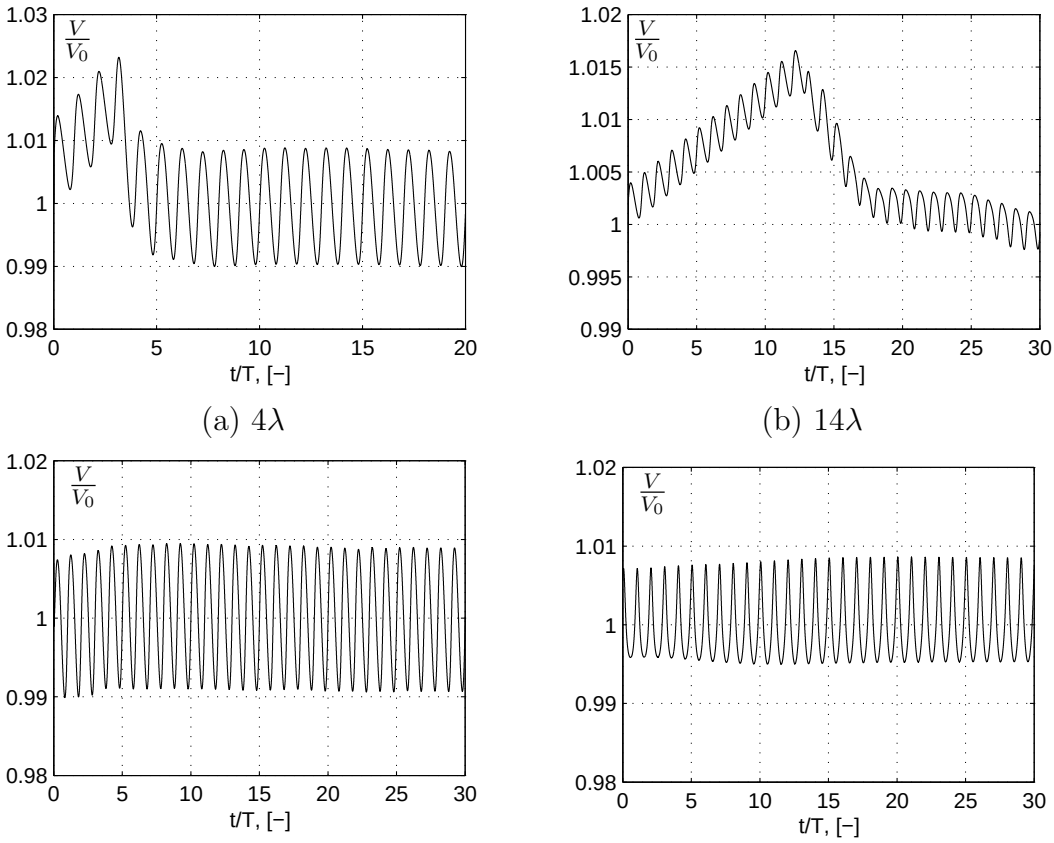

(a) 4λ (b) 14λ

(c) 4λ (d) 4λ, Outlet: SFW

Figure 5.5: The ratio of the total volume of water inside the numerical wave tank. (a) A relatively short wave tank, (b) A long wave tank, (c) The domain is initialized with the target wave field. (d) Same as "c" except that the outlet zone is relaxed toward the stream-function wave solution, see also Fig. 5.6

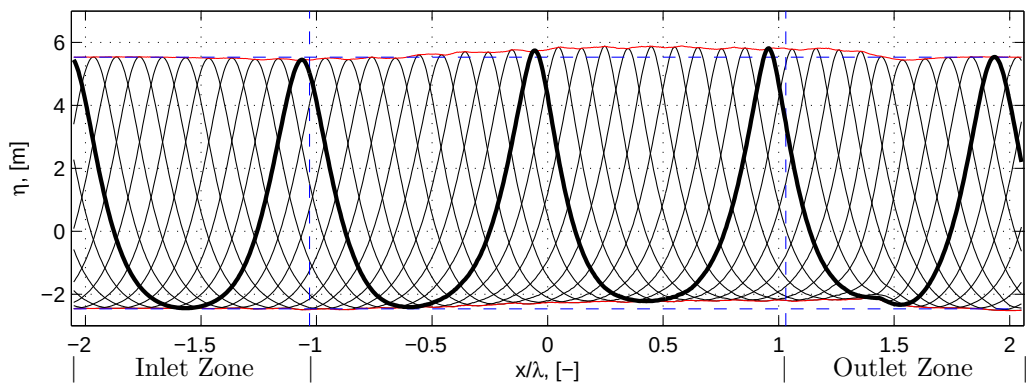

Figure 5.6: The domain is initialed with the target wave field and waves inside the outlet zone are relaxed toward the imposed stream-function wave solution

water in the early stage has a strong effect on the wave solution inside the interesting part of the domain. The free surface elevation corresponding to Fig. 5.5d is shown in Fig. 5.6. The outgoing waves are relaxed forcefully toward the target wave and still, the initial balance of the volume flux between the inlet and the outlet cannot be assured. It is possible to compensate for the non-zero volume flux through the stream-function wave solution generated to fulfill a zero Stokes-drift condition (see e.g. Fenton (1988)), which perhaps is acceptable. Still, the volume flux at the outlet cannot be controlled yielding the same results as shown in Fig. 5.3.

5.1.2 Reflection Coefficient

There are small variations of the free surface indicating an existence of small spurious free waves traveling on top of the incident wave. Some parts of the small variation seen in the amplitudes of the wave are caused by wave reflections from the outlet relaxation zone. The reflected waves propagate upstream toward the inlet zone. The effect of the outlet relaxation zone is clearly observable as the wave amplitude is relaxed toward the zero level. Without the dynamic adjustment of the relaxation profile, Fig. 5.3(c,d), the outlet relaxation zone depends strongly on the size of the time step. The average time step size in Fig. 5.3c is larger than in Fig. 5.3d. It is observed that, there is a stronger reflection when using a smaller time step. The free surface elevation is relaxed toward the zero level too rapidly. For a comparison, the results of the simulation using the dynamic relaxation show that the free surface is relaxed more gently utilizing the whole length of the outlet zone.

To quantify the reflection, Liu & Yue (1998) and Jacobsen et al. (2012) fit the simulated waves to a monochromatic description assuming several discrete frequencies where the higher harmonics are presumed to be a discrete multiplication of the base input frequency. The expression for the free surface elevation is written to account for waves traveling in opposite direction. The equation is cf. Jacobsen et al. (2012),

$$\eta = a_0 + \sum_{j=1}^{N} a_j^- \cos(j\theta^-) + b_j^- \sin(j\theta^-) + a_j^+ \cos(j\theta^+) + b_j^+ \sin(j\theta^+) \tag{5.1}$$

where $\theta^{\pm} = kx \pm \omega t$ are for waves traveling in opposite direction. Here, the superscript "+" and "-" denote the propagation directions, forward and backward, respectively. The symbols a_j, b_j denote the coefficients to be determined by the fitting procedure, e.g. a least-squares method. Time series of the free surface at two locations relatively close to each other are required for the problem to be well-posed. The representation shown in Eq. (5.1) distinguishes between waves traveling forward and backward providing information about the reflected waves. However, spurious free waves may exist and Eq. (5.1) cannot distinguish between the reflected or the spurious waves causing the estimation of the reflection to be somewhat erroneous. The implicit assumption in Eq. (5.1) is that any wave traveling in the opposite direction of the incident wave is due to the reflection. The assumption is not always valid since the spurious waves may be mistakenly seen as the reflected waves. Thus, the reflection coefficients provided in the following are used here only as a means to compare the reflection relatively between two simulations. Using the same definition as in Jacobsen et al. (2012) the reflection coefficient is defined as the ratio between the forward and backward wave coefficients written as

$$R = \frac{||(a^+; b^+)||_2}{||(a^-; b^-)||_2} \tag{5.2}$$

Without the dynamic relaxation profile the reflection coefficient is 4.5% for Fig. 5.3c with the average time step size of $\Delta t \approx 0.0775$ s. In a comparison, the reflection coefficient using the dynamic relaxation profile (Fig. 5.3b) is 1.6%, i.e. almost 3 times smaller. Beside the improvement seen in the smaller reflection coefficient, it is recommendable to use the dynamic relaxation profile since the results will not be affected strongly by the size of the applied time step. As already presented in Jacobsen et al. (2012), the reflection coefficient can be reduced further by expanding the length of the relaxation zone. The reflection also depends on the wave height to depth ratio H/h. For the present wave configuration $H/h = 0.4$ and according to Jacobsen et al. (2012) the reflection coefficient can be reduced to less than 1% if the outlet relaxation zone is expanded to 2 times the wavelength.

5.2 Simulations of Conditional Waves

To estimate slamming pressures accurately, detailed information about the relative velocity between water and the free surface topology is needed in the region where slamming occurs. Therefore, instead of using the simplified model where the ship plunges in a deterministic manner onto an initially calm free surface, we shall apply a more realistic wave scenario, which can be used to identify the most probable extreme whipping loads. This so-called critical wave episode, or most likely response wave, described by Jensen (2009), represents the most likely wave and ship motion associated with a given extreme wave hull girder bending moment response.

When using the first order approximation, the free surface elevation of a conditional wave is written as shown in Eq. (2.55). The equation is repeated in the following for convenience

$$H(x,t) = \sum_{i=1}^{n} a_i \cos(k_i x - \omega_i t + \theta_i) \tag{2.55}$$

This is a typical representation of first-order stochastic waves. The amplitude of each wave component is determined by the target wave spectrum and the phases are randomly chosen. Nevertheless, the conditional wave uses the same representation with deterministic parameters rather than randomly chosen. The deterministic frequencies, phases and amplitudes are determined by performing a statistical reliability analysis e.g. FORM (First-Order Reliability Method) or SORM (Second-Order Reliability Method). Most importantly a set of these parameters describes a sea state which, according to the reliability analysis, is the most probable sea state leading to a given response. There are several methods to determine these stochastic parameters. More details can be found in Chapter 6.

This section provides a discussion on several aspects related to the generation of a conditional wave in a numerical wave tank. The scope of discussion is confined to an examination of one particular conditional wave generated using the Pierson-Moskowitz (PM) spectrum with a significant wave height $H_s = 10$ m and zero

Table 5.2: Dimensions of the 9400 TEU post-Panamax container ship

LOA (Length Overall), [m]	349
Lpp (Length btw. perp.), [m]	333.34
Beam, Molded [m]	43
Draft (max), [m]	15
Gross Tonnage, [-]	107,711
Deadweight, [ton]	114,004

up-crossing period $T_z = 10.44$ s. The wave frequencies vary from 0.25 to 0.9 rad/s discretized using 15 equidistant frequencies. This particular wave has been generated using FORM to induce a hogging vertical bending moment of 4500 MNm in a 9400 TEU post-Panamax container vessel moving in head seas at 5 m/s, the same wave scenario as presented in Seng & Jensen (2012). The vessel particulars are shown in Table 5.2. The response of 4500 MNm VBM amidships is evaluated at a target time $t = 50$ s using a classical nonlinear time-domain strip theory program (see e.g. Xia et al. (1998)). The analysis assumes a steady state response. Thus, the target time of 50 s is considered to be large enough to avoid the memory effect and any transient behavior early in the time domain simulation.

Figure 5.7 shows the resulting free surface elevation evaluated on a non-accelerating frame of reference moving at the same constant speed as the vessel. The conditional wave is used as an input to the CFD simulation. Using Eq. (2.55), the free surface elevation and the wave kinematics are given in any location and at any time. Nevertheless, there are several aspects that are worth mentioning. These are:

- **Linearized free surface** : The first order approximation of the potential wave solution has been derived based on a linearized free surface boundary condition at the initially calm mean water level. The wave kinematics are defined up to $z = 0$ m and some action must taken to evaluate the wave kinematics up to the actual free surface position. One can choose to evaluate the horizontal and vertical fluid velocity up to the instantaneous free surface elevation or to apply the Wheeler stretching where the wave kinematics are evaluated up to the mean water level and stretched up to actual free surface level. The former choice will produce an artificially high velocity due to the exponential dependency of the vertical coordinate. Thus, the latter choice with the Wheeler stretching is more appropriate. However, there will be a slight mismatch between the vertical distributions of the horizontal partial velocity causing artificial local disturbances in the wave profile. It shall be emphasized that it is possible to use a second order wave at the cost of many more wave parameters to be determined from the statistical reliability analysis.

- **Nonlinear wave-wave interactions** : Inside the numerical tank, the flow solution is governed by the fully nonlinear incompressible Navier-Stokes equations. However, the potential wave solutions are imposed at the boundary which do not necessary satisfy the nonlinear equations. The flow solution inside the numerical tank is forced to obey the boundary conditions causing parasitic free higher-harmonic waves to exist. Numerical and experimental studies on the subject can be found in Madsen & Sørensen (1993) and Chapalain et al. (1992). The interactions between the resonant sets of wave components introduce an exchange of energy. In deep water, four-wave interactions (also

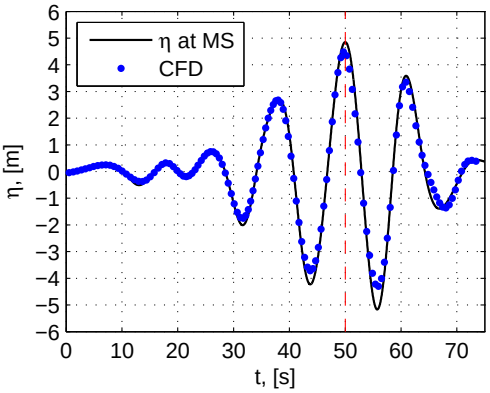

(a) Amidships

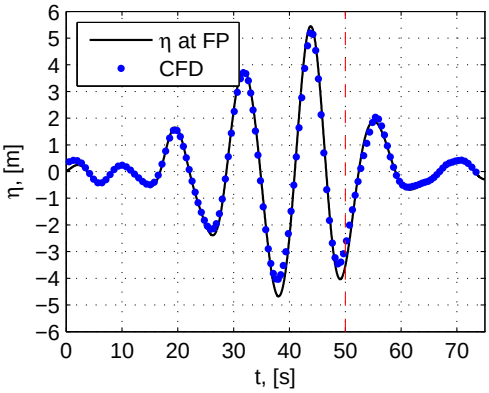

(b) Forward Perpendicular

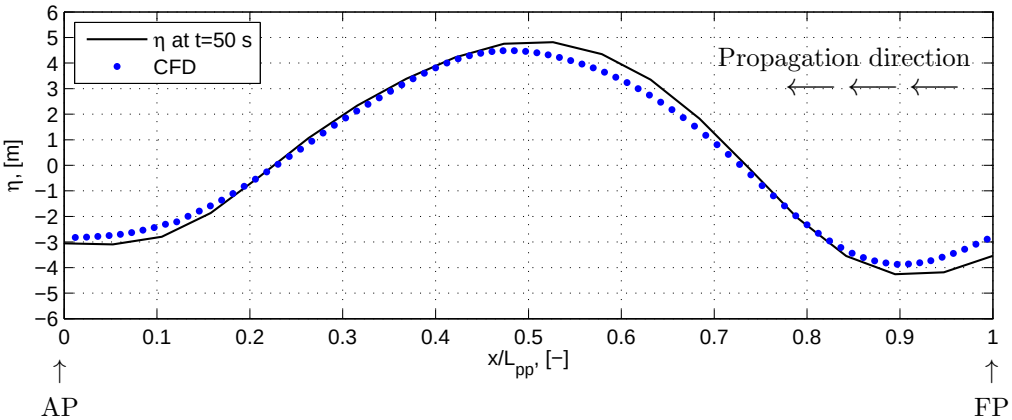

(c) Snapshot of free surface elevation η at the target time, $t = 50$ s

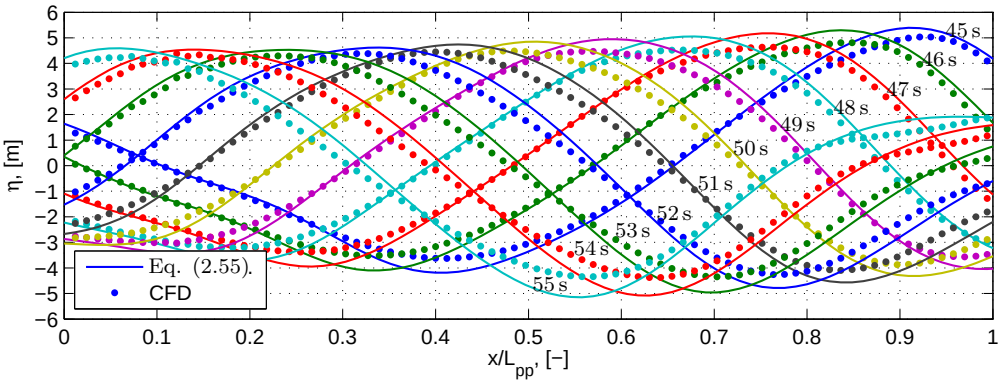

(d) Several snapshots of free surface elevation η around the target time: $t = \{45, 46, 47, ..., 55\}$ s

Figure 5.7: A CFD simulation with the conditional wave imposed at the wave-maker boundary. Responses induced by this particular conditional wave is 4500 MNm hogging VBM evaluated at 50 s using the nonlinear time-domain strip theory.

known as quadruplets) dominate the evolution of the spectrum transferring energy from the spectral peaks to lower and higher frequencies. In relatively shallow water, three-wave interaction (also known as triads) is responsible for an energy transfer from lower frequencies to higher frequencies often seen as higher harmonic waves cf. Beji & Battjes (1993). The energy transfer can take place over a relative short distance e.g. a single peaked spectrum can be changed significantly into a multiple peaked spectra. Using the second order wave description may reduce the contribution from the parasitic free higher-harmonic waves but does not remove it totally.

- **Wave breaking**: Physically, when the free surface becomes steep enough breaking will occur. The formulation presented in Eq. (2.55) is capable of producing a wide range of free surface profiles, but there is no easy way to handle the breaking. When imposing Eq. (2.55) directly at the wave-maker boundary, breaking of the free surface may occur shortly after. The resulting free surface and its evolution will be different from the free surface predicted by the potential flow theory. On the other hand, it has not yet been proven that the present free surface Navier-Stokes solver can predict the breaking mechanism satisfactorily even though in principle it should. Some numerical studies have been carried out in Jacobsen et al. (2012) revealing that the results improve significantly if the aspect ratio of the finite volume cell locally at the breaking location is close to 1. Still, there are several issues related to the numerical handling of the free surface. Presently, the artificial compression term is introduced to keep the interface sharp (see also Section 2.1 and Appendix A). When a complex free surface breaking occurs the modeling of the artificial relative velocity tends to artificially amplify the breaking causing the free surface to break too early and also inconsistently depending on the characteristic size of the local cells, see also Section 4.1 and Fig. 4.3. It shall be emphasized that there are other competitive numerical schemes for handling the free surface using a VOF formulation. While some schemes tend to smooth out the free surface we have no knowledge of any successful and accurate prediction of wave breaking mechanisms. The most popular approach is to compare the simulations with experiments. One of the reasons wave breaking is challenging to simulate is that turbulence may be very important for the breaking mechanism. The fact that turbulence at the vicinity of the free surface is not yet fully understood, the hope of being able to predict an accurate breaking in the near future is very small.

- **Short simulation time** : Evidently, when using a nonlinear time-domain strip theory the wave field can be introduced gradually everywhere in the domain. The memory effect is taken to be less than 50 s and the necessary time duration to simulate is less than 2 minutes. Therefore, only a short simulation is required. The short simulation time appears to be a great advantage since the CFD simulation tends to be very resource demanding. When the vessel is moving at a constant forward speed the introduction of the conditional wave may need to initiate from a fully developed flow field to avoid the initial transient effect of the forward motion. The simplest approach is first to simulate the vessel moving in a calm free surface until the wake is steady; and only then the conditional wave can be introduced at the wave-maker boundary. Thus,

the transient startup time for the nonlinear time-domain strip theory is not necessarily the same as the startup time for the CFD simulation. Counting from the moment the wave maker is activated the startup time in the CFD method is necessarily longer than the strip theory procedure because, in the CFD method, waves need some time to propagate from the wave-maker boundary to the interesting region and to reach a fully developed wave field. Contrary to the CFD method, the wave field can be imposed directly everywhere in the time-domain strip theory. The conditional wave is supposed to induce the target response at a predefined target time. The time for the evaluation of the target response must be the same in CFD as in the strip theory. Therefore, a proper time offset must be introduced to synchronize the reference time in CFD and in the nonlinear strip theory.

It can be expected that the simulated free surface does not match the potential wave exactly but rather includes the effects described above. The conditional wave shown in Fig. 5.7 has been derived under the condition of an infinite depth using the infinite depth linear dispersion relation $\omega_i = \sqrt{kg}$. In the CFD simulation, the water depth must be finite. In example presented in Fig. 5.7 the water depth is set to 300 m. The smallest wave number among the harmonics is $k = 6.37 \cdot 10^{-3}$ corresponded to a wavelength of $\lambda \approx 986.2$ m (linear theory with an infinite water depth). The 300 m water depth is estimated using the exponential decay of the wave kinematics aiming for a small and insignificant depth dependent variation at the bottom such that a slip boundary condition on the flat sea bed can be applied. The slope of $\exp(kz)$ at $z = -300$ m with $k = 6.37 \cdot 10^{-3}$ is less than 0.05% of the slope at $z = 0$ m (mean water level).

The CFD simulation is done on a 2D mesh with the domain specified according to the overall dimensions of the vessel. It shall be stressed that there is no vessel inside the numerical tank since the focus in this section is on simulations of the conditional wave. The size of the numerical tank is defined to be of the same size as if the vessel was included. That is, the wave-maker boundary (inlet) is located in the front (forward speed is 5 m/s, head seas) at about 2/3 L_{pp} from FP (forward perpendicular) and the outlet boundary is at approximately 1.4 L_{pp} from AP (aft perpendicular), see also Fig. 5.8. Wave reflections from the outlet boundary may not be so important in this particular case since the time to be simulated is relatively short. Nonetheless, a relaxation zone at the outlet is introduced with the overall dimension as sketched in Fig. 5.8.

The grid resolution in the vertical direction is $\Delta z = 0.5$ m making up to maximum 20 cells from crest to trough at the steepest location. In the horizontal direction, the grid is set to $\Delta x = 0.5$ m i.e. 75 cells for the shortest wave component (worst case) and almost 2000 cells for the longest wave component (best case). The amplitude of each harmonic is shown in Fig. 5.9. The peak frequency containing most of the energy is approximately $\omega_i = 0.4357$ rad/s (corresponded to freq. of encounter, $\omega_e \approx 0.5325$ rad/s) with a wavelength of 325 m. Thus, the spatial grid resolution used in the simulation can be considered sufficient for carrying the wave propagation over the presented length of the numerical tank.

The results of the CFD simulation show almost the same variation of the free surface profile with some differences in the magnitude. The local variations, as shown in Fig. 5.7a & b, indicate that the major differences occurs around the target time $t = 50$ s. Based on FORM and the nonlinear strip theory, this particular wave

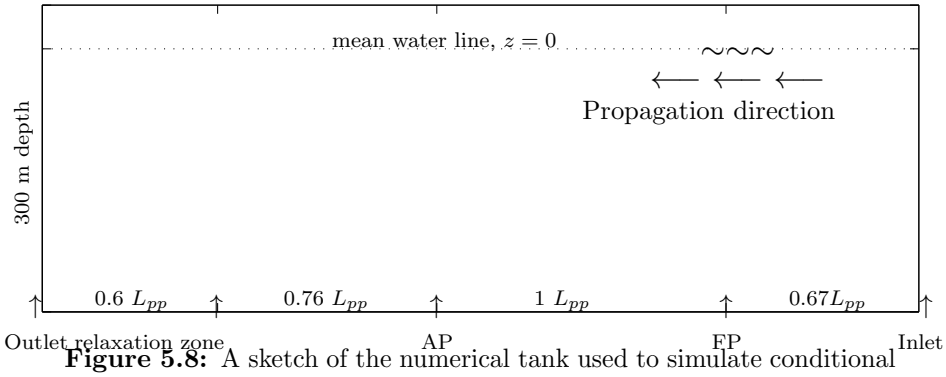

Figure 5.8: A sketch of the numerical tank used to simulate conditional wave presented in Fig. 5.7

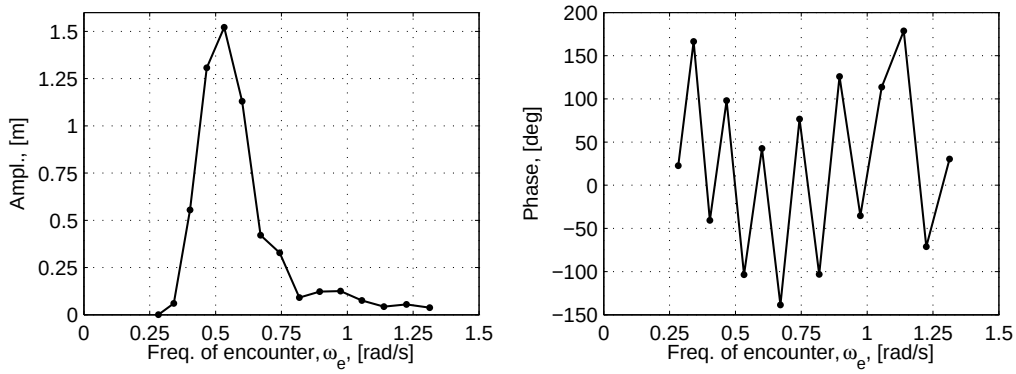

Figure 5.9: Amplitudes and phases of the harmonics of conditional wave presented in Fig. 5.7

scenario was derived conditionally on the response evaluated at the target time ($t = 50$ s). Beyond the target time, the results are of no interest. The fact that the CFD simulation produces a very similar free surface profile at the target time (see Fig. 5.7c and d) provides a strong suggestion that the responses evaluated by the analytical waves, Eq. (2.55), and by the CFD waves should not be very different. Further discussion and comparison of VBM in conditional waves can be found in Chapter 6.

One of the original attractions of the conditional wave is that it is much more realistic than a regular design wave. In this respect, the results of the CFD simulation are even more realistic than the input wave scenarios since the flow solution is fully nonlinear and the nonlinear wave-wave interaction is implicitly accounted for. Another motivation for using the conditional wave in the design is that it provides a reliability index associated with the wave scenario, which can be used to derive many useful statistical quantities, e.g. the probability of exceedance. An important question to ask is whether the reliability index is valid or not for the wave scenario produced by the CFD simulation. Indeed, there is no logical argument that the reliability index should remain unchanged for the same response level when using CFD. That is, if the CFD simulation had been applied directly in the FORM analysis to derive the conditional wave, the reliability index for the same conditional process would most likely be slightly different. However, under certain circumstances as discussed in Chapter 6 it may be possible to associate the reliability index to the new and more accurate response level evaluated by the CFD method. In this respect, the reliability index remains unchanged except that it is an approximation and valid for the new

response level.

5.3 Summary

The flow solution inside the numerical tank is solved for using the current VOF-based Navier-Stokes solver. Taking into account that the numerical wave tank is capable of accounting for nonlinear wave-wave interactions, as also shown in Jacobsen et al. (2012), it is reasonable to expect that the numerical wave tank can produce a sufficiently accurate wave. The potential wave solution is imposed at the wave-maker boundary. In the fluid domain possible unwanted spurious waves and local disturbances due to a mismatch between the potential flow solution and the solution of the VOF-based Navier-Stokes solver may arise. A mismatch in the distribution of the horizontal fluid particle velocity may exist not only in the numerical tank but also in the physical wave tank with a traditional piston-type or a flap-type wave generator. The action that may improve the result of the simulation is to use a high-order potential wave solution imposed at the wave-maker boundary.

Imposing the high-order potential wave solution directly at the wave maker boundary may introduce an accumulation of the volume of fluid due to the nonzero Stoke drift. The disturbance due to the accumulated water is not significant in an infinite depth wave but the effects seen in relatively shallow water cannot be neglected.

Moreover, while the usual errors related to numerical diffusion and dispersion are manageable the results of the numerical simulation may not be reliable when a complicated breaking of the free surface occurs before the evaluation of the responses at the target time.

Chapter 6

Slamming in Conditional Waves

A conditional wave is, here, defined as the most likely wave scenario causing the vessel to respond in a given manner. The conditional process can be an event or a response level. There are two major motivations for using a conditional wave in the design: (a) the wave scenario is realistic; (b) a probability value is associated with the response, which is useful in short-term extreme value statistical analysis. There are several statistical methods for estimating the conditional wave. A few of these methods are discussed in this chapter. The most straightforward, but also very resource demanding method, is the Monte Carlo Simulation (MCS). In this procedure, the statical properties of an event are evaluated directly by a direct random sampling. The random variables are generated according to the target distribution. Thus, MCS can be reasonably accurate and can be usefull for validation pusposes. The major drawback for MCS is that the method is usually associated with a huge computational cost. For an extreme event with a very small probability value, it is more efficient to apply other methods such as FORM (First-order Reliability Method). A review of the FORM analysis is given in Section 6.1. Several state-of-the-art techniques, which can be used to improve the efficiency of rare-event probability estimations, are given in Section 6.2.

A study of slamming events in conditional waves is presented in Section 6.3. Here, the ship is sailing in head seas and the motion is solved for under the assumption of rigid body motion constrained to two degrees-of-freedom, i.e. heave and pitch. Based on a time domain non-linear strip theory, the most probable conditional waves are generated to induce short-term extreme responses amidships VBM (vertical bending moment). Two particular vessels have been used in the study: a modern 9,400-TEU post-Panamax container ship and a Panamax container ship. The results of the strip theory are compared to the results of CFD simulations under the same wave conditions. On the Panamax ship with a moderate bow flare, there is no occurrence of slamming. The structural responses predicted by both methods agree well. On the post-Panamax ship with a larger bow flare, slamming events can be identified from the load distribution. In this case, the strip theory predicts VBM significantly larger than the CFD. However, the peak values of VBM occurs at approximately the same time, indicating that it may be possible to introduce a model correction factor to make the results of the strip theory as accurate as the CFD simulations.

The results may be valid only for these particular cases. Thus, the conclusion can not be generalized to all cases. Furthermore, it is not clear how to evaluate the responses conditionally on the occurrence of slamming, since it is required that the

nonlinear strip theory method must be able to predict the occurrence of slamming consistently with the prediction in the CFD simulation. This is proved challenging as illustrated in Section 6.3.2. Nevertheless, the implication is that it may be possible to introduce a rational correction coefficient making the results of the strip theory as accurate as the CFD results.

6.1 FORM & Probabilistic Design Considerations

Structural reliability analysis is an important engineering practice. If the strength of the structure is σ_s and the load is σ_l, a failure will occur when $\sigma_l > \sigma_s$. More generally a function known as the limit state function can be defined $G = \sigma_s - \sigma_l$ i.e. when the limit state function is less than zero failure will occur. The border line is $G = 0$. A classical approach is to apply a safety factor to the strength or load such that each failure mode have a constant and pre-deterministic safety factor. The safety factor may be set based on several uncertainties associated with the deterministic load and strength as well as the uncertainties covering the expected modelling accuracy and the consequences of the failure.

Nonetheless, the uncertainties in the load and strength have a statistical distribution and they are commonly assumed to be statistically independent. The distribution of the load and strength can be very different. The problem with the classical approach is that it does not provide a probability of failure. A better approach is to apply a statistical analysis to evaluate the probability of failure. Assuming that the marginal probability density function for load $p_l(\sigma_l)$ and for strength $p_s(\sigma_s)$ are known, the joint probability density function (JPDF) is simply the product between $p_l(\sigma_l)$ and $p_s(\sigma_s)$ (i.e. load and strength are statistically independent). The probability of failure can be evaluated from a convolution integral directly as (cf. Jensen (2001)),

$$P_f = Pr\{\sigma_s < \sigma_l\} = \int_{-\infty}^{\infty} \int_{-\infty}^{\sigma_l} p_s(\sigma_s) p_l(\sigma_l) d\sigma_s d\sigma_l \tag{6.1}$$

In general the probability of failure ($P_f \equiv Pr\{G(\underline{X}) < 0\}$) can be evaluated from the JPDF $p_{\underline{X}}(\underline{x})$ as,

$$P_f = Pr\{G(\underline{X}) < 0\} = \int\limits_{G(\underline{X})<0} p_{\underline{X}}(\underline{x})\, d\underline{x} \tag{6.2}$$

An analytical solution exists for P_f when the independent stochastic variables $\underline{x}$ are standard normal distributions, i.e. the JPDF is consequently also a normal distribution. The integration yields:

$$P_f = \int \ldots \int\limits_{G(\underline{X})<0} \prod_{i=1}^{n} \frac{1}{\sqrt{2\pi}} \exp\left(-\frac{x_i^2}{2}\right) dx_1 \ldots dx_n \tag{6.3}$$

or using the first-order approximation of the isosurface $G(\underline{X}) = 0$, the integral is simply

$$P_f = \Phi(-\beta) \tag{6.4}$$

where Φ is the cumulative probability distribution of the standard normal distribution function and β is the Hasofer and Lind safety index (1974) evaluated as the shortest distance from the origin to the surface of $G(\underline{X}) = 0$. If the mean value μ_G and the variance s_G^2 for the function $G(\underline{x})$ are known, the safety index β can be computed as $\beta = \mu_G / s_G$. In one dimension, the normal distribution is the well known Gaussian shape. In multiple dimensions, the shape of the normal distribution is not so easy to visualize.

It is far from always that the stochastic variables $\underline{x}$ are normally distributed. It is, however, possible to transform the real distribution of $\underline{x}$ to the standard normal distribution e.g. by using the Rosenblatt transformation technique (1952). Then, the first-order-reliability method (FORM) makes use of this analytical solution (see Eq. (6.4)) to approximate the probability integral, Eq. (6.2). According to the Gaussian shape of the JPDF $p_{\underline{X}}(\underline{x})$, the peak value of the probability is at the center. The further away from the center, the smaller the probability density becomes. Thus, the shortest distance symbolized by β also provides the most probable combination of the stochastic variables that would cause a failure ($G(\underline{X}) = 0$).

Within the reliability analysis, the problem can be stated as follows: Given a structural strength or a response level, what is the probability of failure? That is, we seek to estimate the probability of exceedance given a response level. Using the FORM analysis, the task can be summarized as follows:

1. Define the limit state function $G(\underline{X})$. The definition can be conditional on several stochastic variables.

2. Determine the probability density function of each basic stochastic variable. Make assumptions if necessary.

3. The stochastic variables must be independent and standard normal distributed. Perform a transformation, e.g. Rosenblatt (1952), if the dependency of the stochastic variables does not fulfill this requirement.

4. Search for a combination of the stochastic variables that provides β, the smallest distance to the failure surface, $G(\underline{X}) = 0$.

5. The isosurface $G(\underline{X}) = 0$ is linearized at the point corresponding to the β value found in the previous step. Thus, the probability of failure can be approximated by $P_f = \Phi(-\beta)$.

The Rosenblatt transformation in step 3 is often relatively computationally intensive. However, the most complicated task is the optimization task performed in step 4.

The accuracy of the FORM analysis depends on the behavior of the limit state function $G(\underline{X}) = 0$. If the failure surface is exactly represented by the linearization, the analytical probabilistic integral in FORM yields the exact value. If the linearization covers more than the actual failure surface, the integral yields a conservative results. The worst case, however, is when the failure surface $G(\underline{X}) = 0$ is ill-behaved

causing the FORM results to be non-conservative. A second order approximation of the failure surface known as SORM (Second-Order-Reliability-Method) has been developed in an attempt to improve the accuracy of the integral. For a SORM analysis, the total number of function evaluations in the optimization task (step 4) may increase by several orders of magnitude and the problems with an ill-behaved limit state function still exist. While SORM provides a better accuracy than FORM, it may suffer from numerical instability since the second derivative of the limit state function is required by the second order approximation and the optimization algorithm.

6.2 Critical Wave Episodes by FORM

Besides providing the probability of failure, the FORM analysis also provides the most central point, which is the most probable combination of the basic stochastic variables that causes a failure. Within the field of offshore and maritime engineering, FORM has been applied to generate the so-called most critical wave episode, see e.g. Jensen et al. (2011) and Jensen & Capul (2006). Using a first order stochastic wave, the free surface elevation as a function of position and time can be written as shown in Eq. (2.55). However, the FORM analysis prefers the following equivalent representation:

$$H(x,t) = \sum_{i=1}^{n} (u_i c_i + \bar{u}_i \bar{c}_i) \tag{6.5}$$

where

$$\begin{aligned} c_i &= c_i(x,t) = \sigma_i \cos(\omega_i t - k_i x) \\ \bar{c}_i &= \bar{c}_i(x,t) = -\sigma_i \sin(\omega_i t - k_i x) \end{aligned} \quad \Big| \quad \sigma_i^2 = S(\omega_i)\Delta\omega_i$$

The n discrete frequencies ω_i and wave spectrum $S(\omega_i)$ (e.g. PM-spectrum) are predetermined to cover the wave spectrum. The corresponding wave number for each individual harmonic is k_i. The stochastic variables are $\underline{u} = \{u_1, \bar{u}_1 \ldots, u_n, \bar{u}_n\}$ which represent the amplitude as well as the phase between each individual wave component. The distribution of these stochastic variables can be assumed independent and with standard normal distribution in agreement with $H(x,t)$ being a normal distribution. Thus, there is no need to carry out a complicated Rosenblatt transformation (Rosenblatt (1952)) to transform the distribution $\underline{u}$ into the standard unit normal space. This is why Eq. (6.5) is a better representation than Eq. (2.55). The stochastic variables can be applied directly in the limit state function defined as

$$G(\underline{u}) = \phi_0 - \phi(t_0|\underline{u}) \tag{6.6}$$

where the function ϕ represents the responses. When complicated and high non-linearity needs to be accounted for, the evaluation of the responses is commonly done in the time domain, which is why the construction of the limit state function is made on a target response level taken at time t_0. Considering a short-term stationary

response, the target time t_0 will have to be set sufficiently large to minimize the influence of memory effects caused by the initial conditions. In theory, ϕ can be a sophisticated CFD model. The huge demand on the computational power to carry out a CFD simulation, however, is the main barrier preventing the advanced CFD method from being applied directly in a statistical analysis.

It shall be noted that the particular construction presented in Eq. (6.5) and (6.6) has several desirable properties. Two interesting properties are pointed out in Jensen & Capul (2006) and Jensen et al. (2011). One of them is that the mean out-crossing rate $\nu(\phi_0)$ has an analytical expression derived from FORM depending only on the most central point $\{u_i^*, \bar{u}_i^*\}$ and the associated reliability index β_{FORM} (cf. Jensen & Capul (2006))

$$\nu(\phi_0) = \nu_0(\phi_0) e^{-(1/2)\beta^2_{\text{FORM}}} \tag{6.7}$$

where

$$\nu_0(\phi_0) \equiv \frac{1}{2\pi}\sqrt{\sum_{i=1}^{n}(\alpha_i^2 + \bar{\alpha}_i^2)\omega_i^2} \quad ; \quad \{\alpha_i, \bar{\alpha}_i\} = \frac{\{u_i^*, \bar{u}_i^*\}}{\beta_{\text{FORM}}}$$

The upcrossing $\nu(\phi_0)$ is the basic parameter in an extreme value assessment. The exceedance probability of each individual peak response can be evaluated from e.g. the Poisson model, cf. Jensen (2009),

$$Pr\{\max(R) < \phi_0 \,|\, 0 < t < T\} = \left(1 - \frac{T\nu(\phi_0)}{N}\right)^N \overset{(N\to\infty)}{\longrightarrow} e^{-\nu(\phi_0)T} \tag{6.8}$$

where $N = \nu(0)T$ is the number of peaks and T is the total time. Another important property is that a scaling of the wave spectrum $S(\omega)$, e.g. by a factor of γ^2, will directly change the most central point $\{u_i^*, \bar{u}_i^*\}$ and the associated reliability index β by a factor of $1/\gamma$, cf. Jensen (2011). The reason is that the first partial derivatives of ϕ which are acquired in the FORM linearization become solely dependent on the products $u_i c_i$ or $\bar{u}_i \bar{c}_i$ such that the relation between the scaled ($\hat{u}_i$) and un-scaled (u_i) stochastic variables is

$$\frac{\partial \phi}{\partial(u_i c_i)} = \frac{\partial \phi}{\partial(\hat{u}_i c_i \gamma)} \Rightarrow \hat{u}_i = \frac{u_i}{\gamma} \tag{6.9}$$

Consider the Pierson Moskowitz (PM) spectrum, the two parameter form is written as

$$S_{\text{PM}}(\omega) = H_s^2 \frac{4\pi^3}{T_z^4 \omega^5} \exp\left[-\frac{1}{\pi}\left(\frac{\omega T_z}{2\pi}\right)^{-4}\right] \tag{6.10}$$

which shows clearly that a scaling of $S(\omega)$ by a constant factor is equivalent to a scaling of H_s. Thus, applying FORM to the construction presented in Eqs. (6.5)

and (6.6) to any continuous linear or nonlinear response will yield a reliability index strictly inversely proportional to H_s (or to the square root of the intensity of the load spectra), i.e.

$$\beta \propto \frac{1}{H_s} \tag{6.11}$$

Only a single FORM analysis for one significant wave height is required to estimate the proportionality constant for a given T_z.

It shall be emphasized that FORM is only asymptotically correct. Nevertheless, Eq. (6.11) inspires Jensen (2011) to propose a functional form for the extrapolation of β estimated from more accurate Monte Carlo simulations (MCS). The proposed functional form is, cf. Jensen (2011)

$$\beta = \frac{c}{\gamma} + a\gamma^b \tag{6.12}$$

Thereby, the coefficients a, b, and c are to be determined from at least three sets of Monte Carlo simulations for an increased intensity of $S(\omega)$, i.e. $\gamma > 1$ and the reliability index relevant for the design is obtained through an extrapolation toward $\gamma = 1$. The examples presented in Jensen (2011) show that the assumed functional form, Eq. (6.12), applied with the definition of the limit state function shown in Eqs. (6.5) and (6.6), can provide an accurate scaling of the reliability index.

While the FORM analysis is known for its efficiency, the MCS is known for its accuracy. As discussed in Bjerager (1991), the two methods are considered complementary to each other. One way to evaluate the accuracy of FORM or SORM is to make a comparison with the results of Monte Carlo Simulations (MCS). Applying the MCS is straightforward. Each basic stochastic variable is chosen randomly according to their probability distribution and the function $G(\underline{X})$ is evaluated. The number of failures N_f is registered and counted against the total number of simulations N. The probability of failure can be evaluated directly as

$$(P_f)_{MCS} = \frac{N_f}{N} \tag{6.13}$$

Here, each of these N simulations cover a pre-selected time interval, e.g. 3 hours, which implies that $(P_f)_{MCS}$ is the probability that a failure occurs in this time interval. The statistical property will become sufficiently accurate, if the number of failures is large enough. The error in the MCS can be estimated from (see e.g. Melchers (1999))

$$Pr\left\{-\epsilon < (P_f)_{MCS} - P_f < \epsilon\right\} = c \quad \Big| \quad \epsilon = k_c\sqrt{\frac{1-P_f}{NP_f}} \tag{6.14}$$

where c and k_c are, respectively, the confidence level and the corresponding percentile value. In the formula, P_f is the expected true probability of failure. Assuming a normal distribution with a confidence level of 95%, the percentile is $k_{95\%} = 1.96$. If the target error is set to 5%, the number of simulations required is

$$N = \frac{1 - P_f}{P_f(5\%/1.96)^2} \tag{6.15}$$

In practical engineering problems, P_f is in the order of 10^{-4}. Thus, the required number of trials is $N = O(10^7)$ and the expected number of failures $N_f = O(10^3)$. Even if the error is relaxed to $\epsilon = 20\%$, the required number of trials is still in the order of $N = O(10^6)$ and $N_f = O(10^2)$.

Equation (6.15) shows clearly that the computational cost grows directly with $1/P_f$, i.e. the smaller probability value, the more expensive it is. This explains why the requirement for the computational power is usually very large; especially for a very low probability of failure.

When it comes to estimating the probability of an extreme and rare event, the FORM analysis is far more efficient in terms of computational power. There is, however, a technique known as importance sampling to improve the performance of MCS. The probability density function (PDF) is either scaled or shifted artificially to increase the failure count. Improper used of the technique, on the other hand, may yield a biased result. The results of the MCS will need to be weighted properly in order to obtain an unbiased estimate. While the importance sampling technique may reduce the simulation time considerably, the method is not always applicable since a prior knowledge about the failure modes is required in order to scale or translate the PDF to obtain a better coverage of the failure region.

The inefficiency of the MCS for small probabilities has been recognized for a long time. Recent efforts on improving the estimation of the probability integral for small probability values are presented in Naess et al. (2009), Bucher (2009), Jensen (2011) and Nishijima et al. (2010). The approach is to apply an extrapolation method where the MCS are performed on several scalings of the probability integral and the results are extrapolated using an assumed functional form of the integral. The scaling parameters are chosen in such a way that the evaluation of the scaled probability integral can be done efficiently using the MCS.

The most difficult part is to determine a valid functional form for the extrapolation. As pointed out by Nishijima et al. (2010) there is no easy way to check the validity of the assumed functional form in the general case. However, the result of the FORM analysis is asymptotically correct for very small probability, and so are the functional forms proposed by Naess et al. (2009), Bucher (2009) and Jensen (2011). The asymptotic expression for the integral is

$$P_f(\lambda) = a_\infty \prod_{i=1}^{K} \Phi(-c_i\lambda) \quad \text{for} \quad \lambda \to \infty \tag{6.16}$$

where K is the total number of failure modes; a_∞ is a constant coefficient and c_i are any set of constants satisfying $\sum_{i=1}^{K} c_i^2 = |\underline{u}_n^*|^2$ with $\underline{u}_n^* = (u_1^*, \ldots, u_n^*)$ being the most central point $|\underline{u}_n^*| = \min_{\underline{u}_n \in D} |\underline{u}_n|$ assuming only one central point exists for each failure mode. In the expression, λ is the dimensionless scaling parameter, which relates to the reliability index as $\beta_i = c_i\lambda$. The target of the extrapolation, $\lambda = 1$, provides the actual unscaled probability of failure. Since Eq. (6.16) is valid only for $\lambda \to \infty$, Nishijima et al. (2010) proposed an approximation to be used when $\lambda = O(1)$, cf. Nishijima et al. (2010),

$$P_f(\lambda) = a(\lambda) \prod_{i=1}^{K} \Phi(-c_i \lambda) \quad \text{where} \quad a(\lambda) \approx a_\infty \frac{1 - b_1 \exp(-b_2 \lambda^2)}{1 - b_3 \exp(-b_4 \lambda^2)} \tag{6.17}$$

The parameters $(a_\infty, b_1, b_2, b_3, b_4, c_1, \ldots, c_K)$ are to be determined from a curve fitting on the results of the MCS for several values of λ. Several examples provided in Nishijima et al. (2010) have shown that this approximation provides reasonably accurate results. Equation (6.17) is intended to be applied to extrapolate the results of scaled MCS. There are still several minor issues, which need to be resolved. These are e.g. the number of points required for the fitting process and the range of λ suitable for generating these points. In a comparison to direct Monte Carlo simulations, the reduction of the required number of simulation is significant. However, compared to FORM, Eq. (6.17) requires far more simulations. Hence, depending on the problems being addressed, the improved accuracy obtained from Eq. (6.17) may not be worth the effort.

6.3 FORM & Slamming on Ships

There are several means to evaluate the slamming load and the hull girder whipping effects. The current free surface CFD method, by which a VOF-based incompressible NS solver is fully coupled with a Timoshenko beam model, is considered the most realistic and accurate method. One of the major issues is the huge demand on the CPU time. A typical performance for a highly optimized CFD code is one hour for every simulated second running in parallel mode using 64 cores of a modern HPC (high-performance computing) cluster. In the following, the CFD code applied in the present study will be referred to as OpenFOAM. The main objective is to determine short-term and long-term statistical properties of the extreme responses caused by slamming and whipping.

Applying OpenFOAM directly in a statistical analysis such as MCS or FORM is not practical. One of the alternatives is to use a non-linear time domain strip theory. The strip theory is faster but less accurate than the CFD method. The strip theory model used here is an in house software called Shipstar, see e.g. Xia et al. (1998). Shipstar is very efficient and demands very little CPU time and thus is suitable to be applied in FORM or MCS. A possible approach to transfer the statistical properties from Shipstar to OpenFOAM will be discussed below. The idea is to use Shipstar to generate a critical wave episode by FORM or MCS as described in the previous section. Thereafter, a more advanced and accurate CFD simulation (OpenFOAM) is done on the critical wave scenario. If the target responses predicted by the two methods have similar features but only different magnitudes, the statistical properties can be transferred to OpenFOAM by means of a model-correction factor approach, see e.g. Ditlevsen & Arnbjerg-Nielsen (1994) and Garré et al. (2006).

The formulation applied in Ditlevsen & Arnbjerg-Nielsen (1994) can be stated as follows:

$$\begin{aligned} \phi_{\text{ADV}}(t_0 \,|\, \underline{\mathrm{u}}) &= c(\underline{\mathrm{u}}) \phi_{\text{SIM}}(t_0 \,|\, \underline{\mathrm{u}}) \\ \Rightarrow \quad G(\underline{\mathrm{u}}) &= \phi_0 - \phi_{\text{ADV}}(t_0 \,|\, \underline{\mathrm{u}}) \end{aligned} \tag{6.18}$$

$$\Rightarrow \quad G(\underline{u}) = \phi_0 - c(\underline{u})\phi_{\text{SIM}}(t_0 \,|\, \underline{u}) \tag{6.19}$$

where the subscripts SIM denotes the simplified but fast method suitable for FORM or MCS analysis. The subscript ADV denotes the more advanced and realistic method but too computationally intensive for a direct statistical analysis. The coefficient $c(\underline{u})$ is the correction factor introduced in the equations to calibrate the results of the simplified model to be as accurate as the advanced model. It should be sufficient to estimate the value of $c(\underline{u})$ at the most probable point, since the intention is to make the simplified model accurate only around this point. Several iterations may be required to determine $c(\underline{u})$ and hopefully only a very few iterations are required. Within each iteration, the evaluation of $\phi_{\text{ADV}}(t_0 \,|\, \underline{u})$ can be done once or several times depending on the applied iteration scheme. The iteration procedure can be constructed as follows:

1. Initially set $c(\underline{u}) = 1$
2. Evaluate the most central point using FORM/MCS with Eq. (6.19)
3. Apply the most central point in $\phi_{\text{ADV}}(t_0 \,|\, \underline{u})$ and update $c(\underline{u})$ using Eq. (6.18)
4. Repeat step 2 until convergence of β

Garré et al. (2006) presented a few examples and the iteration converges very fast with only a few evaluations of $\phi_{\text{ADV}}(t_0 \,|\, \underline{u})$. However, in their examples, $\underline{u}$ contains less than ten elements which is considerably smaller than the number of stochastic variables in the conditional wave. It has not yet been shown that the method presented in Garré et al. (2006) scales well with the size of the problem. Therefore, the iteration scheme may not be feasible.

As an alternative to this iteration scheme, we propose to estimate the reliability index (β) through an interpolation scheme. The final target is not $c(\underline{u})$ but β. First, the simplified method is used to generate β for several limit state functions:

$$\begin{array}{rcll} G_1(\underline{u}_1) & = & (\phi_1)_{\text{SIM}} - \phi_{\text{SIM}}(t_0 \,|\, \underline{u}_1) & \rightarrow \ \beta_1 \\ G_2(\underline{u}_2) & = & (\phi_2)_{\text{SIM}} - \phi_{\text{SIM}}(t_0 \,|\, \underline{u}_2) & \rightarrow \ \beta_2 \\ \ldots & = & \ldots & \\ G_i(\underline{u}_i) & = & (\phi_i)_{\text{SIM}} - \phi_{\text{SIM}}(t_0 \,|\, \underline{u}_i) & \rightarrow \ \beta_i \end{array} \tag{6.20}$$

The choice of $\phi_1, \phi_2, ..., \phi_i$ ($i \in N$) should not be too far from target response, ϕ_0, since the results will be used as the basis for the interpolation. The step shown in Eq. (6.20) provides several central points, i.e. $\underline{u}_1, \underline{u}_2, ..., \underline{u}_i$, which are used in the second step to evaluate the responses more accurately using the advanced method. Each central point and its β value are associated with a more accurate response predicted by the advanced CFD model. Hence,

$$\begin{array}{rcrcl} \beta_1 & \rightarrow & \phi_{\text{ADV}}(t_0 \,|\, \underline{u}_1) & = & (\phi_1)_{\text{ADV}} \\ \beta_2 & \rightarrow & \phi_{\text{ADV}}(t_0 \,|\, \underline{u}_2) & = & (\phi_2)_{\text{ADV}} \\ & & \ldots & = & \ldots \\ \beta_i & \rightarrow & \phi_{\text{ADV}}(t_0 \,|\, \underline{u}_i) & = & (\phi_i)_{\text{ADV}} \end{array} \tag{6.21}$$

Finally, the reliability index for the target response can be interpolated from a set of $\{\beta_i, (\phi_i)_{\text{ADV}}\}$ selected from Eq. (6.21). Using this interpolation scheme, possible

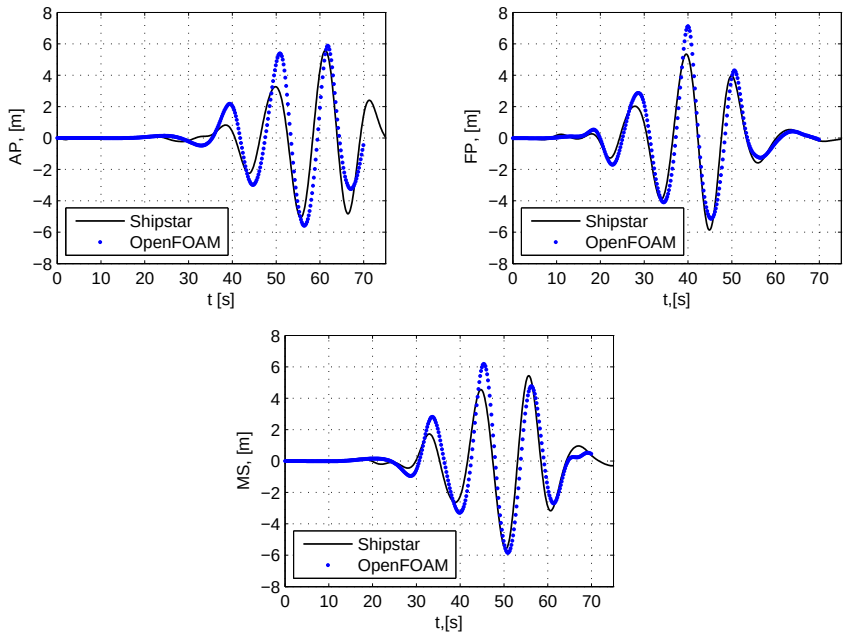

Figure 6.1: Free surface elevation at aft perpendicular (AP), forward perpendicular (FP) and midships (MS)

convergence problems, which may exist in the iteration scheme, can be avoided. In Eq. (6.21), however, it is stated implicitly that β_i can be transferred directly from Eq. (6.20). Indeed, this statement is a fundamental assumption of the present interpolating scheme. Therefore, it is important to ensure that this assumption is valid. One of the possible issues, which can cause this assumption to be invalid, is related to the ability of the simplified model to capture all the relevant physics in slamming. Consequently, the responses cannot be conditioned on slamming easily. A discussion based on two case studies is given in Sections 6.3.1 and 6.3.2.

6.3.1 A Panamax Container Ship (KCS)

Using a stochastic sea defined in Eq. (6.5) with $H_s = 10$ m and $T_z = 10.44$ s the target response level (vertical bending moment amidships) is set to 3000 MNm for a Panamax ship with a moderate bow flare. The ship is a modified version of the so-called KRISO Container Ship (KCS) where the middle block was extended by 40 m making the overall length to be 270 m in total. The target response is evaluated at $t_0 = 50$ s, which is long enough to overcome any significant memory effect of the initial conditions in the fluid domain, loads, and responses. These initial conditions, especially the initial flow in the fluid domain, can be highly random. Thus, the initial start-up time of $t_0 = 50$ is considered essential for the assumption that the short-term responses are evaluated in an approximate stationary sea state. The PM-spectrum is modelled with 15 discrete wave frequencies ranging from 0.25 to 0.9 $[rad/s]$ covering most of the significant wave spectrum.

Figure 6.1 shows the most probable wave generated using Shipstar coupled with a FORM code (PROBAN). The reliability index for the event is $\beta = 2.7532$ corresponding to a return period of approximately 10 minutes in a stationary sea state and operational condition. The same most probable wave is applied in simulations using the current CFD method (OpenFOAM). In a comparison to Shipstar, where

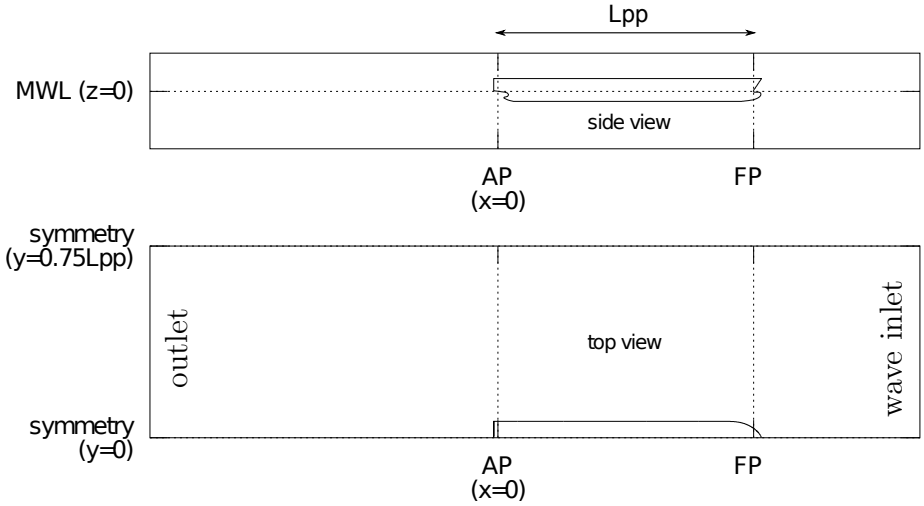

Figure 6.2: A sketch of the computational domain

the wave fields are directly defined everywhere by Eq. (6.5), the wave simulation in OpenFOAM is done by solving the nonlinear Navier-Stokes (NS) equations directly and therefore, accounts implicitly for nonlinear effects as well as nonlinear wave-wave interactions. Equation (6.5) is used in OpenFOAM only to prescribe wave condition at the inlet boundary.

There are potential problems related to numerical diffusion and reflection from outlet boundaries, causing the quality of the OpenFOAM results to depend strongly on the user's experience. A discussion on wave generations has been given in Chapter 5, and more specifically on conditional waves in Section 5.2. Most importantly, when the CFD model is applied, the generated waves in the numerical wave tank are more accurate and realistic than those applied in the simplified nonlinear strip theory (Shipstar). For the current configuration of the conditional wave, the differences of wave fields applied in Shipstar and predicted in OpenFOAM can be seen in Fig. 6.1.

The wave simulation presented in Fig. 6.1 is in two dimensions. With the presence of the vessel inside the wave tank, the simulation needs to be done in a three-dimensional space. To reduce the computational cost, the symmetric hull is exploited, and only its port side of the symmetry plane is included in the numerical model. That is, the flow is assumed symmetric about the vertical longitudinal center plane.

Figure 6.2 shows a sketch of the computational domain and the applied boundary conditions. The sea bed is assumed flat and the water depth is 75 m. Waves are propagated into the domain through the inlet boundary located approximately $0.5L_{pp}$ in front of FP. The total length of the computational domain is about $3L_{pp}$. Relaxation zones (see Chapter 5) and grid stretching have been applied to minimize wave reflection from boundaries. The finite volume meshes are generated using a split unstructured hexagonal mesh generator, "snappyHexMesh", provided by the OpenFOAM package. The grid is stretched toward the mean water level (MWL) to obtain a sufficient grid resolution near the free-surface. A refinement has been made within the free-surface zone in front of FP to let the head sea waves propagate accurately on to the ship yielding a horizontal grid spacing of approximately

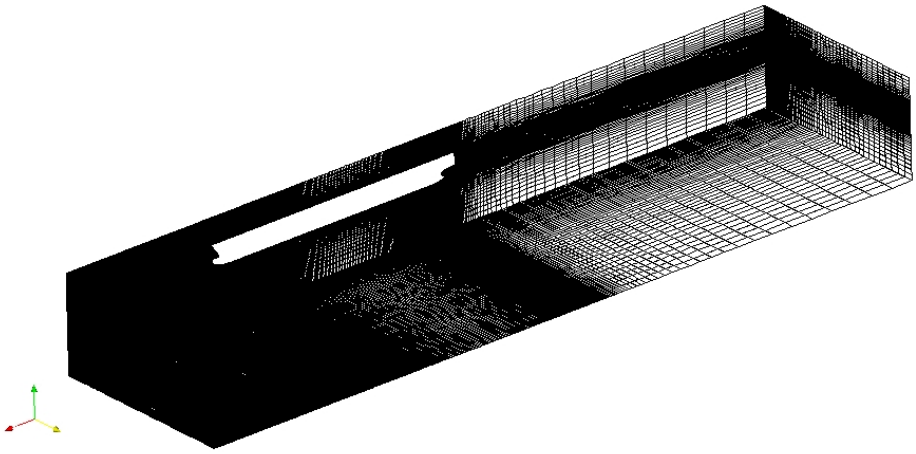

(a) Surface grid on the boundaries of the domain

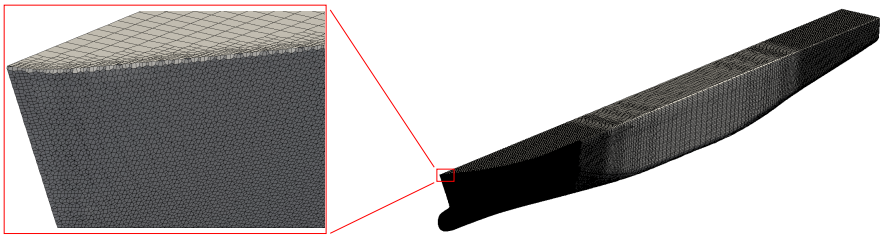

(b) Surface grid on the hull

Figure 6.3: An example of the applied grid configuration (4.1 millions cells). The grid is refined near the free surface, in the wave propagation region, and around the slamming areas on the ship (stern & bow flare)

1 m. Around the aft and forward part of the ship the grid is refined aiming at a characteristic cell size similar to the three-dimensional drop test presented in Section 4.6. In other words, the finite volume cells are clustered significantly around the areas, which are exposed to slamming. The refined grid is suitable for an accurate prediction of slamming loads. The grid configuration with a total 4.1 millions cells is shown in Fig. 6.3.

Figure 6.4 shows VBM amidships corresponding to the most probable wave evaluated within the assumption of a rigid hull. As expected, Shipstar predicts the target response level $\phi_0 = 3000\,\mathrm{MNm}$ at the target time $t_0 = 50\,s$. The more realistic results by OpenFOAM have a slightly different time variation of the responses mostly due the differences between the incoming potential wave and the more realitic CFD simulated wave. Most interestingly, the response at the target time is almost the same as predicted by Shipstar. Thus, for this particular case Shipstar is capable of capturing most of the relevant physics in a wave-induced response problem and the results are directly comparable to the more advanced and realistic CFD method. The model-correction factor evaluated as outlined in Section 6.3 is close to 1 in this example. These results may not be surprising since the strip theory is known to be feasible for predicting ship responses in waves.

Without considering the contribution from slamming induced responses the reliability index β can be transferred to the CFD model providing a reasonable

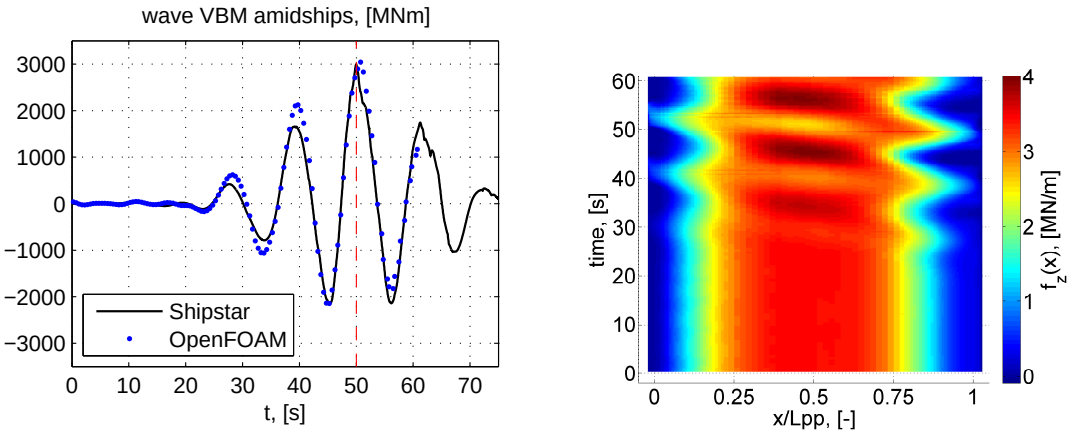

(a) VBM amidships (b) Vertical force

Figure 6.4: VBM amidships on KCS ship (a) and the distribution of the vertical force (b). $H_s = 10\,m$, $T_z = 10.44\,s$, $\phi_0 = 3000$ MNm (sagging VBM) evaluated at target time $t_0 = 50$ s, $\beta = 2.7532$ (corresponded to 10 min. return period)

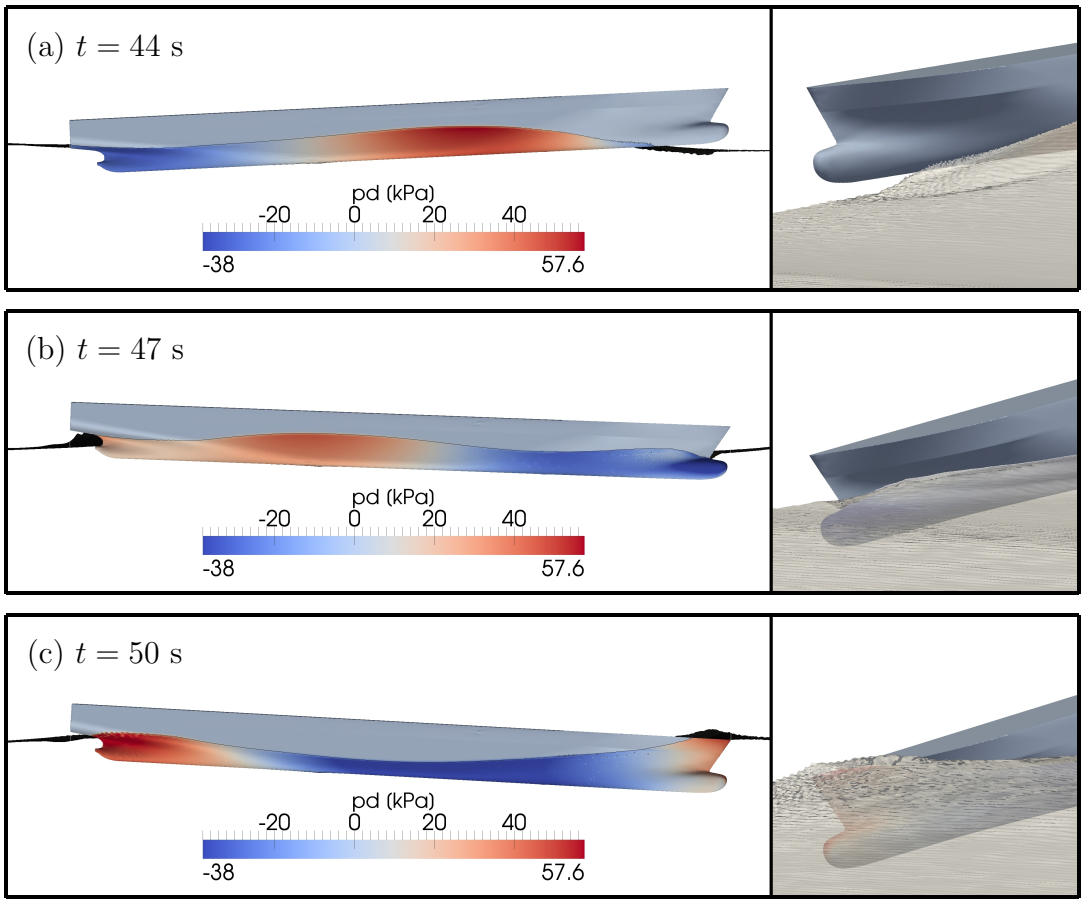

Figure 6.5: Snapshots of the free surface elevation at three different time instants. Colors on the hull show the excess pressure in [kPa]

approximation of the probability value for the CFD results. However, the main interest is how the slamming-induced responses contribute to the extreme value of the vertical bending moment amidships. A closer look at the CFD results reveals that there is no occurrence of severe slamming in the applied wave scenario. This can be confirmed since there is no rapidly increase of vertical forces on the forward and aft part of the ship, see Fig. 6.4b. Several snapshots of the free surface are shown in Fig. 6.5. The forward bottom emerges from the free surface (Fig. 6.5a) at $t = 44$ s, which corresponds to the first peak of the hogging moment seen in the VBM amidships. The re-entry of the bulb occurs smoothly because the forward bottom is relatively sharp and the flare angle is relative small (Fig. 6.5b). Nevertheless, the bow flare penetrates the free surface deeply enough to initiate water-on-deck at $t = 50$ s (Fig. 6.5c).

The occurrence of slamming may depend strongly on many variables e.g. ship motion, wave steepness and the relative encounter velocity. The formulation of the limit state function will need to be conditional on whether slamming occurred at t_s where $0 < t_s < t_0$. The actual value of t_s may not be important in this context as long as the memory effect of slamming induced responses exists at the target time, t_0.

A possible way to include slamming in the formulation of the limit state function is to correlate slamming events to the relative wave steepness. However, this approach has not yet been proved feasible. Nevertheless, Shipstar may have difficulty in detecting correctly whether slamming occurs or not within the time interval $0 \sim t_0$. In such a case, the FORM algorithm will converge to a biased most probable point if the occurrence of slamming is conditionally stated in the limit state function. The slamming prediction problem is illustrated in Sec. 6.3.2 using a Post-Panamax ship with a larger bow flare.

In addition, it is important that Shipstar can account for all relevant physical phenomena related to slamming. For example, wave breaking, which is considered a significant parameter in bow flare slamming problems, cannot be modelled reliably in Shipstar. Thus, the results of the present FORM analysis will most likely never converge to a central point where wave breaking is the major cause of the severe impact load. On the other hand, wave simulations with complicated break-up of the free surface is still a big challenge using the current CFD method.

Assuming that Shipstar can overcome the above mentioned problems, the conditioning on slamming will most likely cause the limit state function to be ill-behaved. The conditioning on the occurrence of slamming is problematic due to the on/off nature of the problems. The corresponding limit state surface does not necessarily have well defined boundaries. The failure regions can easily be composed of several "islands", i.e. a union or intersection between many small regions. Clearly, further investigation is required in order to make a conclusive statement on this issue, which can be very important regarding the feasibility of applying FORM/MCS on slamming problems.

6.3.2 A Post-Panamax Container Ship

Similar to the case shown previously in Section 6.3.1, critical wave episodes are generated for a 9400 TEU Post-Panamax ship. Compared to the KCS (the previous ship) the current Post-Panamax ship has a considerably larger bow flare making it

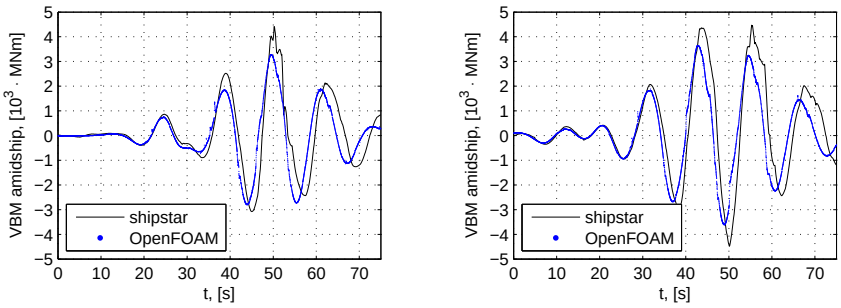

(a) Sag (b) Hog

Figure 6.6: VBM amidships on a post-Panamax ship. Target sagging/hogging VBM $\phi_0 = 4500\,\text{MNm}$ evaluated at $t = 50$ s.

more susceptible to bow flare slamming. The PM-spectrum is applied with $H_s = 10\,m$ and $T_z = 10.44\,s$ and the same range of discrete frequencies (ω_i) as used in Section 6.3.1. The target response level is set to $\phi_0 = 4500\,\text{MNm}$ and two cases are considered: one in sag and one in hog. In both methods (OpenFOAM and Shipstar), the hull girder is assumed rigid.

The responses predicted by OpenFOAM and Shipstar are shown in Fig. 6.6. Similar overall results can be seen. That is, the time variation in the responses are slightly different between OpenFOAM and Shipstar, but the peak responses occur approximately at the same time. Compared to the previous case the interesting feature here is that OpenFOAM predicts a lower peak response at the target time $t_0 = 50\,s$. If the model correction factor method is to be applied the correction coefficient will be approximately $0.72 \sim 0.78$.

Around the target time ($t = 50$ s), Shipstar predicts a sharply rising VBM, see Fig. 6.6a, which can be explained by the way the slamming load is evaluated in Shipstar. The sectional hydrodynamic forces are estimated on the instantaneous wetted surface under the undisturbed incident wave elevation. The formulation, see Xia et al. (1998), is based on the classical strip theory (Salvesen et al. (1970)), but modified to include a non-linear Froude-Krylov force and a non-linear memory function modelled in terms of a set of high-order differential equations. Most importantly, the slamming load is included in the sectional hydrodynamic force in terms of changes in added mass at infinite frequency. The slamming contribution is written (cf. Xia et al. (1998)),

$$F_{slam}(x,t) = -\frac{\partial \bar{m}}{\partial \bar{z}} \left(\frac{\mathrm{D}\bar{z}}{\mathrm{D}t} \right)^2 \tag{6.22}$$

where $\bar{z} = w - x\theta - \kappa\eta$ is the relative vertical motion and w, θ, and η are heave, pitch and the undisturbed wave elevation, respectively. The expression $\mathrm{D}(\cdot)/\mathrm{D}t = \partial(\cdot)/\partial t - U\partial(\cdot)/\partial x$ is the total derivative taking into account the forward speed of the vessel. It has yet to be quantified whether this formulation is capable of predicting not only the appropriate slamming load but also the occurrence of slamming reliably. The formulation is based on a momentum slamming model. The slamming force is included in sectional loads continuously. Thus, there is no need to introduce a triggering mechanism, e.g. a threshold velocity, to activate the slamming calculation explicitly. This formulation depends strongly the added mass $\bar{m}$ evaluated on each

segment of the strip theory. A large vertical motion will result in a rapid change in added mass; thereby a large slamming force on the segment. It is well known that slamming loads estimated in 2D are too conservative (see Section 4.6). The segmented (2D) evaluations over predict the contribution from the momentum slamming and may require an empirical correction to account for the three-dimensional effects.

Initially, the VBM predicted by both methods agree well until approximately $t \approx 35$ s. During these start up periods, the waves around the ship are still small. Therefore, it can be expected that the agreement is good between the results of the strip theory and the CFD. Beyond 35 s, waves are severe enough to induce bow flare slamming on the post-Panamax container ship. Due to the assumption of rigid hull, and the use of the momentum slamming formulation, it is difficult to identify explicit indicators of slamming events from the results of the non-linear strip theory. To some extent, one may guess the occurrence of slamming from steep slopes of VBM curves. In CFD simulations, however, the occurence of slamming can be identified by examining the high-resolution load distribution in the time domain. As seen in Figs. 6.7 and 6.8, the vertical forces on the bow regions rise sharply once in the sagging case and twice in hogging case. In the hogging case, slamming occurs first at time $t \approx 40$ s and a second time at $t \approx 50.1$ s. The duration of slamming can be identified from the force distribution taken at a longitudinal position about 10 % from the fore ship, see Fig. 6.8. The rise time of the vertical forces for both slamming occurences is less than 0.2 s. Due to the rigid body assumption, whipping responses usually seen in VBM do not occur. Instead VBM changes rapidly in the short slamming periods. This observation supports that, theoretically, there is no delay in the structural response when the hull is assumed rigid. An excitation imposed locally on the hull will induce a response on the whole structure instantaneously.

A similar bow flare slamming occurs in the sagging case at $t \approx 46$ s. In all three occurrences, the amidships VBM show that the ship is in a transition from a hogging condition to a sagging condition. The occurrence of bow flare slamming contributes to a larger acceleration of the transitions. Interestingly, the slamming impacts occur when the ship has had a peak hogging response, i.e. the wave crest in head sea has moved beyond the midships section and placed the wave trough at the fore part of the ship. A subsequent impact at the bow flare does not cause peak VBM responses. When taking into account the flexibility of the hull girder, a more realistic transient vibration behaviour in VBM may show that bow flare slamming occured at this time instant actually contributes to a larger peak response several seconds after the impact.

Between the results of the strip theory and the CFD, it is difficult to evaluate whether or not the difference in the target VBM responses (at $t = 50$ s) are caused by slamming. Using the rise-time as an indicator for the results of Shipstar does not seem to be practical. There is a strong indication that Shipstar can not predict the occurrence of slamming reliably. Further evaluation is necessary before drawing conclusions on this issue. In addition, the flexibility of the hull girder shall be accounted for in future investigations. Nevertheless, the results presented in this section illustrate the problems of formulating the limit state function to be conditional on slamming while using a simplified model that cannot evaluate the correct conditional state reliably.

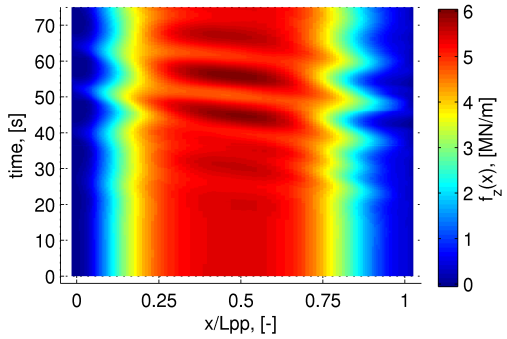

(a) Vertical force (Sag)

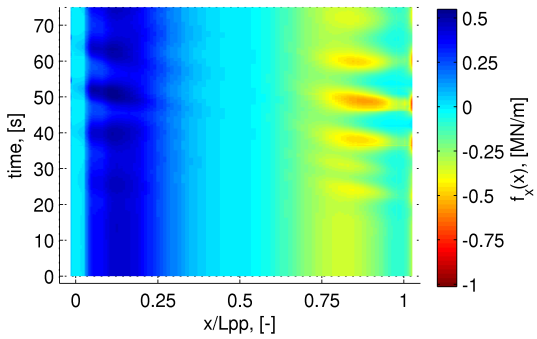

(A) Longitudinal force (Sag)

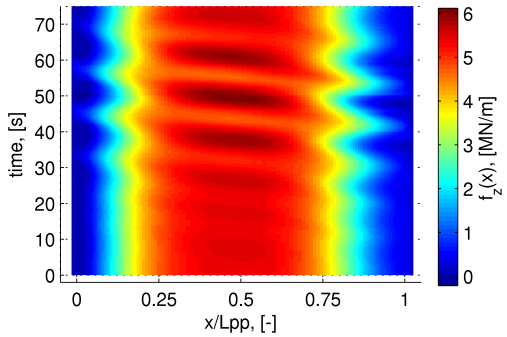

(b) Vertical force (Hog)

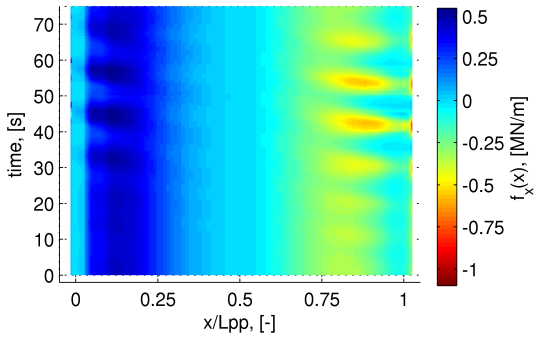

(B) Longitudinal force (Hog)

Figure 6.7: Longitudinal force distribution

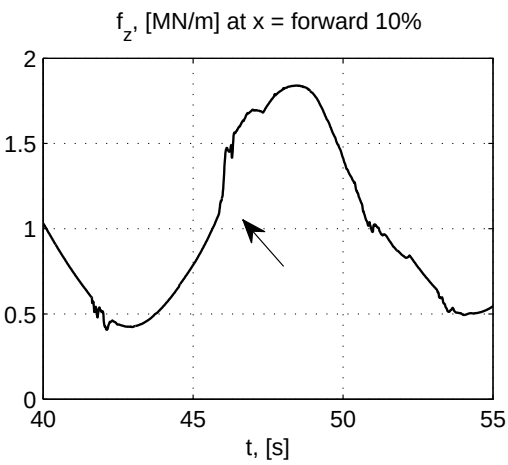

(a) Sag

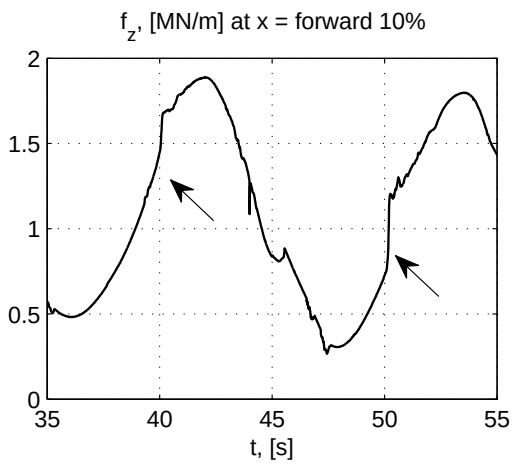

(b) Hog

Figure 6.8: Slamming is identified on rapidly rising forces (arrows)

6.4 Summary

Using the CFD results in a short-term statistical analysis is still very impractical because of the huge CPU requirement. However, the investigation presented in this Chapter shows that it may be possible to use a Model Correction Factor (MCF) approach to attach useful statistical estimates to the CFD results. In short, a very fast but simplified model is applied in the statistical analysis estimating the most probable wave scenario leading to a prescribed event. Using the CFD method, the responses are evaluated more accurately under the same wave scenario. That is, the statistical properties associated with the wave scenario may be transferred from the simplified model to the CFD results with the assumption that the simplified model has captured most of the relevant physics of the flow. Thereby, the evaluation of the target responses can be made as accurate as the CFD results using mainly a correction factor (hence the term Model Correction Factor). The CFD simulations can be limited to a few selected cases leaving the repeated statistical trials (FORM or MCS) to the fast and simplified model.

The initial investigation on the MCF approach is done under the assumption of a rigid hull focusing on responses of amidships VBM. Similar results for the CFD and the nonlinear strip theory have been found for the Panamax container ship. The time history of the responses shows the same predicted behavior in the two methods. At the target time, the responses are almost the same. There is no sign of slamming in the CFD results indicating that the strip theory results have captured most of the important effects that may have an influence on the amidships VBM. In this particular case, the statistical properties can be transferred directly to the CFD results.

For the post-Panamax ship with a large flare angle, there are larger differences in the response level at the target time. The variational trends of the responses are similar in both methods with peak responses occurring almost at the same time. The significant differences are mainly in the magnitude of the responses where the CFD method predicts responses at the target time approximately 20% $\sim$ 30% smaller the predictions of the nonlinear strip theory. Furthermore, the CFD results show several slamming events occurred prior to the target time.

In the current investigation, it cannot be quantified conclusively if the differences are caused by the contributions from slamming. One of the reasons is that the hull is considered rigid, but the most important observation is that the strip theory cannot provide a clear indication on the occurrence of slamming making it very challenging to include slamming in the conditional evaluation of the limit state function for VBM. In the CFD method, the slamming loads are implicitly accounted for. The simplified model must be able to account for slamming in a similar and consistent way in order to apply the MCF approach where the responses are evaluated conditional on the occurrence of slamming.

Finally, the flexibility of the hull girder should be accounted for in order to introduce the contribution of the slamming-induced whipping in the amidships VBM. In addition to the rigid body ship motion, the structural flexibility of the hull girder initiates more complicate fluid-structure interactions usually referred to as hydroelastic problems. This is the topic of the next chapter.

Chapter 7

Hydroelasticity in Slamming

One of the structural responses induced by slamming on ships is the transient vibration of the hull girder known as whipping. During the vibration, the elastic structure of the hull girder creates a flexible fluid-structure-interaction (FSI), where the deformation of the structure affects the surrounding fluid. Vice versa, any change in the fluid surrounding the flexible structure has an effect on the structural response creating a tightly coupled FSI. This interaction is described using a general term called hydroelasticity. Hence, whipping due to slamming excitations is a specific branch of hydroelasticity concerning the large-scale hull girder vibration.

In the present work, the structural response is modelled by a non-uniform Timoshenko beam. Therefore, the natural frequency of the hull-girder vibration is strictly limited to the vertical bending modes. A hydroelastic coupling between the classical Timoshenko beam theory and a strip theory or a potential flow solver (e.g. a BEM code) has been presented in many publications (see Xia et al. (1998) and Tuitman & Malenica (2009)) with the slamming load evaluated explicitly on 2D stations for practical reasons. Several researchers have moved one step further to investigate the hydroelastic effect in water-entry problems with slamming loads evaluated implicitly using a free surface CFD method, e.g. based on level set, VOF or marker-and-cell techniques. Often, the numerical results are only presented for two-dimensional hydroelastic problems due to the huge requirement of CPU time.

In this chapter, three-dimensional numerical results of hydroelastic simulations are presented with slamming loads evaluated implicitly using the current VOF-based NS flow solver. The results of simulations done at full scale are compared with scaled model tests for the purposes of validating the current numerical coupling between the Timoshenko beam solver and the VOF-based Navier-Stokes solver. Section 7.1 provides a description of the experiment, which was done in a towing tank at CEHIPAR, an independent public research center in Spain (Canal de Experimencias Hidrodinámicas de El Pardo).

The hydroelastic simulations are performed for a 9400 TEU post-Panamax container vessel moving in head seas at a constant speed of 15 knots. Wave conditions are long-crested regular waves with wavelength to ship length ratios: $\lambda/L_{pp} \approx 1$ and $\lambda/L \approx 0.65$. The results of the simulations and a discussion on hydroelasticity in slamming problems are presented in Section 7.4. The implicit hydrodynamic load calculations do not treat slamming and springing separately but rather include any instantaneous load caused by the two-phase fluid flow.

Table 7.1: The target weight distribution in full scale. Draft = 13.1 m

x_{min} (m)	x_{max} (m)	Δx (m)	Xcog (m)	Ycog (m)	Zcog (m)	Mass (10^6kg)	10^9 Ixx (kg m^2)	10^9 Iyy (kg m^2)	10^9 Izz (kg m^2)
-5.50	8.60	14.10	1.259	-0.040	18.783	1.297	0.225	0.057	0.227
8.60	23.24	14.64	16.394	0.000	21.003	3.233	0.570	0.224	0.439
23.24	37.88	14.64	30.945	-0.002	18.000	4.939	1.017	0.363	0.801
37.88	52.52	14.64	45.490	-0.001	21.283	5.445	1.205	0.611	0.725
52.52	67.16	14.64	60.157	-0.019	19.867	6.197	1.590	0.859	0.907
67.16	87.96	20.80	77.897	0.084	21.018	6.203	2.552	1.723	1.275
87.96	102.50	14.54	95.168	-0.005	17.736	6.845	1.693	0.883	0.960
102.50	116.94	14.44	110.064	0.000	17.276	7.191	1.880	0.929	1.120
116.94	131.38	14.44	124.170	0.001	17.885	6.754	2.285	1.097	1.404
131.38	145.82	14.44	138.854	-0.001	17.339	7.051	2.432	1.147	1.519
145.82	160.26	14.44	153.053	0.000	17.773	6.637	2.261	1.089	1.381
160.26	174.70	14.44	167.879	-0.167	16.998	7.016	2.424	1.173	1.487
174.70	189.14	14.44	181.921	0.064	17.674	6.690	2.263	1.103	1.371
189.14	203.58	14.44	196.871	-0.387	16.943	7.261	2.509	1.204	1.555
203.58	218.02	14.44	210.706	0.025	17.733	6.785	2.252	1.105	1.365
218.02	232.46	14.44	225.510	0.026	17.577	6.842	2.214	1.107	1.334
232.46	246.90	14.44	239.812	0.000	18.476	6.406	2.030	1.006	1.229
246.90	261.34	14.44	254.099	0.000	18.768	6.247	1.829	0.971	1.058
261.34	275.78	14.44	268.466	-0.011	22.192	4.597	1.191	0.633	0.696
275.78	290.22	14.44	283.086	0.008	23.599	3.944	0.743	0.413	0.408
290.22	304.66	14.44	297.552	0.000	25.729	4.084	0.692	0.404	0.369
304.66	319.10	14.44	311.627	-0.030	25.977	2.574	0.368	0.215	0.214
319.10	343.40	24.30	329.182	0.004	20.431	1.368	0.162	0.147	0.123

7.1 The Elastic Backbone Model

The experimental investigations of the 9400 TEU post-Panamax container vessel were done within the framework of EU-FP7 project "Tools for Ultra Large Container Ships" (TULCS). A scale model (1:80) was built with an aluminum backbone containing 5 cuts (6 segments). The segments are connected using elastic hinges tuned to reflect the main flexural deformation modes of the full scale vessel. A sketch of the aluminum backbone is shown in Fig. 7.1. The backbone was made of a square shaped beam constructed from 5 mm aluminum plate. As seen on the sketch, the forward part of the backbone has an inclination due to practical reasons and the instrument set-up. All the experimental results presented in this chapter are converted to full scale using the Froude scaling law.

The Timoshenko beam solver requires the one dimensional line load $f(x,t)$ from the fluid solution. At each time step, fluid pressures in three-dimensions are converted to one-dimensional line loads using cross-section interpolations. The line loads are evaluated at 128 longitudinal positions distributed appropriately along the hull. The static structural and load properties such as mass per unit length $m(x)$, $EI(x)$, $kGA(x)$ and $r^2(x)$ are shown in Fig. 7.2 with the corresponding draught of 13.1 m. The structural properties and mass-distribution are specified aiming to represent the

Table 7.2: Dry natural frequencies and the structural damping ratio ξ at full scale (converted to full scale using Froude scaling law)

Mode	Deformation	Exp. Freq. in Hz (ξ)	CFD Freq. in Hz (ξ)	Err. (%)
1	2-node vertical bending	0.682 (1.6%)	0.683 (1.0%)	0.15
2	3-node vertical bending	1.588 (1.5%)	1.573 (1.0%)	-0.95

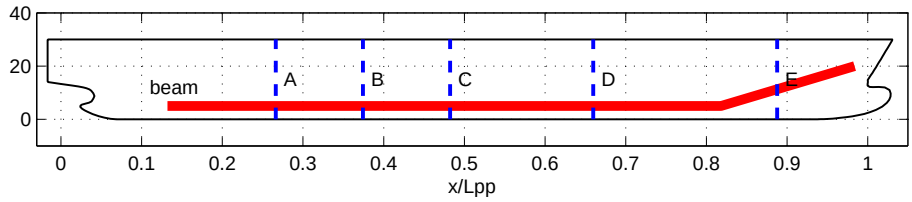

Figure 7.1: A sketch showing the positions of the 5 cuts and the aluminum backbone

target values presented in Table 7.1. There are more stations in the Timoshenko beam model (128) than defined in Table 7.1. Therefore, the structural properties are interpolated for the additional stations. However, the final distribution of the structural and mass properties are adjusted to satisfy the integrated value as presented in Table 7.1.

It is seen that the estimated 2-node vertical vibration agrees well with the measurements by CEHIPAR, see Fig. 7.3. For the higher modes the agreement is less encouraging. It has been reported that the signals are weak in the third mode introducing a large uncertainty in the experimental evaluation of the 3-node vertical bending mode. The difference in frequencies, however, are as small as 0.15 % for the 2-node mode and 0.95 % for the 3-node mode, see the dry mode frequencies shown in Table 7.2. On the other hand, the responses in waves may be dominated by the 2-node mode such that small deviation seen in the 3-node mode may not have a significant influence on the responses.

Using the presented structural properties, the total number of modes applied in the simulations is ten vertical bending modes. Most of these modes are not physically presentable but included for mathematical reasons to describe local deformations as accurately as possible. The maximum number of modes, which can be included in the modal equations, is limited by the discretization of the beam. In the current simulation, the beam is discretized using 128 nodal points (127 segments). Thus, the 10-node vertical bending mode is about the highest mode which can be resolved reasonably well with 127 segments i.e. there are about 12 segments between each node for the 10-node mode.

One of the uncertainties when accounting for the flexibility of the hull girder is the estimation of the structural damping for the vessel at full scale. Even at model scale there are many uncertainties related to the evaluation of a proper structural damping. For the 2-node vertical bending mode, the dry random vibration test of the aluminum backbone model showed a damping ratio of $\xi_1 \approx 1.6\%$ and $\xi_2 \approx 1.5\%$ for the 2-node vertical bending mode. However, the laboratory reports state that there may be a large uncertainties associated with the estimated damping ratio partly

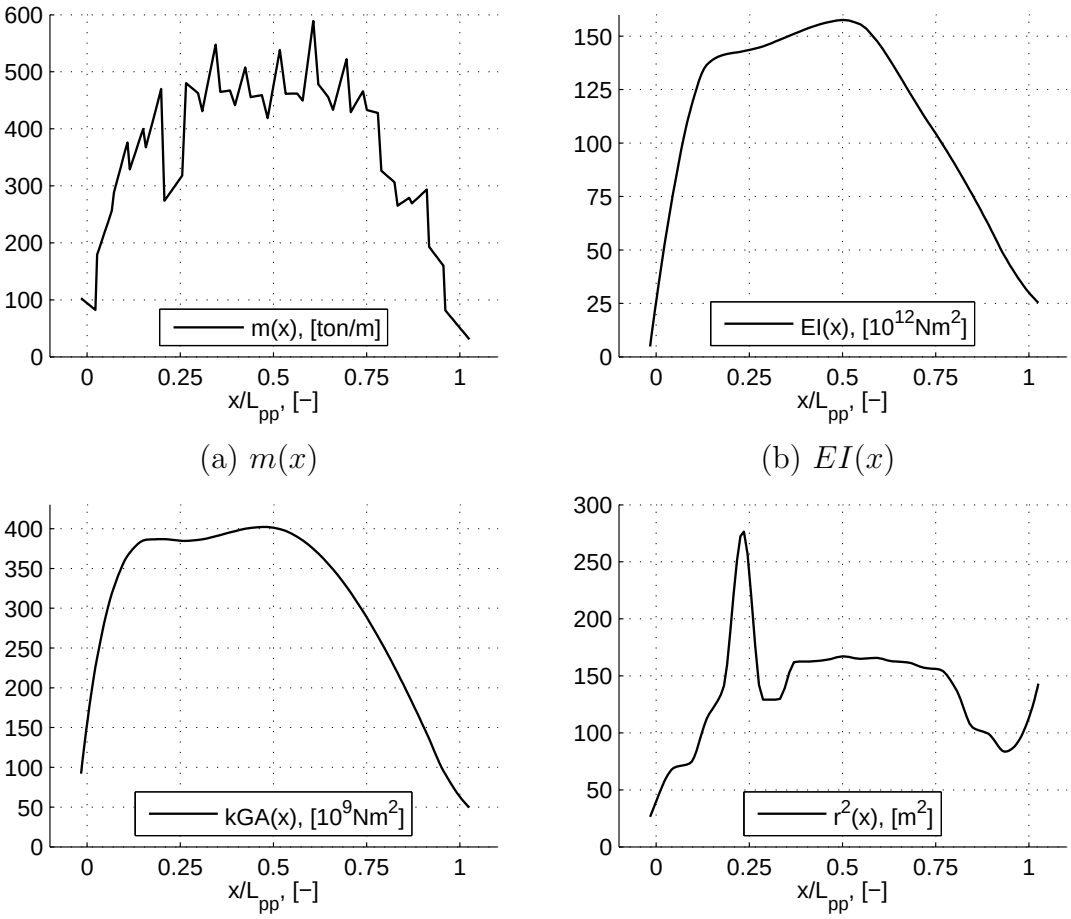

(a) $m(x)$ (b) $EI(x)$

(c) $kGA(x)$ (d) $r^2(x)$

Figure 7.2: Structural properties applied in the Timoshenko beam model

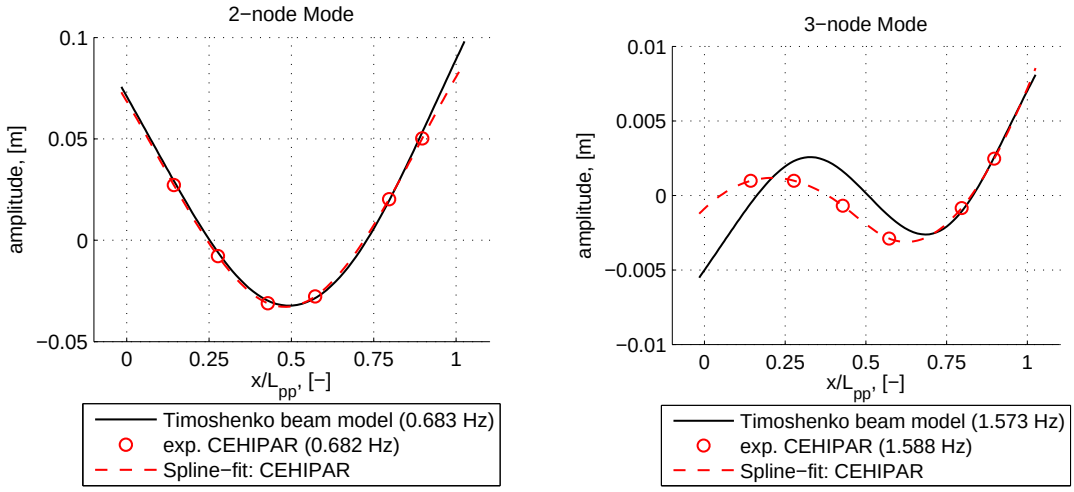

(a) 2-node Vertical bending (b) 3-node Vertical bending

Figure 7.3: Dry mode shapes of the model (scale to full scale using Froude's scaling law) compared with the Timoshenko beam model applied in the CFD simulations (OpenFOAM)

Table 7.3: Properties of the target waves (infinite water depth) and waves realized in the experiment (Converted to full scale using Froude's scaling law)

	Target		Exp.		Err.	
Case	H (m)	T (s)	H (m)	T (s)	Err. H (%)	Err. T (%)
I	8.0	14.91	8.33	14.92	4.13	0.067
II	5.0	14.32	5.35	14.30	7.00	-0.140
III	8.0	14.32	8.49	14.33	6.13	0.070
IV	8.0	11.66	8.66	11.70	8.25	0.343

due to weak signals and the difficulty of clearly distinguishing between the different modes.

A review on the structural damping was done in Jensen & Madsen (1977) showing a large variation of the logarithmic decrement $\delta = 2\pi\xi/\sqrt{1-\xi^2}$ published for a 340,000 dwt tanker. The functional relation of δ with respect to the vibrational frequency can vary from a linear function with a fixed proportionality constant to an exponential relation. An inverse proportional function of the frequency has also been published. These published results prove that there are large uncertainties associated with the estimated damping ratio.

Moreover, the numerical simulation introduces additional numerical damping with a magnitude, which strongly depends on the applied numerical scheme and the particular grid configuration. In the current simulations, the damping ratio is set to 1% for all modes. This particular choice should be compared to the experimental estimated values of $\xi_1 \approx 1.6\%$ and $\xi_2 \approx 1.5\%$. The smaller damping ratio applied in the numerical simulation should compensate for the artificial numerical damping contained in the numerical results. The numerical damping can be estimated from free decays and ambient vibration tests. Depending on the particular numerical set-up and the applied grid configuration, one may even choose to set the damping ratio to zero accounting for a large artificial damping in the numerical results.

7.2 Selected Regular Wave Conditions

The experimental campaign covers three headings: 120°, 150° and 180° (head seas) at two forward speeds (15 and 22 knots) in a wide range of regular waves. For the purpose of validating the hydroelastic code (Timoshenko beam solver coupled with the VOF-based NS flow solver) the head seas condition with a forward speed of 15 knots has been chosen. In total, four regular waves are selected for the simulations, see Table 7.3. The quality of the waves generated in the experiments is discussed in this Section.

In the experiment, the free surface elevation is measured in front of the towed scaled model. Converted to full scale, the location of the wave measurement is about $0.7\,L_{pp}$ forward of FP and $0.5\,Lpp$ to starboard. With the forward speed of 15 knots (Froude number ≈ 0.135), it is reasonable to assume that the free surface elevation measured at this location is not disturbed by the diffraction and radiation waves from the vessel. Thus, the measured free surface can be assumed to represent the incident wave well.

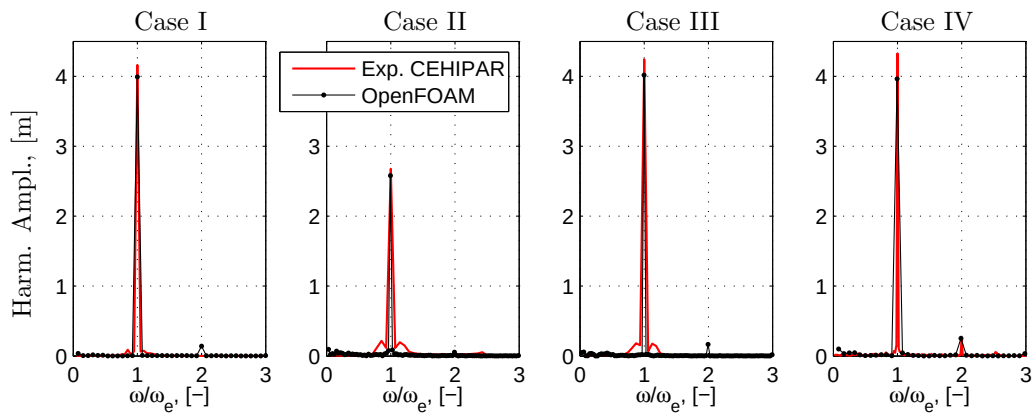

Figure 7.4: The results of a FFT of the measured incident waves

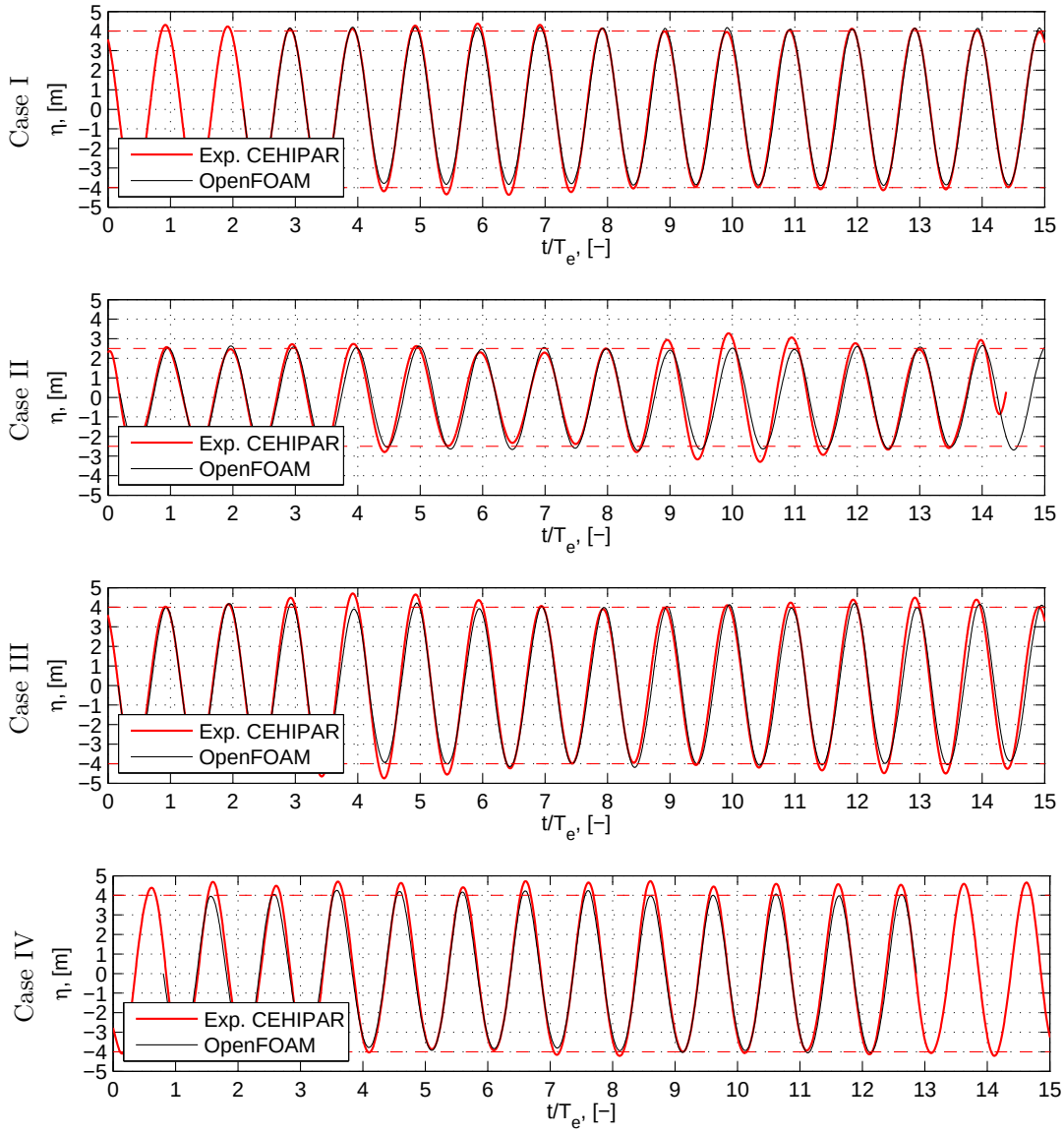

Figure 7.5: Time series of the measured free surface elevation (Converted to full scale using Froude's scaling law)

The time series of the measurement is converted to the frequency domain using the FFT transformation (Fast-Fourier-Transform) and the amplitude of the first harmonic is converted to wave height and shown as the experimental wave height in Table 7.3. Compared to the target wave height, it is seen that the experimental results are consistently larger than the target value. For Case IV, the wave height generated in the experiment is as much as 8.25% larger than the target value. Assuming a linear response, the error seen in the incident wave height will introduce the same percentage error in the responses. When the responses are nonlinear the error may be amplified more. Thus, for comparison purposes it is important to set up the numerical simulations using wave conditions as observed in the measurements and not as the target wave.

On the other hand, some disagreements in the incident wave field cannot be avoided since the exact condition of the experimental wave generator is unknown. The results of a FFT of the four waves (see Fig. 7.4) show that there are higher harmonics in Case IV. For Case I, II, and III, the spectrum contains one harmonic corresponding to the frequency of the target wave but also some broadening of the spectral responses. The spreading of the spectrum is smallest in Case I and IV.

The quality of the waves generated in the experiment can also be assessed qualitatively from the time series data as presented in Fig. 7.5 where is clearly seen that the regular wave profile is more stable in Case I and IV than in Case II and III.

7.3 Numerical Setup & Initial Conditions

The ship response simulations are done in full scale. The main particulars of the 9400 TEU post-Panamax vessel are presented in Table 5.2. The ship is moving in head seas and only half of the ship is included in the simulation due to symmetry. The size of the numerical wave tank is chosen to be 1575x350x300 m (length, width and water depth) which corresponds to a distance of approximately $1.5L_{pp}$ from FP to the wave-maker boundary (inlet). The wake region behind the full scale vessel is approximately $2L_{pp}$, where a relaxation zone with a length of $1L_{pp}$ is located next to the outlet boundary to minimize wave reflection in to the domain.

Figure 7.6 shows a sketch of the computational domain and the grid configuration. The grid is fitted to the hull using split-hexahedral and polyhedral cells. The cells are clustered near the hull, the free surface and the wave propagation zone in front of the ship. On average, the horizontal grid spacing in front of the ship is approximately 1 m producing a total number of cells-per-wave-length of 349, 321, 323, and 217, for Case I, II, III, and IV, respectively.

There are two options to startup the simulations: (a) the vessel is simulated to move in calm water until reaching a quasi-steady state, before waves are introduced at the inlet boundary, (b) the whole domain is initialized with the incident waves and the early transient responses discarded due to the nonphysical initial flow field. The former option was found to be more stable as the simulation of the forward motion in calm water can be done using a more efficient steady state solver. Further more, the results of the calm water simulation can be reused in all the selected wave cases since the forward speed of the vessel is the same in all cases.

With the applied loading condition the ship is in hogging condition in calm water. Therefore, the flow in the calm water simulation must account for the initial deflection. An artificial time delay is introduced to avoid an abrupt transition from

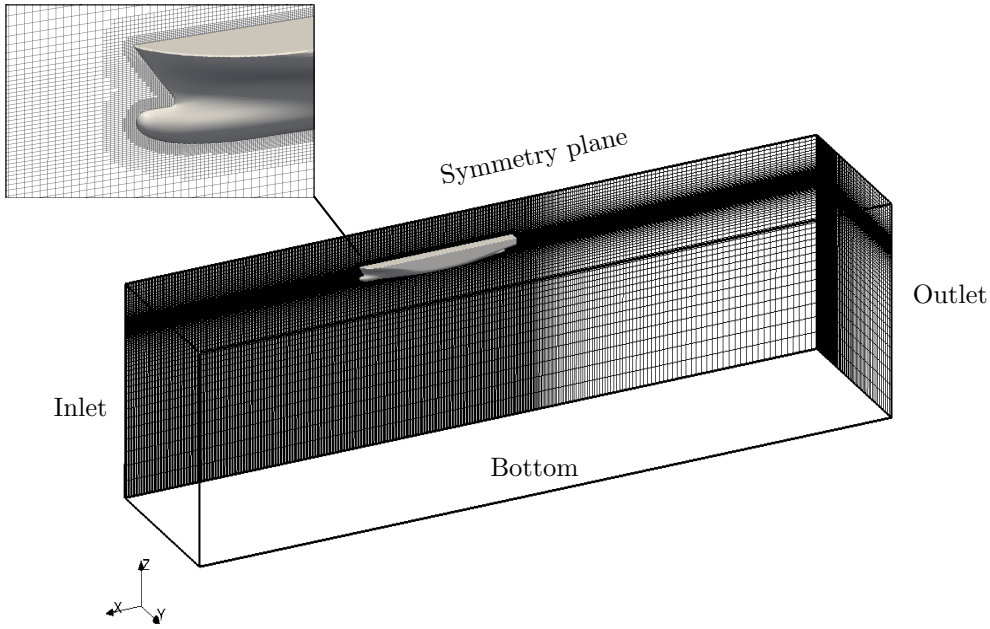

Figure 7.6: A sketch of the grid configuration (4.2 million cells) applied in the hydroelastic simulations

the rigid body mode to the hogging deformation. A rough estimate of the required start-up time can be obtained using a simple linear single-degree-of-freedom damped mass-spring system with damping ratio ξ and natural frequency ω_n. Assuming that the excitation force is purely harmonic, the time to reduce the amplitude to 5% of the initial value is

$$\Delta t = -\frac{\ln 5\%}{\xi \omega_n} \tag{7.1}$$

For example, for $\xi = 1.5\%$ and $\omega_n = 0.56\,\mathrm{rad/s}$ the required time is 356 s. From the CFD point-of-view, this is a long time implying that it is crucial to start up the motion and excitation smoothly. There is, however, a possibility that the motion will never become stationary if there are strong non-linear effects in the system. Thus, the initial deformation is introduced gradually and smoothly during the calm water simulation. According to the rigid body simulation, the VBM amidships at the quasi-steady state becomes 5488 MNm. When accounting for the flexibility of the hull girder, the VBM decreases to 5187 MNm, i.e. the VBM amidships for the flexible hull girder is reduced by 5.5% compared to the rigid-body assumption.

After waves are introduced into the domain, the CPU time seen in the simulations is on average 4 hours for every simulated second using a high performance Intel® Xeon® X5550 cluster with 64 cores. One of the most time consuming parts is the inner iteration of the implicit strong coupling fluid-structure interaction scheme done at each time step. While the size of the time step is dynamically adjusted, the average step size is about $\Delta t \approx 0.005$ s.

The huge demand on CPU time implies a strong need for close attention and care in the numerical setup since there are usually not enough resources to rectify mistakes and redo the simulations.

7.4 Whipping & Springing Responses in Regular Waves

The reference time of the numerical results is defined such that $t = 0$ s corresponds to the time waves are initially introduced at the wave-maker boundary. Because the reference time of the measurement data was not stated in the laboratory reports, a time synchronization was performed using the free surface elevation.

There is a start-up period, where the initial wave front propagates from the wave-maker boundary to the vessel. Once the incident wave has reached FP, it will take additionally a few more wave periods for the responses to reach quasi-steady heave and pitch motions. This start-up time depends strongly on the forward speed (Froude number) and the particular wave configuration. For the current numerical setup, the forward speed motion in calm water is already in a steady state when waves are introduced into the domain with a ramp-up time set to 1 wave period. The smooth introduction of the wave helps the responses to reach a quasi-steady state quickly. To reach a quasi-steady state, it takes approximately 5 wave periods for Case I, II, and III with the wave-length ratio $\lambda/L_{pp} \approx 1$ and 10 wave periods for Case IV where the wave is shorter $\lambda/L_{pp} \approx 0.66$.

For a comparison, time-domain simulations using the nonlinear strip theory (Shipstar, Xia et al. (1998)) have been performed where the same non-uniform Timoshenko beam theory is used for modelling the flexibility of the hull girder. A discussion on the results of the nonlinear strip theory has been published in Andersen & Jensen (2012) and Seng et al. (2012).

7.4.1 VBM at 5 Cuts

In the experiment, VBM at 5 cuts (see Fig. 7.1 for the location of the 5 cuts) was measured. The comparison between the numerical results and measurements are presented in this Section.

As stated in the previous Section, VBM in calm water with the rigid body assumption is not the same as in a flexible hull-girder assumption. For reference purposes, we use VBM from the flexible hull-girder simulations. Thus, the wave-induced VBM presented in this Section is evaluated by taking the total VBM and subtracting the VBM for the flexible hull girder in calm water.

The VBM at the 5 cuts for Case I is shown in Fig. 7.7 (see Table 7.3 for wave properties). Compared to the experimental results, the time history of VBM at the 5 cuts is well predicted by the numerical simulations. The magnitudes of the VBM are approximately the same for Shipstar (the nonlinear strip theory program) and OpenFOAM (the current CFD method). However, the differences between the sagging and hogging VBM are clearly seen in the measurement and in the CFD results. The sign convention applied here is that hogging VBM is positive and sagging VBM is negative. In Fig. 7.7c it is observed that the wave induced sagging VBM amidships is approximately 40% larger than the hogging VBM. The peak-to-peak prediction from the nonlinear strip theory (Shipstar) agrees with the measurements, but there is less difference between the sagging and hogging VBM in the Shipstar results. The reason the strip theory fails to predict the difference in sagging and hogging VBM may relate to the applied linear incident waves. As discussed in the report of ISSC Committee on Loads (2006), there are different levels of nonlinearity

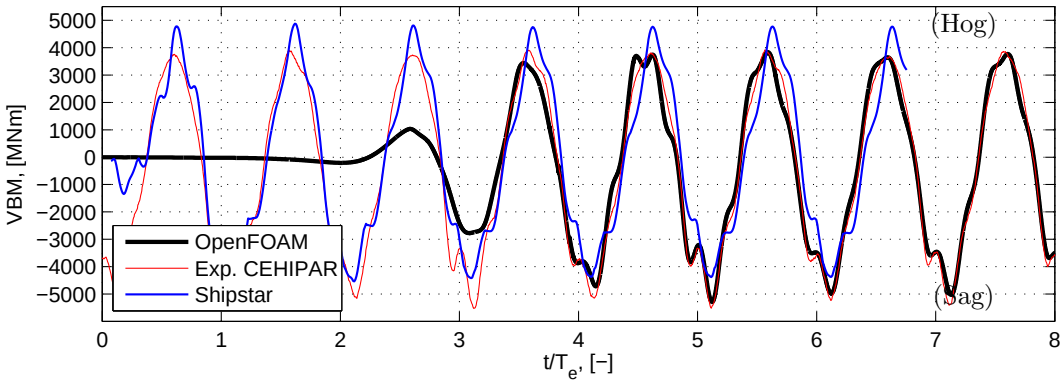

(c) Cut C (amidships)

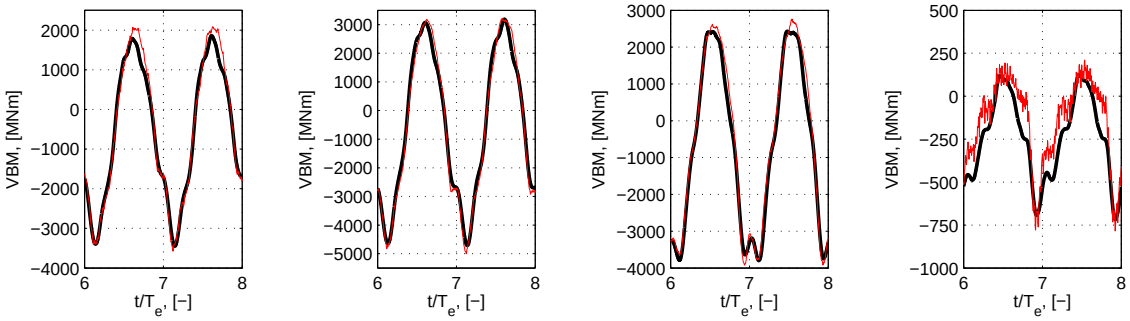

(a) Cut A (b) Cut B (d) Cut D (e) Cut E

Figure 7.7: Case I. VBM at the 5 Cuts. The numerical simulation compared against the experiments. See Fig. 7.1 for the location of the 5 cuts.

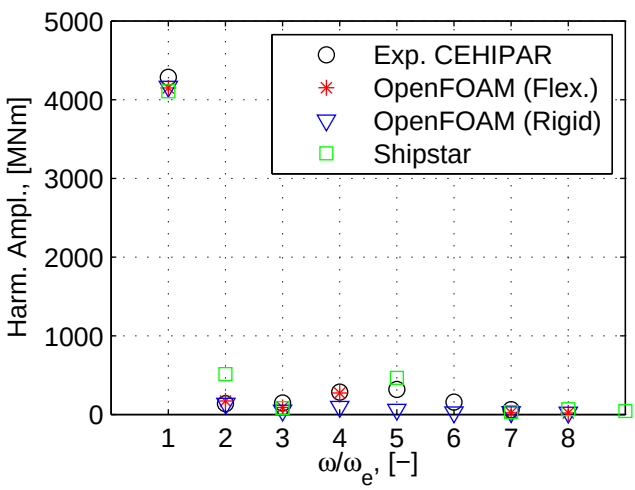

Figure 7.8: Case I. Amplitudes of the harmonics of VBM amidships

accounted for in the numerical calculation. In the current nonlinear strip theory the nonlinearity is introduced mainly in the Froude-Krylov force and in the memory term, while the incident wave is assumed to be a linear infinite-depth water wave. Further discussions on the feasibility of using either one-way or two-way coupling schemes can be found in Seng et al. (2012).

While the CFD seems to be able to reproduce the experimental results, there is no clear evidence showing that the hydroelastic coupling has a strong effect on the responses of the vessel. The response spectra of bending moments amidships show that the major part of the response is due to the global heave and pitch motion of the vessel. As shown in Fig. 7.8, the differences between the rigid body simulation and the flexible body are seen only for the 4th-harmonic. Hence, the local deformation accounts only for a small contribution to VBM.

The small deviations seen in the time series of the responses can also be observed in the spectral analysis. The amplitude of the higher harmonics are almost the same between CFD and experiment except for the 5th and 6th harmonics, where the CFD results do not show any significant spikes.

Most of the energy is in the 1st-harmonic, which corresponds to the excitation frequency of the encounter waves. In this regard, the nonlinear strip theory (Shipstar) predicts similar results compared to the CFD. The major differences between Shipstar and CFD are in the higher harmonics.

VBM amidships for Case II & III are presented in Figs. 7.9 and 7.10. Between Case I, II, and III, there is not much difference in the results. The similarity in these results were expected since the differences in the configuration is only a small change in the wave period and in Case II the wave height is 5 m instead of 8 m. The results of these three cases show that the current hydroelastic coupling using a Timoshenko beam and a VOF-based Navier-Stokes solver can predict the steady-state VBM responses well. It should be emphasized, however, that the uncertainties related to the wave conditions seen in the experiments are possibly the major contribution to some of the deviations seen in the higher harmonics of the responses. Furthermore, the elastic deformation of the hull girder does not contribute much to the responses. A proper validation of the hydroelastic code requires a much more significant contribution from the flexural deformation of the hull girder. On the other hand, Case IV shows a very different comparison. The 4th-harmonic is very close to the wetted natural frequency of the two-node vertical bending mode causing a resonance effect. The next Section is dedicated to discuss this resonance effect.

7.4.2 Resonance Effect

In Case IV, the target wave period is 11.66 s which corresponds to $\lambda/L_{pp} \approx 0.64$ (using the linear dispersion relation for deep water waves). As presented in Table 2, the wave generated in the experiment has an average error of 8.25% in wave height. For comparison purposes, the incident wave in the free surface CFD simulation is defined with the same mean wave properties as seen in the measurement.

The responses seen for Case IV can be characterized as a springing response where the 4th harmonic excites the 2-node vertical bending mode causing a resonance. Using the current VOF-based Navier-Stokes solver, the excitation from the incident wave is evaluated based on an integration of the instantaneous pressure distribution accounting for slamming pressures and any local variation due to the combined effect

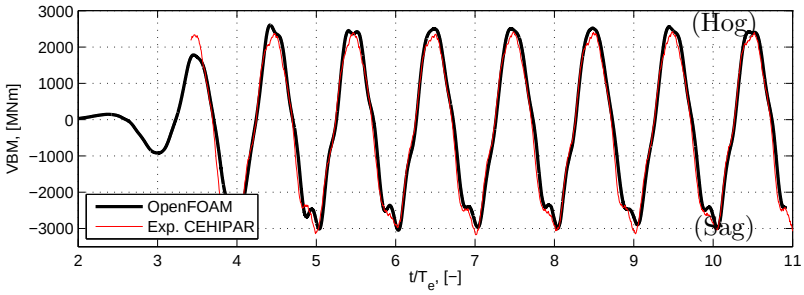

(c) Cut C (amidships)

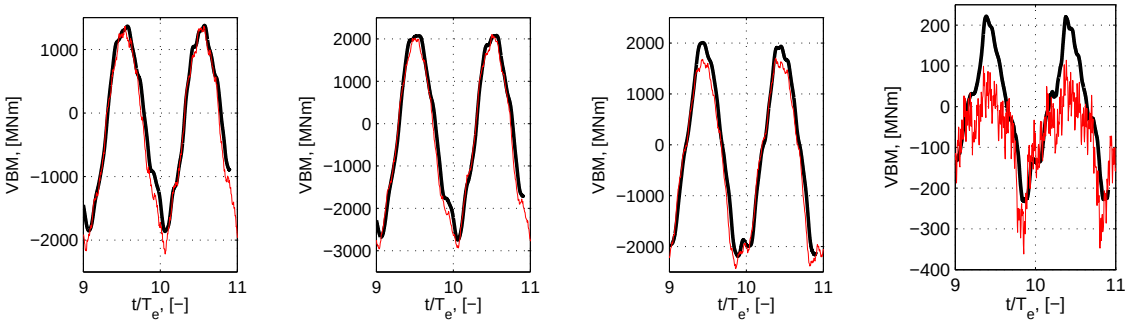

(a) Cut A (b) Cut B (d) Cut D (e) Cut E

Figure 7.9: Case II. VBM at the 5 Cuts. See Fig. 7.1 for the location of the 5 cuts.

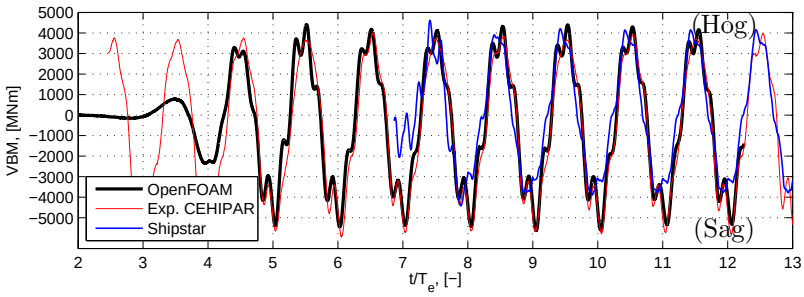

(c) Cut C (amidships)

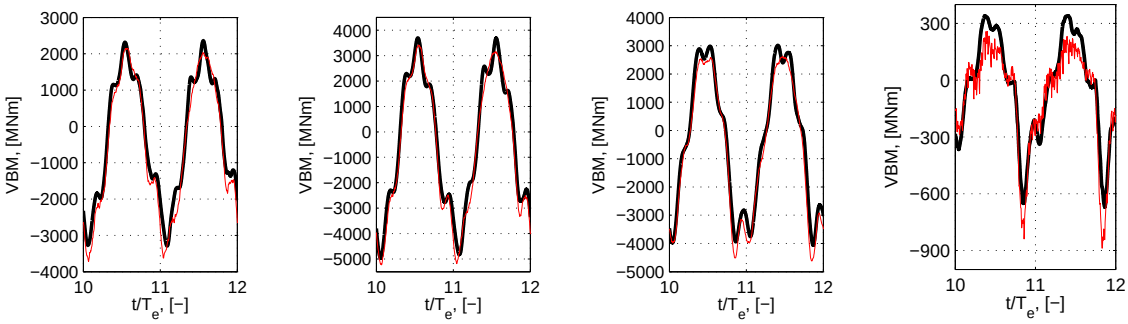

(a) Cut A (b) Cut B (d) Cut D (e) Cut E

Figure 7.10: Case III. VBM at the 5 Cuts. See Fig. 7.1 for the location of the 5 cuts.

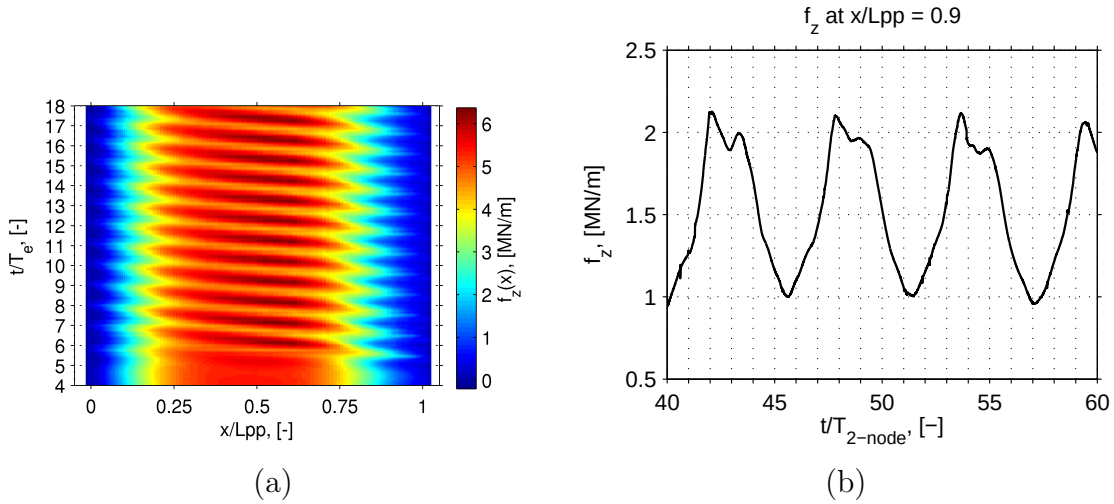

Figure 7.11: The vertical load distribution for Case IV. (a) The time axis is normalized by the period of the encounter frequency. (b) Vertical load at $x/L_{pp} = 0.9$ where the time axis is normalized by the period of the 2-node vertical bending mode.

of the scattering and incident waves. The loads from the waves and the slamming are combined, which makes it difficult to distinguish between the contributions from slamming loads and from wave loads. One of the characteristics of slamming loads is that the duration of the excitation is shorter than the largest natural period of the structural responses. Thus, slamming events can be identified from the excitation pattern (see Fig. 7.11) where the rise time is much smaller than the period of the 2-node vertical bending mode. The sharp spikes seen in Fig. 7.11 in the forward 20% and aft 10% have a rise time of approximately 50% of the period for the 2-node mode. Thus, the excitation is not strong enough to be classified as a severe bow flare slamming. This conclusion supports the fact that there is no sign of whipping vibration in the VBM responses.

The predicted responses of the vessel are shown in Fig. 7.12. Clearly, the peak values of the VBM amidships predicted by the CFD method and the non-linear strip theory are smaller than found in the measurement. The flexible beam model (CFD method or the strip theory) predict the same variation of the VBM amidships as shown in Fig. 7.12c. However, even though the phases and frequencies of the lower and higher harmonics agree with the experiments, the amplitudes are smaller in the numerical results. The results of the rigid body simulation under the same wave condition are also presented in Fig. 7.12c. A comparison with this rigid body simulation shows that there is a strong effect of the flexibility of the hull girder in the responses.

The power spectrum of the responses of the rigid body simulation shows that the responses are non-linear. The 1st harmonic seen in Fig. 7.13 corresponds to the encounter frequency of the incident wave. The super-harmonic frequencies of 2nd, 3rd, 4th and 5th multiples of the encounter wave frequency, can be clearly identified. The spectra of the rigid body simulation compared to the results of the flexible beam model suggests that the 4th harmonic frequency coincides with the eigen-frequency of the wetted two-node vertical bending vibration causing a resonance. Noticeably, the measurement shows that the ratio between the amplitude of the 4th and 1st harmonics is approximately 55%. For Shipstar this ratio is 63% and for CFD, the

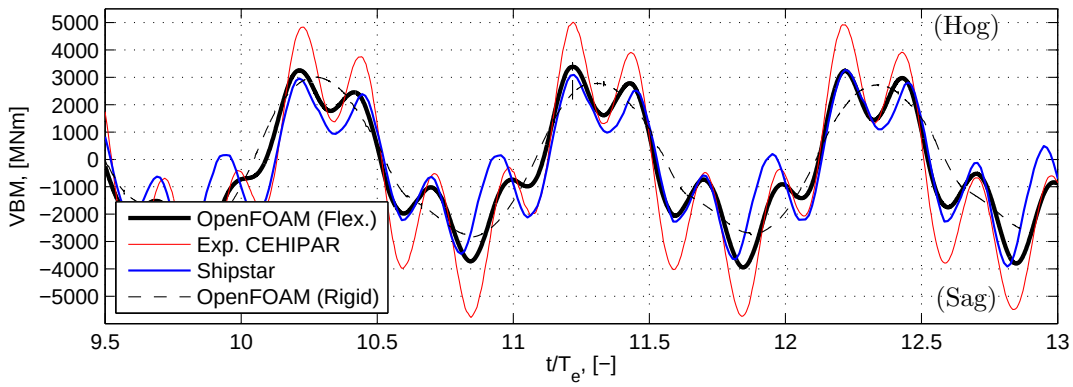

(c) Cut C (amidships)

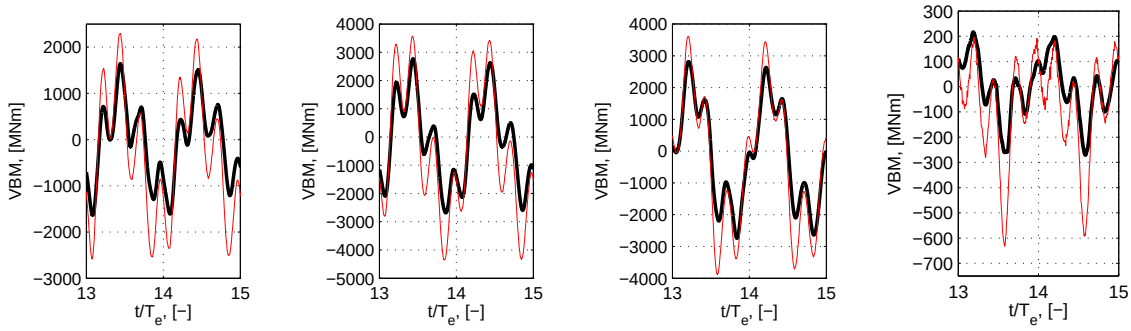

(a) Cut A (b) Cut B (d) Cut D (e) Cut E

Figure 7.12: Case IV. VBM at the 5 Cuts. The 4th-harmonic excites the wetted 2-node vertical bending mode causing a resonance vibration known as springing

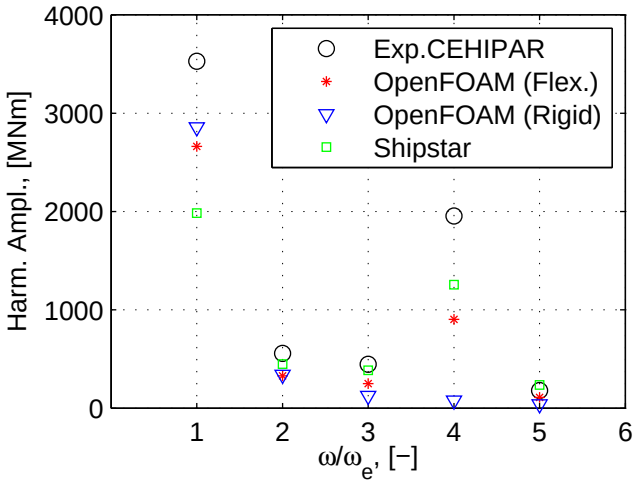

Figure 7.13: Case IV. Amplitudes of the harmonics of VBM amidships

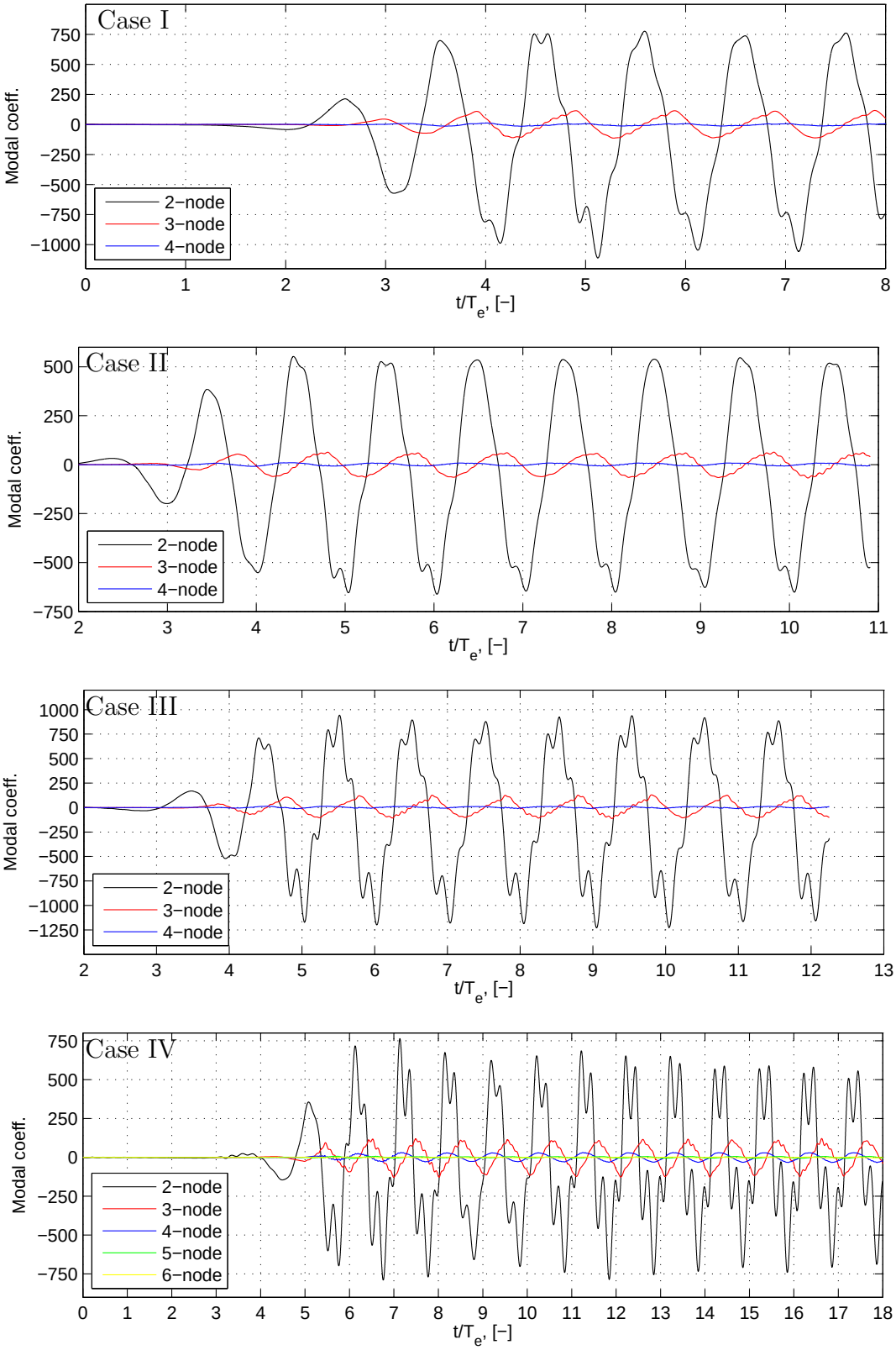

Figure 7.14: Modal coefficients for the vertical bending modes. The reference level for each mode is set to zero level at $t = 0$ s for the comparison purposes.

ratio is 34%. In this regard, the results of Shipstar are much closer to the experiment. Nevertheless, the amplitudes of the harmonics of all numerical simulations are very low compared to the measurement.

Assuming that the responses are linear in wave height, the error in wave height seen in the experiments should account only for 8.25%. However, the responses are non-linear and there is a resonance. A comparison between the amplitudes of the modal coefficients confirms that most of the vibrational responses are in 2-node mode, see Fig. 7.14. In all four cases, the modal coefficient for 3-node mode is approximately 10% of the 2-node mode. For modes higher than 3-node, the modal coefficients are relatively low and contribute very little to the total vibrational responses except for case IV. Figure 7.14 reveals that, in Case IV, where resonance occurs, the 3-node and 4-node mode may have a significant contribution to the overall responses. However, the deviation of the 3-node modes alone cannot explain the difference seen in the VBM responses for Case IV.

7.4.3 Heave & Pitch Motion

The numerical prediction of the VBM at the 5 cuts are comparable to the measurements. Therefore, it should be expected that the predicted motions of the vessel agree as well. However, as presented in Figs. 7.15 and 7.16 only the pitch motions have a reasonable agreement with the experiments. Noticeably, the CFD results show more stable heave and pitch motions. The comparisons of the heave and pitch motions show a contradiction. On one hand, the VBM at the 5 cuts are comparable with the measurements for Case I, II and III, see Section 7.4.1. On the other hand, the amplitudes of the heave motion are smaller than the measurements. This contradiction poses several questions on both the numerical results and the quality of the experimental data. Considering Cases I, II, and III, the magnitudes of the heave motion are consistently smaller than the measurement indicating that the heave damping in the numerical solution is too large. However, the results of Case IV shows a very different scenario. In Case IV, where the resonance occurs, the predicted and the measured heave motions are similar in magnitude but the numerically predicted VBM at the 5 cuts are significantly smaller than the measurements.

It is obvious that there is a need to do a grid convergence study as well as a study on the performance of the applied spatial and temporal schemes. These studies are mandatory to assure the quality of the numerical results. However, these are only done occasionally on the full size simulation due to the limitation on the computational resources. Often, a grid convergence study is done on a smaller problem looking specifically at the interesting features of the flow. Once, the grid requirement for the smaller problem has been determined, a similar grid configuration is applied to the full size problem with the assumption of a similar convergence behavior. From the convergence study presented in Section 4.1, a 1st-order convergence rate is to be expected. The cell size around the hull and the areas exposed to slamming are refined according to the results presented in Chapter 4. Within the wave generation and propagation region in front of the vessel, the characteristic cell size is defined as described in Section 7.3. The interesting subjects which require further investigation are the heave damping in the numerical solutions and the effects of the structural damping on the resonant responses seen in Case IV. Regarding the measurements, there is a need for an error assessment.

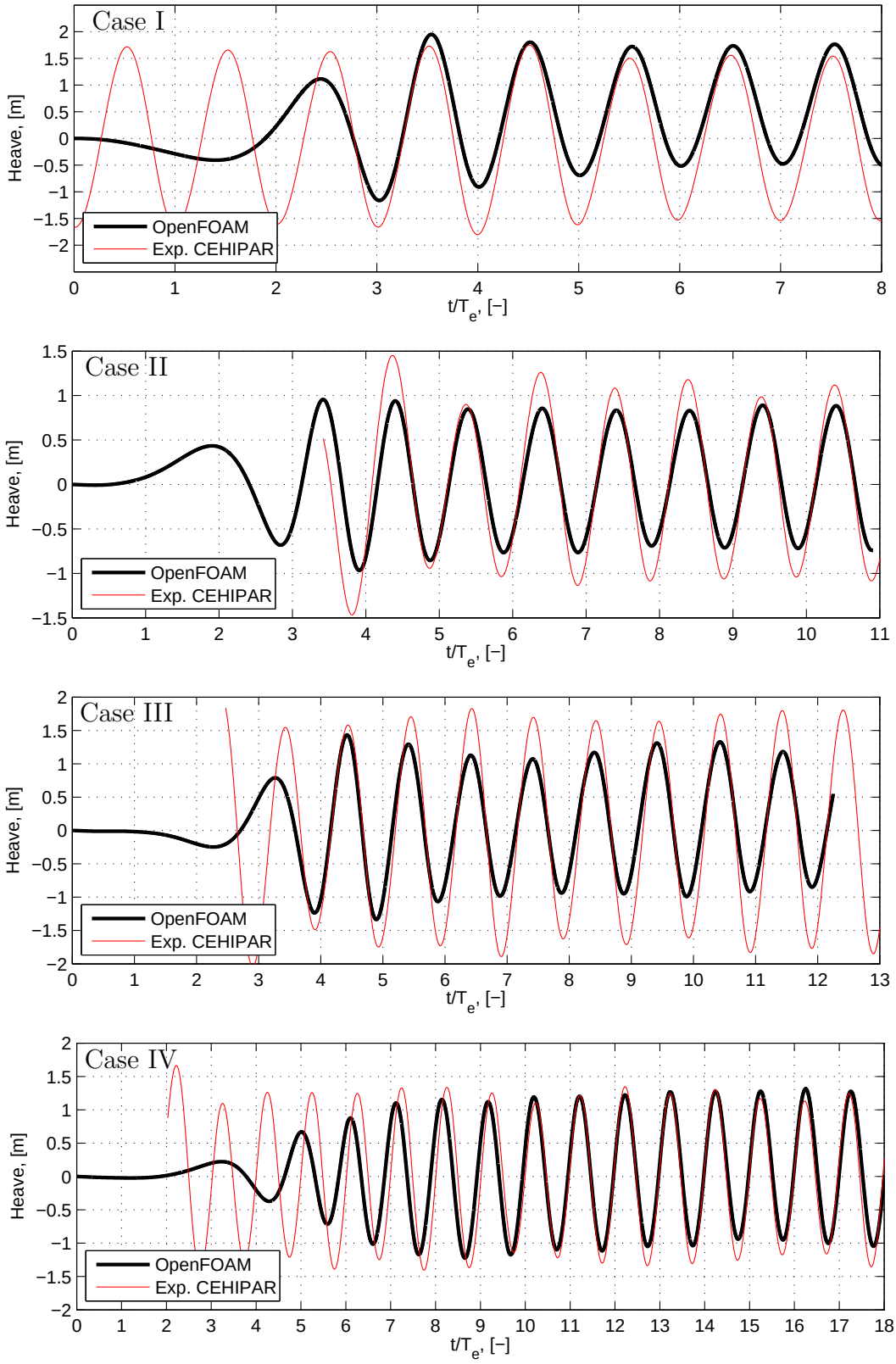

Figure 7.15: Heave motions for Case I, II, III and IV.

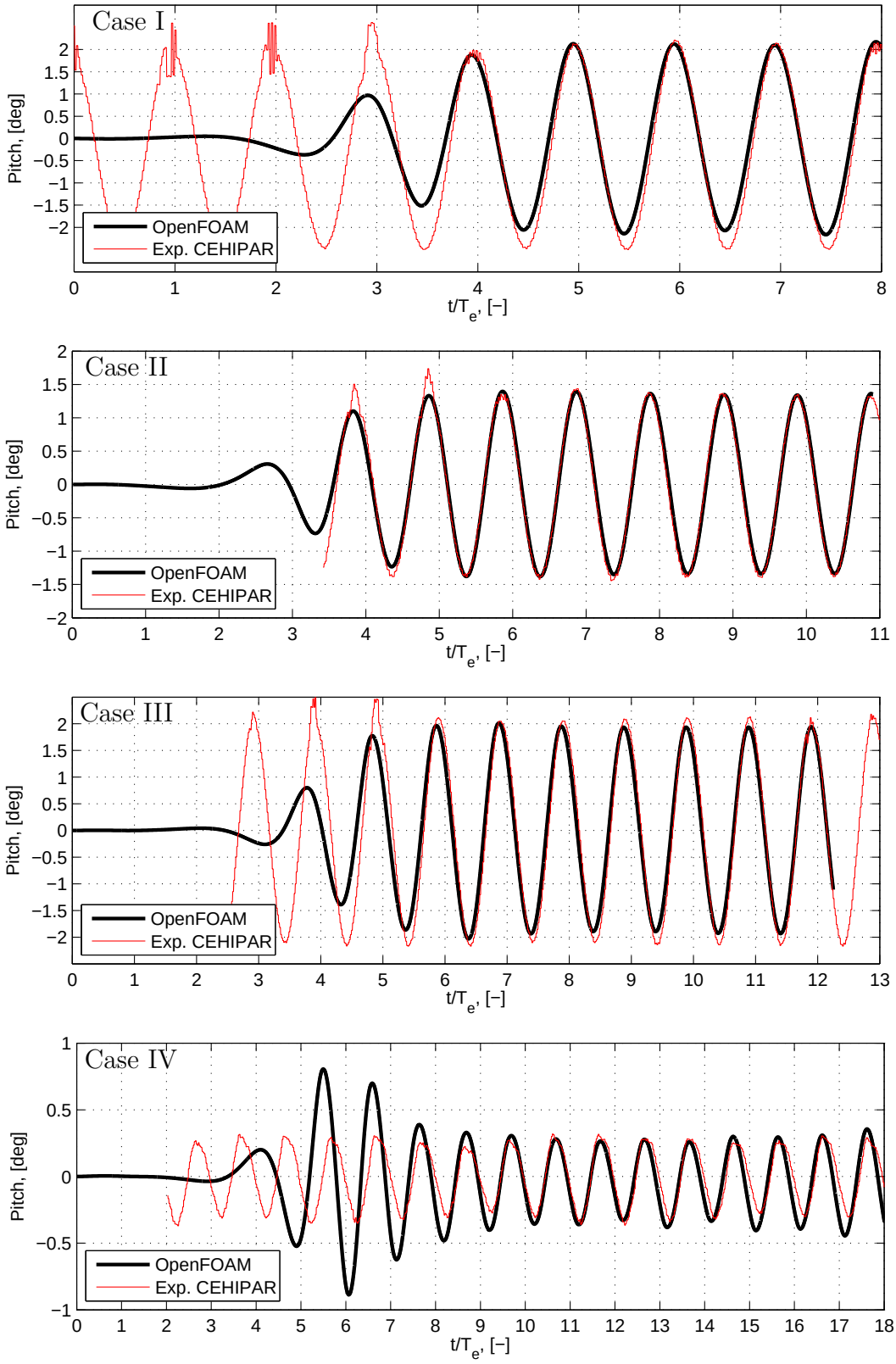

Figure 7.16: Pitch motions for Case I, II, III and IV.

7.5 Summary

It is challenging to solve a fluid-structure-interaction problem using the direct calculation approach. Besides the usual spatial and temporal discretization errors, there is an additional coupling error due to an insufficient coupling mechanism between the structural solver and the fluid solver. The test cases presented in this chapter show, however, that the responses of interests (i.e. VBM amidships) can be predicted well in a head seas condition using the non-uniform Timoshenko beam to model the flexibility of the hull girder. Using the Timoshenko beam theory is very efficient compared to a full FEM solution.

In all 4 test cases, the numerical predictions are compared with the measurements. The beam model has been shown to predict VBM well in those cases where the contribution from the flexibility of the hull girder is small. When resonance occurs, the beam model may have difficulty prediction the actual response level. One of the reasons may relate to the difficulty in evaluating the equivalent structural properties to be applied in the Timoshenko beam model. The simplification of the hull structure may cause some disagreement in the natural frequency as well as the eigenmodes.

Nevertheless, the VOF-based Navier-Stokes solver provides details of the load distribution on the hull. The fluid action on the hull are evaluated as part of the solution and no explicit modelling of the slamming load is required. For this reason, the current CFD approach provides an implicit evaluation of both slamming-induced responses and springing responses.

Chapter 8

Conclusions & Recommendations

This thesis describes the research effort leading to the development and implementation of a fully functional numerical wave tank suitable for a direct calculation of bow flare slamming and the associated whipping responses in realistic sea states. The flow solver is a VOF-based incompressible Navier-Stokes solver validated against experiments in several test cases for its capability of predicting slamming loads on complex bodies such as a bulbous bow. The structural solver based on the classical non-uniform Timoshenko beam model allows the numerical simulations to account for the flexibility of the hull girder for a vessel moving in head seas.

The numerical tank has been applied to investigate the possibility to combine FORM (First-Order Reliability Method) and the CFD method to evaluate the short-term extreme responses taking into account the contribution from the low frequencies as well as high frequencies wave excitations. At first the hull girder is assumed to be rigid and the responses are evaluated looking specifically on the possible introduction of a model correction factor. Within the assumption of a rigid body, the results are encouraging. To account for the whipping responses, however, requires a flexible model of the hull girder, which must be validated before further use. The present implementation of the hydroelastic code using a strongly coupled partition scheme has been validated using experiments done on a segmented elastic backbone model of a 9,400 TEU post-Panamax container vessel.

8.1 Conclusions

From the discussion represented in this thesis many conclusions can be made. The most important of these are highlighted in this section. The general conclusions on the applications of the CFD method in slamming related problems can be summarized as follows:

- The numerically predicted loads in terms of vertical slamming forces and the total impulse of the slamming impact are accurate enough for many practical engineering problems. This conclusion confirms previously published results. Still, the validity of the results are constrained by the underlying flow assumptions. Particularly, the incompressible fluid assumption poses a restriction to two-dimensional results in which the assumption may not be valid when the complicated free surface deformation causes air-pockets to form under the slamming area. A free surface separation during the initial impact,

e.g. the bottom slamming, may cause air-pockets to form. The secondary impact with the presence of an air-pocket causes the two-dimensional slamming loads to be over-predicted. Furthermore, the convergence study reveals that the current VOF-based flow solver may have difficulties predicting a consistent and converged free surface pile-up. The free surface deformation, especially when break-up occurs, may depend strongly on the numerical scheme adopted to prevent a diffusive interface. The possible convergence problems of the break-up of the free surface provides a strong indicator to be cautious when a subsequent severe slamming event occurs due to the free surface pile-up in two-dimensional simulations.

One of the major drawbacks of using the CFD method is a huge demand on the computational power. There is a strong need for a rational and efficient model of the slamming load. For water entry problems, one of the possible models is the decomposition model proposed by Korobkin (2012), see Eq. (4.15). Using the current CFD method, it has been shown that:

- In 2D water-entry problems, vertical forces modelled by Eq. (4.15) can be made as accurate as the CFD results. The model has been tested on a 30° wedge and a 2D bow flare section using randomly chosen kinematics of the falling motions. In these test cases, it has been found that the modelled forces are comparable to the CFD even after separations of the free surface at the upper knuckle.

The CFD method has been applied to get more insight in the three-dimensional flow effects in slamming. More specifically, the truncated 3D bow flare model is studied in a constant speed water-entry problem. The study reveals that, at least for the investigated case,

- The total impulse obtained by a 2D strip integration is comparable to the full 3D simulation even though the slamming forces compared on each segment show an initial over-prediction due to the assumption of the two-dimensional flow. The impact force is less pronounced in the full 3D simulation because the fluid can escape more freely causing the pressure distribution to be smaller in magnitude than observed in the 2D simulations. The over-predicted peak forces have a limited contribution to the total impulse. Less CPU time is required when using the 2D strip approach and the total impulse can be applied in an explicit whipping analysis. However, there is a large uncertainty in choosing the longitudinal extension of the critical slamming area to be included in the 2D impulse calculation.

The application of the CFD method can be extended for an implicit slamming evaluation in realistic sea states. This has been done in the current project using the developed numerical wave tank. Regular waves are introduced into the domain by imposing high-order stream-function wave solutions at the wave-maker boundary. In order to prevent waves from reflecting back into the domain, a relaxation zone is introduced at the outlet with the local relaxation coefficient adaptively modified according to the local flow condition. An important conclusion can be made on the present wave generation and relaxation framework. That is

- The explicit relaxation of the primitive variables is done locally on each cell. The strong Stokes drift of the nonlinear regular wave causes the relaxation mechanism to fail keeping a balance of the net volume flux in the transient phase where the first wave train has not yet reached the outlet. This occurs mainly in the early transient stage causing an accumulation of water inside the numerical tank. In deep water, the additional water does not affect the wave profile much but in shallow water the disturbance can be significant depending on the particular wave system.

Further investigations of the bow flare slamming were done in deep water using conditional waves derived by FORM (First-Order Reliability Method) with the target responses evaluated using a nonlinear time-domain strip theory. The conditional wave provides the most probable wave scenarios leading to a predefined response value of VBM amidships. In three different wave scenarios, it is shown that the target responses evaluated by the CFD method occur at approximately the same time as predicted by the nonlinear strip theory. This makes it possible to use a MCF (Model-Correction Factor) approach to derive useful statistical properties of the CFD results. Using the MCF approach, there is no need to apply the resource demanding CFD method directly in the statistical evaluation. Instead, a simplified and efficient but less accurate model can be applied to derive the statistical properties. The MCF approach should make the results of the simplified model as accurate as the CFD results.

It is obvious that the contribution from slamming-induced whipping can not be quantified due to the rigid body assumption. Nevertheless, the most important insight achieved from this study can be summarized as follows:

- Without occurrences of severe slamming, the results show a strong indicator of the possible use of the model-correction factor approach. However, there is a need for a good slamming prediction in the simplified model. Given a wave scenario, it is important not only to predict a reasonable slamming load, but also the occurrence of slamming which is consistent with the slamming prediction in the CFD method.

The numerical predictions of VBM on an elastic model of the 9,400 TEU container vessel yield a reasonable agreement with the experimental results where the contribution from the elastic deformation to the VBM is small. The comparisons were done in full scale where the results of the measurements are scaled using the Froude's scaling law. In one case (Case IV), there is a resonance effect where the fourth harmonic of the response coincides with the wetted 2-node vertical bending mode. In this case, the numerically predicted VBM also predicts a resonance effect except that the magnitude of the response is smaller than the measurements. Comparing the dry natural frequencies of 2-node and 3-node vertical bending modes, the numerical prediction using the non-uniform Timoshenko beam is very similar to the model tests. The mode shape of the 3-node mode, however, does not agree; maybe due to the difficulty in extracting the mode shapes from weak and inaccurate measurements. Unfortunately, there are many indicators showing several inconsistencies between the measurements and the numerical results.

8.2 Suggestions for Further Work

It is possible to use the free surface CFD method for a direct calculation of slamming and slamming-induced responses. The slamming loads as well as the structural responses are evaluated implicitly in a realistic sea state. Even though the accuracy is in many cases shown to be acceptable, there are still many issues, which need further investigation and development. The work involves four major components:

- **Flow solver**: One of the important issues with the flow solver is the handling of the free surface. The present VOF-based flow solver uses the VOF formulation where the transport equation for the phase fraction is solved for with an additional artificial compressive term. This has proved to be sufficient in many cases, but the break-up of the free surface and jet-flow remains inconsistent and inaccurate. The problem relates directly to the discretization of the convective term in the transport equation. Thus, there is a need for a better convective scheme where the convection of the free surface is performed accurately and at the same time keeping the free surface reasonably sharp. On the other hand, a sharp interface may cause problems for the spatial discretization of the convective term in the momentum equations. The reconstruction of the solution field must be able to handle an abrupt discontinuity in the domain. A good candidate is e.g. a finite-volume weighted essentially non-oscillatory (WENO) schemes, see Hu & Shu (1999). Additional features, which are interesting for slamming related problems, are compressibility effects, air-trapping and air-entrainment.

- **Structural solver**: The use of the classical non-uniform Timoshenko beam is restricted to solve head sea problems. While the current implementation requires more work on validation, the Timoshenko beam model eventually should be replaced by a more sophisticated structural solver where the torsion in the hull girder can be accounted for accurately and efficiently. Recent publications have shown that the modal approach to solve a linear FE model for the structural responses may be more accurate in predicting the torsion than the beam model, see Oberhagemann et al. (2012).

- **Wave generation and absorption**: The present wave framework is stable and versatile and can be applied at the outlet as well as at inlet. Still, there is a need for a better generation and relaxation technique, which can handle the volume flux correctly.

- **Short-term statistical analysis**: The present investigation of the possible use of the MCF approach should be extended to account for the flexibility of the hull girder.

Moreover, the slamming-related issues encountered in a practical engineering application are related not only to the structural design but also to operation of the vessel. At the current stage, the CFD approach has the potential to be further developed for resolving these issues.

References

Aalberts, P. J. and Nieuwenhuijs, M. W. (2006). Full scale wave and whipping induced hull girder loads. In *Proceedings of the* 4th *International Conference on Hydroelasticity in Marine Technology*, pages 65–78.

Aarsnes, J. V. (1996). Drop test with ship sections - effect of roll angle. *Report 603834.00.01. NTNU, Trondheim.*

Aitken, A. (1926). On Bernoulli's numerical solution of algebraic equations. In *Proceedings of the Royal Society of Edinburgh*, number 46, pages 289–305.

Andersen, I. M. V. and Jensen, J. J. (2012). On the effect of hull girder flexibility on the vertical wave bending moment for ultra large container vessels. In *OMAE2012-83043*.

Ascher, U. M., Ruuth, S. J., and Wetton, B. T. R. (1997). Implicit-explicit methods for time-dependent PDEs. *SIAM J. Numer. Anal*, 32:797–823.

Batina, J. T. (1990). Unsteady Euler airfoil solutions using unstructured dynamic meshes. *AIAA Journal*, 28(8):1381–1388.

Beji, S. and Battjes, J. (1993). Experimental investigation of wave propagation over a bar. *Journal of Coastal Engineering*, 19(1-2):151–162.

Belytschko, T., Liu, W. K., and Moran, B. (2000). *Nonlinear Finite Elements for Continua and Structures.* John Wiley and Sons, Ltd., New York.

Berberović, E., van Hinsberg, N. P., Jakirlić, S., Roisman, I. V., and Tropea, C. (2009). Drop impact onto a liquid layer of finite thickness: Dynamics of the cavity evolution. *Phys. Rev. E*, 79.

Bertram, V. (2000). *Practical Ship Hydrodynamics.* Elsevier.

Bishop, R. E. D. and Price, W. G. (1979). *Hydroelasticity of Ships.* Cambridge University Press.

Bjerager, P. (1991). Methods for structural reliability computation. In Casciati, F. and Roberts, J. B., editors, *Reliability problems: general principles and applications in mechanics of solid and structures*, pages 89–136. New York: Springer Verlag Wien.

Bos, F. M. (2009). *Numerical simulations of flapping foil and wing aerodynamics: Mesh deformation using radial basis functions.* PhD thesis, Delft University of Technology, Netherlands.

Bredmose, H. and Bullock, G. N. (2008). Scaling of wave-impact pressures in trapped air pockets. In *Proceedings of the* 23rd *International Workshop on Water Waves and Floating Bodies, 2008, IWWWFB, Jeju Island, Korea.*

Brizzolara, S., Couty, N., Hermundstad, O., Ioan, A., Kukkanen, T., Viviani, M., and Temarel, P. (2008). Comparison of experimental and numerical loads on an impacting bow section. *Ships and Offshore Structures*, 3(4):305–324.

Bucher, C. (2009). Asymptotic sampling for high-dimensional reliability analysis. *Probabilistic Engineering Mechanics*, 24:504–510.

Bullock, G. N., Obhrai, C., Peregrine, D. H., and Bredmose, H. (2007). Violent breaking wave impacts. part 1: Results from large-scale regular wave tests on vertical and sloping walls. *Coastal Engineering*, 54(8):602–617.

Cabos, C., Dilba, B., Krömer, M., and Schwenkenberg, A. (2011). Modal approach to fluid structure interaction applied to a ship in waves. In *Proceedings of the 3rd International Conference on Marine Structures, MARSTRUCT 2011, Hamburg, Germeny*, pages 9–17.

Campbell, I. and Weynberg, P. (1980). *Measurement of Parameters Affecting Slamming.* Report - University of Southampton, Dept. of Aeronautics and Astronautics. University of Southampton, Department of Aeronautics and Astronautics.

Chapalain, G., Cointe, R., and Temperville, A. (1992). Observed and modeled resonantly interacting progressive water-waves. *Coastal Engineering*, 16(3):267 – 300.

Chen, H., Patel, V., and Ju, S. (1990). Solutions of Reynolds-averaged Navier-Stokes equations for three-dimensional incompressible flows. *Journal of Computational Physics*, 88(2):305 – 336.

Chen, H. C., Lee, S. K., and Seah, A. K. (2008). Overset grid CFD applications for challenging offshore hydrodynamic problems. In *ABS TECHNICAL PAPERS 2008*, pages 111–117.

Clément, A. (1996). Coupling of two absorbing boundary conditions for 2D time-domain simulations of free surface gravity waves. *Journal of Computational Physic*, 126:139–151.

Cointe, R. (1991). Free surface flows close to a surface-piercing body. In Miloh, T., editor, *Mathematical Approaches in Hydrodynamics, SIAM*, pages 319–334.

Colicchio, G., Colagrossi, A., Greco, M., and Landrini, M. (2002). Free-Surface Flow After a Dam Break: A Comparative Study. *Ship Technology Research - Shiffstechnik*, 49(3):95–104.

Collatz, L. (1963). *Eigenwertaufgaben mit technischen anwendungen.* Akademische Verlagsgesellschaft, Leipzig.

Dean, R. G. and Dalrymple, R. A. (1991). *Water Wave Mechanics For Engineers And Scientists.* World Scientific Publishing Co. Pte. Ltd.

Demirdžić, I. A. (1982). *A finite volume method for computation of fluid flow in complex geometries*. PhD thesis, University of London.

Demirdžić, I. and Perić, M. (1988). Space conservation law in finite volume calculations of fluid flow. *International Journal for Numerical Methods in Fluids*, 8(9):1037–1050.

Ditlevsen, O. and Arnbjerg-Nielsen, T. (1994). Model-correction-factor method in structural reliability. *Journal of Engineering Mechanics*, 120:1–10.

Dobrovol'skaya, Z. N. (1969). On some problems of similarity flow of fluid with a free surface. *J. Fluid Mech.*, 36:805–829.

Donea, J. and Huerta, A. (2003). *Finite Element Methods for Flow Problems*. Wiley, Chichester.

Engsig-Karup, A. P. (2006). *Unstructured Nodal DG-FEM Solution of High-order Boussinesq-type Equations*. PhD thesis, Technical University of Denmark.

Fairlie-Clarke, A. C. and Tveitnes, T. (2008). Momentum and gravity effects during the constant velocity water entry of wedge-shaped sections. *Ocean Engineering*, 35(7):706–716.

Faltinsen, O., Kjærland, O., Nøttveit, A., and Vinje, T. (1977). Water impact loads and dynamic response of horizontal circular cylinders in offshore structures. In *Offshore Technology Conference, 2-5 May, Houston, Texas*.

Faltinsen, O. M. (1993). *Sea Loads on Ships and Offshore Structures*. Cambridge University Press.

Farhat, C., Degand, C., Koobus, B., and Lesoinne, M. (1998). Torsional springs for two-dimensional dynamic unstructured meshes. *Comput. Methods Appt. Mech. Engrg.*, 163:231–245.

Fenton, J. D. (1988). The numerical solution of steady water wave problems. *Computers and Geosciences*, 14:357–368.

Ferziger, J. H. and Perić, M. (2001). *Computational Methods for Fluid Dynamics*. Springer, 3rd edition.

Fowler, J. (1958). Generalized missile dynamics analysis: Calculation of bending modes. Technical report, Space Technology Labs, Rep. No. EM 8-16, GM-TR-0165-00445.

Franck, R. M. and Lazarus, R. B. (1964). Mixed Eulerian-Lagrangian method. *Methods in Computational Physics*, 3:47–67.

Fuhrman, D. R. (2004). *Numerical Solutions of Boussinesq Equations for Fully Nonlinear and Extremely Dispersive Water Waves*. PhD thesis, Technical University of Denmark.

Garré, L., Friis-Hansen, P., and Rizzuto, E. (2006). The model correction factor method: an efficient response surface technique. In 3rd *Internaltional ASRANet Colloquium, Glasgow, UK*.

Greenhow, M. and Lin, W. M. (1983). Nonlinear free surface effects: Experiments and theory. *MIT Report No. 83-19*.

Greenhow, M. and Lin, W. M. (1985). Numerical simulation of nonlinear free surface flows generated by wedge entry and wavemaker motions. In 4th *International Conference on Numerical Ship Hydrodynamics, Washington, DC*.

Hänninen, S. K., Mikkola, T., and Matusiak, J. (2012). On the numerical accuracy of the wave load distribution on a ship advancing in short and steep waves. *Journal of Marine Science and Technology*, 17:125–138.

Hasofer, A. M. and Lind, N. (1974). Exact and invariant second moment code format. *J. Eng. Mechanics Div.*, 100:111–121.

Hirdaris, S. E., Miao, S. H., and Temarel, P. (2009). The effect of structural discontinuity on antisymmetric response of a container ship. In *Proceedings of the 5th International Conference on Hydroelasticity in Marine Technology*, pages 57–68.

Hirt, C. and Nichols, B. (1981). Volume of fluid (VOF) method for the dynamics of free boundaries. *Journal of Computational Physics*, 39.

Hirt, C. W., Amsden, A. A., and Cook, J. L. (1974). An Arbitrary Lagrangian-Eulerian computing method for all flow speeds. *Journal of Computational Physics*, 14:227–253.

Howison, S. D., Ockendon, J. R., and Wilson, S. K. (1991). Incompressible water-entry problems at small deadrise angles. *J. Fluid Mech.*, 222:215–230.

Hu, C. and Shu, C. W. (1999). Weighted essentially non-oscillatory schemes on triangular meshes. *Journal of Computational Physics*, 150(1):97 – 127.

Inman, D. J. (2001). *Engingeering Vibration*. Prentice Hall International, Inc.

Issa, R. I. (1985). Solution of the Implicitly Discretised Fluid Flow Equations by Operator-Splitting. *Journal of Computational Physics*, 62:40–65.

Jacobsen, N. G. (2011). *A Full Hydro- and Morphodynamic Description of Breaker Bar Development*. PhD thesis, Technical University of Denmark.

Jacobsen, N. G., Fuhrman, D. R., and Fredsøe, J. (2012). A Wave Generation Toolbox for the Open-Source CFD Library: OpenFOAM® . *International Journal for Numerical Methods in Fluids*, 70(9):1073–1088.

JAIC (1997). Final report on the capsizing on 28 September 1994 in the Baltic sea of the ro-ro passenger vessel MV Estonia. *Helsinki, Finland*.

Jasak, H. (1996). *Error analysis and estimation for the Finite Volume method with applications to fluid flows*. PhD thesis, Imperial College, University of London.

Jasak, H. and Tuković, Z. (2007). Automatic mesh motion for the unstructured finite volume method. *Transactions of FAMENA*, v30.

Jasak, H. and Weller, H. (2000). Application of the finite volume method and unstructured meshes to linear elasticity. *Int. J. Num. Meth. Engineering*, 48:267–287.

Jasak, H., Weller, H., and Nordin, N. (2004). In-Cylinder CFD Simulation Using a C++ Object-Oriented Toolkit. *SAE Technical Paper 2004-01-0110, 2004, doi:10.4271/2004-01-0110.*

Jensen, J. J. (2001). *Load and Global Response of Ships*, volume 4. Elsevier Science Ltd.

Jensen, J. J. (2009). Stochastic procedures for extreme wave load predictions - wave bending moment in ships. *Marine Structures*, 22:194–208.

Jensen, J. J. (2011). Extreme value predictions using Monte Carlo simulations with artificially increased load spectrum. *Probabilistic Engineering Mechanics*, 26:399–404.

Jensen, J. J. and Capul, J. (2006). Extreme response predictions for jack-up units in second order stochastic waves by FORM. *Probabilistic Engineering Mechanics*, 21:330–337.

Jensen, J. J. and Madsen, N. F. (1977). A review of ship hull vibration. *Shock and Vibr. Digest*, 9(4-6).

Jensen, J. J., Olsen, A. S., and Mansour, A. E. (2011). Extreme wave and wind response predictions. *Ocean Engineering*, 38:2244–2253.

Jensen, J. J., Pedersen, P. T., Shi, B., Wang, S., Petricic, M., and Mansour, A. (2009). *Wave induced extreme hull girder loads on containerships*, volume 116, pages 128–152. Society of Naval Architects and Marine Engineers, The.

Johnson, A. A. and Tezduya, T. E. (1994). Mesh update stategies in parallel finite element computations of flow problems with moving boundaries and interfaces. *Comput. Methods Appt. Mech. Engrg.*, 119:73–94.

Kapsenberg, G. K. and Thornhill, E. T. (2010). A practical approach to ship slamming in waves. In *Proc. 8th Symp. on Naval Hydrodynamics, Pasadena, CA.*

Kim, S. K., Novak, D., Weems, K. M., and Chen, H.-C. (2008). Slamming impact design loads on large high speed naval craft. In *SuperFAST 2008 International Conference, Saint-Petersburg, Russia.*

Kim, W., Van, D., and Kim, D. (2001). Measurement of flows around modern commercial ship models. *Exp. in Fluids*, 31:567–578.

Kleefsman, K., Fekken, G., Veldmann, A., Iwanowski, B., and Buchner, B. (2005). A volume-of-fluid based simulation method for wave impact problems. *Journal of Computational Physics*, 206(1):363–393.

Korobkin, A. (2004). Analytical models of water impact. *Euro. J. Appl. Math.*, 15:821–838.

Korobkin, A. and Scolan, Y. (2006). Three dimensional theory of water impact. part 2: Linearized Wagner problem. *Journal of Fluid Mechanic*, 549:343–373.

Korobkin, A. A. (2012). Decomposition of pressure and force in slamming models. Technical Note TULCS WP5, (unpublished).

Krenk, S. (2006). State-space time integration with energy control and fourth-order accuracy for linear dynamic systems. *International Journal for Numerical Methods in Engineering*, 65(5):595–619.

Landweber, L. and Macagno, M. (1967). Added masses of two-dimensional forms by conformal mapping. *Journal of Ship Research*, 11:109–116.

Liu, Y. and Yue, D. K. P. (1998). On generalized Bragg scattering of surface waves by bottom ripples. *Journal of Fluid Mechanics*, 356:297–326.

Logvinovich, G. (1969). *Hydrodynamics of flows with free boundaries.* Naukova Dumka, Translated from Russian by Lederman, D., Israel Program for Scientific Translations Ltd. 1972.

Luppes, R., Veldman, A. E., and Wellens, P. R. (2010). Absorbing boundary conditions for wave simulations around offshore structures. In Pereira, J. C. F. and Sequeira, A., editors, *Proc. ECCOMAS CFD 2010 Lisbon.*

Löhner, R. and Yang, C. (1996). Improved ALE mesh velocities for moving bodies. *Communications in Numerical Methods in Engineering*, 12:599–608.

Madsen, P. and Sørensen, O. (1993). Bound waves and triad interactions in shallow water. *Ocean Engineering*, 20(4):359 – 388.

MAIB (2008). Report on the investigation of the structural failture of MSC Napoli, English Channel on 18 January 2007. MAIB Report No. 9/2008.

Marsden, J. E. and Ratiu, T. S. (1999). *Introduction to Mechanics and Symmetry: A Basic Exposition of Classical Mechanical Systems.* Springer, New York.

Mayer, S., Garapon, A., and Sørensen, L. S. (1998). A fractional step method for unsteady free-surface flow with applications to non-linear wave dynamics. *Int. J. Numer. Meth. Fluids*, 28:293 – 315.

Mei, X., Liu, Y., and Yue, D. K. P. (1998). On the water impact of general two-dimentional sections. *Applied Ocean Research*, 21:1–15.

Melchers, R. E. (1999). *Structural Reliability: Analysis and Prediction.* John Wiley & Sons Ltd.

Mittal, R. and Iaccarino, G. (2005). Immersed Boundary Methods. *Annu. Rev. Fluid Mech.*, 37:239–261.

Miyake, R., Matsumoto, T., Zhu, T., Usami, A., and Dobashi, H. (2009). Experimental studies on the hydroelastic responses using a flexible mega-container ship model. In *Proceedings of the 5th International Conference on Hydroelasticity in Marine Technology*, pages 161–171.

Muzaferija, S. (1994). *Adaptive Finite Volume Method for Flow Prediction Using Unstructured Meshes and Multigrid Approach.* PhD thesis, Imperial College, University of London.

Muzaferija, S., Peric, M., Sames, P., and Schellin, T. (1999). A two-fluid Navier-Stokes solver to simulate water entry. *Twenty-Second Symposium on Naval Hydrodynamics*, pages 638–651.

Naess, A., Leira, B. J., and Batsevych, O. (2009). System reliability analysis by enhanced Monte Carlo simulation. *Structural Safety*, 31:349–355.

Newman, J. N. (1977). *Marine Hydrodynamics.* Cambridge. The MIT Press.

Nichols, B. and Hirt, C. (1975). Methods for calculating multi-dimensional, transient free surface flows past bodies. In *Proc. First Intern. Conf. Num. Ship Hydrodynamics, Gaithersburg, ML, USA, Oct. 20-23.*

Nielsen, K. B. (2003). *Numerical Prediction of Green Water Loads on Ships.* PhD thesis, Technical University of Denmark.

Nishijima, K., Qin, J., and Faber, M. (2010). A scalable parametric approximation to multi-normal probability integrals. In *Proceedings IFIP WG 7.5, The 15th Scientific Meeting of the IFIP Working Group on Reliability and Optimization of Structural Systems, Munich, Germany, April 7-10, 2010.*

Noh, W. F. (1964). A time-dependent two-space dimensional coupled Eulerian-Lagrangian code. *Methods in Computational Physics*, 3:117–179.

Oberhagemann, J., El Moctar, O., Holtmann, M., Schellin, T., Bertram, V., and Kim, D. (2008). Numerical simulation of stern slamming and whipping. In *11th Numerical Towing Tank Symposium (NuTTS), Aberwrach.*

Oberhagemann, J., Krömer, M., Cabos, C., and el Moctar, O. (2012). A fluid-structure coupling method based on field methods and a structural mode decomposition. In *Proceedings of the 6th International Conference on Hydroelasticity in Marine Technology, Tokyo, Japan*, pages 267–276.

Ochi, M. K. (1964a). Extreme behavior of a ship in rough seas: slamming and shipping of green water. In *SNAME Annual Meeting, New York, NY.*

Ochi, M. K. (1964b). Prediction of occurrence and severity of ship slamming at sea. In *Proc. 5th Symp. on Naval Hydrodynamics, Bergen, Norway. Washington, DC: National Academy Press.*

Ochi, M. K. and Motter, L. E. (1974). Prediction of extreme ship responses in rough seas of the North Athlantic. In *Proc. Int. Symp. Dynamics of Marine Vehicles and Structures in Waves*, pages 187–197.

OpenFOAM (2012). *OpenFOAM The Open Source CFD Toolbox: Programmer's Guide*, version 2.1.1 edition.

Osher, S. and Sethian, J. A. (1988). Fronts Propagating with Curvature-Dependent Speed: Algorithms Based on Hamilton-Jacobi Formulations. *J. Computational Phys.*, 79(1):12–49.

Patankar, S. V. (1980). *Numerical Heat Transfer and Fluid Flow.* Taylor & Francis.

Payne, P. R. (1994). Recent Developments in Added-Mass Planing Theory. *Ocean Engineering*, 21(3):257–309.

Payne, P. R. (1995). Contributions to Planing Theory. *Ocean Engineering*, 22(7):699–729.

Pedersen, P. and J.J., J. (2009). Estimation of hull girder vertical bending moments including non-linear and flexibility effects using closed form expressions. *Proc. IMechE, Part M: J. Engineering for the Maritime Environment*, 223(3):377–390.

Rezende, F. and Chen, X. (2008). Bureau veritas report on load and strength assessment. MSC Napoli - ultimate strength analysis. *Marine Accident Investigation Branch, UK, MAIB Report No. 9/2008 Annex E.*

Rhie, C. M. and Chow, W. L. (1983). Numerical study of the turbulent flow past an airfoil with trailing edge separation. *AIAA Journal*, 21:1525–1532.

Rienecker, M. M. and Fenton, J. D. (1981). A Fourier approximation method for steady water waves. *Journal of Fluid Mechanics*, 104:119–137.

Rosenblatt, M. (1952). Remarks on a multivariate transformation. *Annals of Mathematical Statistic*, 23:470–472.

Rusche, H. (2002). *Computational Fluid Dynamics of Dispersed Two-Phase Flows at High Phase Fractions.* PhD thesis, Imperial College of Science, Technology & Medicine.

Salvesen, N., Tuck, E. O., and Faltinsen, O. (1970). Ship motions and sea loads. *Trans. SNAME*, 78:250–287.

Sand, S. E. (1979). Three-dimensional deterministic structure of ocean waves. *Series Paper No. 24, Institute of Hydrodynamics and Hydraulic Engineering, Technical University of Denmark.*

Scanlan, R. H. (1948). A note on transverse bending of beams having both translating and rotating mass elements. *J. Aeron. Sci.*, 15(7):425–426.

Scolan, Y. and Korobkin, A. (2001). Three dimensional theory of water impact. part 1: Inverse Wagner problem. *Journal of Fluid Mechanic*, 440:293–326.

Seng, S., Andersen, I. M. V., and Jensen, J. J. (2012). On the influence of hull girder flexibility on the wave induced bending. In *Proceedings of the 6th International Conference on Hydroelasticity in Marine Technology, Tokyo, Japan*, pages 341–353.

Seng, S. and Jensen, J. J. (2012). Slamming simulations in a conditional wave. In *ASME Conference Proceedings, OMAE2012-83310.* ASME.

Senjanović, I., Tomašević, S., Vladimir, N., Tomić, M., and Malenica, v. (2009). Ship hydroelastic analysis with sophisticated beam model and consistent restoring stiffness. In *Proceedings of the 5th International Conference on Hydroelasticity in Marine Technology*, pages 69–80.

SNAME (1950). Nomenclature for treating the motion of a submerged body through a fluid. *The Society of Naval Architects and Marine Engineers*, Technical and Reserach Bulletin No. 1-5:1–15.

Svendsen, I. A. (2006). *Introduction To Nearshore Hydrodynamics.* World Scientific Publishing Co. Pte. Ltd.

Temarel, P., Chen, X., Engle, A., Hermanski, G., Jankowski, J., Kapsenberg, G., Kawabe, H., Kruger, S., Kukkanen, T., Mavrakos, S., Pastoor, W., Pedersen, B., Ren, H., Sebastiani, L., and Xia, J. (2006). [report of] issc committee: Loads. In Frieze, P. and Shenoi, R. A., editors, *Proceedings of the 16th International Ship and Offshore Structures Congress (v.1)*, volume 1, page 68pp. University of Southampton.

Thomas, P. D. and Lombard, C. K. (1979). Geometric Conservation Law and Its Application to Flow Computations on Moving Grids. *AIAA Journal*, 17:1030–1037.

Tuitman, J. T. and Malenica, Š. (2009). Fully coupled seakeeping, slamming, and whipping calculations. *Proceedings of the Institution of Mechanical Engineers, Part M: Journal of Engineering for the Maritime Environment*, 223(3):439–456.

Tveitnes, T., Fairlie-Clarke, A., and Varyani, K. (2008). An experimental investigation into the constant velocity water entry of wedge-shaped sections. *Ocean Engineering*, 35:1463–1478.

Ubbink, O. and Issa, R. (1999). Method for capturing sharp fluid interfaces on arbitrary meshes. *J. Comput. Phys.*, 153:26–50.

von Kerczek, C. and Tuck, E. (1964). The representation of ship hulls by conformal mapping functions. *Journal of Ship Research*, 13:284–298.

von Kármán, T. (1929). The impact on seaplane floats during landing. *NACA Technical Note No. 321, Washington DC, USA.*

Wagner, H. (1932). Über stoss- und gleitvorgänge an der oberfläche von flüssigkeiten. *Zeitschriff fur Angewandte Mathematik und Mechanik*, 12(4):193–215.

Warsi, Z. U. A. (1981). Conservation form of the Navier-Stokes equations in general nonsteady coordinates. *AIAA Journal*, 19(2):240–242.

Weller, H. G. (2002). Derivation, modelling and solution of the conditionally averaged two-phase flow equations. Technical Report TR/HGW/02, Nabla Ltd. (unpublished).

Weller, H. G., Tabor, G., Jasak, H., and Fureby, C. (1998). A tensorial approach to computational continuum mechanics using object orientated techniques. *Computers in physics*, 12:620–631.

Xia, J., Wang, Z., and Jensen, J. (1998). Non-linear wave loads and ship responses by a time-domain strip theory. *Marine Structures*, 11:101–123.

Yamamato, Y., Iida, K., Fukasawa, T., Murakami, T., Arai, M., and Ando, A. (1985). Structural damage analysis of a fast ship due to bow flare slamming. *Int. Shipbuild. Progr.*, 32:124–136.

Yettou, E.-M., Desrochers, A., and Champoux, Y. (2006). Experimental study on the water impact of a symmetrical wedge. *Fluid Dynamics Research*, 38(1):47–66.

Yettou, E.-M., Desrochers, A., and Champoux, Y. (2007). A new analytical model for pressure estimation of symmetrical water impact of a rigid wedge at variable velocities. *Journal of Fluids and Structures*, 23(3):501–522.

Youngs, D. L. (1982). Time-dependent multi-material flow with large fluid distortion. In Morton, K. W. and Baines, M. J., editors, *Numerical Methods for Fluid Dynamics*, pages 273–285. Academic Press.

Yu, K. and Chen, H. C. (2007). Chimera RANS simulations of slamming and wave overtopping around offshore structures. In *Proceedings of the 17th (2007) International Offshore and Polar Engineering Conference, July 1-6, Lisbon, Portugal*, page 3642.

Zhang, Y., Zou, Q., Greaves, D., Reeve, D., Hunt-Raby, A., Graham, D., James, P., and Lv, X. (2010). A Level Set Immersed Boundary Method for Water Entry and Exit. *Commun. Comput. Phys.*, 8:265–288.

Zhao, R. and Faltinsen, O. (1993). Water entry of twodimensional bodies. *Journal of Fluid Mechanics*, 246:593–612.

Zhao, R., Faltinsen, O., and Aarsnes, J. (1996). Water entry of arbitrary two-dimensional sections with and wihtout flow separation. In *Proceedings of the Twenty-First Symposium on Naval Hydrodynamics*, pages 408–423.

Zhou, Z. Q., Kat, J. O. D., and Buchner, B. (1999). A nonlinear 3D approach to simulate green water dynamics on deck. In *7th Intl. Conf. Num. Ship Hydrodynamics, Nantes*, pages 1–4.

Zhu, S., Wu, M., and Moan, T. (2011). Experimental investigation of hull girder vibrations of a flexible backbone model in bending and torsion. *Applied Ocean Research*, 33:252–274.

Appendix A

Artificial Compressive Term

Using a VOF technique to capture the free surface in an incompressible flow, the volume fraction α is freely convected with the flow. The transport equation follows directly from the principle of mass conservation and yields,

$$\frac{\partial \alpha}{\partial t} + \nabla \cdot (\alpha \boldsymbol{u}) = 0 \tag{A.1}$$

where the incompressible fluid requires $\nabla \cdot \boldsymbol{u} = 0$ and by definition $\alpha = [0,\, 1]$. There are many difficulties associated with obtaining a numerical solution of the transport equation. Many numerical techniques have been developed to deal with two common problems: (1) the boundedness constraint is difficult to obey and (2) the numerical diffusion is causing a diffusive interface.

In 2002, Weller (2002) made an unpublished note on introduction of an artificial compressive term into the transport equation. The new term helps to keep the interface sharp and has been adopted in Rusche (2002) and in the open-source toolbox OpenFOAM. A brief description can also be found in Berberović et al. (2009). A discussion on the mathematical justification and on the physical aspect of the formulation are provided in the following. The modified equations read

$$\frac{\partial \alpha}{\partial t} + \nabla \cdot (\alpha \boldsymbol{u}) + \nabla \cdot \gamma \boldsymbol{u}_r = 0 \tag{A.2}$$

$$\boldsymbol{u}_r \equiv \boldsymbol{u}_a - \boldsymbol{u}_b \tag{A.3}$$

$$\boldsymbol{u} \equiv \alpha \boldsymbol{u}_a + (1-\alpha)\boldsymbol{u}_b \tag{A.4}$$

where $\gamma \equiv \alpha(1-\alpha)$. In the above expression, $\boldsymbol{u}_r$ is the relative velocity between fluid a (water) and fluid b (air). The convective velocity is evaluated as a weighted average between the two fluids. The relative velocity is unknown and must be modelled. While there are many possible model for $\boldsymbol{u}_r$, the model implemented in OpenFOAM is (cf. Rusche (2002) and Berberović et al. (2009))

$$\boldsymbol{u}_{r,f} \equiv \boldsymbol{n}_f \min\left[C_\alpha \frac{|\phi|}{|\boldsymbol{S}_f|}, \max \frac{|\phi|}{|\boldsymbol{S}_f|}\right] \tag{A.5}$$

where the subscript f denotes the surface of the control volume, $|\phi|$ is the absolute

volume metric flux across the surface, $|\boldsymbol{S}_f|$ represents the area and $\boldsymbol{n}_f$ is the unit normal vector of the interface which can be evaluated as

$$\boldsymbol{n}_f = \frac{\nabla \alpha_f}{|\nabla \alpha_f| + \delta} \tag{A.6}$$

where δ is a very small numerical stabilization term to prevent problems in case $|\nabla \alpha_f| \approx 0$.

It is clear to see that the compressive term, i.e. the third term in Eq. (A.2), is only active within the interface region due to the coefficient γ becomes exactly 0 for $\alpha = 0$ or $\alpha = 1$. The non-zero value for γ can be found at the smeared out interface where α is between $]0, 1[$. Mathematically, the artificial compressive term comes from a two-fluid formulation where each fluid is described separately using two different sets of equations where each set is weighed by the phase fraction α. The mass conservation law applied to each fluid yields,

$$\text{Fluid } a \text{ (water):} \quad \frac{\partial \alpha}{\partial t} + \nabla \cdot (\alpha \boldsymbol{u}_a) = 0 \tag{A.7}$$

$$\text{Fluid } b \text{ (air):} \quad \frac{\partial (1-\alpha)}{\partial t} + \nabla \cdot \Big[(1-\alpha)\boldsymbol{u}_b\Big] = 0 \tag{A.8}$$

which can be expanded to

$$\text{Fluid } a \text{ (water):} \quad \frac{\partial \alpha}{\partial t} + \boldsymbol{u}_a \cdot \nabla \alpha + \alpha \nabla \cdot \boldsymbol{u}_a = 0 \tag{A.9}$$

$$\text{Fluid } b \text{ (air):} \quad \frac{\partial \alpha}{\partial t} + \boldsymbol{u}_b \cdot \nabla \alpha - (1-\alpha) \nabla \cdot \boldsymbol{u}_b = 0 \tag{A.10}$$

Thus, Eqs. (A.7) and (A.8) are equivalent taken that u_a is the same as u_b and they are divergence free. Using Eq. (A.4) with some simple manipulation it can be verified that

$$\alpha \boldsymbol{u}_a = \alpha \boldsymbol{u} + \gamma \boldsymbol{u}_r \tag{A.11}$$

i.e. the modified transport equation (Eq. (A.2)) is essentially the same as the transport equation for fluid a (water) Eq. (A.7). Furthermore, the divergence of Eq. (A.4) is

$$\nabla \cdot \boldsymbol{u} = \nabla \cdot [\alpha \boldsymbol{u}_a + (1-\alpha)\boldsymbol{u}_b] \tag{A.12}$$

$$= (\boldsymbol{u}_a - \boldsymbol{u}_b) \cdot \nabla \alpha + \alpha \nabla \cdot (\boldsymbol{u}_a - \boldsymbol{u}_b) + \nabla \cdot \boldsymbol{u}_b \tag{A.13}$$

Insert the divergence-free constraint in Eq. (A.13) and use the definition $\boldsymbol{u}_r \equiv \boldsymbol{u}_a - \boldsymbol{u}_b$ yields

$$\boldsymbol{u}_r \cdot \nabla \alpha = 0 \tag{A.14}$$

which must be satisfied everywhere in the domain. It is important to note that this constraint is a direct consequence of applying Eq. (A.4) to describe the two-phase flow using the single fluid formulation. The gradient of α is zero everywhere except at the interface where α has a variation between $]0, 1[$. That is, by definition, the relative velocity $\boldsymbol{u}_r$ must be zero at the interface and the modified Eq. (A.2) becomes the same as Eq. (A.1).

Modelling $\boldsymbol{u}_r$ to be non-zero otherwise will introduce errors to the convection of the free surface. Assuming that the chosen model of $\boldsymbol{u}_r$ satisfies the divergence free condition, the non-conservative form of Eq. (A.2) is

$$\frac{\partial \alpha}{\partial t} + \Big[\boldsymbol{u} + \boldsymbol{u}_r(2\alpha - 1)\Big] \cdot \nabla \alpha = 0 \tag{A.15}$$

where the term $\boldsymbol{u}_r(2\alpha - 1)$ is the artificial convective velocity introduced into the velocity field. This term vanishes when $\alpha = 0.5$ which can be taken as the location of the sharp interface. Thus, in order to minimize the influence of the artificial compressive velocity on the convection of the free surface, it is important to model the relative velocity such that it is divergence free and its direction is always pointing normal to the nearest exact interface. The suggested and implemented model shown in Eq. (A.5) satisfies these criteria. Therefore, the main influence of the artificial compressive term is that the phase fraction field near the interface is compressed toward a sharper interface.

Appendix B

The Convective Velocity in ALE Formulation

The relation between the two domains can be described by a mapping function $\boldsymbol{\varphi}(\boldsymbol{X}, t)$ such that

$$(\boldsymbol{X}, t) \rightarrow \boldsymbol{\varphi}(\boldsymbol{X}, t) = (\boldsymbol{x}, t) \quad \Rightarrow \quad \begin{cases} \dfrac{\partial \boldsymbol{\varphi}}{\partial \boldsymbol{X}} = \dfrac{\partial \boldsymbol{x}}{\partial \boldsymbol{X}} \\ \dfrac{\partial \boldsymbol{\varphi}}{\partial t} = \dfrac{\partial \boldsymbol{x}}{\partial t}\Big|_{\boldsymbol{X}} + 1 \end{cases} \tag{B.1}$$

$$\Rightarrow \quad f_{\mathrm{L}}(\boldsymbol{X}, t) = f_{\mathrm{E}}(\boldsymbol{\varphi}(\boldsymbol{X}, t), t) \tag{B.2}$$

where $f_{\mathrm{L}}(\boldsymbol{X}, t)$ is some physical quantity in the Lagrangian frame and $f_{\mathrm{E}}(\boldsymbol{x}, t)$ is the same quantity described in the Eulerian frame. While the functional relation $\boldsymbol{x} = \boldsymbol{x}(\boldsymbol{X}, t)$ exists, the time variable t remains the same in the two reference domains. Evaluating the time derivative of $f_{\mathrm{L}}(\boldsymbol{X}, t)$ and apply the chain rule yields the relation between the material and the spatial time derivative

$$\frac{\partial f_{\mathrm{L}}}{\partial t}\Big|_{\boldsymbol{X}} = \frac{\partial f_{\mathrm{E}}}{\partial t}\Big|_{\boldsymbol{x}} + \boldsymbol{u} \cdot \nabla f_{\mathrm{E}} \tag{B.3}$$

where $\boldsymbol{u}(\boldsymbol{X}, t) \equiv \partial \boldsymbol{x}/\partial t|_{\boldsymbol{X}}$ is the velocity of the fluid particles. The notation $\partial \boldsymbol{x}/\partial t|_{\boldsymbol{X}}$ shall be understood as $\boldsymbol{x}$ is a functional form of $(\boldsymbol{X}, t)$ and $\boldsymbol{X}$ is held fixed while taking the first derivative of $\boldsymbol{x}$ with respect to t. Equation (B.3) is also known as the material derivative describing the rate of change of $f_{\mathrm{E}}(\boldsymbol{x}, t)$ subjected to a space and time dependent velocity field. The derivative $\partial f_{\mathrm{L}}/\partial t$ is the material derivative in the Lagrangian frame which is a simple time derivative since the mesh points coincide with the material points. Every mesh point represents a fluid particle in the Lagrangian formulation and as these particles move, the mesh can easily become too distorted and useless.

Using the Lagrangian frame, the computational mesh may become severely distorted when large material deformation occurs, e.g. vortex formation in the fluid. Thus, it is important to choose an appropriate reference domain. The choice determines the relationship between the continuum and the computational mesh, which has a strong influence on the ability, limitation and accuracy of the numerical

method.

A formulation combining the two kinematic descriptions known as the Arbitrary Lagrangian Eulerian (ALE) formulation was developed, see e.g. Noh (1964), Franck and Lazarus (1964), and Hirt et al. (1974). The fundamental ALE equation are described in many standard textbook, see e.g. Donea & Huerta (2003). The following derivation follows closely the demonstration presented in Donea & Huerta (2003).

The ALE formulation is a generalization of the Lagrangian and Eulerian descriptions and the computational mesh is independent from the material motion and can be moved in an arbitrary manner allowing complex body motions to be simulated. The reference domain is neither the Lagrangian domain nor the Eulerian domain. Instead a new arbitrary reference domain $(\boldsymbol{\chi}, t)$ is introduced with two mapping functions, Φ and Ψ. The mapping from the reference domain to the spatial (Eulerian) domain is done through Φ, i.e.

$$(\boldsymbol{\chi}, t) \rightarrow \boldsymbol{\Phi}(\boldsymbol{\chi}, t) = (\boldsymbol{x}, t) \quad \Rightarrow \quad \begin{cases} \dfrac{\partial \boldsymbol{\Phi}}{\partial \boldsymbol{\chi}} = \dfrac{\partial \boldsymbol{x}}{\partial \boldsymbol{\chi}} \\ \dfrac{\partial \boldsymbol{\Phi}}{\partial t} = \dfrac{\partial \boldsymbol{x}}{\partial t}\Big|_{\boldsymbol{\chi}} + 1 \end{cases} \tag{B.4}$$

The term $\partial \boldsymbol{x}/\partial t|_{\boldsymbol{\chi}}$ is the velocity of the Eulerian grid points as seen in the ALE reference domain. For convenience, we define mesh velocity $\boldsymbol{u}_m(\boldsymbol{\chi}, t) \equiv \partial \boldsymbol{x}/\partial t|_{\boldsymbol{\chi}}$ with the subscript m referred to the computational mesh. The mapping from the reference domain to the material (Lagrangian) domain can be defined conveniently using the inverse mapping Ψ^{-1}

$$(\boldsymbol{X}, t) \rightarrow \boldsymbol{\Psi}^{-1}(\boldsymbol{X}, t) = (\boldsymbol{\chi}, t) \quad \Rightarrow \quad \begin{cases} \dfrac{\partial \boldsymbol{\Psi}^{-1}}{\partial \boldsymbol{X}} = \dfrac{\partial \boldsymbol{\chi}}{\partial \boldsymbol{X}} \\ \dfrac{\partial \boldsymbol{\Psi}^{-1}}{\partial t} = \dfrac{\partial \boldsymbol{\chi}}{\partial t}\Big|_{\boldsymbol{X}} + 1 \end{cases} \tag{B.5}$$

such that the material mapping function $\boldsymbol{\varphi}$ can be written as

$$\boldsymbol{\varphi}(\boldsymbol{X}, t) = \boldsymbol{\Phi}(\boldsymbol{\Psi}^{-1}(\boldsymbol{X}, t), t) \quad \Rightarrow \quad \begin{cases} \dfrac{\partial \boldsymbol{x}}{\partial \boldsymbol{X}} = \dfrac{\partial \boldsymbol{x}}{\partial \boldsymbol{\chi}} \dfrac{\partial \boldsymbol{\chi}}{\partial \boldsymbol{X}} \\ \dfrac{\partial \boldsymbol{x}}{\partial t}\Big|_{\boldsymbol{X}} = \dfrac{\partial \boldsymbol{x}}{\partial t}\Big|_{\boldsymbol{\chi}} + \dfrac{\partial \boldsymbol{x}}{\partial \boldsymbol{\chi}} \dfrac{\partial \boldsymbol{\chi}}{\partial t}\Big|_{\boldsymbol{X}} \\ \Leftrightarrow \quad \boldsymbol{u} = \boldsymbol{u}_m + \dfrac{\partial \boldsymbol{x}}{\partial \boldsymbol{\chi}} \dfrac{\partial \boldsymbol{\chi}}{\partial t}\Big|_{\boldsymbol{X}} \end{cases} \tag{B.6}$$

and the transformation of any physical quantity $f_{\mathrm{L}}(\boldsymbol{X}, t)$ is

$$f_{\mathrm{L}}(\boldsymbol{X}, t) = f_{\mathrm{ALE}}(\boldsymbol{\Psi}^{-1}(\boldsymbol{\chi}, t), t) \tag{B.7}$$

where f_{ALE} is the functional form of the same physical quantity as seen in the ALE

reference domain. The corresponding space and time derivatives are

$$\frac{\partial f_{\mathrm{L}}}{\partial \boldsymbol{X}} = \frac{\partial f_{\mathrm{ALE}}}{\partial \boldsymbol{\chi}} \frac{\partial \boldsymbol{\chi}}{\partial \boldsymbol{X}} \tag{B.8}$$

$$\begin{aligned} \frac{\partial f_{\mathrm{L}}}{\partial t} &= \frac{\partial f_{\mathrm{ALE}}}{\partial t} + \frac{\partial f_{\mathrm{ALE}}}{\partial \chi} \frac{\partial \boldsymbol{\chi}}{\partial t}\Big|_{\boldsymbol{X}} \\ &= \frac{\partial f_{\mathrm{ALE}}}{\partial t} + \frac{\partial f_{\mathrm{ALE}}}{\partial \boldsymbol{x}} \frac{\partial \boldsymbol{x}}{\partial \chi} \frac{\partial \boldsymbol{\chi}}{\partial t}\Big|_{\boldsymbol{X}} \end{aligned} \tag{B.9}$$

Equation (B.9) is similar to Eq. (B.3) in the sense that it describes the material time derivative in the reference domain. Applying Eq. (B.6) this relation can be simplified to

$$\frac{\partial f_{\mathrm{L}}}{\partial t}\Big|_{\boldsymbol{X}} = \frac{\partial f_{\mathrm{ALE}}}{\partial t}\Big|_{\boldsymbol{\chi}} + \boldsymbol{u}_c \cdot \nabla f_{\mathrm{ALE}} \tag{B.10}$$

where $\boldsymbol{u}_c \equiv \boldsymbol{u} - \boldsymbol{u}_m$ is the so-called convective velocity expressing the particle velocity relative to the mesh as seen from the Eulerian frame. The term $\partial \boldsymbol{\chi}/\partial t|_{\boldsymbol{X}}$, however, expresses the particle velocity as seen from the reference domain. Between Eq. (B.3) and (B.10) the major difference is the convective velocity $\boldsymbol{u}_c$ which requires the mesh velocity $\boldsymbol{u}_m$ to be evaluated.

Appendix C

Stodola's Method

Stodola's method is an iterative procedure to determine eigenmodes and the associated frequency of a one-dimensional non-uniform Timoshenko beam. There are several other methods, which competes directly with the Stodola's method, see e.g. the modified Myklestad method presented in Fowler (1958) and a technique based on a matrix iteration described in Scanlan (1948). In the present work, however, it is found that the performance and the accuracy of the Stodola's method are sufficient. Furthermore, the numerical implementation of the Stodola's method is straight forward. In general the eigenvalue problem can be written in a matrix notation as

$$\mathbf{A}\mathbf{x} = \lambda \mathbf{x} \tag{C.1}$$

i.e. to find non-zero vectors x and positive scalars λ such that the above matrix equation is satisfied. The Stodola's iteration scheme starts with a guess, $\mathbf{x}^{(k)}$. Then, the left-hand side is evaluated such that a different set, $\mathbf{x}^{(k+1)}$ is obtained. The process repeats until convergence. The recursive form is

$$\mathbf{A}\mathbf{x}^{(k)} = \lambda \mathbf{x}^{(k+1)} \tag{C.2}$$

The iteration will converge toward the highest value of λ. The orthogonality conditions must be applied to obtain the higher modes. For the free-free Timoshenko beam, the governing equations (ODE) for the normal modes and frequencies are

$$-\Big(EI\varphi'\Big)' - kGA\Big(u' - \varphi\Big) = \omega^2 m r^2 \varphi \tag{C.3a}$$

$$-\Big[kGA(u' - \varphi)\Big]' = \omega^2 m\, u \tag{C.3b}$$

which is an eigenvalue problem with the free-free boundary condition applied to both end of the beam i.e. $M(0) = M(L) = 0$ and $Q(0) = Q(L) = 0$. The prime symbol (') denotes a spatial derivative. The orthogonality condition is

$$\int_L \Big(mr^2\varphi_i\varphi_j + mu_iu_j\Big)\, dx = \begin{cases} 0 & \text{for} \quad \omega_i \neq \omega_j \\ A_j & \text{for} \quad \omega_i = \omega_j \end{cases}$$

The rigid body modes i.e. heave and pitch are

$$\begin{aligned} \text{heave, j=0}: \quad & u_0 = 1 && \varphi_0 = 0 && \omega_0 = 0 \\ \text{pitch, j=1}: \quad & u_1 = x - x_{\text{CG}} && \varphi_1 = 1 && \omega_1 = 0 \end{aligned}$$

The following scheme are for calculating the flexible mode shapes i.e. $j = 2, 3, ..., n$.

1. **Define next mode:** Increase j by one, initial value shall be $j = 2$.

2. **Inertial guess:** Use the previous result as the initial guess, $u_j = u_{j-1}$, $\varphi_j = \varphi_{j-1}$

3. **Apply ODE:** Evaluate $Q(x)$, $M(x)$, and a new guess of φ_j and u_j in the following order

$$Q(x) = -\int_{x_{\text{min}}}^{x} m u_j(\tilde{x})\, d\tilde{x} \tag{C.4a}$$

$$M(x) = -\int_{x_{\text{min}}}^{x} \left[m r^2 \varphi_j(\tilde{x}) + Q(\tilde{x}) \right] d\tilde{x} \tag{C.4b}$$

$$\varphi_j(x) = \int_{x_{\text{min}}}^{x} \frac{M(\tilde{x})}{EI}\, d\tilde{x} \tag{C.4c}$$

$$u_j(x) = \int_{x_{\text{min}}}^{x} \left[\frac{Q(\tilde{x})}{kGA} + \varphi_j(\tilde{x}) \right] d\tilde{x} \tag{C.4d}$$

4. **Normalize the new guess:**

$$\begin{aligned} \tilde{\varphi}_j(x) &= \frac{\varphi_j(x)}{\beta} \\ \tilde{u}_j(x) &= \frac{u_j(x)}{\beta} \end{aligned} \qquad \text{where} \quad \beta = \sqrt{\int_L \left(m r^2 \varphi_j^2 + m u_j^2 \right) dx} \tag{C.5}$$

5. **Enforce the orthogonality with previous mode shapes:**

$$\varphi_j(x) = \tilde{\varphi}_j - \sum_{i=0}^{j-1} \frac{\varphi_i}{A_i} \int_L \left(m r^2 \varphi_i \tilde{\varphi}_j + m u_i \tilde{u}_j \right) dx \tag{C.6a}$$

$$u_j(x) = \tilde{u}_j - \sum_{i=0}^{j-1} \frac{u_i}{A_i} \int_L \left(m r^2 \varphi_i \tilde{\varphi}_j + m u_i \tilde{u}_j \right) dx \tag{C.6b}$$

6. **Check for convergence:** Repeat from Step 3 if β has not yet converged to a pre-specified tolerance.

7. **End iteration:** Repeat from Step 1 until all interested mode shapes have been determined.

Notice that the rigid body mode must be accounted for in the orthogonal condition. Once the iteration has converged, the frequency can be evaluated from $\omega_j = 1/\sqrt{\beta}$.

PhD Theses
Department of Naval Architecture and Offshore Engineering
Technical University of Denmark · Kgs. Lyngby

1961 Strøm-Tejsen, J.
Damage Stability Calculations on the Computer DASK.

1963 Silovic, V.
A Five Hole Spherical Pilot Tube for three Dimensional Wake Measurements.

1964 Chomchuenchit, V.
Determination of the Weight Distribution of Ship Models.

1965 Chislett, M.S.
A Planar Motion Mechanism.

1965 Nicordhanon, P.
A Phase Changer in the HyA Planar Motion Mechanism and Calculation of Phase Angle.

1966 Jensen, B.
Anvendelse af statistiske metoder til kontrol af forskellige eksisterende tilnærmelsesformler og udarbejdelse af nye til bestemmelse af skibes tonnage og stabilitet.

1968 Aage, C.
Eksperimentel og beregningsmæssig bestemmelse af vindkræfter på skibe.

1972 Prytz, K.
Datamatorienterede studier af planende bådes fremdrivningsforhold.

1977 Hee, J.M.
Store sideportes indflydelse på langskibs styrke.

1977 Madsen, N.F.
Vibrations in Ships.

1978 Andersen, P.
Bølgeinducerede bevægelser og belastninger for skib på lægt vand.

1978 Römeling, J.U.
Buling af afstivede pladepaneler.

1978 Sørensen, H.H.
Sammenkobling af rotations-symmetriske og generelle tre-dimensionale konstruktioner i elementmetode-beregninger.

1980 Fabian, O.
Elastic-Plastic Collapse of Long Tubes under Combined Bending and Pressure Load.

1980 Petersen, M.J.
Ship Collisions.

1981 Gong, J.
A Rational Approach to Automatic Design of Ship Sections.

1982 Nielsen, K.
Bølgeenergimaskiner.

1984 Nielsen, N.J.R.
Structural Optimization of Ship Structures.

1984 Liebst, J.
Torsion of Container Ships.

1985 Gjersøe-Fog, N.
Mathematical Definition of Ship Hull Surfaces using B-splines.

1985 Jensen, P.S.
Stationære skibsbølger.

1986 Nedergaard, H.
Collapse of Offshore Platforms.

1986 Yan, J.-Q.
3-D Analysis of Pipelines during Laying.

1987 Holt-Madsen, A.
A Quadratic Theory for the Fatigue Life Estimation of Offshore Structures.

1989 Andersen, S.V.
Numerical Treatment of the Design-Analysis Problem of Ship Propellers using Vortex Lattice Methods.

1989 Rasmussen, J.
Structural Design of Sandwich Structures.

1990 Baatrup, J.
Structural Analysis of Marine Structures.

1990 Wedel-Heinen, J.
Vibration Analysis of Imperfect Elements in Marine Structures.

1991 Almlund, J.
Life Cycle Model for Offshore Installations for Use in Prospect Evaluation.

1991 Back-Pedersen, A.
Analysis of Slender Marine Structures.

1992 Bendiksen, E.
Hull Girder Collapse.

1992 Petersen, J.B.
Non-Linear Strip Theories for Ship Response in Waves.

1992 Schalck, S.
Ship Design Using B-spline Patches.

1993 Kierkegaard, H.
Ship Collisions with Icebergs.

1994 Pedersen, B.
A Free-Surface Analysis of a Two-Dimensional Moving Surface-Piercing Body.

1994 Hansen, P.F.
Reliability Analysis of a Midship Section.

1994 Michelsen, J.
A Free-Form Geometric Modelling Approach with Ship Design Applications.

1995 Hansen, A.M.
Reliability Methods for the Longitudinal Strength of Ships.

1995 Branner, K.
Capacity and Lifetime of Foam Core Sandwich Structures.

1995 Schack, C.
Skrogudvikling af hurtiggående færger med henblik på sødygtighed og lav modstand.

1997 Simonsen, B.C.
Mechanics of Ship Grounding.

1997 Olesen, N.A.
Turbulent Flow past Ship Hulls.

1997 Riber, H.J.
Response Analysis of Dynamically Loaded Composite Panels.

1998 Andersen, M.R.
Fatigue Crack Initiation and Growth in Ship Structures.

1998 Nielsen, L.P.
Structural Capacity of the Hull Girder.

1999 Zhang, S.
The Mechanics of Ship Collisions.

1999 Birk-Sørensen, M.
Simulation of Welding Distortions of Ship Sections.

1999 Jensen, K.
Analysis and Documentation of Ancient Ships.

2000 Wang, Z.
Hydroelastic Analysis of High-Speed Ships.

2000 Petersen, T.
Wave Load Prediction—a Design Tool.

2000 Banke, L.
Flexible Pipe End Fitting.

2000 Simonsen, C.D.
Rudder, Propeller and Hull Interaction by RANS.

2000 Clausen, H.B.
Plate Forming by Line Heating.

2000 Krishnaswamy, P.
Flow Modelling for Partially Cavitating Hydrofoils.

2000 Andersen, L.F.
Residual Stresses and Deformations in Steel Structures.

2000 Friis-Hansen, A.
Bayesian Networks as a Decision Support Tool in Marine Applications.

PhD Theses
Maritime Engineering · Department of Mechanical Engineering
Technical University of Denmark · Kgs. Lyngby

2001 Lützen, M.
Ship Collision Damage.

2001 Olsen, A.S.
Optimisation of Propellers Using the Vortex-Lattice Method.

2002 Rüdinger, F.
Modelling and Estimation of Damping in Non-linear Random Vibration.

2002 Bredmose, H.
Deterministic Modelling of Water Waves in the Frequency Domain.

2003 Urban, J.
Crushing and Fracture of Lightweight Structures.

2003 Lazarov, B.S.
Slepian Simulations of Plastic Displacement of Randomly Excited Hysteretic Structures.

2003 Ravn, E.S.
Probabilistic Damage Stability of Ro-Ro Ships.

2003 Törnqvist, R.
Design of Crashworthy Ship Structures.

2003 Nielsen, K.B.
Numerical Prediction of Green Water Loads on Ships.

2004 Folsø, R.
Comfort Monitoring of High Speed Passenger Ferries.

2004 Fuhrman, D.R.
Numerical Solutions of Boussinesq Equations for Fully Nonlinear and Extremely Dispersive Water Waves.

2004 Hjort, S.
Incompressible Boundary Layer Instability and Transition.

2004 Dietz, J. S.
Application of Conditional Waves as Critical Wave Episodes for Extreme Loads on Marine Structures.

2004 Berggreen, C.
Damage Tolerance of Debonded Sandwich Structures.

2005 Berntsen, K. N.
Modelling granular media and molecular Dynamics Simulations of Ellipses.

2005 Høgsberg, J. R.
Modelling of Dampers and Damping in Structures.

2005 Nielsen, U. D.
Estimation of Directional Wave Spectra from Measured Ship Responses.

2005 Reck, M.
Computational fluid dynamics, with detached eddy simulation and the immersed boundary technique, applied to oscillating airfoils and vortex generators.

2005 Vidic-Perunovic, J.
Springing Response due to Bidirectional Wave Excitation.

2005 Zhang, H.
A Deterministic Combination of Numerical and Physical Models for Coastal Waves.

2006 Cavar, D.
Large Eddy Simulation of Industrially Relevant Flows.

2006 Engsig-Karup, A. P.
Unstructured Nodel DG-FEM Solution of High-order Boussinesq-type Equations.

2006 Yamada, Y.
Bulbous Buffer Bows: A Measure to Reduce Oil Spill in Tanker Collisions.

2007 Dam, B. S.
Experimental and numerical investigations of sprays in two stroke diesel engines.

2007 Zhu, W. J.
Aero-Acoustic Computations of Wind Turbines.

2008 Lundsgaard-Larsen, C.
Predicting and Improving Damage Tolerance of Composite Structures.

2008 Troldborg, N.
Actuator Line Modeling of Wind Turbine Wakes.

2009 Joncquez, S. A. G.
Second-order Forces and Moments acting on Ships in Waves.

2009 Velte, C. M.
Characterization of Vortex Generator Induced Flow.

2010 Lajic, Z.
Fault - Tolerant Onboard Monitoring and Decision Support Systems.

2010 Rasmussen, J. K.
Inside-out electrical capacitance tomography for downhole multiphase flow evaluation.

2010 Shin, K. W.
Cavitation simulation on marine propellers.

2011 Kærgård, K.
Numerical Modeling of Shoreline Undulations.

2011 Bhowmik, S.
Modelling and Control of Magnetorheological Damper: Real-time implementation and experimental verification.

2011 Moslemian, R.
Residual Strength and Fatigue Lifetime of Debond Damaged Sandwich Structures.

2011 Zambrano, H. A.
Molecular Dynamics Studies of Nanofl uidic Devices.

2011 Blasques, J. P.
Optimal Design of Laminated Composite Beams.

2011 Jacobsen, N. G.
A Full Hydro- and Morphodynamic Description of Breaker Bar Development.

2011 Svendsen, M. N.
Wind Turbine Rotors with Active Vibration Control.

2012 Hansen, N. M.
Interaction between Seabed Soil and Offshore Wind Turbine Foundations.

2012 Lindberg, O.
Multiscale Simulation of Wave Forces on Ocean Energy Devices.

2012 Hansen, S. V.
Optimization and Validation of Mathematical Ship Models used in Routing and Performances Systems.

DTU Mechanical Engineering
Section of Fluid Mechanics, Coastal and Maritime Engineering
Technical University of Denmark

Nils Koppels Allé, Bld. 403
DK- 2800 Kgs. Lyngby
Denmark
Phone (+45) 4525 1360
Fax (+45) 4588 4325
www.mek.dtu.dk

ISBN. 978-87-7475-356-8

DCAMM
Danish Center for Applied Mathematics and Mechanics

Nils Koppels Allé, Bld. 404
DK-2800 Kgs. Lyngby
Denmark
Phone (+45) 4525 4250
Fax (+45) 4593 1475
www.dcamm.dk
ISSN: 0903-1685